

# REPORT DOCUMENTATION PAGE

Form Approved  
OMB NO. 0704-0188

Public Reporting burden for this collection of information is estimated to average 1 hour per response, including the time for reviewing instructions, searching existing data sources, gathering and maintaining the data needed, and completing and reviewing the collection of information. Send comment regarding this burden estimate or any other aspect of this collection of information, including suggestions for reducing this burden, to Washington Headquarters Services, Directorate for Information Operations and Reports, 1215 Jefferson Davis Highway, Suite 1204, Arlington, VA 22202-4302, and to the Office of Management and Budget, Paperwork Reduction Project (0704-0188), Washington, DC 20503.

1. AGENCY USE ONLY (Leave Blank)		2. REPORT DATE 7 Feb 01		3. REPORT TYPE AND DATES COVERED Final: 1 Sept 96 - 31 Aug 00	
4. TITLE AND SUBTITLE Supercapacitors and Batteries from Sol-Gel Derived Carbon - Metal Oxide Electrodes				5. FUNDING NUMBERS G-No. DAAH04-96-1-0421	
6. AUTHOR(S) James A. Ritter, PI					
7. PERFORMING ORGANIZATION NAME(S) AND ADDRESS(ES) University of South Carolina Columbia, SC 29208				8. PERFORMING ORGANIZATION REPORT NUMBER	
9. SPONSORING / MONITORING AGENCY NAME(S) AND ADDRESS(ES) U. S. Army Research Office P.O. Box 12211 Research Triangle Park, NC 27709-2211				10. SPONSORING / MONITORING AGENCY REPORT NUMBER ARO36360.9-RT-DPS	
11. SUPPLEMENTARY NOTES The views, opinions and/or findings contained in this report are those of the author(s) and should not be construed as an official Department of the Army position, policy or decision, unless so designated by other documentation.					
12 a. DISTRIBUTION / AVAILABILITY STATEMENT Approved for public release; distribution unlimited.				12 b. DISTRIBUTION CODE	
13. ABSTRACT (Maximum 200 words) The duration of this program was 48 months (7 Sept. 96-31 Aug. 00). During this time, significant accomplishments were achieved. Eight refereed research articles are in print; one proceedings volume publication is in print; and four manuscripts are under review. They collective deal with the synthesis, characterization and modeling of supercapacitors and lithium ion batteries. Six graduate students contributed to the accomplishments of this research program: four have received Ph.D. degrees, one has received an M.S. degree, and one will defend his Ph.D. in the Spring of 2001. All those that received degrees are either employed in a major US company or carrying out postgraduate research at a US institution. These students were supervised by a unique research team comprised of five experts with wide ranges of expertise in the electrochemical area, including materials synthesis and characterization, mathematical modeling, and molecular modeling. Major accomplishments are too numerous to list here, but they encompass the objectives of this program, which were to produce a new class of sol-gel based capacitors and batteries, and to develop a detailed understanding of how the microscopic material properties control the macroscopic material performance, and ultimately provide new mathematical screening tools that will reduce the cost of sol-gel materials synthesis and characterization, and aid in the systematic design and development of novel electrode systems as electrochemical power sources. Many of these goals were achieved, and research is continuing in these areas that were initiated with this grant.					
14. SUBJECT TERMS Supercapacitors, Batteries, Composite Materials, Carbon-Metal Materials, Carbon Metal Oxide Materials				15. NUMBER OF PAGES 9	
				16. PRICE CODE	
17. SECURITY CLASSIFICATION OR REPORT UNCLASSIFIED	18. SECURITY CLASSIFICATION ON THIS PAGE UNCLASSIFIED	19. SECURITY CLASSIFICATION OF ABSTRACT UNCLASSIFIED	20. LIMITATION OF ABSTRACT UL		

20010409 055

---

**REPORT DOCUMENTATION PAGE (SF298)**  
**(Continuation Sheet)**

---

**Contract No. DAAH04-96-1-0421, James A. Ritter, PI**

**Supercapacitors and Batteries from  
Sol-Gel Derived Carbon Metal Oxide Electrodes  
Final Report**

- 1. Forward:** Not applicable.
- 2. Table of Contents:** Not applicable.
- 3. List of Appendixes:**

The appendix contains copies of refereed articles, proceedings volume publications, and manuscripts. A blue sheet of paper is used to separate each publication. The title of each publication is given in chronological order in section 10 of this report.

**4. Statement of the Problem Studied:**

With a one-year, no cost extension, the duration of this three-year program was forty-eight months (7 September 1996 to 31 August 2000). One objective of this program was to produce a new class of sol-gel based capacitors and batteries. Another objective was to develop a detailed understanding of how the microscopic material properties control the macroscopic material performance, and ultimately provide new mathematical screening tools that will reduce the cost of sol-gel materials synthesis and characterization, and aid in the systematic design and development of novel electrode systems as electrochemical power sources. Significant accomplishments were achieved in each of these areas. The team that carried out the research, and highlights of these accomplishments are given below.

**5. Summary of the Most Important Results:**

A systematic experimental and theoretical program was carried out, with a unique research team comprised of five experts whose expertise spans sol-gel synthesis, characterization and modeling of controlled pore materials, to electrochemical materials characterization and electrode fabrication and testing, to first-principle mathematical modeling of battery and capacitor systems, to molecular modeling of electrode materials. Three of the experts were listed in the original proposal (J. A. Ritter, J. W. Weidner and R. E. White). The two additional experts (B. N. Popov and P. B. Balbuena) were involved with similar projects being funded elsewhere and were willing to contribute to this project by way of co-advising graduate students, etc. Another contribution to this program came from J. W. Weidner during his sabbatical leave at UC-Berkeley, where he collaborated with J. Newman on a project. The numerous accomplishments that were achieved are summarized below. More details on these

---

REPORT DOCUMENTATION PAGE (SF298)  
(Continuation Sheet)

---

accomplishments are reported in the refereed articles, proceedings volume publications, and manuscripts given in the appendix, section 10.

Very fine cobalt oxide xerogel powders were prepared using a unique solution chemistry associated with the sol-gel process. The effect of thermal treatment on the surface area, pore volume, crystallinity, particle structure, and corresponding electrochemical properties of the resulting xerogels was investigated and found to have significant effects on all of these properties. The xerogel remained amorphous as  $\text{Co}(\text{OH})_2$  up to 160 °C, and exhibited maxima in both the surface area and pore volume at this temperature. With an increase in the temperature above 200 °C, both the surface area and pore volume decreased sharply, because the amorphous  $\text{Co}(\text{OH})_2$  decomposed to form  $\text{CoO}$  that was subsequently oxidized to form crystalline  $\text{Co}_3\text{O}_4$ . In addition, the changes in the surface area, pore volume, crystallinity, and particle structure all had significant but coupled effects on the electrochemical properties of the xerogels. A maximum capacitance of 291 F/g was obtained from an electrode prepared with the  $\text{CoO}_x$  xerogel calcined at 150 °C, which was consistent with the maxima exhibited in both the surface area and pore volume; this capacitance was attributed solely to a surface redox mechanism. The cycle life of this electrode was also very stable for many thousands of cycles.

A full  $2^4$  factorial design study was carried out on sol-gel derived resorcinol-formaldehyde carbonized resins for use as the anode in the lithium ion battery. This statistical design approach was used to determine the effect of initial solution pH, wt% solids, pyrolysis temperature and gel type (aerogel or xerogel) on the final carbon product. The response variables were surface area, pore volume, and reversibility of the first and second cycle charge/discharge capacities. The results from the sixteen different carbon gels showed that the carbon gel with nearly the lowest surface area and pore volume gave rise to the highest reversible capacity and coulombic efficiency, consistent with results reported in the literature. Moreover, the statistical design approach proved to be very useful in relating many synthesis parameters to the physical properties of the materials, based on a minimal number of actual syntheses. The traditional one-at-a-time approach would have required many more actual syntheses to be carried to obtain the same level of information.

Sol-gel derived high surface area carbon-ruthenium xerogels were prepared from carbonized resorcinol-formaldehyde resins containing an electrochemically active form of ruthenium oxide. The electrochemical capacitance of these materials increased with an increase in the ruthenium content indicating the presence of pseudocapacitance associated with the ruthenium oxide undergoing reversible faradaic redox reactions. A specific capacitance of 256 F/g (single electrode) was obtained from the carbon xerogel containing 14 wt% Ru, which corresponded to more than 50% utilization of the ruthenium. The double layer accounted for 40% of this capacitance. This material was also electrochemically stable, showing no change in a cyclic voltammogram for over 2000 cycles.

20010409 055

---

REPORT DOCUMENTATION PAGE (SF298)  
(Continuation Sheet)

---

A mathematical model of an electrochemical capacitor with hydrous ruthenium oxide ( $\text{RuO}_2 \cdot x\text{H}_2\text{O}$ ) electrodes including both double-layer and surface Faradaic processes is developed to predict the behavior of the capacitor under the conditions of galvanostatic charge and discharge. The effect of  $\text{RuO}_2 \cdot x\text{H}_2\text{O}$  particle size is studied and shows that the smaller the particles the better the performance because of the increased surface area per unit volume or mass. The model also predicts that the Faradaic process increases significantly the energy per unit volume of the capacitor for power densities of 100 kW/l or less.

Nine different sol-gel derived carbon xerogels were prepared with different pore structures by varying the carbonization temperature (in flowing  $\text{N}_2$ ) and activation time (in 5%  $\text{CO}_2$  in  $\text{N}_2$ ). For each of these carbon xerogels, mesopore and micropore size distributions and cumulative surface areas were extracted from a density functional theory analysis. Increasing the carbonization temperature caused a decrease in the number of micropores in the 6 Å range but had little effect on the mesopore size distribution and thus mesopore cumulative surface area. Increasing the  $\text{CO}_2$ -activation time caused an increase in the number of both micro and mesopores where pores in the 6 Å width range eventually became pores in the 12 Å width range. The electrochemical double-layer capacitance of the carbon xerogels was found to correlate well with changes in the pore structure, and it was determined that pores less than about 8 Å in width did not contribute to the DLC.

Nickel oxide films were prepared by electrochemically precipitating the hydroxide and heating it in air to form the oxide. The resulting oxide films behave as a capacitor. The capacitance of the oxide depends on the heating temperature, and it shows a maximum at 300°C. The mechanism of charge storage was studied by measuring the capacitance and surface area as a function of heating temperature, and the capacitance in different electrolytes and potential windows. The charge-storage mechanism is believed to be a surface redox reaction involving adsorbed hydroxyl ion.

A novel approach for suppressing the solvated lithium intercalation in graphite was developed by microencapsulating graphite with nanosized Ni-composite particles. The Ni-composite graphite showed a great improvement in the charge-discharge performance, coulomb efficiency and cycling behavior when used as the negative electrode in a Li-ion cell with propylene carbonate (PC)-based electrolyte. For example, a 10 wt% Ni-composite coating increased the initial charge-discharge coulomb efficiency of SFG75 graphite from 59 to 84% and the reversible discharge capacity by 30~40 mAh/g. This Ni-composite coating consisted of nanosized particles distributed over the surface of the graphite particle, which effectively blocked some of the edge surfaces exposed to the electrolyte. This minimized solvated lithium intercalation at these edge sites, which subsequently minimized PC reduction within and exfoliation of the graphene layers, and also gas evolution; a corresponding improvement in both the charge discharge performance and safety of the negative electrode in a rechargeable Li-ion cell resulted.



---

REPORT DOCUMENTATION PAGE (SF298)  
(Continuation Sheet)

---

Electrochemical impedance and self-discharge studies were carried out to investigate the kinetics of lithium intercalation into bare and Ni coated KS10 graphite. Values of the charge transfer resistances, exchange current densities, surface film resistances and lithium ion diffusion coefficients as functions of the state of charge (SOC) all favored the 10 wt% Ni-composite KS10 graphite over bare KS10 graphite when these materials were used as the negative electrode in a Li-ion cell with propylene carbonate (PC)-based electrolyte. The charge transfer resistances were always lower and gave rise to 24 to 32 % larger exchange current densities, which increased from 103 and 425 mA/g as the SOC increased; the surface film resistances for both materials were similar and both decreased with increasing SOC from 0.24 to 0.05  $\Omega \cdot g$ ; and the lithium ion diffusion coefficients were always slightly larger, ranging between  $1.09 \times 10^{-9}$  and  $6.7 \times 10^{-9}$  cm<sup>2</sup>/s. Results from the self-discharge study also favored the 10 wt% Ni-composite KS10, which exhibited less capacity loss over a ten day period compared to bare KS10.

The effects of the carbonization temperature (in N<sub>2</sub>) and CO<sub>2</sub>-activation time (in 5% CO<sub>2</sub> in N<sub>2</sub>) on the pore structure of carbon xerogels, derived from the sol-gel polymerization of resorcinol-formaldehyde resins, were studied in detail. As the carbonization temperature increased, the number of micropores in the 6 Å range decreased, with essentially no effect on the pores in the mesopore range, and the cumulative surface areas and pore volumes both decreased, but only marginally. As the CO<sub>2</sub>-activation time increased, the number of micropores and mesopores both increased, where pores in the 6 Å range eventually became pores in the 13 Å range, and the cumulative surface areas and pore volumes both increased significantly. The skeletal densities also increased significantly, approaching that of graphite, with an increase in both the carbonization temperature and CO<sub>2</sub>-activation time, but the nanoparticle size was largely unaffected. Weight loss was nearly independent of the carbonization temperature at about 50 %; but it was strongly dependent on the CO<sub>2</sub>-activation time with a maximum weight loss of about 75 %.

A procedure is developed whereby experimental changes in capacity and mass can be correlated with the nonstoichiometry and point defect structure of nickel hydroxide thin films. The capacity and mass of the films are simultaneously monitored using an electrochemical quartz crystal microbalance (EQCM). This information is used as input into the point defect-containing structural model to track the changes that occur during short term cycling. Pure nickel hydroxide films have been chosen as the test material. The loss in capacity on cycling is explained based on incomplete incorporation of potassium ions in (or near) the nickel vacancy during charge, as additional protons are then allowed to occupy the vacant lattice site. The model and methodology developed in this paper can be used to correlate electrochemical signatures with material microstructure.

Carbon gels were synthesized via the sol-gel polycondensation of resorcinol with formaldehyde using a sodium carbonate catalyst. A full 2<sup>4</sup> factorial design study was performed to study the effect of initial solution pH, wt% solids, pyrolysis temperature and gel type (aerogel or xerogel) on the surface area, pore volume and electrochemical capacitance. It has been found

---

REPORT DOCUMENTATION PAGE (SF298)  
(Continuation Sheet)

---

that the gels showing the highest surface area also show the highest capacitance. These include the aerogels made with a high initial solution pH and a low pyrolysis temperature. Pore volume is also maximized with an aerogel and a high initial gel pH. Results also indicate there are interaction effects occurring between factors, especially between initial solution pH and gel type which make this factorial design approach an effective means of studying these materials.

Approximate models are developed, based on second, fourth and sixth order polynomials, that describe the concentration profile of an electrochemically active species in a spherical electrode particle. Analytical expressions are obtained that describe how the concentration profiles, surface concentrations and electrode utilization change during the galvanostatic discharge of an electrode particle. Based on a comparison with an exact analytical model over a wide range of dimensionless current densities, all three approximate models performed extremely well in predicting these quantities. Quantitative criterion for the validity of these models is also developed and shows that the sixth order, four parameter approximate model is the best. These approximate models, or similarly developed models, should find extensive use in simplifying the modeling of complex electrochemical systems without sacrificing much accuracy.

The nickel hydroxide electrode is known to exhibit a stable hysteresis loop, with the potential on charge being higher than that on discharge at every state-of-charge. What we show here is that this loop created during a complete charge and discharge (*i.e.*, boundary curves) is not sufficient to define the state of the system. Rather, internal loops within the boundary curves (*i.e.*, scanning curves) can be generated that access potentials between the boundary curves. The potential obtained at any state-of-charge, as well as how the material charges and discharges from that point, depends on the cycling history of the material. Analysis of the boundary and scanning curves suggests that the electrode consists of a number of individual units or domains, each of which exhibits two or more metastable states. The cycling behavior of the nickel hydroxide electrode is discussed within the context of previously developed theoretical arguments regarding domain theory. Although the specific cause for the metastability in each domain is not understood, considerable insights are provided into the history-dependent behavior of the nickel hydroxide electrode. Finally, an empirical procedure is developed to predict the scanning curves based on the boundary curves.

Many researchers, based on the primitive diffuse layer model of the electrical double layer, have carried out Monte Carlo and other molecular simulations, and density functional theory (DFT) analyses, of the ion distribution near a charged wall over a range of reduced surface charge densities. At higher reduced surface charge densities, they revealed two fundamental phenomena: layering of the counter-ions and charge inversion. All of the results from these various studies in the literature agree well with each other; however, none of them contrasted their results against those expected in an actual electrochemical system to determine whether they were physically realistic. Therefore, the objective of this note is to report on a density functional theory (DFT) analysis of the same system and under the same conditions; but in this

---

REPORT DOCUMENTATION PAGE (SF298)  
(Continuation Sheet)

---

case, a significant effort is expended on comparing the results with those that are expected in an actual electrochemical system. It is shown that the DFT approach does very well in predicting reasonable values of the double layer capacitance of aqueous-based systems, based on the restricted primitive model of the double layer. But this is true only when the surface charge density is limited to physically realistic values, and also when the effect of the Stern layer is accounted for in the analysis. It is anticipated that the other models discussed in this work would also give reasonable values of the double layer capacitance under these circumstances.

**6. List of Refereed Articles, Proceedings Volume Publications, and Manuscripts:**

- C. Lin, J. A. Ritter and B. N. Popov, "Characterization of Sol-Gel Derived Cobalt Oxide Xerogels as Electrochemical Capacitors," *J. Electrochemical Society*, 145, 4091-4103 (1998).
- E. J. Zanto, J. A. Ritter and B. N. Popov, "Sol-Gel Derived Carbon Aerogels and Xerogels for Use as the Anode in the Lithium Ion Battery," in *Lithium Batteries, Vol. 98-16*, (S. Surampudi and R. Marsh, eds.), The Electrochemical Society Proceedings Series, NJ (1998).
- C. Lin, J. A. Ritter and B. N. Popov, "Development of Carbon-Metal Oxide Supercapacitors from Sol-Gel Derived Carbon-Ruthenium Xerogels," *J. Electrochemical Society*, 146, 3155-3160 (1999).
- C. Lin, J. A. Ritter, B. N. Popov and R. E. White, "A Mathematical Model of an Electrochemical Capacitor with Double Layer and Faradaic Processes," *J. Electrochemical Society*, 146, 3168-3175 (1999).
- C. Lin, J. A. Ritter and B. N. Popov, "Correlation of the Double-Layer Capacitance with the Pore Structure of Sol-Gel Derived Carbon Xerogels," *J. Electrochemical Society*, 146, 3639-3643 (1999).
- V. Srinivasan and J. W. Weidner, "Studies on the Capacitance of Nickel Oxide Films: Effect of Heating Temperature and Electrolyte Concentration," *J. Electrochemical Society*, 147, 880-885 (2000).
- P. Yu, J. A. Ritter, R. E. White and B. N. Popov, "Ni-Composite Microencapsulated Graphite as the Negative Electrode in Lithium-Ion Batteries. Part I. Initial Irreversible Capacity Study" *J. Electrochemical Society*, 147, 1280-1285 (2000).
- P. Yu, J. A. Ritter, B. N. Popov, and R. E. White, "Ni-Composite Microencapsulated Graphite as the Negative Electrode in Lithium-Ion Batteries. Part II. Electrochemical Impedance and Self-Discharge Studies," *J. Electrochemical Society*, 147, 2081-2085 (2000).
- C. Lin and J. A. Ritter, "Carbonization and Activation of Sol-Gel Derived Carbon Xerogels," *Carbon*, 38, 849-861 (2000).
- V. Srinivasan, B. C. Cornilsen, and J. W. Weidner, "A Nonstoichiometric Structural Model to Characterize Changes in the Nickel Hydroxide Electrode During Cycling," *J. Electrochemical Society*, submitted (2000).
- E. J. Zanto, J. A. Ritter, and B. P. Popov, "Sol-Gel Derived Carbon Aerogels and Xerogels 1. Electrochemical Characterization from a Statistical Design Approach," *Carbon*, submitted (2000).

---

**REPORT DOCUMENTATION PAGE (SF298)**  
**(Continuation Sheet)**

---

- V. R. Subramanian, J. A. Ritter, and R. E. White, "Approximate Solutions for Galvanostatic Discharge of Spherical Particles-1. Constant Diffusion Coefficient," *J. Electrochemical Society*, submitted (2000).
- V. Srinivasan, J. W. Weidner, and J. Newman, "Hysteresis During Cycling of Nickel Hydroxide Active Material," *J. Electrochemical Society*, submitted (2000).
- H. Pan, J. A. Ritter, and P. B. Balbuena, "Practical Considerations in Modeling the Electrochemical Double Layer by Density Functional Theory," *Langmuir*, submitted (2000).

**7. Scientific Personnel:**

Six senior personnel contributed to the accomplishments of this research program: Dr. James A. Ritter served as the Principal Investigator (PI), and Drs. J. W. Weidner and R. E. White served as co-PIs. Other senior personnel included Drs. B. N. Popov, P. B. Balbuena and J. Newman. These senior personnel collectively served as graduate student research advisors, co-advisors, or collaborators.

Six graduate students contributed to the accomplishments of this research program. Four have received Ph.D. degrees, one has received an M.S. degree, and one will defend his Ph.D. in the Spring of 2001.

- Chuan Lin, received his Ph.D. entitled, "Sol-Gel Derived Electrode Materials for Supercapacitor Applications," in August 1998.
- Emily Zanto, received her M.S. entitled, "Sol-Gel Derived Materials for Use as Adsorbents, Double Layer Capacitors and Lithium Ion Intercalation Compounds," in August 1999.
- Huanhua Pan, Ph.D. received his Ph.D. entitled, "Application of Density Functional Theory to Interfacial Phenomena," in August 1999.
- Ping Yu, Ph.D. received her Ph.D. entitled, "Synthesis and Characterization of Composite Graphite as the Negative Electrode in the Lithium-Ion Batteries," in August 2000.
- Venkat Srinivasan, received his Ph.D. entitled, "Characterization and Analysis of Thin-Film Nickel Oxide and Hydroxide for use in High-Power Energy-Storage Devices," in August 2000.
- Venkat R. Subramanian, Ph.D. graduate student, focusing on developing more efficient solution techniques for use in the simulation of complex electrochemical systems.

**8. Report of Inventions:** None to report.

**9. Bibliography:** Not applicable.

---

REPORT DOCUMENTATION PAGE (SF298)  
(Continuation Sheet)

---

**10. Appendix: Copies of Refereed Articles, Proceedings Volume Publications, and Manuscripts:**

1. C. Lin, J. A. Ritter and B. N. Popov, "Characterization of Sol-Gel Derived Cobalt Oxide Xerogels as Electrochemical Capacitors," *J. Electrochemical Society*, 145, 4091-4103 (1998).
2. E. J. Zanto, J. A. Ritter and B. N. Popov, "Sol-Gel Derived Carbon Aerogels and Xerogels for Use as the Anode in the Lithium Ion Battery," in *Lithium Batteries, Vol. 98-16*, (S. Surampudi and R. Marsh, eds.), The Electrochemical Society Proceedings Series, NJ (1998).
3. C. Lin, J. A. Ritter and B. N. Popov, "Development of Carbon-Metal Oxide Supercapacitors from Sol-Gel Derived Carbon-Ruthenium Xerogels," *J. Electrochemical Society*, 146, 3155-3160 (1999).
4. C. Lin, J. A. Ritter, B. N. Popov and R. E. White, "A Mathematical Model of an Electrochemical Capacitor with Double Layer and Faradaic Processes," *J. Electrochemical Society*, 146, 3168-3175 (1999).
5. C. Lin, J. A. Ritter and B. N. Popov, "Correlation of the Double-Layer Capacitance with the Pore Structure of Sol-Gel Derived Carbon Xerogels," *J. Electrochemical Society*, 146, 3639-3643 (1999).
6. V. Srinivasan and J. W. Weidner, "Studies on the Capacitance of Nickel Oxide Films: Effect of Heating Temperature and Electrolyte Concentration," *J. Electrochemical Society*, 147, 880-885 (2000).
7. P. Yu, J. A. Ritter, R. E. White and B. N. Popov, "Ni-Composite Microencapsulated Graphite as the Negative Electrode in Lithium-Ion Batteries. Part I. Initial Irreversible Capacity Study" *J. Electrochemical Society*, 147, 1280-1285 (2000).
8. P. Yu, J. A. Ritter, B. N. Popov, and R. E. White, "Ni-Composite Microencapsulated Graphite as the Negative Electrode in Lithium-Ion Batteries. Part II. Electrochemical Impedance and Self-Discharge Studies," *J. Electrochemical Society*, 147, 2081-2085 (2000).
9. C. Lin and J. A. Ritter, "Carbonization and Activation of Sol-Gel Derived Carbon Xerogels," *Carbon*, 38, 849-861 (2000).
10. V. Srinivasan, B. C. Cornilsen, and J. W. Weidner, "A Nonstoichiometric Structural Model to Characterize Changes in the Nickel Hydroxide Electrode During Cycling," *J. Electrochemical Society*, submitted (2000).
11. E. J. Zanto, J. A. Ritter, and B. P. Popov, "Sol-Gel Derived Carbon Aerogels and Xerogels 1. Electrochemical Characterization from a Statistical Design Approach," *Carbon*, submitted (2000).
12. V. R. Subramanian, J. A. Ritter, and R. E. White, "Approximate Solutions for Galvanostatic Discharge of Spherical Particles-1. Constant Diffusion Coefficient," *J. Electrochemical Society*, submitted (2000).
13. V. Srinivasan, J. W. Weidner, and J. Newman, "Hysteresis During Cycling of Nickel Hydroxide Active Material," *J. Electrochemical Society*, submitted (2000).
14. H. Pan, J. A. Ritter, and P. B. Balbuena, "Practical Considerations in Modeling the Electrochemical Double Layer by Density Functional Theory," *Langmuir*, submitted (2000).



11. D. T. Chin and S. Venkatesh, *J. Electrochem. Soc.*, **128**, 1439 (1981).
12. R. Ramanauskas, R. Juskenas, and M. Gladkovas, *Plat. Surf. Finish.*, 54 (July 1996).
13. C. Biddulph and M. Marzano, in *Metal Finishing*, 65th Guidebook and Directory Issue, Vol. 95, No. 1A, p. 323 (1997).
14. H. Gedulp, *Zinc Plating*, Finishing Publications Ltd., Middlesex (1988).
15. F. A. Lowenheim, Editor, *Modern Electroplating*, 3rd ed., John Wiley & Sons, New York (1974).
16. M. Smith and A. E. Martell, *Critical Stability Constants*, Vol. 4, Plenum Press, New York (1979).
17. A. Rojas and I. Gonzalez, *Anal. Chim. Acta*, **187**, 279 (1986).
18. A. Rojas-Hernandez, M. T. Ramirez, I. Gonzalez, and J. G. Ibanez, *Anal. Chim. Acta*, **259**, 95 (1992).
19. A. Rojas-Hernandez, M. T. Ramirez, J. G. Ibanez, and I. Gonzalez, *J. Electrochem. Soc.*, **138**, 365 (1991).
20. A. Rojas-Hernandez, M. T. Ramirez, and I. Gonzalez, *Anal. Chim. Acta*, **278**, 321 (1993).
21. A. Rojas-Hernandez, M. T. Ramirez, and I. Gonzalez, *Anal. Chim. Acta*, **278**, 335 (1993).
22. G. J. Hills, D. J. Schiffrin, and J. Thompson, *Electrochim. Acta*, **19**, 657 (1974).
23. S. Fletcher, *Electrochim. Acta*, **28**, 917 (1983).
24. S. Fletcher and G. S. Halliday, *J. Electroanal. Chem.*, **159**, 167 (1983).
25. G. Gunawardena, G. Hills, I. Montenegro, and B. Scharifker, *J. Electroanal. Chem.*, **138**, 225 (1982).
26. W. C. Hsieh and J. R. Selman, *Electrochim. Acta*, **30**, 1381 (1985).
27. B. Scharifker and G. Hills, *Electrochim. Acta*, **28**, 879 (1983).
28. A. Serruya, B. R. Scharifker, I. Gonzalez, M. T. Oropeza, and M. Palomar-Pardave, *J. Appl. Electrochem.*, **26**, 451 (1996).
29. G. Trejo, A. F. Gil, and I. Gonzalez, *J. Electrochem. Soc.*, **142**, 3404 (1995).
30. G. Trejo, A. F. Gil, and I. Gonzalez, *J. Appl. Electrochem.*, **26**, 1287 (1996).
31. 1993 *Annual Book of ASTM Standards*, Vol. 03.02, *Wear and Erosion; Metal Corrosion*, P. C. Fazio et al., Editors, ASTM G 5. Standard Reference Test for Making Potentiostatic and Potentiodynamic Anodic Polarization Measurements, p. 71, ASTM, Philadelphia, PA (1993).

## Characterization of Sol-Gel-Derived Cobalt Oxide Xerogels as Electrochemical Capacitors

Chuan Lin, James A. Ritter,\* and Branko N. Popov\*

Department of Chemical Engineering, University of South Carolina, Columbia, South Carolina 29208, USA

### ABSTRACT

Very fine cobalt oxide xerogel powders were prepared using a unique solution chemistry associated with the sol-gel process. The effect of thermal treatment on the surface area, pore volume, crystallinity, particle structure, and corresponding electrochemical properties of the resulting xerogels was investigated and found to have significant effects on all of these properties. The xerogel remained amorphous as  $\text{Co}(\text{OH})_2$  up to  $160^\circ\text{C}$ , and exhibited maxima in both the surface area and pore volume at this temperature. With an increase in the temperature above  $200^\circ\text{C}$ , both the surface area and pore volume decreased sharply, because the amorphous  $\text{Co}(\text{OH})_2$  decomposed to form  $\text{CoO}$  that was subsequently oxidized to form crystalline  $\text{Co}_3\text{O}_4$ . In addition, the changes in the surface area, pore volume, crystallinity, and particle structure all had significant but coupled effects on the electrochemical properties of the xerogels. A maximum capacitance of 291 F/g was obtained for an electrode prepared with the  $\text{CoO}_x$  xerogel calcined at  $150^\circ\text{C}$ , which was consistent with the maxima exhibited in both the surface area and pore volume; this capacitance was attributed solely to a surface redox mechanism. The cycle life of this electrode was also very stable for many thousands of cycles.

### Introduction

Interest in electrochemical capacitors for high-power devices in energy-storage systems has risen in recent years.<sup>1-5</sup> Moreover, the energy density of the relatively new pseudocapacitor devices that are based on faradaic processes has been reported to be many times greater than that of the more traditional double-layer capacitors.<sup>1-6</sup> Noble metal oxides, such as  $\text{RuO}_2$  and  $\text{IrO}_2$ , have been identified as possibly the best electrode materials for pseudocapacitors. For example, Zheng et al.<sup>7</sup> achieved a remarkable specific capacitance of 760 F/g from a sol-gel-derived amorphous  $\text{RuO}_2$  with a very high electrical conductivity; but the high cost of this and other noble metal materials may be a limiting factor. Thus, other efforts have aimed at making a lower cost electrode material that has a relatively high capacitance. For example, Liu et al.<sup>8</sup> developed an ultracapacitor device based on a sol-gel-derived porous metal oxide  $\text{NiO}_x/\text{Ni}$  film. The specific capacitance of this device, ranging from 50 to 64 F/g (equivalent to 200 to 256 F/g for a single electrode), is considerably higher than that obtained from carbon-based capacitors. Srinivasan and Weidner<sup>9</sup> also developed an electrochemical route for making nickel oxide capacitors with relatively large specific capacitances of about 240 F/g (from a single electrode). Cobalt oxide electrode materials have

also been studied extensively due to a variety of applications in electrocatalysis<sup>10-13</sup> and lithium-ion batteries.<sup>14</sup> However, cobalt oxides have not been examined for use as electrochemical capacitors (with one recent exception<sup>9</sup>), most likely because the common preparation method, involving the thermal decomposition of a metal salt,<sup>15,16</sup> usually yields low surface area oxides. Even the electrochemical precipitation technique,<sup>9</sup> which produced an acceptable nickel oxide capacitor, resulted in a rather low specific capacitance for cobalt oxide of about 40 F/g (single electrode, fired at  $250^\circ\text{C}$ ). Nevertheless, it is clear that sol-gel<sup>7,8,17,18</sup> and other precipitation processes<sup>9</sup> have been receiving increasing attention in the electrochemical research community for making high surface area metal oxides.

The sol-gel process is quickly becoming one of the most promising materials synthesis techniques, because it readily allows for control of the texture, composition, homogeneity, and structural properties of the resulting materials.<sup>19</sup> Moreover, numerous studies have been devoted recently to understanding how the synthesis conditions affect the porous structure of sol-gel derived materials.<sup>20-24</sup> But only limited information is available on sol-gel-derived cobalt oxides.<sup>17,25</sup> Also, a paucity of information is available that correlates the surface area and pore structure with the electrochemical properties of the electrode materials.

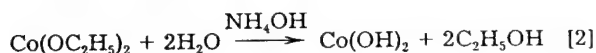
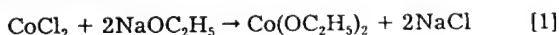
Therefore, the objective of this work was to develop a new sol-gel synthesis route<sup>26</sup> for making high surface area cobalt

\* Electrochemical Society Active Member.

oxide xerogel powders with a controlled pore structure for use as an electrode material in electrochemical capacitors. Another objective was to study the effect of the calcination temperature on the surface area, pore volume, particle structure, and corresponding electrochemical properties of the  $\text{CoO}_x$  xerogels. Physical adsorption, transmission electron microscopy (TEM), X-ray diffraction (XRD), thermogravimetric analysis (TGA), differential scanning calorimetry (DSC), and electrochemical techniques were used to correlate the electrochemical performance of the material with its physical properties.

### Experimental

Reagent-grade cobalt chloride ( $\text{CoCl}_2$ , 98%, Aldrich), sodium ethoxide ( $\text{NaOC}_2\text{H}_5$ , 96%, Aldrich), dehydrated ethanol ( $\text{EtOH}$ , 200 proof, Quantum), ammonium hydroxide ( $\text{NH}_4\text{OH}$ , 50 vol %, Alfa), and potassium hydroxide ( $\text{KOH}$ , 85% assay, Alfa) were used as received.  $\text{CoCl}_2$ ,  $\text{NaOC}_2\text{H}_5$  (mole ratio of  $\text{CoCl}_2$  to  $\text{NaOC}_2\text{H}_5$  = 1:2) and dehydrated  $\text{EtOH}$  were added to a three-necked flask equipped with a  $\text{N}_2$  purge, cooling water condenser, and magnetic stirrer. The mixture was heated and refluxed for 3 h, and then cooled to room temperature. Next, while agitating, a 0.2 M solution of  $\text{NH}_4\text{OH}$  was added dropwise to form the hydrogel; agitation was continued overnight. The reactions for the synthesis are summarized below



In order to remove  $\text{NaCl}$  from the hydrogel, the gel was washed with a 50 vol % solution of distilled water and  $\text{EtOH}$ , and vacuum filtered three times. This step was followed by a final wash with dehydrated  $\text{EtOH}$ . Temperature-programmed drying and calcination in air were used in the final preparation step. With a heating rate of  $0.5^\circ\text{C}/\text{min}$ , the gel was heated to  $65^\circ\text{C}$  and held there for 5 h. It was then heated to  $110^\circ\text{C}$  and held there for another 5 h. Finally, it was heated at a rate of  $5^\circ\text{C}/\text{min}$  to the calcination temperature (varied as a parameter in this study), and held there for 3 h.

The surface area and pore volume were obtained with a Micromeritics Pulse Chemisorb 2700 analyzer, and skeletal densities were measured with a Quatachrome ultrapycnometer 1000. TEM were obtained with a Hitachi H-8000 TEM, and XRD patterns were collected using a Rigaku-D-max B diffractometer equipped with a Cu source. A Perkin-Elmer thermogravimetric analyzer (TGA-7) and a Perkin-Elmer differential scanning calorimeter (DSC-7) were used to determine the weight loss and corresponding thermal effects of the dried gel during calcination in air at a heating rate of  $5^\circ\text{C}/\text{min}$ .

Cyclic voltammetric and chronopotentiometric measurements were performed with an EG&G PAR model 273 computer-controlled potentiostat-galvanostat, driven by model 273 electrochemical analysis software. A three-electrode system was used for the electrochemical measurements. The working electrode contained about 5 mg  $\text{CoO}_x$  xerogel bound with 5 wt % polytetrafluoroethylene (PTFE, Aldrich). It was rolled to a thickness of about 100  $\mu\text{m}$ , cut into a circular piece with a diameter of 0.75 cm, and pressed at 3 tons/ $\text{cm}^2$  between two pieces of nickel gauze with nickel wire leads for connection. Platinum gauze served as a counter electrode; and a saturated calomel electrode (SCE) was used as a reference electrode. A 1 M  $\text{KOH}$  solution was used as the electrolyte. All of the electrochemical measurements were conducted at room temperature.

X-ray diffraction peak widths were used to estimate the average size of the crystallite in the  $\text{CoO}_x$  xerogels from the Scherrer equation<sup>27</sup>

$$d = \frac{K\lambda}{b \cdot \cos \theta} \quad [3]$$

where  $b$  is the peak width at its half-height in terms of  $2\theta$ ,  $\lambda$  is the incident radiation wavelength (1.5406 Å for Cu K $\alpha$  radiation),  $\theta$  is the angle of the diffraction,  $K$  is a constant

(taken as 0.9), and  $d$  is the crystallite size. The pore volume and skeletal density measurements were used to obtain the particle density from the following relationship

$$d_p = \frac{1}{V_p + \frac{1}{d_s}} \quad [4]$$

where  $V_p$  is the specific pore volume,  $d_s$  is the skeletal density, and  $d_p$  is the particle density.

### Results

The effect of thermal treatment on the surface area and pore volume of the  $\text{CoO}_x$  xerogels is shown in Fig. 1. The surface area initially increased with an increase in temperature from 110 to  $150^\circ\text{C}$ , and it reached a maximum of 198  $\text{m}^2/\text{g}$  at  $150^\circ\text{C}$ . Beyond  $150^\circ\text{C}$ , the surface area decreased sharply to about 120  $\text{m}^2/\text{g}$  at  $250^\circ\text{C}$  and 50  $\text{m}^2/\text{g}$  at  $400^\circ\text{C}$ , and finally it reached 20  $\text{m}^2/\text{g}$  at  $600^\circ\text{C}$ . The pore volume exhibited similar trends and increased slightly from 0.40 to 0.43  $\text{cm}^3/\text{g}$  with an increase in temperature from 110 to  $150^\circ\text{C}$ . Beyond  $150^\circ\text{C}$ , it decreased linearly with increasing temperature down to 0.04  $\text{cm}^3/\text{g}$  at  $600^\circ\text{C}$ .

The effect of the calcination temperature on the crystalline structure of the  $\text{CoO}_x$  xerogels is shown in Fig. 2 in terms of the XRD patterns. Between 110 and  $150^\circ\text{C}$  the XRD patterns were essentially identical exhibiting only two small featureless peaks at  $2\theta = 32$  and  $58^\circ$ , which were probably associated with amorphous  $\text{Co}(\text{OH})_2$ . At higher temperatures, the XRD patterns exhibited the characteristic peaks of  $\text{Co}_3\text{O}_4$ <sup>17</sup> at  $36.6$ ,  $59.2$ , and  $65.1^\circ$ , which first appeared following calcination at  $200^\circ\text{C}$ ; and as the temperature increased the intensities of the peaks increased, indicating that more crystallization was taking place. This increase in intensity with an increase in the calcination temperature is also shown in Fig. 3, where the average crystallite size and intensity of the XRD peak at  $2\theta = 36.6^\circ$  are plotted as a function of the calcination temperature. Linear relationships were exhibited in both cases. The crystallite size was initially about 4 nm for the  $\text{CoO}_x$  xerogel calcined at  $200^\circ\text{C}$ , and it grew to about 25 nm as the calcination temperature increased to  $600^\circ\text{C}$ . The TEM images of the  $\text{CoO}_x$  xerogels shown in Fig. 4A and B, respectively, were qualitatively consistent with these results. They show that the  $\text{CoO}_x$  xerogel calcined at  $150^\circ\text{C}$  was comprised of 10 nm particles, whereas that calcined at  $600^\circ\text{C}$  was comprised of larger 30 to 40 nm particles.

Figure 5 displays the skeletal densities of the  $\text{CoO}_x$  xerogels calcined at different temperatures. The skeletal density increased slightly from 3.19 to 3.34  $\text{g}/\text{cm}^3$  with an increase in temperature from 110 to  $150^\circ\text{C}$ , and then it increased linearly to about 5.45  $\text{g}/\text{cm}^3$  at  $300^\circ\text{C}$ . Between 300 and  $600^\circ\text{C}$ , the skeletal density remained essentially constant, and finally it reached 5.74  $\text{g}/\text{cm}^3$  at  $600^\circ\text{C}$ , which is about 94% of the theoretical density of  $\text{Co}_3\text{O}_4$ .<sup>28</sup> In contrast, the particle

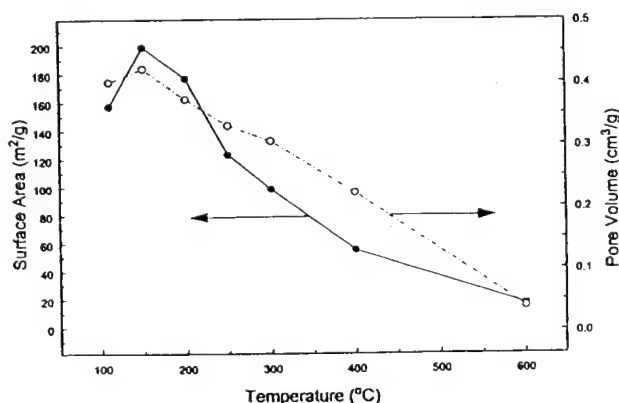


Fig. 1. Effect of the calcination temperature on the surface area and pore volume of the  $\text{CoO}_x$  xerogels.

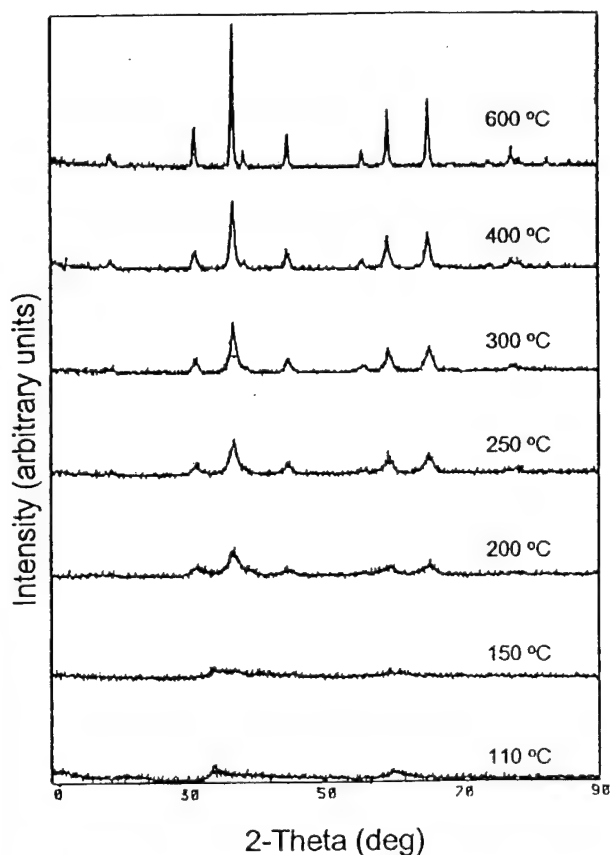


Fig. 2. Effect of the calcination temperature on the XRD patterns of the fresh  $\text{CoO}_x$  xerogels.

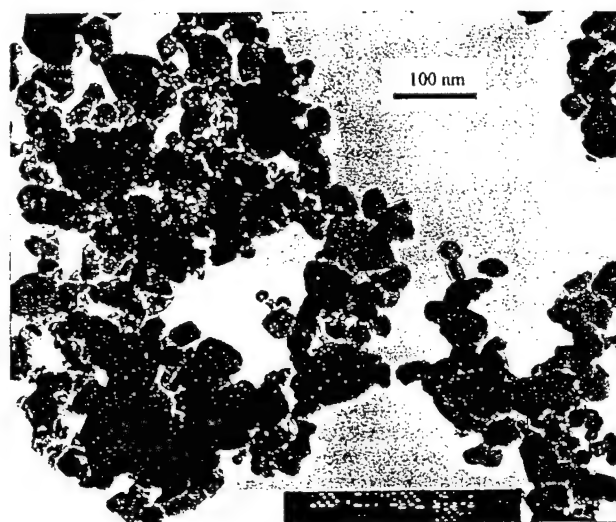
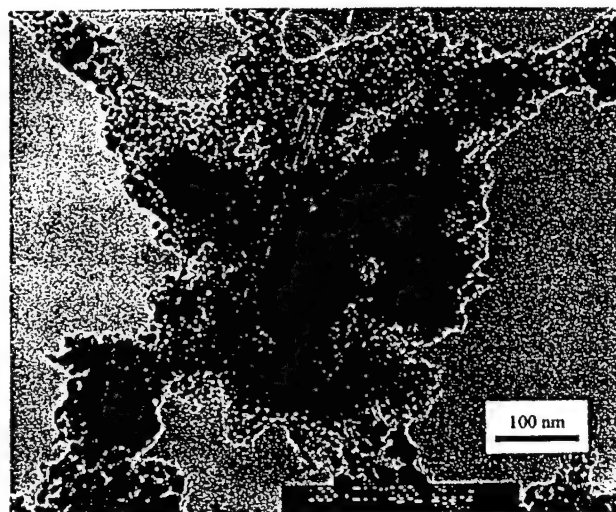


Fig. 4. TEM images of the  $\text{CoO}_x$  xerogels calcined at (A, top) 150°C and (B, bottom) 600°C.

density essentially increased from 3.1 to 4.7  $\text{g/cm}^3$  with an increase in temperature from 150 to 600°C.

The TGA and corresponding DSC analyses are illustrated in Fig. 6. The weight loss of the  $\text{CoO}_x$  xerogel occurred in three stages: an initial loss of about 13% up to 160°C, followed by a rapid loss of around 14% between 160 and 170°C, and an additional but gradual loss of around 4% up to 750°C. The initial weight loss up to 160°C was not associated with any thermal events as seen in the DSC trace. However, between 160 and 170°C, the weight loss was accompanied by a marked endothermic event that extended over a broader temperature range (up to 270°C) than the weight loss. The final small weight loss between 400 and 650°C was accompanied by another marked thermal event; however, in this temperature range an exothermic event occurred.

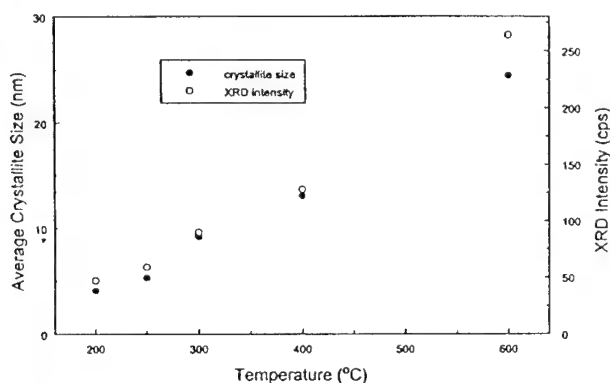


Fig. 3. Effect of the calcination temperature on the average crystallite size and intensity of the fresh  $\text{CoO}_x$  xerogels from XRD peaks at  $2\theta = 36.6^\circ$ .

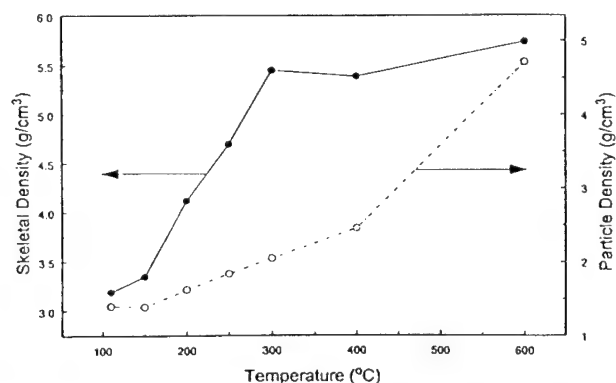


Fig. 5. Effect of the calcination temperature on the skeletal and particle densities of the  $\text{CoO}_x$  xerogels.

Cyclic voltammetry (CV) and galvanostatic techniques were used to determine the electrochemical properties of the  $\text{CoO}_x$  xerogels as a function of the calcination temperature. Figure 7A shows the characteristic shapes of the CV curves for the  $\text{CoO}_x$  xerogels calcined at three different temperatures (150, 200, and 600°C). The potential was scanned between  $-0.3$  and  $0.5$  V (vs. SCE) in both directions and the current response was measured for a scan rate of 5 mV/s. In all cases, a single anodic peak was

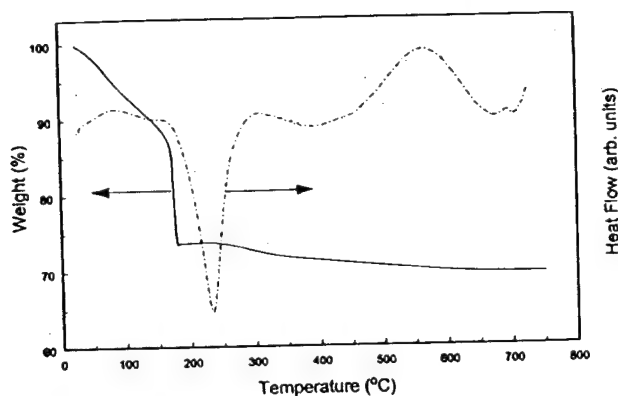


Fig. 6. Thermogravimetric analysis (TGA) and differential scanning calorimetry (DSC) of the  $\text{CoO}_x$  xerogels heated in air at  $5^\circ\text{C}/\text{min}$ .

exhibited at about 0.45 V, and a corresponding cathodic peak at about 0.30 V. In addition, a shoulder appeared between 0 and 0.3 V for the xerogel calcined at  $150^\circ\text{C}$ . The electrochemical stability of the  $\text{CoO}_x$  xerogel electrode calcined at  $150^\circ\text{C}$  was also studied; the result is shown in Fig. 7B. Essentially no change is exhibited in the initial cycle and after several thousand cycles, indicating that this electrode was very stable.

Figure 8 shows the dependence of the cathodic peak current on the calcination temperature. It exhibited a similar trend to the surface area and pore volume plots shown in Fig. 1. A maximum current was obtained for the xerogel

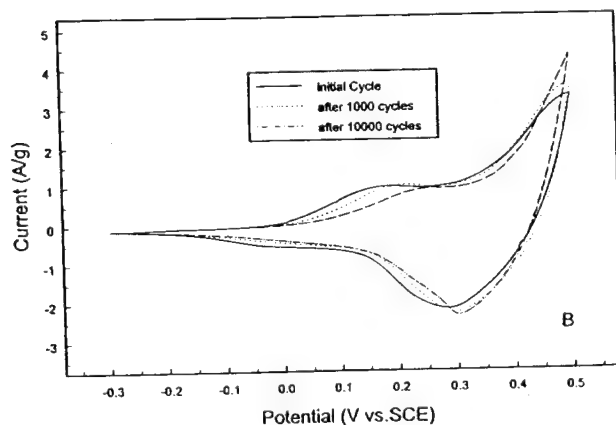
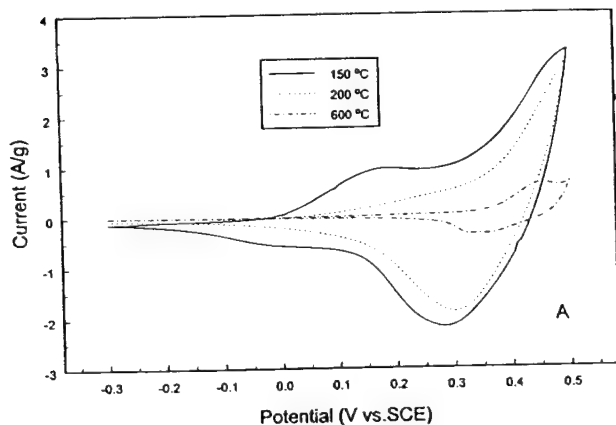


Fig. 7. Cyclic voltammograms (CVs) of (A) the  $\text{CoO}_x$  xerogels calcined at three different temperatures, and (B) the  $\text{CoO}_x$  xerogel calcined at  $150^\circ\text{C}$  for the first and after several thousand cycles. The curves were normalized to the current response for 1 g of active material; and the CV was measured in 1 M KOH with a sweep rate of  $5\text{ mV}/\text{s}$ .

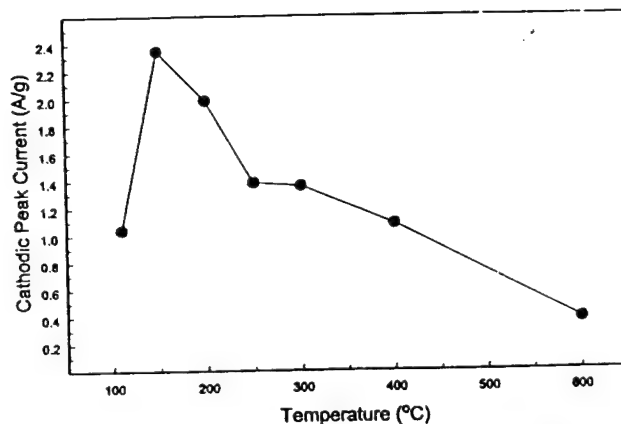


Fig. 8. Effect of the calcination temperature on the cathodic peak currents obtained from the CV results of the  $\text{CoO}_x$  xerogel electrodes.

calcined at  $150^\circ\text{C}$ , which was the same temperature at which the surface area and pore volume exhibited maxima. Constant-current ( $2.26\text{ mA}/\text{cm}^2$ ) discharge profiles of the  $\text{CoO}_x$  xerogels are shown in Fig. 9. The corresponding specific capacitances were calculated from

$$C = \frac{I \cdot \Delta t}{m \cdot \Delta V} \quad [5]$$

and are displayed in Fig. 10.  $I$  is the discharge current,  $\Delta t$  is the total discharge time,  $m$  is the mass of the  $\text{CoO}_x$  xerogel,  $\Delta V$  is the potential drop during discharging, and  $C$  is the specific capacitance. The total discharge time was used because it was difficult to determine the transition time for the material calcined at  $150^\circ\text{C}$ . In this way, the  $\text{CoO}_x$  xerogel calcined at  $150^\circ\text{C}$  exhibited the highest specific capacitance of  $291\text{ F/g}$ . The curves in Fig. 10 also exhibited similar trends to those shown in Fig. 1 and 8; thus, these results were consistent with those obtained from the CVs (Fig. 7A).

### Discussion

The chemistry depicted in Eq. 1 and 2 gives rise to unique cobalt oxides via the hydrolysis and condensation of the transition metal alkoxide. However, because the hydrolysis of transition metal alkoxides is so rapid,<sup>19</sup> this chemistry results in sol-gel-derived precipitates instead of gels. Nevertheless, cobalt oxide precipitates can be synthesized with rather interesting physical and electrochemical properties, as discussed above and shown in Fig. 1 to 10.

The increases in the surface area and pore volume from 110 to  $150^\circ\text{C}$  (Fig. 1) was attributed to the removal of physisorbed water or some solvent, which may have open-

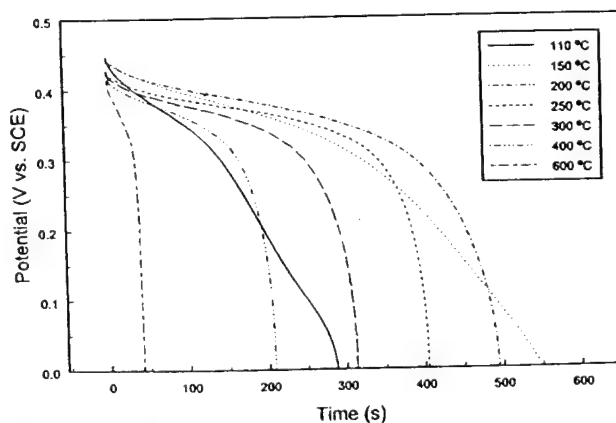


Fig. 9. Effect of the calcination temperature on the constant current discharge curves of the  $\text{CoO}_x$  xerogel electrodes measured with a current density of  $2.26\text{ mA}/\text{cm}^2$  in 1 M KOH solution. The electrodes were approximately  $100\text{ }\mu\text{m}$  in thickness and  $7.5\text{ mm}$  in diameter, and they contained approximately  $4.2\text{ mg}$  of  $\text{CoO}_x$  xerogel.

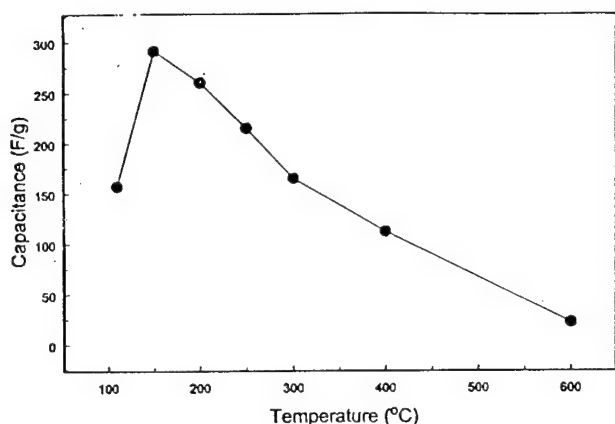
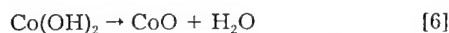
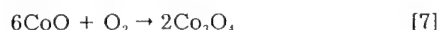


Fig. 10. Effect of the calcination temperature on the specific capacitance of the CoO<sub>x</sub> xerogel electrodes.

ed the pore structure of the material.<sup>20</sup> The maxima in both the surface area and pore volume exhibited at 150°C, and the sharp weight loss from 160 to 170°C were most likely due to the decomposition of cobalt hydroxide to form amorphous cobalt oxide by removal of chemisorbed water according to Eq. 6<sup>29,30</sup>



because no CoO peaks were observed in the XRD pattern (see Fig. 2). The theoretical weight loss to form CoO from Co(OH)<sub>2</sub> was about 19.4%, which was larger than the 14% obtained from the TGA results for the temperature change from 160 to 170°C (see Fig. 6). This difference was most likely caused by OH groups still remaining in the bulk within this temperature range, that could only be eliminated at higher temperatures. As the temperature was increased above 170°C, the oxidation of CoO to Co<sub>3</sub>O<sub>4</sub> began to take place according to Eq. 7<sup>29,30</sup>



which was consistent with the XRD results, in that the intensity of the Co<sub>3</sub>O<sub>4</sub> peaks increased with increasing temperature. According to the TGA results, this reaction was completed between 400 and 500°C.<sup>29</sup> The theoretical weight loss corresponding to the change from Co(OH)<sub>2</sub> to Co<sub>3</sub>O<sub>4</sub> was about 13.6%, but the weight loss obtained with the TGA during the temperature excursion from 150 to 450°C was about 17%. The difference was most likely associated with the removal of additional physisorbed/chemisorbed water at about 160°C.

In the temperature range from 170 to 400°C, primary amorphous CoO<sub>x</sub> particles aggregated and formed larger secondary crystalline particles, thus eliminating some of the smallest intra- and interparticle voids and resulting in a sharp drop in the surface area and a gradual drop in the pore volume. These explanations are consistent with the XRD results shown in Fig. 2 and 3, which show that in the 200 to 400°C temperature range the average crystallite size more than doubled. In fact, the particle sizes of the xerogels obtained from the TEM images were larger than those estimated from the XRD results, which suggests that the particles seen in the TEM images consisted of an aggregate of crystallites, instead of single crystallites. This aggregation phenomenon occurred with minimal weight loss and an initial endothermic event that ceased at about 250°C (Fig. 6). This endothermic event was most likely caused by the decomposition of Co(OH)<sub>2</sub> to form CoO by elimination of chemisorbed water according to Eq. 6 and the subsequent oxidation of CoO to Co<sub>3</sub>O<sub>4</sub> according to Eq. 7. Moreover, a significant structural change occurred in this temperature range, during which the xerogel converted from an essentially amorphous structure into an essentially crystalline structure. What was most interesting, however, is that in this temperature range, Fig. 5 shows that

the skeletal density increased dramatically and attained nearly the theoretical density of Co<sub>3</sub>O<sub>4</sub> at about 275°C, but the particle density was still increasing, thereby indicating the continued loss of surface area and pore volume.

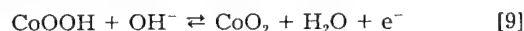
In the final temperature range from 400 to 600°C, the secondary particles began to grow into even larger crystallites, which necessarily eliminated some of the large intra- and interparticle voids. As a result, the pore volume decreased continuously, but the surface area decreased more slowly. Again, the average crystallite size nearly doubled; and the results in Fig. 2 and 4 show that a highly crystalline Co<sub>3</sub>O<sub>4</sub> structure was created at the final temperature of 600°C. The final weight loss and corresponding exothermic event that took place in this temperature range was assigned to structural relaxation,<sup>31</sup> a process whereby intra- and interparticle voids are eliminated but with little weight loss. During this structural relaxation, the surface area and pore volume of the CoO<sub>x</sub> xerogel continuously decreased, but the crystallite size grew as shown in Fig. 1, 2, and 3.

It was also interesting to ascertain whether the Brunauer, Emmett, and Teller (BET) surface area corresponded to intra- or interparticle voids, depending on the calcination temperature. To illustrate, the CoO<sub>x</sub> xerogels calcined at 250 and 600°C were selected with corresponding particle sizes of 15 and 35 nm (as determined from XRD) and skeletal densities of 4.10 and 5.74 g/cm<sup>3</sup>, respectively. The external surface areas of these particles were calculated from the relationship

$$S = \frac{6}{D \cdot d_s} \quad [8]$$

where  $D$  is the particle diameter,  $d_s$  is the skeletal density, and  $S$  is the specific surface area; they were 98 and 30 m<sup>2</sup>/g, respectively. For the xerogel calcined at 600°C, the calculated external surface area of 30 m<sup>2</sup>/g was close to that obtained from the BET measurement of 20 m<sup>2</sup>/g, indicating that the particles were nonporous and that both the BET surface area and pore volume were due to interparticle voids. In contrast, for the xerogel calcined at 250°C, the calculated external surface area of 98 m<sup>2</sup>/g accounted for only half of the BET surface area of 180 m<sup>2</sup>/g, indicating that significant intraparticle voids were present in the form of various sizes of pores. The highly porous structure of the CoO<sub>x</sub> xerogels calcined below ca. 250°C was manifest through the sol-gel chemistry depicted in Eq. 1 and 2.

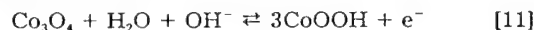
The sol-gel chemistry associated with transition metal alkoxides was also responsible for the unique electrochemical properties of the CoO<sub>x</sub> xerogels, as shown in Fig. 7 to 10. For example, the very stable and reproducible peaks in the CVs shown in Fig. 7A and B between 0.3 and 0.5 V (vs. SCE) corresponded to the oxidation of CoOOH to CoO<sub>2</sub> according to Eq. 9<sup>13</sup>



where the CoOOH under open-circuit potential conditions was formed initially from<sup>17</sup>



for the xerogels calcined at the lower temperatures, e.g., below 200°C; and from<sup>17</sup>



for the xerogels calcined at the higher temperatures, e.g., above 200°C.

To illustrate a charge-storage mechanism associated with the CoO<sub>x</sub> xerogel electrodes, a theoretical capacitance,  $C_T$ , for the one-electron exchange redox reaction (Eq. 9) that is assumed to take place only on the surface of each particle was estimated from

$$C_T = \frac{sF}{h^2 L_A \Delta V} \quad [12]$$

where  $s$  is the specific surface area,  $F$  is Faraday's constant,  $h$  is the length of a crystal lattice and taken as 4.26 Å



for crystalline  $\text{CoO}$ ,<sup>28</sup>  $L_A$  is Avogadro's number, and  $\Delta V$  is the potential range from 0 to 0.5 V for the current measured. Equation 12 implies that there is only one Co atom in the square area of  $h$  on the surface; thus, at 150 and 300°C, corresponding surface areas of 199 and 99  $\text{m}^2/\text{g}$  give rise to  $C_s$  of 351 and 175  $\text{F/g}$ , respectively. These values are very close to the measured capacitances of 291 and 163  $\text{F/g}$  at these two temperatures, respectively. This result suggested that the  $\text{CoO}_x$  redox reaction was taking place only on the surface of each particle that was in direct contact with the electrolyte, and that the charge-storage mechanism was based solely on the surface redox reaction and thus pseudocapacitance. Moreover, if the reaction involved all of the bulk material, a specific capacitance of 2100  $\text{F/g}$  would have been observed, which is about six to seven times the theoretical capacitance. This result implies that 14 to 17% of the material was utilized for energy storage, a fairly large percentage for a surface redox reaction. This unique feature of the  $\text{CoO}_x$  xerogels was attributed to the high surface area of this sol-gel-derived cobalt oxide.

According to the literature,<sup>13,17</sup> the anodic shoulder in the CVs shown in Fig. 7A and B for the xerogel calcined at 150°C was associated with the oxidation process given in Eq. 10, whereas the cathodic shoulder corresponded to the reverse of Eq. 10. This very stable redox reaction (Fig. 7B), which disappeared at higher temperatures, most likely gave rise to the very high capacitance observed with this material (291  $\text{F/g}$ ). The appearances of these CV curves were also very similar to those reported by Boggio et al.<sup>13</sup> for a  $\text{Co}_3\text{O}_4$  thin film deposited by thermal decomposition of  $\text{Co}(\text{NO}_3)_2$  on a titanium support, which further substantiates that the origin of the capacitance in these bulk cobalt oxide materials is due solely to surface redox reactions depicted by Eq. 9 to 11, as explained in more detail elsewhere.<sup>13</sup> Figure 7A also shows that with an increase in temperature, both of the anodic and cathodic shoulders disappeared; and the peak currents of both the cathodic peak at 0.3 V and the corresponding anodic peak decreased with increasing calcination temperature, indicating that crystalline, nonelectrochemically active species with a smaller active surface area had been formed. At the highest calcination temperature, the anodic potential limit extended fully into the oxygen evolution region, indicating that the only process occurring on the surface was the formation of oxygen.

The discharge curves shown in Fig. 9 are also explained by taking into account the structure and electrochemically active surface area of the  $\text{CoO}_x$  xerogels. According to Fig. 2, the electrodes prepared with the  $\text{CoO}_x$  xerogels calcined at the lower temperatures had an amorphous structure of  $\text{Co}(\text{OH})_2$ . Thus, the high intraparticle surface area of this amorphous material contributed to the large charging and discharging currents observed in the potential range from 0 to 0.3 V. However, at temperatures above 200°C, the xerogel was converted into a crystalline structure of  $\text{Co}_3\text{O}_4$  that resulted in a decrease of the electrochemically active surface area. Consequently, a loss in capacity was observed for all materials prepared at temperatures above 200°C (see Fig. 9). These results suggested that the surface area played a major role in controlling the electrochemical properties of the  $\text{CoO}_x$  xerogel electrodes. The highest surface area electrode (calcined at 150°C) had the highest redox current, because of its unique amorphous structure. These trends were also apparent in Fig. 10, where the amorphous structure of the  $\text{CoO}_x$  xerogel electrode calcined at 150°C resulted in the highest specific capacitance of all of the  $\text{CoO}_x$  xerogels studied.

### Conclusions

The calcination temperature had a significant impact on the structure of the sol-gel derived  $\text{CoO}_x$  xerogel powders and their corresponding electrochemical properties. The xerogels essentially exhibited both high surface area and pore volume at relatively low calcination temperatures; but after some characteristic calcination temperature was exceeded, both the surface area and pore volume decreased with an increase in temperature. The maximum surface area and pore volume were observed for the xerogel cal-

cined at 150°C, which yielded a unique amorphous structure of  $\text{Co}(\text{OH})_2$ . At calcination temperatures above 160°C, however, the amorphous  $\text{Co}(\text{OH})_2$  began to decompose to form  $\text{CoO}$  that was subsequently oxidized to form crystalline  $\text{Co}_3\text{O}_4$  with an increase in temperature, thereby resulting in lower surface areas and pore volumes. The electrochemical study showed that the xerogel electrode calcined at 150°C was very stable over several thousand charging/discharging (CV) cycles, and it exhibited the highest surface redox currents, which were clearly associated with the high surface area and pore volume of the amorphous  $\text{Co}(\text{OH})_2$  structure. However, the redox currents began disappearing at temperatures above 200°C, as a result of structural changes that took place during formation of the crystalline  $\text{Co}_3\text{O}_4$ , and the corresponding decreases in the surface area and pore volume. The highest average specific capacitance obtained was 291  $\text{F/g}$  for a single electrode, and it corresponded to the  $\text{CoO}_x$  xerogel electrode calcined at 150°C. This result was very close to the theoretical capacitance of 351  $\text{F/g}$  that was obtained based on a surface redox mechanism; thus, the charge-storage mechanism was due solely to a surface redox reaction. The unique physical and electrochemical properties of these  $\text{CoO}_x$  xerogels were attributed to the sol-gel chemistry of transition metal alkoxides.

### Acknowledgments

This material is based upon work supported in part by the U.S. Army Research Office under grant no. DAAH04-96-1-0421 and in part by the U.S. Department of Energy under cooperative agreement no. DE-FC02-91ER75666.

Manuscript submitted January 20, 1998; revised manuscript received July 17, 1998.

The University of South Carolina assisted in meeting the publication costs of this article.

### REFERENCES

1. B. E. Conway, *J. Electrochem. Soc.*, **138**, 1539 (1991).
2. B. E. Conway, in *Third International Seminar on Double Layer Capacitors and Similar Energy Storage Devices*, Vol. 3, Florida Educational Seminar, Inc., Boca Raton, FL (1993).
3. S. Trasatti and P. Kurzweil, *Plat. Met. Rev.*, **38**, 46 (1994).
4. S. Sarangapani, B. V. Tilak, and C. P. Chen, *J. Electrochem. Soc.*, **143**, 3791 (1994).
5. I. D. Raistrick, in *Electrochemistry of Semiconductors and Electrodes*, J. McHardy and F. Ludwig, Editors, p. 297-355, Noyes Publications, Park Ridge, NJ (1992).
6. A. Rudge, I. Raistrick, S. Gottesfeld, and J. Ferraris, *Electrochim. Acta*, **39**, 279 (1994).
7. J. P. Zhang, P. J. Cygan, and T. R. Jow, *J. Electrochem. Soc.*, **142**, 2699 (1995).
8. K. C. Liu and M. A. Anderson, *J. Electrochem. Soc.*, **143**, 124 (1996).
9. V. Srinivasan and J. W. Weidner, *J. Electrochem. Soc.*, **144**, L210 (1997).
10. V. S. Bagotsky, N. A. Shumilova, and E. I. Khrushcheva, *Electrochim. Acta*, **21**, 916 (1976).
11. C. Iwakura, A. Honji, and H. Tamura, *Electrochim. Acta*, **26**, 1319 (1981).
12. S. Trasatti, *Electrochim. Acta*, **29**, 1503 (1984).
13. R. Boggio, A. Carugati, and S. Trasatti, *J. Appl. Electrochem.*, **17**, 828 (1987).
14. E. Zhecheva, R. Stoyanova, M. Gorova, R. Alcantara, J. Morales, and J. L. Tirado, *Chem. Mater.*, **8**, 1429 (1996).
15. R. N. Singh, J. F. Koenig, G. Poillerat, and P. Chartier, *J. Electrochem. Soc.*, **137**, 1408 (1990).
16. T. Maruyama and S. Arai, *J. Electrochem. Soc.*, **143**, 1383 (1996).
17. F. Svegl, B. Orel, M. G. Hutchins, and K. Kalcher, *J. Electrochem. Soc.*, **143**, 1532 (1996).
18. I. Serebrennikova and V. I. Birss, *J. Electrochem. Soc.*, **144**, 566 (1997).
19. C. J. Brinker and G. W. Scherer, *Sol-Gel Science*, Academic Press, San Diego, CA (1990).
20. P. J. Davis, C. J. Brinker, D. M. Smith, and R. A. Assink, *J. Non-Cryst. Solids*, **142**, 197 (1992).
21. C. Lin and J. A. Ritter, in *Fundamentals of Adsorption*, M. D. LeVan, Editor, Kluwer Academic Publishers, Boston, MA (1996).

22. C. Lin, J. A. Ritter, and M. D. Amiridis, *J. Non-Cryst. Solids*, **215**, 146 (1997).
23. E. M. Rabinovich, in *Sol-Gel Technology for Thin Films, Fibers, Preforms, Electronics and Specialty Shapes*, L. C. Klien, Editor, Noyes Publications, Park Ridge, NJ (1988).
24. W. F. Maier, I. C. Tilgner, W. Wiedron, and H. C. Ko, *Adv. Mater.*, **5**, 726 (1993).
25. F. Svegl and B. Orel, *J. Sol-Gel Sci. Technol.*, **8**, 765 (1997).
26. Y. Takasu, S. Onoue, K. Kameyama, Y. Murakami, and K. Yahikozawa, *Electrochim. Acta*, **39**, 1993 (1994).
27. H. P. Klug and L. E. Alexander, *X-Ray Diffraction Procedures*, John Wiley & Sons, New York (1962).
28. *CRC Handbook of Chemistry and Physics*, 62nd ed., R. C. Weast and M. J. Astle, Editors, CRC Press, Inc., Boca Raton, FL (1981-1982).
29. F. A. Cotton and C. Wilkinson, *Advanced Inorganic Chemistry-A Comprehensive Text*, 4th ed., John Wiley & Sons, Inc., New York (1980).
30. M. Pourbaix, *Atlas of Electrochemical Equilibria in Aqueous Solutions*, p. 325, NACE, Houston, TX (1974).
31. G. W. Scherer, *Relaxation in Glasses and Composites*, John Wiley & Sons, Inc., New York (1986).

# Characterization of Electropolymerized Polyindole

## Application in the Construction of a Solid-State, Ion-Selective Electrode

P. C. Pandey and R. Prakash\*

Department of Chemistry, Banaras Hindu University, Varanasi-221 005, India

### ABSTRACT

The characterization of polyindole made by anodic electropolymerization of indole monomer in dichloromethane is reported based on scanning electron microscopy (SEM) and differential scanning calorimetry (DSC). The results on SEM show that the granules in the polymer film are arranged in an ordered manner. The domain of the nuclei in the film made under potentiostatic condition is much smaller as compared to the domain of the nucleation in the polymer film made under potentiodynamic condition. The DSC data shows that the polymer is stable at higher temperature. A solid-state potassium ion-selective electrode (ISE) using polyvinyl chloride (PVC) matrix membrane impregnated with valinomycin at the surface of the polyindole-modified electrode is reported. Neutral-carrier impregnated PVC membrane is formed by casting over the surface of the polyindole-modified electrode. The resulting ISE without the incorporation of polyanions in the polyindole film shows high selectivity to  $K^+$  with negligible drift of the baseline potential with a slope of 59 mV/dec within Nernstian behavior. The detection limit of the potassium ion sensor is  $6 \times 10^{-6}$  M with a wide linearity over almost 5 dec. Typical responses of the neutral-carrier impregnated PVC membrane over the polyindole-modified electrode to potassium ion is reported.

### Introduction

The electrochemical synthesis of polyindole has received a significant share of attention during recent years.<sup>1-9</sup> Recently we have reported the electrochemical synthesis of polyindole by anodic oxidation of indole monomers in dichloromethane<sup>9</sup> containing tetrabutylammonium perchlorate. The resulting polymer shows better stability and improved conductivity as compared to the polymer synthesized earlier.<sup>1,2</sup> The application of the polymer in the construction of rechargeable batteries has been reported.<sup>9</sup> However, the results of the surface structure and stability of the film at higher temperature were not reported. The results based on scanning electron microscopy (SEM) and differential scanning calorimetry (DSC) of the polymer film, made by electropolymerization of polyindole in dichloromethane, are reported in this present communication.

Over the last 35 years development of ion-selective electrodes (ISEs) has grown at an ever-increasing rate due to their need in various spheres of life, particularly in the analytical, biological, and clinical areas. Accordingly, extensive studies have been made on the development of ISEs based on unblocked (with conventional single/double-barrel configuration) and blocked (coated wire electrode, CWE) interfaces. Extensive investigations on ISEs based on unblocked interfaces have been made, several of them on a commercial scale. However, the problems with such a configuration exist in the applications, mainly due to (i) use in upright position and (ii) use of internal filling solution and internal reference element. The coated wire electrodes have gained attention due to the simplicity involved in the construction of the ISEs, avoiding the problems associated with single/double-barrel configuration. However, there still exists a need for further research to overcome the problems asso-

ciated with the drift and overshoot of the potential leading to the variable baseline (stead-state potential) recovery during the potentiometric operation. A significant share of attention on these problems has been paid during last few years.<sup>10-15</sup> The application of conducting polymers<sup>10-15</sup> has been demonstrated along these lines. Quite recently<sup>10</sup> all-solid-state potassium-ion-selective electrodes have been reported on a Pt disk using a bilayer film of polypyrrole/poly(4-styrenesulfonate) (PPy/PSS) composite covered with a plasticized polyvinyl chloride (PVC) matrix membrane impregnated with valinomycin. The problem associated with the overshoot of the baseline potential was reduced due to the electroactivity and cation-exchange behavior of the PPy/PSS film, resulting in the formation of the concentration cells also referred to as symmetric cells (ions-in, ions-out) at the test solution/PVC and PVC/(PPy/PSS) interfaces. Because of the high thermal stability and good electroactivity of the polyindole, it is of great interest to study the potentiometric behavior of polyindole-modified electrode in the construction of ISEs. This is attempted in the present communication. An ISE for potassium ion using valinomycin-impregnated, plasticized PVC over the surface of polyindole-modified electrode is reported.

### Experimental

Indole (analytical reagent grade), PVC powder, dibutyl phthalate, and valinomycin were obtained from Aldrich Chemical Co. Tetraphenyl borate was obtained from E-Merck, India, Ltd; tetrabutylammonium perchlorate (TBAP) was obtained from Sigma Chemical Co. TBAP was dried in a drying piston below 100°C for a period of 24 h under vacuum. The aqueous solutions were prepared in double-distilled deionized water.

The electrochemical synthesis of polyindole was performed with a Solartron electrochemical interface (model

\* Present address: ITRC, M.G. Marg., Lucknow, India.

# SOL-GEL DERIVED CARBON AEROGELS AND XEROGELS FOR USE AS THE ANODE IN THE LITHIUM ION BATTERY

E. J. Zanto, J. A. Ritter\* and B. N. Popov

Department of Chemical Engineering  
Swearingen Engineering Center  
University of South Carolina  
Columbia, SC 29208

A full  $2^4$  factorial design study was carried out on sol-gel derived resorcinol-formaldehyde carbonized resins for use as the anode in the lithium ion battery. This statistical design approach was used to determine the effect of initial solution pH, wt% solids, pyrolysis temperature and gel type (aerogel or xerogel) on the final carbon product. The response variables were surface area, pore volume, and reversibility of the first and second cycle charge/discharge capacities. The results from the sixteen different carbon gels showed that the carbon gel with nearly the lowest surface area and pore volume gave rise to the highest reversible capacity and coulombic efficiency, consistent with results reported in the literature.

## INTRODUCTION

It has been shown that disordered, amorphous carbons can store more lithium than graphite, giving them a much higher specific capacity than expected from the stoichiometry of graphite intercalation compounds GIC ( $C_6Li$ , 372 Ahr/kg) [1-5]. There are many forms of disordered carbons typically that are derived from organic precursors carbonized below 1000 °C [3, 5-7]. As a result, there has been increasing interest in the pyrolysis of various organic polymers and resins for use as the anode in the lithium ion battery. However, carbonized resorcinol-formaldehyde resins, derived from the sol-gel process, have not been examined for this purpose, even though they are showing considerable promise for use as an electrochemical capacitor [8-11]. What makes these kinds of sol-gel derived carbon gels attractive are their tunable physical, chemical and thus electrochemical properties [12-17], which is also the impetus behind the use of other types of pyrolyzed resins derived from organic precursors.

Within this type of resorcinol-formaldehyde carbon gel, many different carbon structures can be formed depending on the parameters used in making the gel. Results in the literature have shown that parameters such as initial solution pH, wt% solids, pyrolysis temperature, and gel type all affect the outcome of the final carbon product [13, 17]. For example, increasing the initial solution pH, while keeping the wt% solids and pyrolysis temperature constant, decreased the surface area of the xerogels; and increasing the pyrolysis temperature, with all parameters constant, also decreased the surface area. The problem with the previous work, however, is that only one parameter at a time was studied. Not only is this extremely time consuming, it also fails to show how the parameters affect one another. This is very important in optimizing the method used to

create a material for a specific use. Therefore, the objective of this current work was to use statistical design methods to gain insight into the effects of these four parameters on carbons made from carbonized resorcinol-formaldehyde resins. The response variables of interest were surface area, pore volume, and especially first and second cycle reversible  $\text{Li}^+$  storage capacities and coulombic efficiencies.

## EXPERIMENTAL

### Materials and Synthesis Procedure

Resorcinol (ACS, 99+%, Alfa Aesar), formaldehyde (37% in water, Aldrich), sodium carbonate (anhydrous, ACS, Fisher), and acetone (optima, 99.6%, Fisher) were used as received. The synthesis procedure for these gels was developed based on the procedure for making carbon aerogels [12] and xerogels [13]. The solutions contained either 5 or 20 w/v% solids and the R/F (resorcinol/formaldehyde) mole ratio was fixed at 1:2.

Sodium carbonate was used as the catalyst with the R/C (resorcinol/sodium carbonate) mole ratio fixed at 50:1. Four, one liter batches of gel were made in a glove box under a nitrogen atmosphere. These four batches included one with a low initial solution pH and low wt% solids, one with a high initial solution pH and low wt% solids, one with a low initial solution pH and high wt% solids, and one with a high initial solution pH and high wt% solids. These solutions were then poured into 100 ml glass containers with caps and tightly sealed. They were removed from the glove box and placed in an oven at 87 °C for one week to form and cure the gel. When removed from the oven, each batch was divided into two parts. The first part was dried as a xerogel [13] and the second part was dried supercritically in  $\text{CO}_2$  to create an aerogel [12]. Each type of gel was then separated again into two parts. Half was calcined at 800 °C and the other half at 1050 °C in a tube furnace under nitrogen flow. In this way, the initial four batches of gel created sixteen different carbon materials as prescribed by a  $2^4$  factorial design.

### Characterization

A Micromeritics Pulse Chemisorb 2700 Analyzer was used to obtain the surface areas and pore volumes using the single point BET method and  $\text{N}_2$  at 77 K. An eight channel Arbin Electrochemical Instruments charge/discharge station was used to measure the lithium storage capacity of each sample. A small pellet was made for each sample by combining the carbonized resin powder with a Teflon binder in a 20:1 mass ratio. T-cells were then made in an argon-atmosphere glove box. The pellets and the stainless steel rods used in the t-cells were first heated to 200 °C for one hour in an oven located in the glove box. Once they had cooled, lithium foil was placed on the end of the rods being used as the counter and reference electrodes. The t-cells were then assembled using 1:1 EC:DMC in  $\text{LiPF}_6$  as the electrolyte. Once the t-cells were assembled, they were tested for two cycles using a current density of 1 mA/g between 0 and 2 volts.

## RESULTS AND DISCUSSION

Table 1 details the factors and their levels that were used in the  $2^4$  factorial design. These factors and their high and low ranges were chosen because they have been shown to have a significant effect on the final carbon product [13, 17]. The raw results from the surface area and pore volume tests are shown in Table 2. For all sixteen carbon gels, the surface areas ranged from a high of 929 m<sup>2</sup>/g to a low of 460 m<sup>2</sup>/g with a mean of 607 m<sup>2</sup>/g; and the pore volumes ranged from a high of 1.42 cm<sup>3</sup>/g to a low of 0.20 cm<sup>3</sup>/g with a mean of 0.54 cm<sup>3</sup>/g. It was interesting that these maxima and minima in the surface areas and pore volumes did not correspond to the same material, further establishing the unique and diverse properties that can be obtained with these kinds of carbonized resins. Moreover, although it is tempting to do so, factorial design methods do not allow for the trends depicted in Table 2 to be analyzed directly. Instead, for each response variable (in this case surface area and pore volume), the sixteen different carbon gels were analyzed using Taguchi's statistical design methods [18]. This analysis included first completing a response table, calculating the effects, plotting the effects on a probability plot, and then from this plot, determining which effects were significant. The probability and parameter interaction plots for surface area and pore volume are shown in Figures 1 and 2, respectively.

Table 1.  $2^4$  Factorial Design Factors and Their Settings

Factor	High Setting	Low Setting
A. Initial Solution pH	7.0	5.5
B. Wt% Solids	20	5
C. Pyrolysis Temperature	1050 °C	800 °C
D. Gel Type	Xerogel	Aerogel

Once the surface area results were analyzed statistically, the following effects were found to be significant: initial solution pH, pyrolysis temperature, gel type, and the initial solution pH-gel type interaction. Figure 1a shows that increasing the pyrolysis temperature from the low to the high setting caused a significant decrease in the surface area. The other two significant factors (A and D) could not be analyzed separately because they were found to interact with each other. Figure 1b shows the extent of this interaction (if no interaction existed, the two lines in Figure 1b would be parallel to each other). This interaction was interpreted in the following way. For the xerogel (D2), in going from the low to the high pH setting, the surface area did not change much; however, for the aerogel, the surface area changed significantly in going from the low to the high pH. Also, at the low pH setting, there was little change between the xerogel and aerogel compared to that exhibited at the high pH setting. A summary of these effects on the surface area is given in Table 3. The predicted response values are based on the mean response values combined with the responses from those effects that proved to be significant [18]. For example, it was found that the high pH aerogel at the low pyrolysis



temperature resulted in the maximize surface area, based on a statistically predicted response. Within the range of this study, wt% solids did not affect surface area, and the minimum surface area resulted from the opposite settings. For pore volume, Figure 2a shows that the gel pH, gel type and gel pH-gel type interaction were the only parameters that significantly affected the pore volume, and Figure 2b shows the effect of each combination of the interacting parameters on the response variable. A statistical summary of these effects on the pore volume is given in Table 3. The statistically predicted response for the maximum pore volume resulted from the high pH aerogel. Wt% solids and pyrolysis temperature did not affect the pore volume in the range of this study. It was also interesting that all of the pore volumes obtained for the xerogels, ranging only from 0.20 to 0.44 cm<sup>3</sup>/g, were not significantly affected by any of the chosen factors and their settings.

Table 2. Surface Area and Pore Volume Results

Initial Solution pH	Weight % Solids	Pyrolysis Temperature (°C)	Gel Type	Surface Area (m <sup>2</sup> /g)	Pore Volume (cm <sup>3</sup> /g)
5.5	5%	800	Aerogel	561	0.32
5.5	5%	800	Xerogel	569	0.36
5.5	5%	1050	Aerogel	508	0.30
5.5	5%	1050	Xerogel	521	0.28
5.5	20%	800	Aerogel	517	0.24
5.5	20%	800	Xerogel	493	0.26
5.5	20%	1050	Aerogel	474	0.23
5.5	20%	1050	Xerogel	460	0.25
7.0	5%	800	Aerogel	900	0.92
7.0	5%	800	Xerogel	591	0.20
7.0	5%	1050	Aerogel	753	1.32
7.0	5%	1050	Xerogel	540	0.40
7.0	20%	800	Aerogel	929	1.31
7.0	20%	800	Xerogel	586	0.44
7.0	20%	1050	Aerogel	804	1.42
7.0	20%	1050	Xerogel	515	0.44
Mean				607	0.54

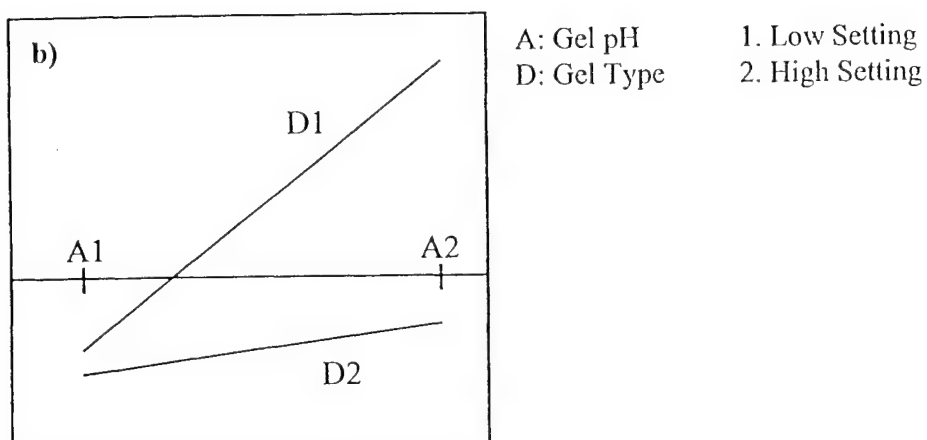
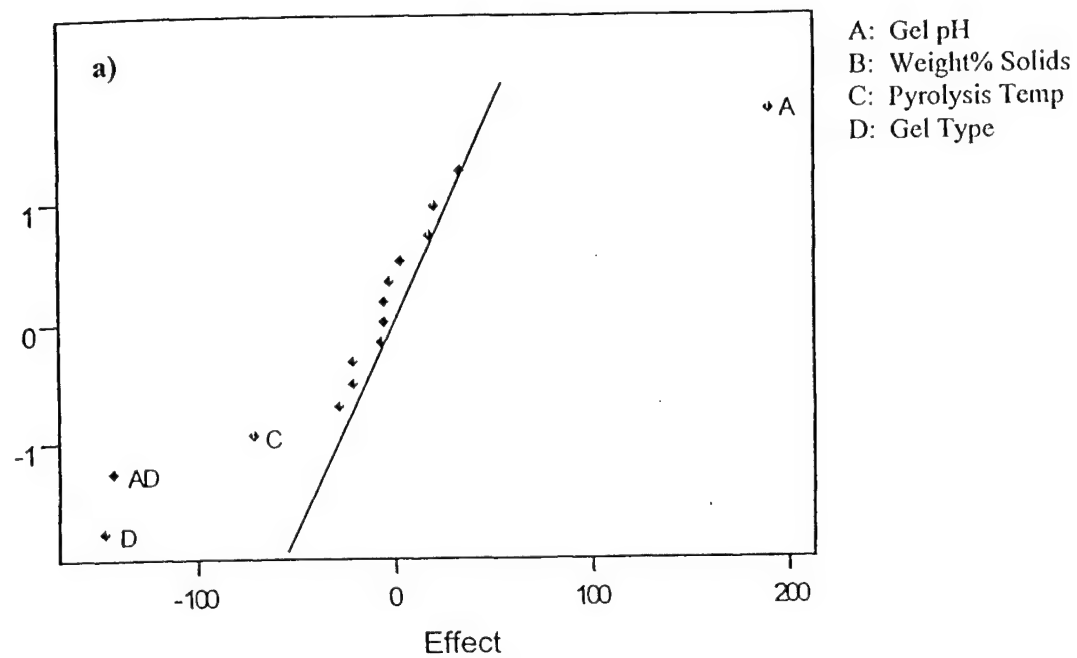


Figure 1. a) Normal probability and b) interaction plots for surface area.

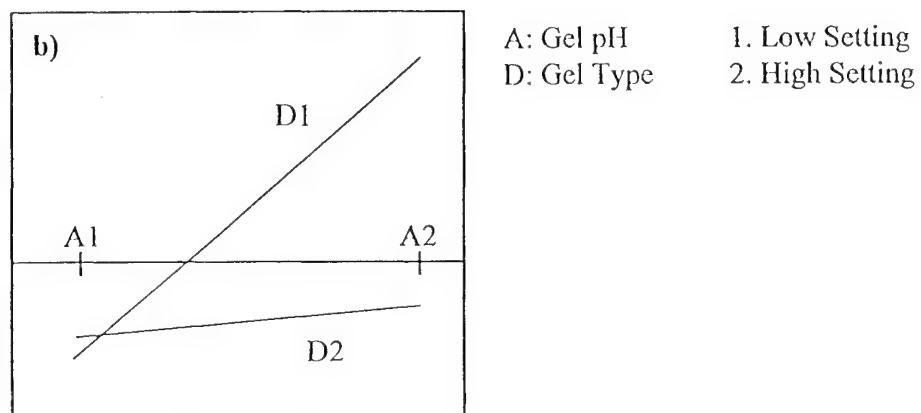
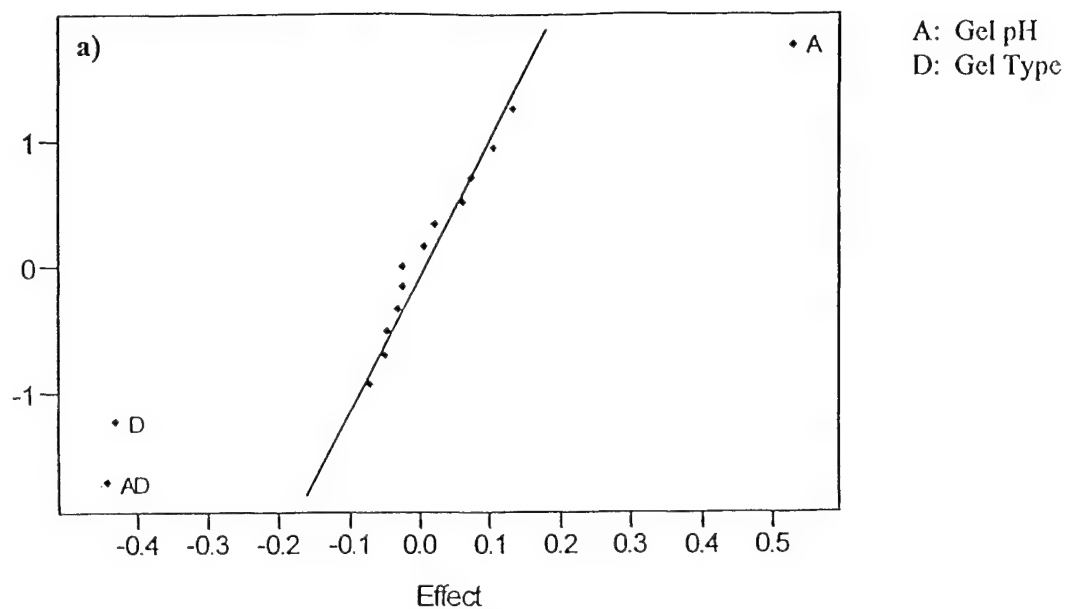


Figure 2. a) Normal probability and b) interaction plots for pore volume.

Table 3. Summary of 2<sup>4</sup> Factorial Design Results

	Predicted Response	Gel pH	Wt% Solids	Pyrolysis Temp.	Gel Type
Max. Surface Area	882 m <sup>2</sup> /g	High	*	Low	Aerogel
Min. Surface Area	475 m <sup>2</sup> /g	Low	*	High	Xerogel
Max. Pore Volume	1.24 cm <sup>3</sup> /g	High	*	*	Aerogel
1 <sup>st</sup> Cycle Capacity	371 Ahr/kg	*	*	*	*
2 <sup>nd</sup> Cycle Capacity	306 Ahr/kg	*	*	*	*
Max. 1 <sup>st</sup> Cycle Eff.	43%	High	N/A	N/A	N/A
Max. 2 <sup>nd</sup> Cycle Eff.	79%	Low	High	N/A	Aerogel

\* Indicates no significant effect of this parameter on the response variable.

The raw results from the Li<sup>+</sup> charge/discharge tests are shown in Table 4 in terms of the first and second cycle charge/discharge capacities and coulombic efficiencies, where the coulombic efficiency is defined as the ratio of the discharge capacity to that of the charge capacity in each cycle. The first cycle charge and discharge capacities of all sixteen carbon gels varied significantly with a mean charge capacity of 1373 Ahr/kg, a mean discharge capacity of 371 Ahr/kg and a mean coulombic efficiency of 33%. In contrast, the second cycle charge and discharge capacities did not vary as much with a mean charge capacity of 378 Ahr/kg, a mean discharge capacity of 306 Ahr/kg and a mean coulombic efficiency of 83%. The wide ranges of capacities and coulombic efficiencies exhibited by these sol-gel derived resorcinol-formaldehyde carbonized resins were typical of that reported elsewhere for other types of carbonized resins derived from organic precursors [3, 5-7]. The best material for use as the anode in the lithium ion battery was that corresponding to a high wt% solids, high pyrolysis temperature, low pH aerogel with first and second cycle coulombic efficiencies of 62 and 93%, respectively and a second cycle discharge capacity of 492 Ahr/kg. These were also the conditions that resulted in nearly the lowest surface area and pore volume (see Table 2), in agreement with that typically reported in the literature. However, recall that the specific trends depicted in Table 4 could not be analyzed directly; they had to be analyzed using Taguchi's methods [18]. The probability plots for the first cycle reversible capacity and coulombic efficiency are shown in Figure 3, and the probability and interaction plots for the second cycle reversible capacity and coulombic efficiency are shown in Figure 4.

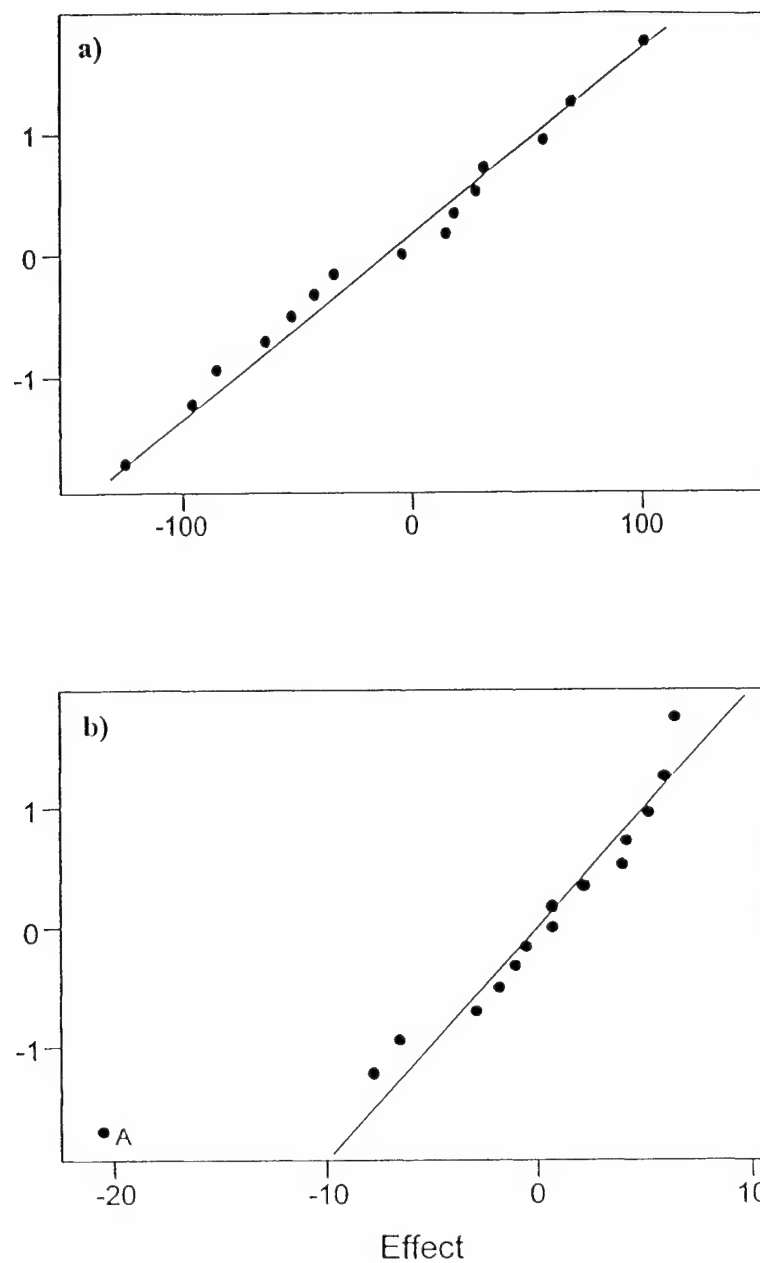
Analysis of the first and second cycle reversible (discharge) capacities using Taguchi's methods [18] revealed that there were no significant effects from any of the four parameters, as shown in Figures 3a and 4a. Furthermore, Figure 3b shows that the first cycle coulombic efficiency was affected only by the gel pH, whereas Figure 4b shows that the second cycle coulombic efficiency was affected by the gel pH, wt% solids, gel type and gel pH-gel type interaction. The interaction plot in Figure 4c shows that the second cycle coulombic efficiencies at the low pH setting were similar for the aerogel

and xerogel but differed significantly at the high pH setting. Moreover, the xerogel consistently gave a high coulombic efficiency for both high and low pH settings, where the aerogel exhibited a marked decrease in the second cycle coulombic efficiency going from the low to the high pH setting. A statistical summary of these effects on the first and second cycle capacities and coulombic efficiencies is given in Table 3. Since there were no statistically significant effects of any of the four parameters on the first or second cycle reversible capacities, the predicted responses corresponded to the means given in Table 4, which were very similar to the maximum capacity exhibited by graphite. In contrast, the parameter settings corresponding to the first and second cycle coulombic efficiencies were different. For example, the statistically predicted response for the maximum first cycle coulombic efficiency resulted from the high pH gel (no other factors were significant), whereas that for the second cycle coulombic efficiency resulted from a low pH high wt% solids aerogel. Based on these perplexing results for the first and second cycle coulombic efficiencies, it was clear that this statistical design approach only allowed for a single response variable to be minimized or maximized. It did not give any insight into how to maximize or minimize multiple response variables, like the first and second cycle coulombic efficiencies. Nevertheless, the overall results from this study did indicate that to maximize both reversible capacity and coulombic efficiency, a set of parameters that minimizes both surface area and pore volume simultaneously would be advantageous.

Table 4. Charge/Discharge Capacity (Ahr/kg) and Coulombic Efficiency (%) Results

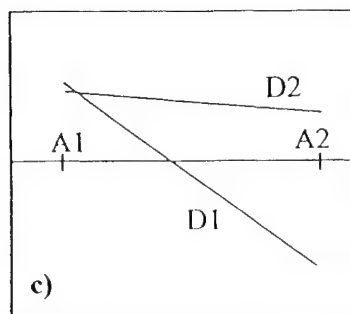
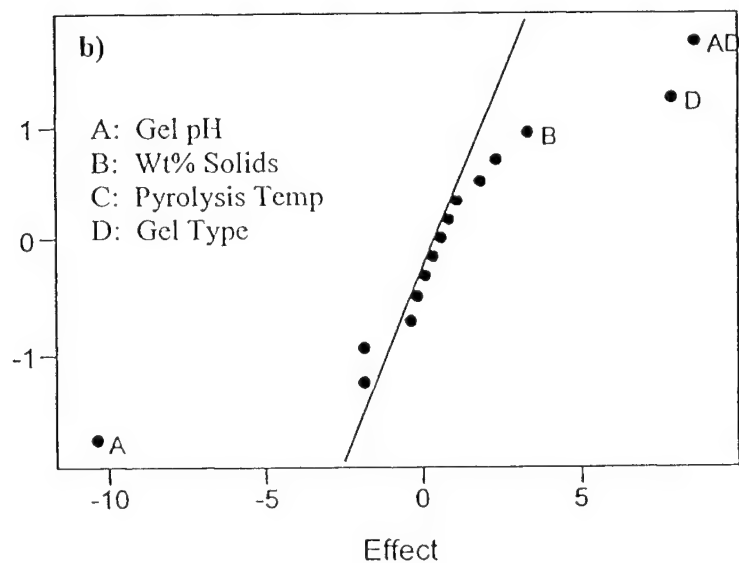
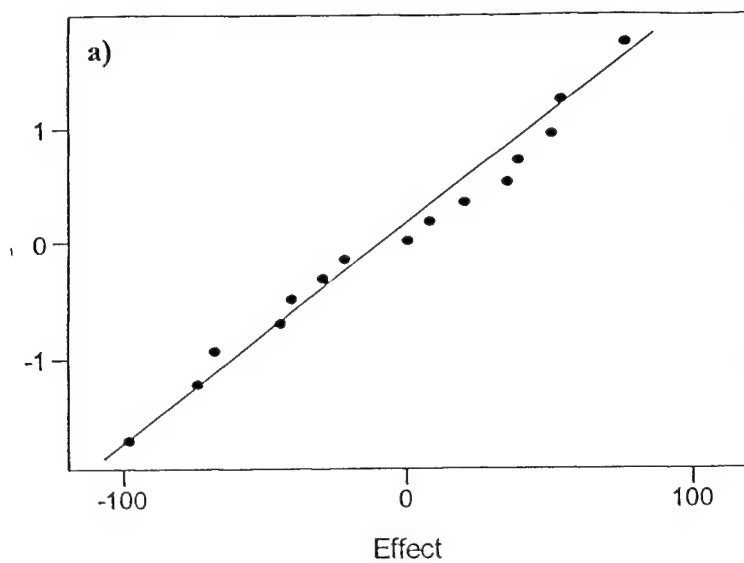
Initial Solution pH	Weight % Solids	Pyrolysis Temp. (°C)	Gel Type	Cycle 1			Cycle 2		
				Charge	Dis- charge	Eff.	Charge	Dis- charge	Eff.
5.5	5%	800	A	955	359	38	342	294	86
5.5	5%	800	X	965	396	41	377	326	86
5.5	5%	1050	A	724	272	38	280	242	87
5.5	5%	1050	X	806	322	40	316	271	86
5.5	20%	800	A	819	310	38	267	243	91
5.5	20%	800	X	790	235	30	216	189	88
5.5	20%	1050	A	975	605	62	531	492	93
5.5	20%	1050	X	638	350	55	273	256	94
7.0	5%	800	A	3064	553	18	667	449	67
7.0	5%	800	X	1164	302	26	298	252	84
7.0	5%	1050	A	2031	237	12	273	201	74
7.0	5%	1050	X	926	243	26	251	216	86
7.0	20%	800	A	2862	605	21	698	496	71
7.0	20%	800	X	1092	335	31	333	292	87
7.0	20%	1050	A	3062	518	17	624	429	69
7.0	20%	1050	X	1040	285	27	295	265	90
Mean				1373	371	33	378	306	83





A: Gel pH

Figure 3. Normal probability plots for first cycle a) reversible capacity and b) coulombic efficiency.



A: Gel pH  
B: Wt% Solids  
C: Pyrolysis Temp  
D: Gel Type

Figure 4. Normal probability plots for second cycle a) reversible capacity b) coulombic efficiency, and c) interaction plot for coulombic efficiency.

## ACKNOWLEDGMENTS

This material is based upon work supported in part by the U. S. Army Research Office under Grant No. DAAH04-96-1-0421 and in part by the U. S. National Science Foundation under Grant No. GER-9554556.

## REFERENCES

1. M. S. Dresselhaus and G. Dresselhaus, *Adv. Phys.* **30**, 139 (1981).
2. K. Sato, M. Noguchi, A. Demachi, N. Oki and M. Endo, *Science*, **264**, 556 (1994).
3. T. Zheng, Y. Liu, E. W. Fuller, S. Tseng, U. von Sacken and J. R. Dahn, *J. Electrochem. Soc.*, **142**, 2581 (1995).
4. J. R. Dahn, T. Zheng, Y. Liu and J. S. Xue, *Science*, **270**, 590 (1995).
5. Y. Jung, M. C. Suh, S. C. Shim and J. Kwak, *J. Electrochem. Soc.*, **145**, 3123 (1998).
6. H. Q. Xiang, S. B. Fang and Y. Y. Jiang, *J. Electrochem. Soc.*, **144**, L187 (1997).
7. T. Zheng, Q. Zhong and J. R. Dahn, *J. Electrochem. Soc.*, **142**, L211 (1995).
8. S. T. Mayer, R. W. Pekala and J. L. Kaschnitter, *J. Electrochem. Soc.*, **140**, 447 (1993).
9. C. Lin, J. A. Ritter and B. N. Popov, Abstract No. 77, 193<sup>rd</sup> Meeting of The Electrochemical Society, Inc. (1998).
10. C. Lin, J. A. Ritter and B. N. Popov, *J. Electrochem. Soc.*, submitted (1998).
11. E. J. Zanto, J. A. Ritter and B. N. Popov, *Carbon* submitted (1998).
12. R. W. Pekala, *J. Materials Science*, **24**, 3221 (1989).
13. C. Lin, J. A. Ritter, *Carbon*, **35**, 1271 (1997).
14. H. Tamon, H. Ishizaka, T. Araki and M. Okazaki, *Carbon*, **36**, 1257 (1998).
15. H. Tamon and H. Ishizaka, *Carbon*, **36**, 1397 (1998).
16. H. Tamon, H. Ishizaka, M. Mikami and M. Okazaki, *Carbon*, **35**, 791 (1997).
17. C. Lin and J. A. Ritter, *Carbon*, submitted (1998).
18. R. H. Lochner and J. E. Matar, *Designing for Quality*, ASQC Quality Press, Milwaukee, 1990.

# Development of Carbon-Metal Oxide Supercapacitors from Sol-Gel Derived Carbon-Ruthenium Xerogels

Chuan Lin,<sup>a</sup> James A. Ritter,<sup>a,z</sup> and Branko N. Popov\*

Department of Chemical Engineering, Swearingen Engineering Center, University of South Carolina, Columbia, South Carolina 29208, USA

Sol-gel derived high surface area carbon-ruthenium xerogels were prepared from carbonized resorcinol-formaldehyde resins containing an electrochemically active form of ruthenium oxide. The electrochemical capacitance of these materials increased with an increase in the ruthenium content indicating the presence of pseudocapacitance associated with the ruthenium oxide undergoing reversible faradaic redox reactions. A specific capacitance of 256 F/g (single electrode) was obtained from a carbon xerogel containing 14 wt % Ru, which corresponded to more than 50% utilization of the ruthenium. The double layer accounted for 40% of this capacitance. This material was also electrochemically stable, showing no change in a cyclic voltammogram for over 2000 cycles.

© 1999 The Electrochemical Society. S0013-4651(98)12-085-2. All rights reserved.

Manuscript submitted December 28, 1998; revised manuscript received May 5, 1999.

There has been increasing interest in electrochemical capacitors<sup>1-5</sup> as energy storage systems because of their high power density and long cycle life, compared to battery devices. According to the mechanism of energy storage, there are two types of electrochemical capacitors. One type is based on double layer (dl) formation due to charge separation, and the other type is based on a faradaic process due to redox reactions. These dl devices are referred to as electrochemical dl capacitors (EDLCs), and faradaic devices are called pseudocapacitors. Depending on the origin of the interaction between the electrode and electrolyte, the associated capacitance is usually in the range of tens (for dl capacitors) to hundreds (for pseudocapacitors) of  $\mu\text{F}$  per  $\text{cm}^2$  of interfacial area.

Carbon materials, such as activated carbons,<sup>6,7</sup> carbon fibers,<sup>8</sup> and carbon aerogels,<sup>9</sup> are widely used for dl capacitors because of their high surface area. The specific capacitance of these kinds of carbon materials typically ranges from 40 to 160 F/g (single electrode). On the other hand, comparatively lower surface area transition metal oxides, such as amorphous hydrous ruthenium oxide,  $\text{RuO}_2 \cdot x\text{H}_2\text{O}$ ,<sup>10</sup> have been studied for pseudocapacitors. A remarkable specific capacitance of 760 F/g (single electrode) was achieved for this material made by the sol-gel technique. Moreover, a recent modeling study has shown that electrode materials possessing both double layer and reversible redox processes can enhance the energy density of a device.<sup>11</sup>

The dl mechanism of energy storage is strictly a surface phenomenon, with higher active surface areas giving rise to higher specific capacitances. In contrast, the faradaic mechanism of energy storage is not limited to surface reactions; bulk reactions are also possible and contribute to energy storage in these kinds of materials.<sup>10</sup> However, proton diffusion into the bulk of the material, an inherently slow transport mechanism, would likely limit the power of such a device and thus the utilization of the material. It would be advantageous to disperse a relatively low surface area, redox-active transition metal oxide such as  $\text{RuO}_2 \cdot x\text{H}_2\text{O}$  throughout a high surface area, double layer support such as activated carbon. The resulting small particle size of the  $\text{RuO}_2 \cdot x\text{H}_2\text{O}$  would increase the redox-active surface area of the material, giving rise to higher-power devices and more utilization of this expensive transition metal oxide. The sol-gel technique is well suited for making this kind of material, because it readily allows for control of the texture, composition, homogeneity, and structural properties of the resulting materials.<sup>12</sup> Recently, Miller *et al.* prepared an electrode material for superca-

pacitors, with ruthenium nanoparticles deposited via chemical vapor deposition within the pore of a carbon aerogel.<sup>13</sup> They achieved a specific capacitance of 206 F/g (single electrode) for an aerogel containing 35 wt % ruthenium.

The objective of this work is to present an alternative method for making high surface area carbon-ruthenium xerogel composites for use as supercapacitors. This new method is based on a sol-gel route for making high surface area carbon xerogels from carbonized resorcinol-formaldehyde (R-F) resins.<sup>14</sup> Physical properties of these unique xerogel composites, such as surface area, pore volume, crystallinity, and surface morphology, are reported along with their performance as electrochemical capacitors utilizing both dl and faradaic processes.

## Experimental

The synthesis procedure presented below for making carbon-ruthenium xerogels was based on similar procedures that have been used for making carbon aerogels<sup>9</sup> and carbon xerogels.<sup>14</sup> Reagent-grade resorcinol (98%, Aldrich), formaldehyde (37% in water, Aldrich), sodium carbonate (GR, EM Science, Germany), acetone (ACS, 99.5%, Alfa), and  $\text{RuO}_2 \cdot x\text{H}_2\text{O}$  (Ru 55.29%, Alfa) were used as received. Briefly, solutions containing 20 wt/vol % solids were prepared, in which the R-F mole ratio (R/F) was fixed at 1:2. Sodium carbonate was used as a catalyst and the resorcinol/sodium carbonate mole ratio (Ru/R) was fixed at 50. The  $\text{RuO}_2 \cdot x\text{H}_2\text{O}$ /resorcinol mole ratio (Ru/R) was varied to make carbon-ruthenium xerogels with different Ru loadings.  $\text{RuO}_2 \cdot x\text{H}_2\text{O}$  was added as a powder prior to the partial polymerization of R-F to a sol state, and its addition slightly decreased the pH of the initial R-F solution from 7.5 (Ru/R = 0) to 6.9 (Ru/R = 0.1). The solutions were sealed in a glass bottle and magnetically stirred at room temperature until gelation occurred, and then the gels were placed in an oven ( $85 \pm 3^\circ\text{C}$ ) for curing for 1 week. The resultant gels were opaque instead of the characteristic deep red color of unmodified R-F gels.<sup>9</sup> After curing, the gels were washed with acetone for three days. Fresh solvent was replaced daily after vacuum filtration. Then the washed gels were dried under  $\text{N}_2$  in a tube furnace. Using a heating rate of  $0.5^\circ\text{C}/\text{min}$ , the furnace was heated to  $65^\circ\text{C}$  and held at that temperature for 5 h; it was then heated to  $110^\circ\text{C}$  and held there for another 5 h. Finally, the carbon-ruthenium xerogels were formed by pyrolysis of the dried gels at  $750^\circ\text{C}$  in a  $\text{N}_2$  atmosphere for 3 h with both heating and cooling rates set at  $5^\circ\text{C}/\text{min}$ .

The surface areas and pore volumes of the carbon-ruthenium xerogels were measured using a Micromeritics Pulse Chemisorb 2700 analyzer. Transmission electron micrographs were recorded with a Hitachi H-8000 transmission electron microscope (TEM), and X-ray diffraction (XRD) patterns were collected using a Rigaku-D-max B diffractometer equipped with a Cu source. Electrochemical

\* Electrochemical Society Active Member.

<sup>a</sup> Present Address: Department of Chemical Engineering, Center for Advanced Engineering Fibers and Films, Clemson University, Clemson, South Carolina 29634, USA.

<sup>z</sup> E-mail: ritter@enr.sc.edu.

measurements were carried out at room temperature using an EG&G 273A potentiostat.

A three-electrode test system was used to make the electrochemical measurements. The working electrode, containing about 1 to 2 mg of active material and 5 wt % Teflon as binder, was hand-pressed into a disk with a diameter of 0.75 cm and thickness of about 50  $\mu\text{m}$ . The disk was then pressed between two pieces of platinum gauze at 3 tons/cm<sup>2</sup> with a hydraulic press and held there for 10 min. A saturated calomel electrode (SCE) was used as the reference electrode, a piece of platinum gauze (large, relative to the working electrode) was used as the counter electrode, and a solution of 30 wt % H<sub>2</sub>SO<sub>4</sub> was used as the electrolyte. Galvanostatic charge/discharge was performed between 0 and 1 V (vs. SCE) by varying the current density (0.1 to 50 mA/mg), and cyclic voltammetry (CV) was carried out between 0 and 1 V (vs. SCE) with a sweep rate of 5 mV/s. The electrochemical measurements were conducted at room temperature.

The specific capacitances of the single electrode were calculated from the galvanostatic discharge using the following equation

$$C = \frac{it_d}{m\Delta V_{CC}} \quad [1]$$

where  $C$  is the specific capacitance,  $i$  is the total current,  $t_d$  is the discharge time,  $\Delta V_{CC}$  is the potential drop during constant current discharge, and  $m$  is the mass of the active material. For comparison, the specific capacitances were also calculated from the cathodic part of the CV results using the following equation

$$C = \frac{1}{m\Delta V_{CV}} \int_{t_1}^{t_2} i_c dt \quad [2]$$

where  $i_c$  is the cathodic current,  $t$  is the time,  $t_1$  is the time when  $V = 0.9$  V,  $t_2$  is the time when  $V = 0.1$  V, and  $\Delta V_{CV}$  is the potential difference (0.8 V). The specific energy and power of the single electrode were also calculated from the galvanostatic discharge results using the following equations

$$\text{Specific energy} = \frac{i\bar{V}t_d}{m} \quad [3]$$

$$\text{Specific power} = \frac{i\bar{V}}{m} \quad [4]$$

where the average potential,  $\bar{V}$ , is given by

$$\bar{V} = \frac{1}{t_d} \int_0^{t_d} V dt \quad [5]$$

## Results

Different carbon-ruthenium xerogels were made by varying the Ru/R mole ratio in the initial R-F solution between 0 and 0.1 (Ru/R = 0.1 is equivalent to 14 wt % Ru in the resultant carbon-ruthenium xerogel). It is noteworthy that gelation did not occur above Ru/R = 0.1. Figure 1 shows the effect of the Ru content on the surface area and pore volume of the carbon-ruthenium xerogels. The surface area was 563 m<sup>2</sup>/g for the pure carbon xerogel (Ru/R = 0). It then dropped sharply to 520 m<sup>2</sup>/g with an increase of Ru/R from 0 to 0.01. With an increase of Ru/R up to 0.1, the surface area decreased more slowly and almost linearly to 475 m<sup>2</sup>/g. In contrast, the pore volume increased significantly and linearly from 0.23 to 0.59 cm<sup>3</sup>/g with an increase of Ru/R from 0 to 0.1.

The effect of Ru content on the crystalline structure of fresh carbon-ruthenium xerogels is shown in Fig. 2A. The XRD patterns for the pure carbon xerogel exhibited two broad humps at  $2\theta = 22$  and  $43^\circ$ , which corresponded to a typical microcrystalline carbon structure. As the Ru content increased, however, the carbon humps decreased gradually and almost disappeared for the carbon-ruthenium xerogel with Ru/R = 0.1. The XRD patterns for the carbon-ruthenium xerogels also showed characteristic peaks of Ru metal at  $2\theta = 38.4, 42.2, 44.0, 58.3,$  and  $69.5^\circ$ , and the intensities of these peaks increased with increasing Ru content. Figure 2B displays

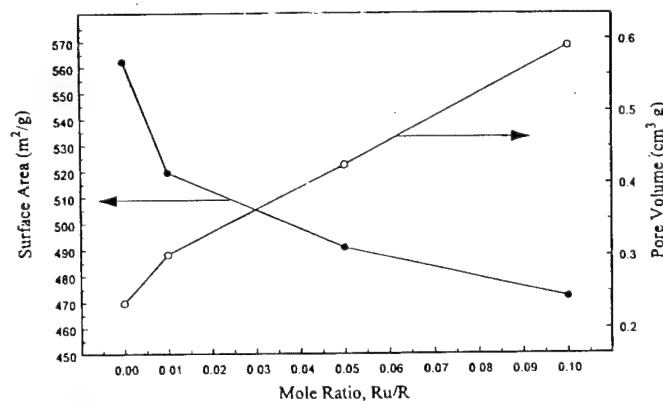


Figure 1. Effect of Ru content on the surface area and pore volume of the carbon-ruthenium xerogels.

XRD patterns for different Ru materials. The as-received RuO<sub>2</sub>·xH<sub>2</sub>O, which was used for making the carbon-ruthenium xerogels in the initial solution, was essentially amorphous. For the carbon-ruthenium xerogel with Ru/R = 0.1, the XRD patterns for fresh xerogel, and that after 2000 CV cycles, both exhibited peaks that are characteristic of Ru metal, but the intensities of the peaks decreased by about 80% after CV cycling. In addition, the XRD pattern of RuO<sub>2</sub>, which was made by calcining the as-received RuO<sub>2</sub>·xH<sub>2</sub>O at

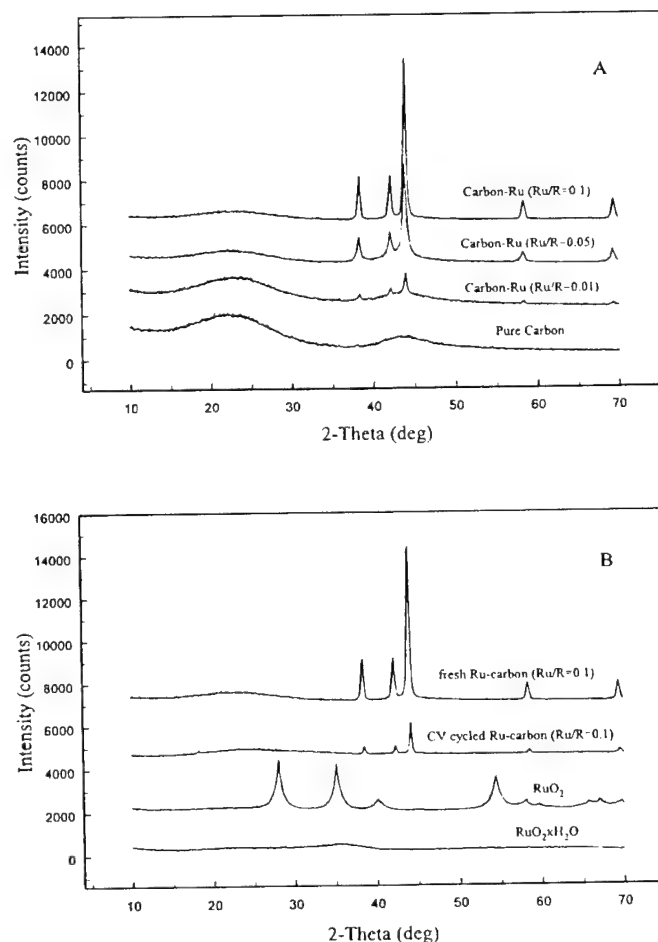
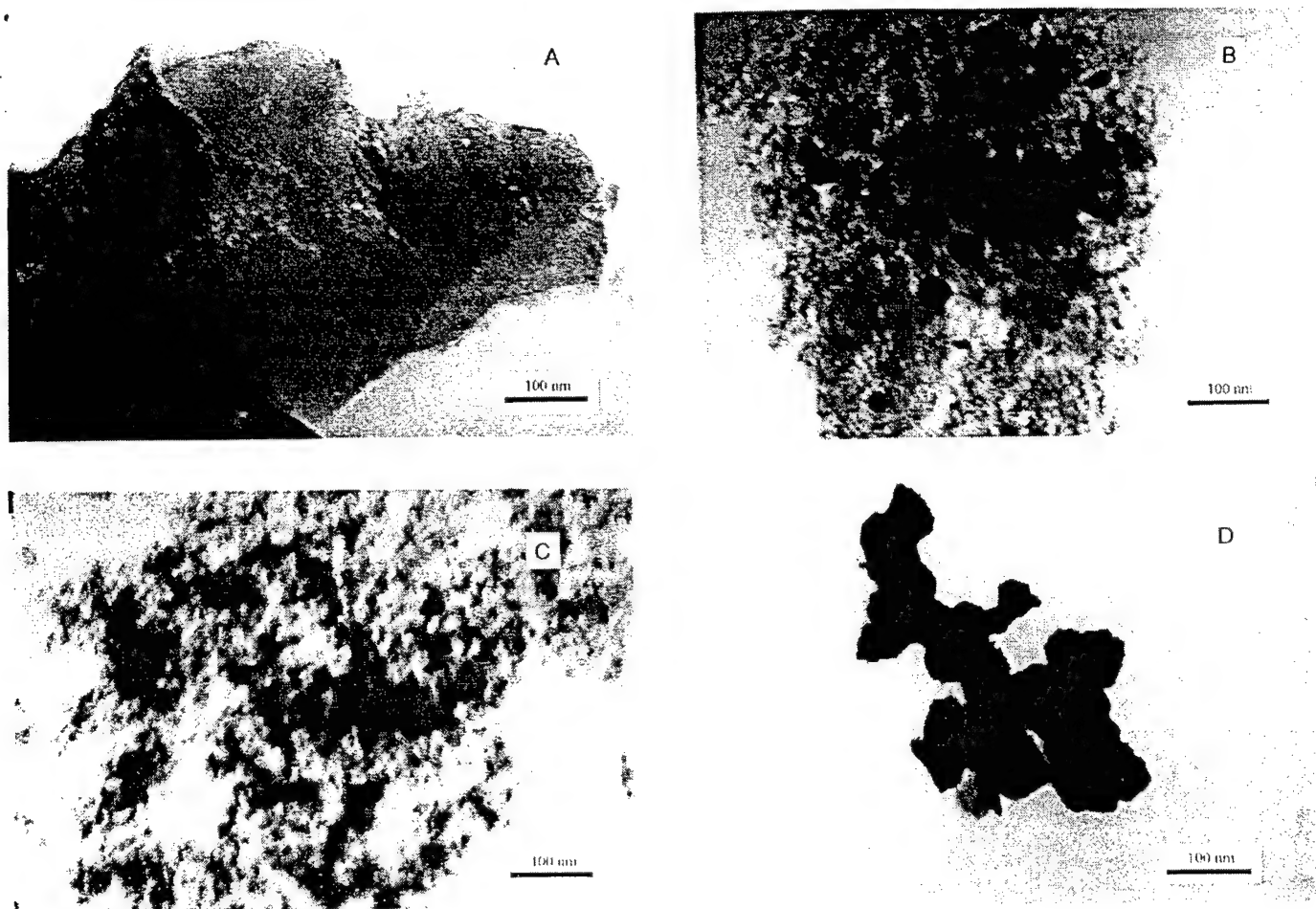


Figure 2. (A) XRD patterns of carbon-ruthenium xerogels with different Ru loadings; and (B) comparison of XRD patterns of carbon-ruthenium xerogels (Ru/R = 0.1) before and after 2000 CV cycles, as-received RuO<sub>2</sub>·xH<sub>2</sub>O, and RuO<sub>2</sub> (i.e., calcined RuO<sub>2</sub>·xH<sub>2</sub>O at 400°C in air for 3 h).



**Figure 3.** TEM images: (A) pure carbon xerogel; (B) carbon-Ru xerogel with  $Ru/R = 0.01$ ; (C) carbon-Ru xerogel with  $Ru/R = 0.1$ ; and (D) as-received  $RuO_2 \cdot xH_2O$ .

400°C in air for 3 h, indicated that both the fresh and CV cycled carbon-ruthenium xerogels did not contain any crystalline  $RuO_2$ .

The surface morphology of the carbon-ruthenium xerogels was studied with TEM; the TEM micrographs are shown in Fig. 3A to C. The pure carbon xerogel (Fig. 3A) exhibited a very fine pore structure. In contrast, the xerogel with  $Ru/R = 0.01$  (Fig. 3B) had black spots dispersed randomly in the carbon matrix that ranged from 10 to 30 nm in diam. These spots were identified as metallic Ru nano-

particles. The xerogel with  $Ru/R = 0.1$  (Fig. 3C), as expected, showed a higher population of ruthenium particles with sizes similar to those in Fig. 3B. For comparison, a TEM micrograph of the as-received  $RuO_2 \cdot xH_2O$  is shown in Fig. 3D; particle sizes for this material ranged from 50 to 100 nm in diam.

CV and galvanostatic techniques were used to determine the electrochemical properties of the carbon-ruthenium xerogels and also the as-received  $RuO_2 \cdot xH_2O$ . Figure 4A shows CVs of the car-

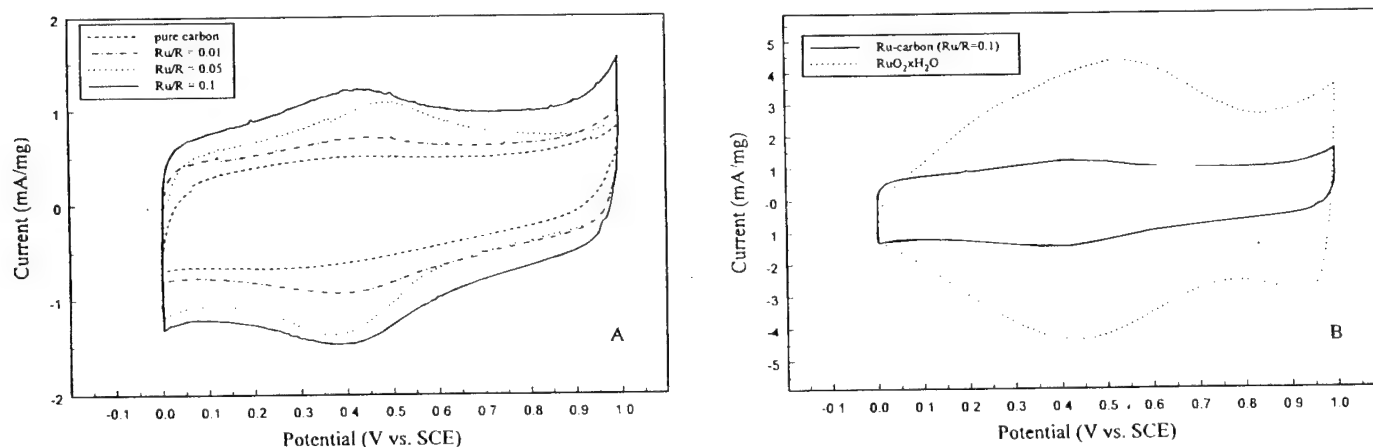


**Figure 4.** CVs of Ru-carbon xerogels with different Ru loadings; and (B) comparison of CVs for the carbon-ruthenium xerogel with  $Ru/R = 0.1$  and as-received  $RuO_2 \cdot xH_2O$ . In all cases, the scan rate was 5 mV/s.

bon-ruthenium xerogels as a function of the Ru content. The constant current observed with variation in potential was characteristic of capacitive behavior. The CV curve also exhibited ideal pseudocapacitive behavior between the hydrogen and oxygen evolution reactions. The current increased with an increase in the Ru content, indicating a higher capacitance for xerogels with a higher Ru content. Figure 4B presents CVs for the carbon-ruthenium xerogel with  $Ru/R = 0.1$  and the as-received  $RuO_2 \cdot xH_2O$ . The as-received  $RuO_2 \cdot xH_2O$  had a much higher capacitance than the carbon-ruthenium xerogel. In addition, the shapes of their respective voltammograms were different. The carbon-ruthenium xerogel behaved more like a capacitor material and exhibited a relatively flat current response over a broad potential range. In contrast,  $RuO_2 \cdot xH_2O$  behaved more like a redox material with distinguishable broad peaks. The electrochemical stability of the carbon-ruthenium xerogel with  $Ru/R = 0.1$  was studied using CV; the results are shown in Fig. 5. Essentially, no change was observed between the initial cycle and after 2000 cycles, indicating that the electrode was very stable and that much of the Ru metal in the carbonized material was converted to an electrochemically active form during the first cycle.

Figure 6A shows constant-current discharge profiles of the carbon-ruthenium xerogels at a current density of 1 mA/mg. The profiles were similarly shaped for all of the carbon-ruthenium xerogels; however, the discharge time for the potential change from 1 to 0 V increased with an increase in Ru content, indicating that the capacitance increased with increasing Ru content. The initial potential drops observed in Fig. 6A were caused by non-uniform current distributions as a result of ohmic and pore resistances.<sup>11,15</sup> Figure 6B presents constant-current discharge profiles of the carbon-ruthenium xerogel with  $Ru/R = 0.1$  and the as-received  $RuO_2 \cdot xH_2O$ , both at a current density of 1 mA/mg. The corresponding capacitances were 232 and 675 F/g, respectively. It was interesting that the essentially faradaic electrode ( $RuO_2 \cdot xH_2O$ ) did not exhibit the initial drop in potential, which was more characteristic of a battery discharged at high current densities. Figure 7 shows the effect of Ru content on the capacitance of the carbon-ruthenium xerogels, measured by constant-current discharge at a current density of 1 mA/mg and by CV at a sweep rate of 5 mV/s. As shown in Fig. 7, the capacitance obtained by constant-current discharge was always about 10 to 15% higher than that obtained by CV. Because the transition discharge time was easier to determine and thus more accurate than the total cathodic or anodic charge from the CV, any capacitance referred to below is based on the constant-current discharge method unless stated otherwise. The capacitance was about 120 F/g for pure carbon xerogel, and it increased with an increase in Ru content and reached 232 F/g for the xerogel with  $Ru/R = 0.1$ .

During galvanostatic experiments, the capacitance of the carbon-ruthenium xerogels also varied with current density. The results for

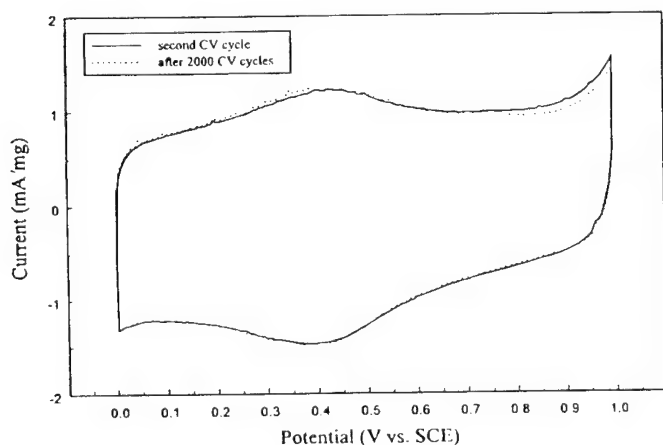


Figure 5. Stability of the carbon-ruthenium xerogel with  $Ru/R = 0.1$ , measured at a scan rate of 5 mV/s.

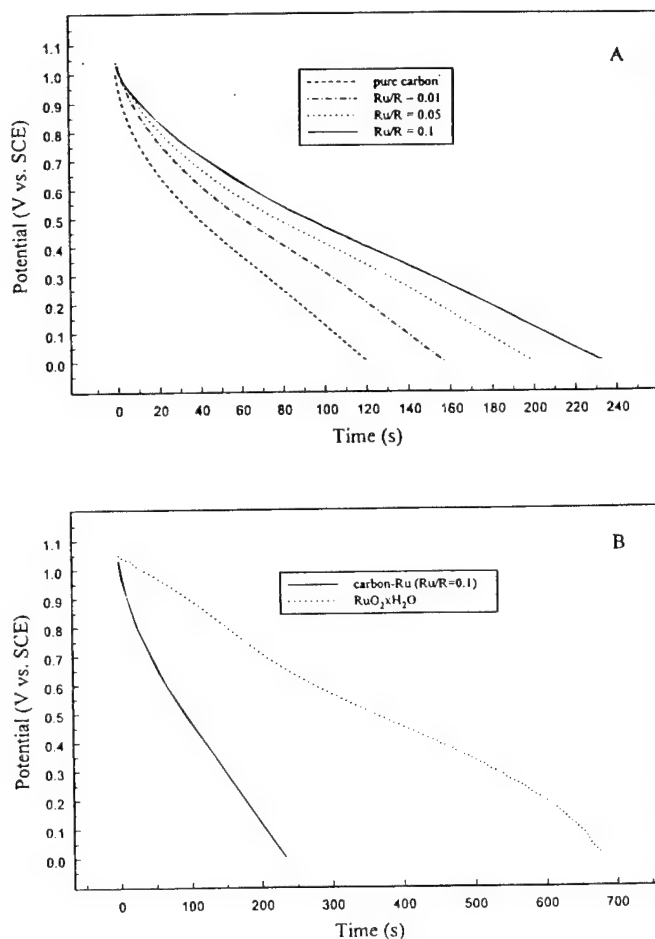


Figure 6. (A) Constant current discharge profiles of carbon-ruthenium xerogels with different Ru loadings; and (B) comparison of constant current discharge profiles for the carbon-ruthenium xerogel with  $Ru/R = 0.1$  and as-received  $RuO_2 \cdot xH_2O$ . In all cases, the current density was 1 mA/mg.

the carbon-ruthenium xerogel with  $Ru/R = 0.1$  and the pure carbon xerogel are shown in Fig. 8A. The capacitance decreased almost linearly with an increase in the log of the current density in both cases. For the carbon-ruthenium xerogel, a capacitance as high as 256 F/g was obtained at a current density of 0.1 mA/mg; however, it dropped

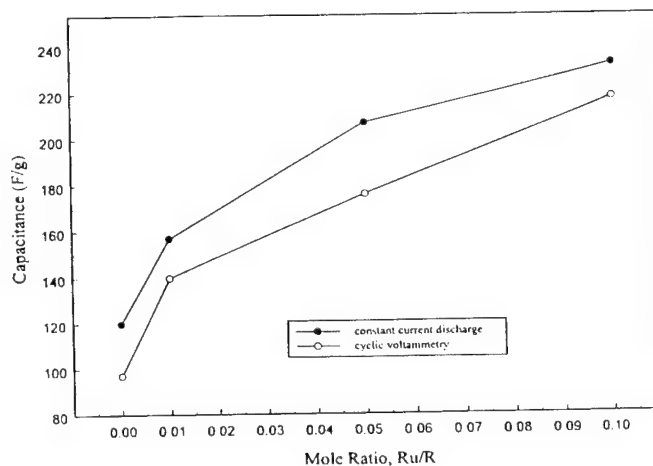


Figure 7. Effect of Ru content on the capacitance of the carbon-ruthenium xerogels, measured by constant current discharge at a current density of 1 mA/mg and by CV at a sweep rate of 5 mV/s.



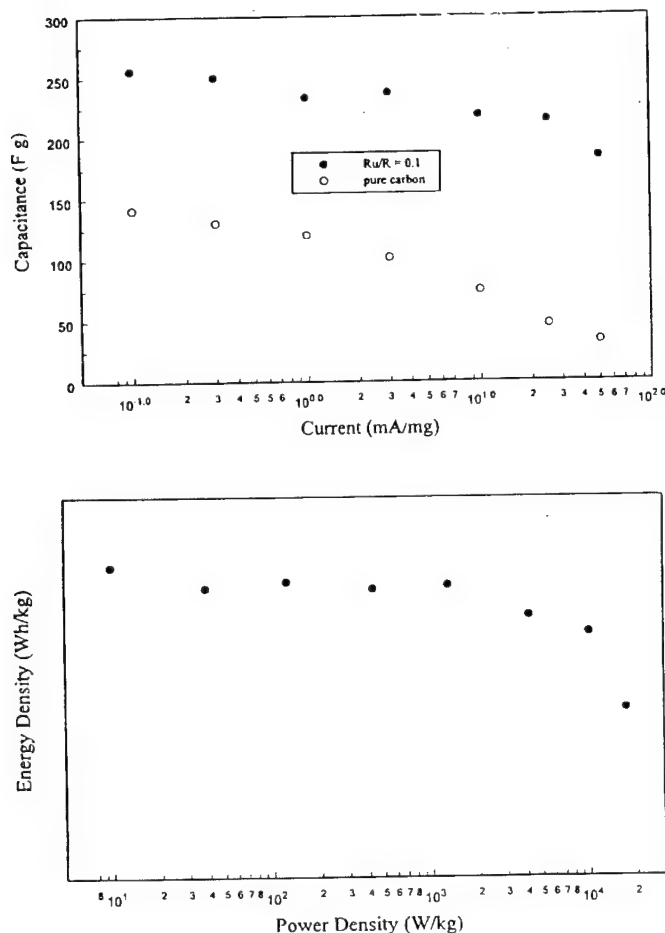


Figure 8. (A) Effect of current density on the capacitance of the carbon-ruthenium xerogel with Ru/R=0.1 and the pure carbon xerogel; and (B) Ragone plot for the single electrode containing the carbon-ruthenium xerogel with Ru/R = 0.1.

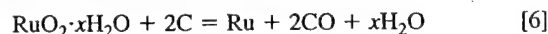
to about 184 F/g at a current density of 50 mA/mg. For the pure carbon xerogel, the capacitances were 142 and 34 F/g at current densities of 0.1 and 50 mA/mg, respectively. A Ragone plot for the single electrode containing the carbon-ruthenium xerogel with Ru/R = 0.1 is presented in Fig. 8B. The energy density remained constant at about 30 Wh/kg up to a power density of 1000 W/kg, then the energy density began to drop off at higher power densities. It is noteworthy that these are average power densities, not peak power densities; and that the per kilogram basis includes only the mass of the electrode material.

### Discussion

High surface area carbon-ruthenium xerogels were made with the sol-gel technique, and their pore structure was measured in terms of surface area and total pore volume (Fig. 1). The surface area of the carbon-ruthenium xerogels decreased with an increase in Ru content; however, the pore volume increased with an increase in Ru content. A decreasing surface area with an increasing pore volume is indicative of the presence of larger pores with an increase in Ru content, which implies less shrinkage of the gel structure with an increase in Ru content. Less shrinkage of the gel structure may have also been caused by the slight decrease in pH of the initial R-F solution that occurred after addition of the RuO<sub>2</sub>·xH<sub>2</sub>O. This decrease in pH may have enhanced the condensation reaction<sup>14</sup> of the R-F system, thereby leading to a more cross-linked R-F resin and hence, larger pores.

The XRD patterns in Fig. 2A revealed that the ruthenium in the carbon xerogels was in the form of metal dispersed throughout the carbon matrix, even though it was added as an oxide (RuO<sub>2</sub>·xH<sub>2</sub>O)

to the initial R-F solution. The ruthenium metal likely formed during carbonization according to the following reaction, because carbon is a good reductant at high temperatures

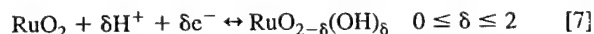


Nevertheless, after one charge/discharge cycle, the majority of the ruthenium metal inside the carbon matrix was converted into a hydrous oxide form similar to the as-received RuO<sub>2</sub>·xH<sub>2</sub>O. This hydrous oxide was electrochemically active and gave rise to the higher capacitances observed with the carbon xerogels containing ruthenium as shown in Fig. 7. This explanation is consistent with the XRD patterns shown in Fig. 2B. Birss *et al.*<sup>16</sup> studied the formation of oxide films on Ru metal electrodes. They found that after charge/discharge between 0 and 1.4 V (vs. saturated hydrogen electrode, SHE), a hydrous ruthenium oxide film formed on the Ru metal surface and its thickness increased with cycling. This oxide film was also not reducible to metal in the positive potential range. The results presented here are consistent with their finding<sup>16</sup> in that the Ru metal nanoparticles were converted to a very stable form of hydrous ruthenium oxide after charge/discharge.

The TEM results indicated that the ruthenium particles in the carbon-ruthenium xerogels, ranging between 10 and 30 nm, were smaller than those in the as-received RuO<sub>2</sub>·xH<sub>2</sub>O, which ranged between 50 and 100 nm (Fig. 3). There are two plausible reasons for this difference. First, Fig. 3D shows that the RuO<sub>2</sub>·xH<sub>2</sub>O particles were comprised of aggregates of smaller particles in the range of 30 to 70 nm. These aggregates most likely broke up into individual particles in the initial R-F solution, especially because RuO<sub>2</sub>·xH<sub>2</sub>O is slightly soluble in aqueous solutions. Second, the ruthenium particles in the carbon xerogels were metallic and formed according to Eq. 6. These consecutive events of aggregate breakup, followed by dispersion in the carbon matrix and subsequent dehydration and reduction to ruthenium metal likely gave rise to the smaller metallic ruthenium nanoparticles of about 10 to 30 nm in diam. These metallic particles also converted into an electrochemically active form after CV cycling, as explained above. Note that the particle size after cycling was not investigated, because it was very difficult to recover the active electrode material from the cell after cycling.

The electrochemical studies also showed that these carbon-ruthenium xerogels utilized both the dl capacitance associated with the high surface area carbon xerogel and the pseudocapacitance associated with the ruthenium redox reactions. For example, the capacitance increased with an increase in Ru content (Fig. 7) from 120 F/g for the pure carbon to 232 F/g for the xerogel with Ru/R = 0.1. This result was clearly due to the pseudocapacitance associated with the ruthenium inside the carbon matrix. The results in Fig. 8 show that at a current density of 0.1 mA/mg, the capacitances were 256 and 142 F/g for the carbon-ruthenium xerogel with Ru/R = 0.1 and pure carbon xerogel, respectively. Because there was 0.14 g of Ru in 1 g of the carbon-ruthenium xerogel (*i.e.*, with Ru/R = 0.1), the capacitance from the ruthenium redox reaction was approximately 956 F/g of Ru after subtracting the carbon contribution, based on the ruthenium-free carbon xerogel (*i.e.*, with Ru/R = 0.0). Also, assuming a two-electron transfer for Eq. 7, the theoretical capacitance for the ruthenium redox reaction was 1907 F/g of Ru. Therefore, the ruthenium utilization was about 50% for the carbon-ruthenium xerogel with Ru/R = 0.1 at a current density of 0.1 mA/mg. Actually, the ruthenium utilization was probably somewhat higher than 50% because  $\delta$  was actually a little less than 2, and also according to the surface area and pore volume results. The surface area and pore volume decreased and increased, respectively, with an increase in Ru content (Fig. 1). Therefore, the dl capacitance alone probably decreased slightly compared to the pure carbon xerogel, which suggests even more electrochemical activity for the ruthenium inside the carbon matrix.

The charge storage mechanism for the reversible ruthenium redox reaction has been explained in terms of a proton-electron reaction mechanism in which ruthenium oxide and RuO<sub>2</sub>·xH<sub>2</sub>O can be reduced and oxidized reversibly through electrochemical protonation<sup>17,18</sup>



This reversible redox reaction gives rise to the broad anodic and cathodic peaks in the CV curves for the samples containing ruthenium, as shown in Fig. 4. The ruthenium valence state changes from  $\text{Ru}^{2+}(\text{OH})_2$  at about 0 V (vs. SHE) to  $\text{Ru}^{4+}\text{O}_2$  at about 1.4 V (vs. SHE) upon complete oxidation, with proton diffusion within the bulk of the material being the rate-determining step for the faradaic reaction. In this study, the maximum charge potential was up to 1 V (vs. SCE), which is 0.16 V lower than 1.4 V (vs. SHE). As a result, no crystalline ruthenium oxide formed during charge/discharge and again,  $\delta$  was probably less than 2.

Figure 8A also shows that carbon-ruthenium xerogel with  $\text{Ru/R} = 0.1$  consistently exhibited a much higher capacitance over a very broad range of currents compared to the pure carbon xerogel. The decrease in the capacitance that was exhibited by both materials with increased current was also less pronounced for the carbon-ruthenium xerogel with  $\text{Ru/R} = 0.1$ . This last result is also reflected in Fig. 8B, which shows that the carbon-ruthenium xerogel with  $\text{Ru/R} = 0.1$  maintained an energy density of approximately 30 Wh/kg up to a power density of 1000 W/kg. The capacitance of a pure carbon xerogel is linked directly to its specific surface area. However, increasing the surface area above that corresponding to the formation of micropores less than about 0.5 nm in diam does not necessarily result in a corresponding increase in capacitance, because pores in this size range remain inaccessible to the electrolyte and thus do not form a dl.<sup>19</sup> Consequently, there is a limit to the energy and power densities that can be obtained from any carbonaceous materials. As shown in Fig. 8A and B, however, it is possible to further increase the energy density of a material, beyond that which is possible based solely on a dl mechanism, by utilizing a faradaically active material such as  $\text{RuO}_2 \cdot x\text{H}_2\text{O}$ . Thus, the clear advantage of this kind of carbon-ruthenium xerogel material is that it utilizes both the faradaic capacitance of the metal oxide and the dl capacitance of the carbon. Also, the results in Fig. 8 tend to suggest that the ability of the carbon-ruthenium xerogel with  $\text{Ru/R} = 0.1$  to sustain a high energy density over a broad range of power density is due to the faradaic contributions arising from the ruthenium. Similar trends have been reported recently based on a modeling study of a capacitor with dl and faradaic processes.<sup>11</sup>

### Conclusions

Sol-gel derived high surface area carbon-ruthenium xerogels were prepared from R-F resins containing  $\text{RuO}_2 \cdot x\text{H}_2\text{O}$ . Carbonization at 750°C in nitrogen converted the resin into a conductive carbon xerogel and the  $\text{RuO}_2 \cdot x\text{H}_2\text{O}$  into metallic ruthenium particles 10

to 30 nm in diam that were subsequently oxidized to an electrochemically active form of ruthenium oxide after one charge/discharge cycle. A very high specific capacitance of 256 F/g (single electrode) was obtained from a carbon xerogel containing 14 wt % Ru. This corresponded to utilizing more than 50% of the ruthenium. Moreover, about 40% of the capacitance was attributed to the formation of a dl within the pores of the high surface area carbon xerogel support during charge/discharge, and about 60% of the capacitance was attributed to the ruthenium oxide dispersed throughout the carbon xerogel matrix undergoing reversible redox reactions during charge/discharge. This material also showed no change in electrochemical capacitance after 2000 charge/discharge cycles, indicating that the material was very stable and the redox reactions associated with the ruthenium oxide were completely reversible.

### Acknowledgments

This material is based upon work supported in part by the U.S. Army Research Office under grant no. DAAH04-96-1-0421 and in part by the U.S. Department of Energy under Cooperative Agreement no. DE-FC02-91ER75666.

University of South Carolina assisted in meeting the publication costs of this article.

### References

1. B. E. Conway, *J. Electrochem. Soc.*, **138**, 1539 (1991).
2. I. D. Raistrick, in *Electrochemistry of Semiconductors and Electrodes*, J. McHardy and F. Ludwig, Editors, pp. 297-355, Noyes Publications, Park Ridge, NJ (1992).
3. B. E. Conway, in *Third International Seminar on Double Layer Capacitors and Similar Energy Storage Devices*, Boca Raton, FL (1993).
4. S. Trasatti and P. Kurzweil, *Platinum Met. Rev.*, **38**, 46 (1994).
5. S. Sarangapani, B. V. Tilak, and C.-P. Chen, *J. Electrochem. Soc.*, **143**, 3791 (1996).
6. M. Aoki, K. Sato, and Y. Kobayashi, *IEICE Trans. Fundamentals Electronics, Communications, and Computer Sciences*, **E77-A**, 208 (1994).
7. H. Shi, *Electrochim. Acta*, **41**, 1633 (1996).
8. I. Tanahashi, A. Yoshida, and A. Nishino, *Carbon*, **29**, 1033 (1991).
9. S. T. Mayer, R. W. Pekala, and J. L. Kaschmitter, *J. Electrochem. Soc.*, **140**, 446 (1993).
10. J. P. Zheng, P. J. Cygan, and T. R. Jow, *J. Electrochem. Soc.*, **142**, 2699 (1995).
11. C. Lin, J. A. Ritter, B. N. Popov, and R. E. White, *J. Electrochem. Soc.*, **146**, 3168 (1999).
12. C. J. Brinker and G. W. Scherer, *Sol-Gel Science*, Academic Press, San Diego, CA (1990).
13. J. M. Miller, B. Dunn, T. D. Tran, and R. W. Pekala, *J. Electrochem. Soc.*, **144**, L309 (1997).
14. C. Lin and J. A. Ritter, *Carbon*, **35**, 1271 (1997).
15. V. Srinivasan and J. W. Weidner, *J. Electrochem. Soc.*, **146**, 1650 (1999).
16. V. Birss, R. Myers, H. Angerstein-Kozłowska, and B. E. Conway, *J. Electrochem. Soc.*, **131**, 1502 (1984).
17. D. Michell, D. A. J. Rand, and R. Woods, *J. Electroanal. Chem.*, **89**, 11 (1978).
18. S. Trasatti and G. Lodi, in *Electrodes of Conductive Metallic Oxides-Part A*, S. Trasatti, Editor, p. 301, Elsevier, New York (1980).
19. C. Lin, J. A. Ritter, and B. N. Popov, *J. Electrochem. Soc.*, Accepted for publication.

# A Mathematical Model of an Electrochemical Capacitor with Double-Layer and Faradaic Processes

Chuan Lin, James A. Ritter,\* Branko N. Popov,\* and Ralph E. White\*,<sup>‡</sup>

Department of Chemical Engineering, Swearingen Engineering Center, University of South Carolina, Columbia, South Carolina 29208, USA

A mathematical model of an electrochemical capacitor with hydrous ruthenium oxide ( $\text{RuO}_2 \cdot x\text{H}_2\text{O}$ ) electrodes including both double-layer and surface faradaic processes is developed to predict the behavior of the capacitor under conditions of galvanostatic charge and discharge. The effect of  $\text{RuO}_2 \cdot x\text{H}_2\text{O}$  particle size is studied and shows that the smaller the particles the better the performance because of the increased surface area per unit volume or mass. The model also predicts that the faradaic process increases significantly the energy per unit volume of the capacitor for power densities of 100 kW/L or less.  
© 1999 The Electrochemical Society. S0013-4651(98)11-057-1. All rights reserved.

Manuscript submitted November 16, 1998; revised manuscript received April 28, 1999.

Electrochemical capacitors have been receiving increased attention during recent years<sup>1-5</sup> as high-power devices in energy-storage systems. There are two mechanisms of energy storage in electrochemical capacitors: (i) a double-layer (DL) charging process due to charge separation, and (ii) a faradaic process due to redox reactions. Devices based on the DL phenomenon are referred to as electrochemical DL capacitors, and those based on faradaic reactions are termed pseudocapacitors. Very high-surface-area carbon materials<sup>6-9</sup> are widely used for DL capacitors. On the other hand, relatively high-surface-area transition metal oxides, such as amorphous  $\text{RuO}_2 \cdot x\text{H}_2\text{O}$ ,<sup>10</sup> porous  $\text{NiO}_x$ ,<sup>11,12</sup> and  $\text{CoO}_x$ ,<sup>12,13</sup> have been identified as possible electrode materials for pseudocapacitors.

A number of models have been developed for analyzing the behavior of DL capacitors. Posey and Morozumi<sup>14</sup> developed a model for potentiostatic and galvanostatic charging of the DL in porous electrodes. Johnson and Newman<sup>15</sup> also developed a model for a porous electrode to analyze desalting processes in terms of ionic adsorption on porous carbon, and Tiedemann and Newman<sup>16</sup> used the results from that model to evaluate the DL capacity of porous electrodes. Recently, Srinivasan *et al.*<sup>17</sup> developed an analytic model and used it to study constant-current discharging, cyclic voltage sweeping, and the ac impedance of carbon xerogel DL capacitors. Also, an analytic model was developed by Farahmandi<sup>18</sup> and used to study the effects of both ionic and solid-phase conductivities on the behavior of an electrochemical capacitor. More recently, Pillay and Newman<sup>19</sup> modeled the influence of side reactions on the performance of electrochemical capacitors. However, none of these capacitor models accounted for both pseudocapacitance and DL capacitance. In fact, few capacitor models have considered faradaic reactions, and for those that did,<sup>20,21</sup> only the approximation of linear faradaic kinetics was considered.

Therefore, the objective of this work is to develop a mathematical model of an electrochemical capacitor with both DL and faradaic processes. These two capacitive processes can occur simultaneously with both contributing to the overall capacitance of the material. This is especially true in the relatively high-surface area transition metal oxide pseudocapacitor materials.<sup>5</sup> The specific system used to illustrate the complementary effects of DL and faradaic processes is a symmetric capacitor comprised of uniformly sized spherical hydrous ruthenium oxide ( $\text{RuO}_2 \cdot x\text{H}_2\text{O}$ ) particles with 30 wt % sulfuric acid as the electrolyte. In the model, the diffusion of protons into the solid  $\text{RuO}_2 \cdot x\text{H}_2\text{O}$  particles is ignored for simplicity; consequently, the DL and faradaic processes take place only on the external surface of the particles. This simplification can be removed, however, by following the procedure presented by Doyle *et al.*<sup>22</sup> for ionic diffusion in the particles. The effects of particle size and cell

current density on the charge/discharge behavior are studied, and the roles of the DL and Faradaic processes are delineated with specific reference to Ragone plots.

## Model Description

Figure 1 displays a schematic of a typical capacitor cell. Two identical  $\text{RuO}_2 \cdot x\text{H}_2\text{O}$  electrodes are separated by an ionically conductive glass fiber and are contacted on one side, as shown in Fig. 1, with tantalum current collectors. A solution of 30 wt %  $\text{H}_2\text{SO}_4$  is used as the electrolyte, which completely fills the pores in the electrodes and the separator. A one-dimensional model is developed using the macrohomogeneous theory of porous electrodes, reviewed by Newman and Tiedemann,<sup>23</sup> and De Vids and White.<sup>24</sup> In the model presented here, the electrolyte concentration is assumed to be invariant and side reactions and thermal effects are ignored, along with the variation of the DL capacitance with potential.

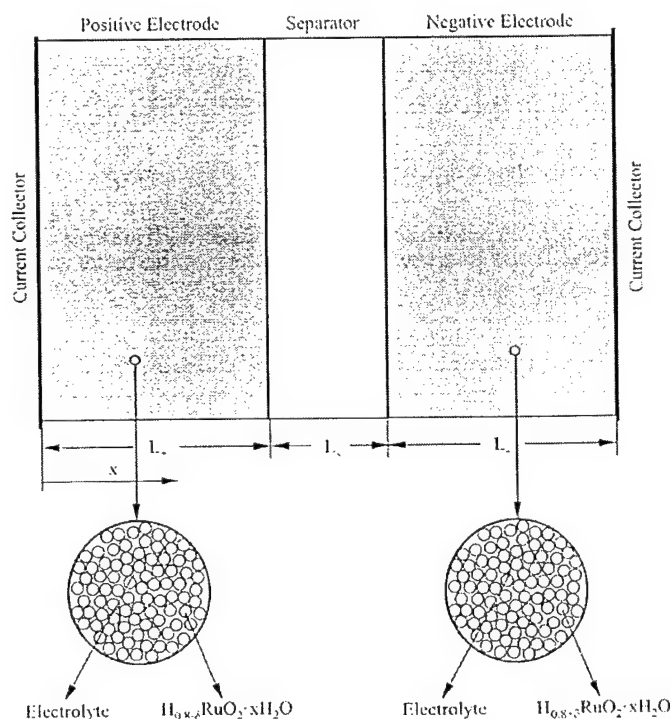
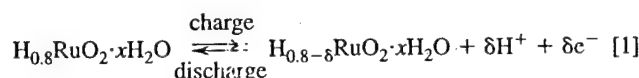


Figure 1. Schematic of an electrochemical capacitor cell upon which the model is based.

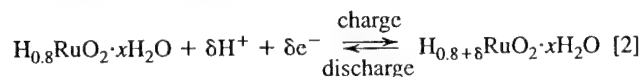
\* Electrochemical Society Active Member.

<sup>‡</sup> E-mail: rew@sc.edu

The faradaic reactions occurring in the electrodes during charge/discharge are expressed as<sup>25</sup>



for the positive electrode, and as



for the negative electrode, where the state of charge,  $\delta$ , is 0.5 for a cell to be charged to 1 V. These reactions show that initially the active materials in both electrodes are  $\text{H}_{0.8}\text{RuO}_2 \cdot x\text{H}_2\text{O}$ , which may be obtained by discharging each  $\text{RuO}_2 \cdot x\text{H}_2\text{O}$  electrode separately using external electrodes. Then, during charge, the oxidation reaction (Eq. 1) takes place in the positive electrode and the reduction reaction (Eq. 2) occurs in the negative electrode. Finally, during discharge, the opposite reactions take place in both electrodes, which brings both electrodes to their original states after full discharge, thereby completing a charge/discharge cycle. Thus, during charge, the oxidation state of Ru changes from 3.2 to 3.7 in the positive electrode and from 3.2 to 2.7 in the negative electrode, and during discharge, it changes back from 3.7 to 3.2 in the positive electrode and from 2.7 to 3.2 in the negative electrode.

In an electrode, the total current transferred from the matrix phase to the electrolyte phase is expressed in terms of the DL current and the faradaic current as<sup>19,26</sup>

$$\frac{\partial i_2}{\partial x} = s_v C_d \frac{\partial(\Phi_1 - \Phi_2)}{\partial t} + s_v j_f \quad [3]$$

where  $i_2$  is the superficial current density based on the projected electrode area in the electrolyte phase,  $x$  is the position coordinate,  $s_v$  is the specific surface area per unit volume of the electrode,  $C_d$  is the DL capacitance,  $\Phi_1$  and  $\Phi_2$  are the potentials in the matrix and electrolyte phases, respectively, and  $j_f$  is the faradaic transfer current density.  $\Phi_2$  is defined as the potential<sup>19,25</sup> of a saturated calomel reference electrode (SCE) connected to the electrolyte phase at the position of interest relative to an identical electrode connected to the electrolyte phase just inside the left current collector ( $x = 0$ ). Thus,  $\Phi_2$  is zero at  $x = 0$ . The faradaic transfer current,  $j_f$ , is taken in the form of the Butler-Volmer equation<sup>27</sup>

$$j_f = i_0 \{ \exp[\alpha_a f(\Phi_1 - \Phi_2 - U_1)] - \exp[-\alpha_c f(\Phi_1 - \Phi_2 - U_1)] \} \quad [4]$$

where  $i_0$  is the exchange current density of the faradaic reaction,  $f$  is equal to  $F/RT$ ,  $F$  is Faraday's constant,  $R$  is the universal gas constant,  $T$  is the absolute temperature,  $\alpha_a$  and  $\alpha_c$  are the anodic and cathodic transfer coefficients for the reactions, respectively, and  $U_1$  is the equilibrium potential of the faradaic reaction.  $U_1$  is a function of the state of charge,<sup>25</sup> which can be expressed by  $\theta$ , the fraction of oxidized species in the electrode. By introducing another variable,  $Q_f$ , the faradaic charge of the electrode,  $\delta$ ,  $\theta$ , and  $j_f$  are related by the following equations

$$\theta = \frac{Q_f - Q_{f,\text{red}}}{Q_{f,\text{oxd}} - Q_{f,\text{red}}} \quad [5]$$

$$\delta = 0.5\theta \quad [6]$$

$$\frac{\partial Q_f}{\partial t} = s_v j_f \quad [7]$$

where  $Q_{f,\text{red}}$  is the faradaic charge of a fully reduced electrode, and  $Q_{f,\text{oxd}}$  is the faradaic charge of a fully oxidized electrode. Equation 7 relates the rate of accumulation of the faradaic charge within the electrode to the faradaic transfer current. For simplicity, Eq. 4, 5, and 7 are combined into a single equation

$$\frac{\partial \theta}{\partial t} = \frac{s_v i_0}{Q_{f,\text{oxd}} - Q_{f,\text{red}}} \{ \exp[\alpha_a f(\Phi_1 - \Phi_2 - U_1)] - \exp[-\alpha_c f(\Phi_1 - \Phi_2 - U_1)] \} \quad [8]$$

Conservation of charge leads to

$$\frac{\partial i_1}{\partial x} + \frac{\partial i_2}{\partial x} = 0 \quad [9]$$

where  $i_1$  is the superficial current density based on the projected electrode area in the matrix phase of the porous electrode. With the assumption of no concentration gradients in the electrodes, Ohm's law applies in both the matrix and electrolyte phases as

$$i_1 = -\sigma \frac{\partial \Phi_1}{\partial x} \quad [10]$$

$$i_2 = -\kappa_p \frac{\partial \Phi_2}{\partial x} \quad [11]$$

where  $\sigma$  is the electronic conductivity of the matrix, and  $\kappa_p$  is the ionic conductivity of the electrolyte inside the pores of the electrodes. In order to solve the system of equations more efficiently, Eq. 3, 4, 9, 10, and 11 are combined into a single equation

$$\frac{\partial^2 E}{\partial \xi^2} = \tau \frac{\partial E}{\partial t} + \frac{\tau i_0}{C_d} \{ \exp[\alpha_a f(E - U_1)] - \exp[-\alpha_c f(E - U_1)] \} \quad [12]$$

with the local electrode potential,  $E$ , defined as

$$E = \Phi_1 - \Phi_2 \quad [13]$$

and the DL time constant as

$$\tau = s_v C_d L^2 \left( \frac{1}{\sigma} + \frac{1}{\kappa_p} \right) \quad [14]$$

where  $L$  is the thickness of one electrode ( $L = L_+ = L_-$ ), and the dimensionless distance  $\xi$  is defined as  $x/L$ . In the separator, because the electronic conductivity in the glass fiber is zero

$$i_1 = 0 \quad [15]$$

and thus the total transfer current is zero

$$\frac{\partial i_2}{\partial x} = 0 \quad [16]$$

However, Ohm's law still applies to the current in the electrolyte within the pores of the separator, as

$$i_2 = -\kappa_s \frac{\partial \Phi_2}{\partial x} \quad [17]$$

where  $\kappa_s$  is the ionic conductivity in the pores of the separator.

To solve this system of partial differential and algebraic equations, the following boundary and initial conditions are used. For the case of a constant-current charge/discharge between 0 and 1 V, the boundary conditions for the positive electrode are

$$\text{at } \xi = 0, t > 0 \quad \frac{\partial E}{\partial \xi} = -\frac{i_{\text{cell}} L}{\sigma} \quad [18]$$

$$\frac{\partial \theta}{\partial t} = \frac{s_v i_0}{Q_{f,\text{oxd}} - Q_{f,\text{red}}} \{ \exp[\alpha_a f(E - U_1)] - \exp[-\alpha_c f(E - U_1)] \} \quad [19]$$

$$\text{at } \xi = 1, t > 0 \quad \frac{\partial E}{\partial \xi} = -\frac{i_{\text{cell}} L}{\kappa_p} \quad [20]$$

$$\frac{\partial \theta}{\partial \xi} = 0 \quad [21]$$

The boundary conditions are set such that at the interface between the current collector and the electrode ( $\xi = 0$ ), the current arises from the matrix phase, and at the interface between the electrode and separator ( $\xi = 1$ ), the current arises from the solution phase. The initial conditions are<sup>25</sup>

$$\text{at } t = 0 \text{ for charge } E = V_0 \text{ and } \theta = 0 \quad [22]$$

$$\text{at } t = 0 \text{ for discharge } E = 2V_0 \text{ and } \theta = 1 \quad [23]$$

where  $V_0$  is the initial potential before charge and is taken as 0.5 V (SCE) for a cell charge/discharge between 0 and 1 V. Similar boundary and initial conditions can be set for the negative electrode. However, in this model only the positive electrode is simulated; because of the symmetrical feature of the two electrodes, results for the negative electrode are calculated based on the simulation results for the positive electrode.

The entire system of equations to be solved is comprised of two equations and two unknowns, which are Eq. 8 and 12, and  $E$  and  $\theta$ , respectively. The system of equations for the positive electrode is solved using a backward finite difference method<sup>28</sup> with Newman's BAND(J) algorithm.<sup>29</sup> It is noteworthy that Eq. 17 is used to evaluate the potential in the solution phase of the separator, which is also solved simultaneously with the system of equations for the positive electrode. Once  $E$  and  $\theta$  are obtained, the other unknowns are calculated using these above equations; for example, Eq. 11, 13, and 4 are used to calculate  $\Phi_1$ ,  $\Phi_2$ , and  $j_F$ , respectively. The DL and faradaic currents in each electrode are defined by and obtained from the following two equations, respectively

$$i_c = -s_v C_d \frac{\partial E}{\partial t} \quad [24]$$

$$i_f = -s_v j_f \quad [25]$$

### Model Parameters

In this study, the  $\text{RuO}_2 \cdot x\text{H}_2\text{O}$  particles are assumed to be non-porous spheres with a uniform size; thus, the pores in the electrodes are composed of the spaces between the particles, and the surface area per unit volume,  $s_v$ , of the electrode is expressed as

$$s_v = \frac{6(1 - \epsilon)}{D} \quad [26]$$

where  $D$  is the diameter of the particles and  $\epsilon$  is the electrode porosity (taken as 0.25). Many of the other parameters associated with the  $\text{RuO}_2 \cdot x\text{H}_2\text{O}$  are unavailable in the literature; therefore, the following reasonable assumptions are made. The DL capacitance on the  $\text{RuO}_2$  surface is assumed to be  $2.0 \times 10^{-5} \text{ F/cm}^2$ , which is the same for carbon materials.<sup>30</sup> Both of the anodic and cathodic transfer coefficients,  $\alpha_a$  and  $\alpha_c$ , are taken as 0.5; and the exchange current density of the faradaic reactions,  $i_0$ , is taken as  $10^{-5} \text{ A/cm}^2$ . The equilibrium potential,  $U_1$ , for the faradaic reactions is estimated from a linear relationship between the potential and the state of charge ( $\delta$ ), as reported by Jow and Zhang.<sup>25</sup> At  $\delta = 0$ ,  $U_1$  is equal to 0.5 V for both the electrodes, and at  $\delta = 0.5$ ,  $U_1$  is equal to 1 and 0 V for the positive and negative electrodes, respectively. Also, according to the relationship between  $\delta$  and  $\theta$  (Eq. 6),  $U_1$  is equal to  $0.5(1 + \theta)$  and 0.50 for the reactions in the positive (Eq. 1) and negative electrodes (Eq. 2), respectively. Here  $\theta$  is the fraction of oxidized species in the faradaic reaction.

In addition, it is assumed that the faradaic reactions take place only on the surface of the  $\text{RuO}_2 \cdot x\text{H}_2\text{O}$  particles inside the electrodes. As a result, the faradaic charge of a fully oxidized electrode,  $Q_{f,\text{oxd}}$ , is estimated from

$$Q_{f,\text{oxd}} = \frac{s_v \delta F}{h^2 L_A} \quad [27]$$

where  $s_v$  is obtained from Eq. 26,  $\delta$  is equal to 0.5 for the fully charged cell,  $h$  is the length of the crystal lattice on the surface and taken approximately as 4 Å,<sup>31</sup> and  $L_A$  is Avogadro's number. Equation 27 implies that there is only one Ru atom in the area of  $h^2$  on the surface of the  $\text{RuO}_2 \cdot x\text{H}_2\text{O}$  particles and that  $Q_{f,\text{oxd}}$  is a function of the particle size. The faradaic charge of a fully reduced electrode,  $Q_{f,\text{red}}$ , is taken as zero.

The electronic conductivity of the matrix,  $\sigma$ , is taken as  $10^5 \text{ S/cm}$ ,<sup>32</sup> and the ionic conductivity of bulk 30 wt %  $\text{H}_2\text{SO}_4$ ,  $\kappa_0$ , is 0.8 S/cm.<sup>33</sup> The ionic conductivity of the electrolyte inside the pores of the electrode is frequently expressed as<sup>29</sup>

$$\kappa_p = \kappa_0 \epsilon^{1.5} \quad [28]$$

Similarly, the ionic conductivity of the electrolyte inside the pores of the separator is given by

$$\kappa_s = \kappa_0 \epsilon_s^{1.5} \quad [29]$$

where the separator porosity,  $\epsilon_s$ , is taken as 0.7. The electrode thickness for both the positive and negative electrodes is 50  $\mu\text{m}$ , the separator thickness is 25  $\mu\text{m}$ , and the temperature is 25°C. All these values are summarized in Tables I and II, along with the values of other parameters used in this model.

### Results

At the outset, it is useful to verify the accuracy of the numerical method, which is done by comparing the numerical results for the

Table I. Model parameters that describe the Faradaic kinetics and open-circuit potentials of the electrodes.

Parameter	Value	Reference
$i_0$	$10^{-5} \text{ A/cm}^2$	Assumed
$\alpha_a$	0.5	Assumed
$\alpha_c$	0.5	Assumed
$U_1$ (positive electrode)	$0.5(1 + \theta) \text{ V (vs. SCE)}$	Jow and Zhang <sup>25</sup>
$U_1$ (negative electrode)	0.50 V (vs. SCE)	Jow and Zhang <sup>25</sup>

Table II. Model parameters that describe the electrodes and separator.

Parameter	Value	Reference
$D$	5, 10, 30 nm	Assumed
$\epsilon$	0.25	Assumed
$\epsilon_s$	0.7	Pillay and Newman <sup>19</sup>
$L = L_+ = L_-$	$5 \times 10^{-3} \text{ cm}$	Assumed
$L_s$	$2.5 \times 10^{-3} \text{ cm}$	Assumed
$C_d$	$2 \times 10^{-5} \text{ F/cm}^2$	Assumed
$s_v$	$1.5 \times 10^6, 4.5 \times 10^6$ , and $9.0 \times 10^6 \text{ cm}^2/\text{cm}^3$ for the particle sizes of $D = 30, 10$ , and 5 nm, respectively	From Eq. 26
$h$	$4.0 \times 10^{-8} \text{ cm}$	Pollak and O'Grady <sup>31</sup>
$Q_{f,\text{oxd}}$	150.2, 450.6, and 901.2 C/cm <sup>3</sup> for the particle sizes of $D = 30, 10$ , and 5 nm, respectively	From Eq. 27
$Q_{f,\text{red}}$	0	Assumed
$\sigma$	$10^5 \text{ S/cm}$	Trasatti and Lodi <sup>32</sup>
$\kappa_0$	0.8 S/cm	Darling <sup>33</sup>
$\kappa_p$	0.1 S/cm	From Eq. 28
$\kappa_s$	0.469 S/cm	From Eq. 29
$T$	298.15 K	Assumed
$\tau$	$7.5 \times 10^{-3}, 2.25 \times 10^{-2}, 4.5 \times 10^{-2} \text{ s}$ for the particle sizes of $D = 30, 10$ , and 5 nm, respectively	From Eq. 14
$V_0$	0.5 V (vs. SCE)	Assumed

DL process alone (*i.e.*, faradaic process is shut off) with those generated from a completely analytical model for DL capacitors developed by Srinivasan *et al.*<sup>17</sup> Some dimensionless variables are also introduced, such as dimensionless cell potential,  $\Phi_{\text{cell}}^*$ , dimensionless local potential,  $E^*$ , dimensionless time,  $\tau^*$ , dimensionless cell current,  $i_{\text{cell}}^*$ , etc. The definitions of these dimensionless variables are given in the List of Symbols. Finally, the results presented here are

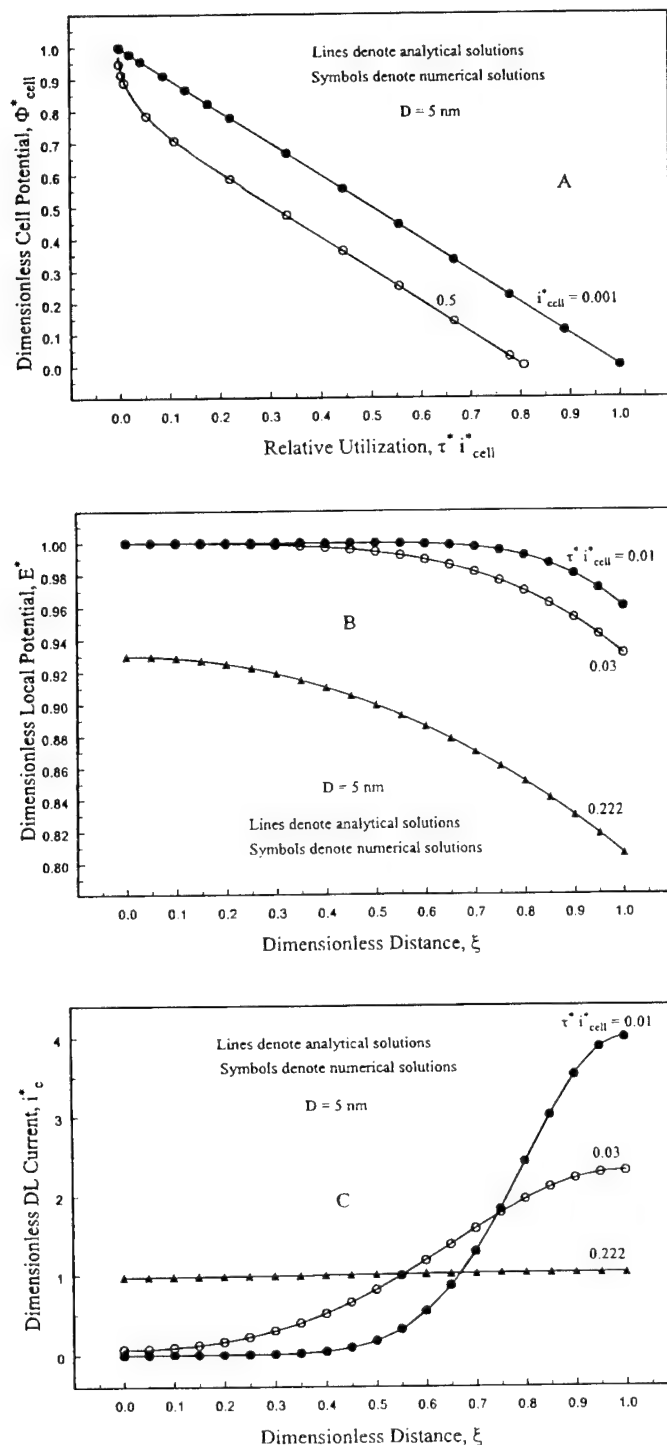


**Figure 2.** Comparisons of the numerical solutions with the analytic ones for the DL process alone and 5 nm diam RuO<sub>2</sub>·xH<sub>2</sub>O particles: (A) constant-current discharge curves at two dimensionless currents; (B) potential distribution through the positive electrode at different times during discharge at a constant current of  $i_{\text{cell}}^* = 0.5$ ; and (C) DL current distribution through the positive electrode at different times during discharge at a constant current of  $i_{\text{cell}}^* = 0.5$ .

for discharge only, because the results for charge are simply the mirror image of those for discharge.

Figure 2A, B, and C compares the results for the change in the dimensionless cell potential with time at two different cell currents, the dimensionless potential distribution at different discharge times, and the dimensionless DL current distribution at different discharge times, respectively. In Fig. 2A, the dimensionless cell potential,  $\Phi_{\text{cell}}^*$ , is defined as  $\Phi_{\text{cell}}/2V_0$ , where  $\Phi_{\text{cell}}$  represents the matrix potential difference between the two current collectors. Also, the relative utilization,<sup>17</sup>  $\tau^* i_{\text{cell}}^*$ , represents the fraction of the available capacity extracted from the cell. The RuO<sub>2</sub>·xH<sub>2</sub>O particles are 5 nm in diameter. The results show that the numerical solutions agree very well with the analytical solutions up to the fourth digit, which is sufficient for numerical simulations. It is noteworthy that this numerical accuracy is achieved by taking 101 space node points and a time step of  $10^{-6}$  s up to 2 s and  $10^{-4}$  s thereafter. All of the results presented were obtained from the numerical model using these discretization grid sizes.

Figure 3A shows discharge curves for the combined DL and faradaic processes at a constant cell current of  $i_{\text{cell}}^* = 0.001$  for three different RuO<sub>2</sub>·xH<sub>2</sub>O particle sizes, and Fig. 3B compares the discharge behavior of each of their contributions for a capacitor with 5 nm diam RuO<sub>2</sub>·xH<sub>2</sub>O particles at a constant cell current of  $i_{\text{cell}}^* = 0.001$  to examine how the DL and faradaic processes separately affect the cell potential. Linear relationships of the cell potential with discharge time are observed in Fig. 3A for all three particle

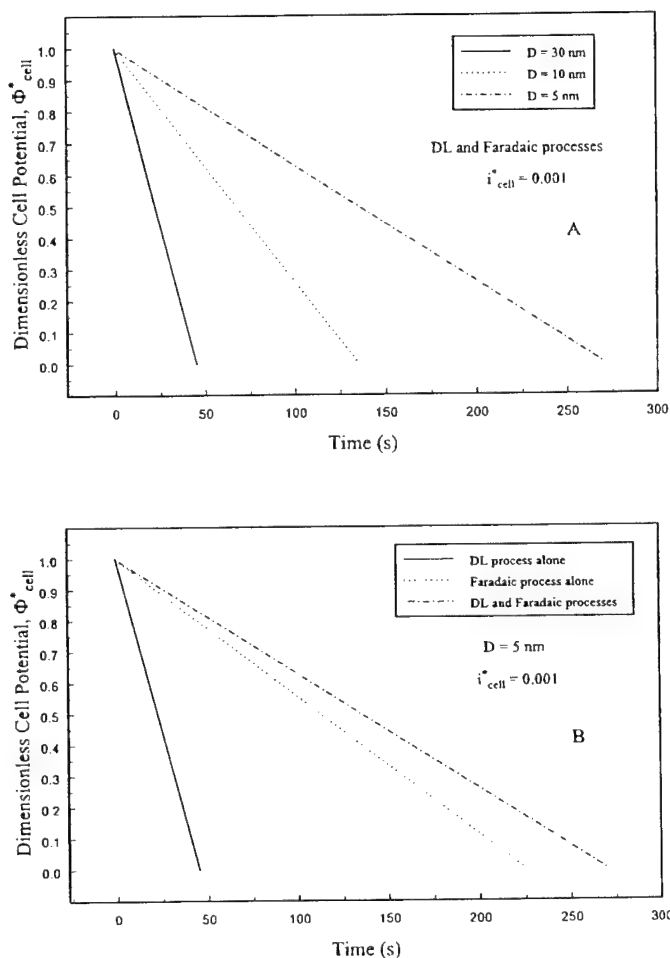


**Figure 3.** (A) Effect of RuO<sub>2</sub>·xH<sub>2</sub>O particle size on constant-current discharge behavior for the combined DL and faradaic processes at  $i_{\text{cell}}^* = 0.001$  and (B) comparison of constant-current discharge behavior for the DL process alone, faradaic process alone, and combined DL and faradaic processes at  $i_{\text{cell}}^* = 0.001$  and with 5 nm diam RuO<sub>2</sub>·xH<sub>2</sub>O particles.



sizes, and the discharge time increases with a decrease in the particle size. The actual discharge time is used here instead of relative utilization ( $\tau^* i_{\text{cell}}^*$ ), because the DL time constant ( $\tau$ ) depends on the particle size, which makes the discharge curves incomparable in terms of relative utilization. Linear relationships are again observed in Fig. 3B for the DL process alone, faradaic process alone, and the combined DL and faradaic processes; and the DL process alone has the shortest discharge time, the faradaic process alone has a discharge time five times longer than the DL process alone, and the combined DL and faradaic processes has the longest discharge time, appearing as a linear combination of the two individual processes. The linear behavior of the change in cell potential with time is characteristic of a DL capacitor when the DL capacitance is independent of the potential. As for the faradaic process simulated here, the linear behavior is most likely due to the linear relationship between the equilibrium potential and the state of charge, which makes this faradaic material of  $\text{RuO}_2 \cdot x\text{H}_2\text{O}$  behave like a simple DL capacitor.

Figure 4A and B illustrates the effect of cell current on the cell potential for the combined DL and faradaic processes and for the faradaic process alone, respectively. The  $\text{RuO}_2 \cdot x\text{H}_2\text{O}$  particles are 5 nm in diam. For the combined DL and faradaic processes (Fig. 4A), at the smaller current (*i.e.*,  $i_{\text{cell}}^* = 0.001$ ), the cell potential decreases linearly with time. However, at the larger current (*i.e.*,  $i_{\text{cell}}^* = 0.5$ ), a sharp drop in potential at the start of discharge is observed, which is followed by a linear decrease in potential for the remainder of the discharge. These discharge curves are similar in shape to those for the DL process alone, as shown in Fig. 2A, but the potential drop is larger for the combined DL and faradaic processes.

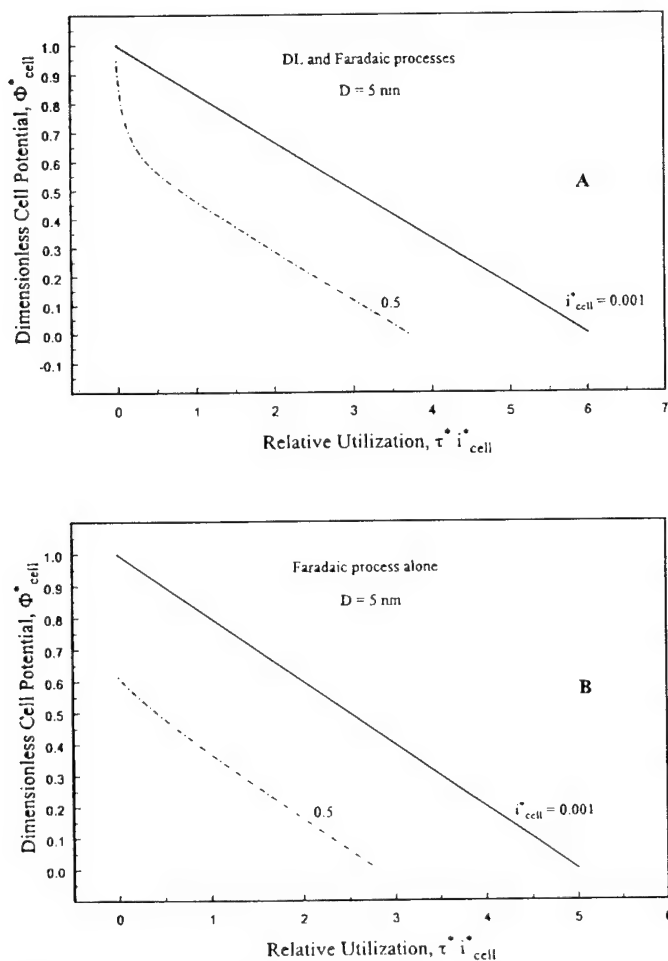


**Figure 4.** Constant-current discharge curves at two dimensionless currents: (A) for the combined DL and faradaic processes and (B) for the faradaic process alone.

For the faradaic process alone (Fig. 4B), at the smaller current, the cell potential also decreases linearly as those observed for the combined DL and faradaic processes (Fig. 4A) and for the DL process alone (Fig. 2A). At the larger current, however, the cell potential behaves differently from that for the DL process alone. The potential decreases almost linearly with time but with a marked drop at the start of discharge, unlike the initial potential drops for the DL process alone that exhibit curvature. This marked potential drop is believed to be associated with the faradaic kinetic resistance; the result is consistent with a larger drop in potential for the combined DL and faradaic processes than that for the DL process alone.

To examine how potentials and currents inside the electrode change during discharge, the distributions of the potential throughout the positive electrode at different discharge times at a cell current of  $i_{\text{cell}}^* = 0.5$  are shown in Fig. 5A and B for the combined DL and faradaic processes and for the faradaic process alone, respectively. The corresponding distributions of the currents are illustrated in Fig. 6A and B for the combined DL and faradaic processes and in Fig. 6C for the faradaic process alone. For the combined DL and faradaic processes (Fig. 5A), the potential distribution changes gradually from the initial uniform distribution at the start of discharge to a steady-state nonuniform profile at about  $\tau^* i_{\text{cell}}^* = 0.222$ . Then the cell potential decreases with this steady-state profile until the cell is totally discharged. The nonuniform potential distribution is due mainly to the ohmic potential drop in the solution phase (the conductivity in the matrix phase is much greater than that in the solution phase in this modeling simulation), and the transition time to reach the steady-state profile is determined by the DL time constant.

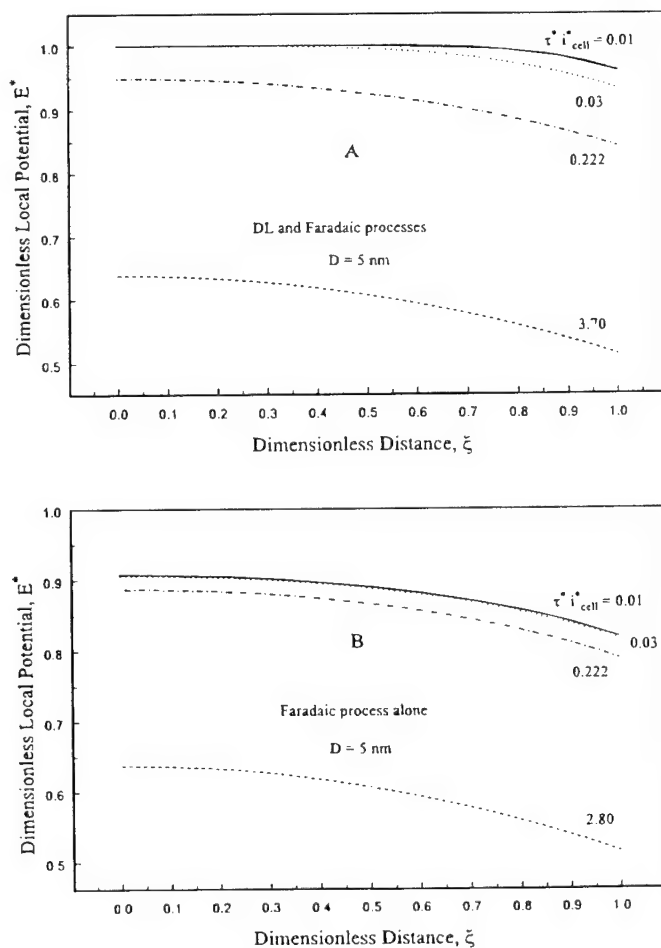


**Figure 5.** Potential distributions throughout the positive electrode at different times during discharge at a constant current of  $i_{\text{cell}}^* = 0.5$ : (A) for the combined DL and faradaic processes and (B) for the faradaic process alone.

Again, these distributions are similar in shape to those at the same discharge times for the DL process alone, as shown in Fig. 2B, but the decrease in potential is slower for the combined DL and faradaic processes because it holds more energy compared with the DL process alone. For the faradaic process alone (Fig. 5B), the potential distribution changes immediately to a steady-state nonuniform profile after the start of the discharge, then the potential decreases with this profile until the cell is fully discharged. The reason for this immediate change in potential distribution is that in this case there is

no DL time constant that controls the transition of the potential distribution to gradually reach a steady-state profile. Again, the nonuniform potential distribution is largely due to the ohmic resistance in the solution phase.

For the combined DL and faradaic processes, the DL current distribution throughout the electrode (Fig. 6A) is very nonuniform at short times, and the degree of this nonuniformity decreases with time. The DL current attains a uniform profile at about  $\tau^* i_{\text{cell}}^* = 0.222$ , and then decreases continuously with this uniform profile until the cell is totally discharged at  $\tau^* i_{\text{cell}}^* = 3.7$  and it reaches 0.2. These distributions are also similarly shaped to those for the DL process alone, as shown in Fig. 2C. Meanwhile, the faradaic current (Fig. 6B) increases with time and its distribution reaches a maximum of nonuniformity at about  $\tau^* i_{\text{cell}}^* = 0.222$ . Finally, a uniform distribution is attained and the faradaic current reaches 0.8 at  $\tau^* i_{\text{cell}}^* = 3.7$ , which is four times greater than the final current for the DL process alone, as shown in Fig. 6A. For the faradaic process alone (Fig. 6C), the faradaic current distribution is at a maximum of nonuniformity at the start of discharge, then the degree of this nonuniformity decreases with time, and finally it reaches a uniform profile at  $\tau^* i_{\text{cell}}^* = 2.8$ .

Because local potentials are related to local currents, a change in local potential must result in a change in local current. However, for the DL and faradaic processes alone, they are related in different ways. The DL current is proportional to the derivative of the local potential with respect to time (Eq. 24), but the faradaic current is nonlinearly related to the local potential with an exponential dependence (Eq. 25 and 4). These different features for the two processes determine their different current distributions in response to a change in local potential. For the DL process alone (Fig. 2B and C), the change in local potential is the greatest at the start of discharge; as a result, the DL current distribution reaches a maximum of nonuniformity. As the change in local potential becomes smaller with time, the DL current distributions become more uniform. Finally, as the potential distribution attains a steady-state profile, the change in local potential with time is the same throughout the electrode, which leads to a uniform DL current distribution. For the faradaic process alone (Fig. 5B and 6C), the change in local potential is also the greatest at the start of discharge, which leads to a very nonuniform faradaic current distribution; meanwhile, the potential distribution reaches a steady-state profile instantly. This steady-state potential profile does not translate into a uniform faradaic current distribution because of the nonlinear relationship between the local potential and the local current as shown in Eq. 4. The final uniform faradaic current distribution is likely reached because the difference between the two exponential terms approaches a constant. For the combined DL and faradaic processes, the potential and the DL current distributions are similar to those for the DL process alone; its faradaic current distributions are similar to those for the faradaic process alone. However, the relative magnitudes of the DL and faradaic currents are determined by how they are related in the governing equations (Eq. 4, 24, and 25).

The results in Fig. 3A show that the particle size is extremely important to the discharge behavior of the capacitor. It is therefore of interest to investigate the performance of this model capacitor in terms of Ragone plots, *i.e.*, in terms of the energy and power densities. The energy and power densities are calculated as follows

$$\text{Energy density} = \frac{I_{\text{cell}} \Phi_{\text{ave}} t_d}{V_{\text{cell}}} \quad [30]$$

$$\text{Power density} = \frac{I_{\text{cell}} \Phi_{\text{ave}}}{V_{\text{cell}}} \quad [31]$$

where  $I_{\text{cell}}$  is the total cell current, which is obtained by multiplying the cell current density ( $i_{\text{cell}}$ ) by the cross-sectional area of the electrode,  $A$ .  $\Phi_{\text{ave}}$  is the average cell potential,  $t_d$  is the discharge time, and  $V_{\text{cell}}$  is the volume of the cell including the electrodes, electrolyte, and separator. The average cell potential is given by

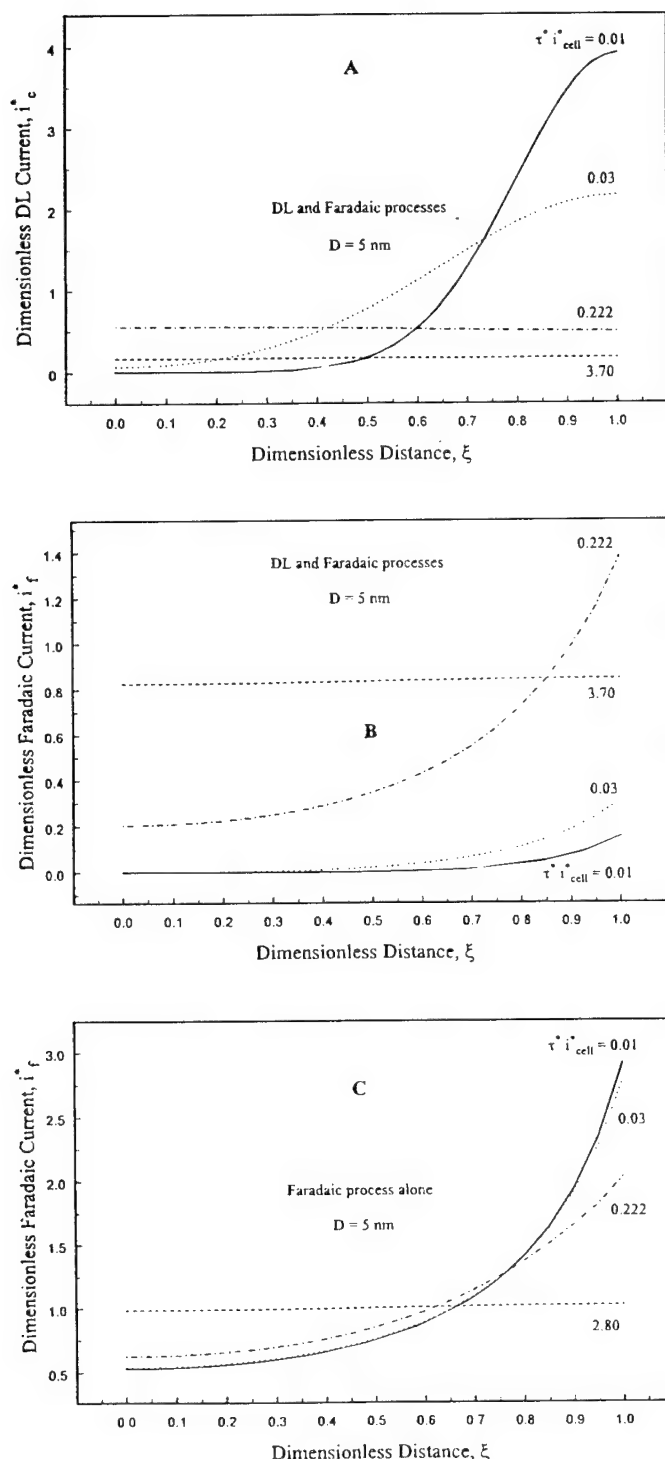


Figure 6. Current distributions throughout the positive electrode at different times during discharge at a constant current of  $i_{\text{cell}}^* = 0.5$ : (A) and (B) for the combined DL and faradaic processes, and (C) for the faradaic process alone.

$$\Phi_{\text{ave}} = \frac{1}{t_d} \int_0^{t_d} \Phi_{\text{cell}} dt \quad [32]$$

Figure 7A shows Ragone plots for the combined DL and faradaic processes and for three different particle sizes. The curves are all similarly shaped, but the energy density decreases with an increase in particle size over the entire range of power densities, and it begins to drop off sooner but more slowly as the power density increases. To examine how the DL and faradaic processes independently affect the energy and power densities in a capacitor, Fig. 7B shows the contributions from each process for a capacitor with 5 nm diam  $\text{RuO}_2 \cdot x\text{H}_2\text{O}$  particles. The Ragone plots exhibit similar trends for the combined DL and faradaic processes and the DL and faradaic processes alone, except at very high powers. For the DL process alone, the energy density is essentially independent of the power density up to about 20 kW/L, and then it drops sharply at higher power densities. In contrast, the energy density decreases a little faster with an increase in power density for the faradaic process alone. At very high power densities (above 100 kW/L), however, the faradaic process fails because the potential in the positive electrode drops instantly below 0.5 V at the start of discharge, and no energy can be drawn from the cell at such high power densities. For the combined DL and faradaic processes, a higher energy density over a broader range of power densities is due largely to the faradaic process; however, it approaches the energy density obtained for the DL process alone at very high power densities, again indicating that the contribution from the faradaic process becomes negligibly small at

very high power densities. Overall, these Ragone plots show very clearly that for a capacitor utilizing both DL and faradaic processes, a higher energy density results from the faradaic process and a higher power density results from the DL process, as compared to either of the individual processes alone.

### Discussion

Both of the DL and faradaic processes studied here are surface phenomena which take place at the interface between the electrode and electrolyte. For the DL process, more surface area and a higher specific capacitance both give rise to more energy storage at the interface. Also, for the surface faradaic process, more surface area gives rise to more energy storage at the interface. Moreover, the more active the surface material is toward reversible redox reactions (determined by the value of the exchange current density,  $i_0$ ), the higher the power density. In this study, however, the specific capacitance of the DL process and the exchange current density of the faradaic process are all fixed; so the only variable is the surface area, which is changed by varying the size of the  $\text{RuO}_2 \cdot x\text{H}_2\text{O}$  particles in the electrode. In fact, some researchers<sup>34</sup> reported much higher DL capacitance of 60  $\mu\text{F}/\text{cm}^2$  for oxide electrode systems based on a proton-exchange mechanism. In this case, the calculated DL current would be expected to be tripled, which in turn would result in a threefold increase in the energy density contributed from the DL process.

According to Eq. 26, the surface area is inversely proportional to the particle size. As the particle size decreases from 30 to 10 to 5 nm, the surface area increases three times and six times, respectively, which is proportionally the same as the increase in the discharge times shown in Fig. 3A. In addition, the results in Fig. 3B show clearly that the discharge time for the faradaic process alone is five times higher than that for the DL process alone, indicating the importance of the faradaic process for increasing the energy density of a capacitor. Furthermore, Eq. 30 and 31 state that the energy density is proportional to the total cell current,  $I_{\text{cell}}$ , average cell potential,  $\Phi_{\text{ave}}$ , and discharge time,  $t_d$ , but it is inversely proportional to the cell volume,  $V_{\text{cell}}$ . The power density is the same as the energy density except that it is independent of  $t_d$  (which may not be true because  $\Phi_{\text{ave}}$  is a function of  $t_d$ ). Although a first glance at these equations suggests that an increase in cell current results in an increase in energy density, actually this is not true because the discharge time decreases with an increase in cell current. The overall effect is that the energy density decreases with an increase in power density. The results in Fig. 7A show that the ratio of the increase in energy density at the same power density is roughly the same as the ratio of the increase in surface area for the three different sizes of  $\text{RuO}_2 \cdot x\text{H}_2\text{O}$  particles.

In addition, in order to increase the power density, the cell current density must be increased, as shown in Fig. 7A and B. However, the resulting increase in power density is obtained at the expense of decreasing energy density, mainly because of the ohmic resistance in the solution phase for the DL process alone. For the faradaic process alone, the energy loss at higher power densities is due to the ohmic resistance in the solution phase as well as the faradaic kinetic resistance. The faradaic kinetic resistance even makes the faradaic process alone fail, because the cell potential cannot hold at the working potential range. What is even more interesting, however, is that for the combined DL and faradaic processes, the energy loss is less compared with that for the faradaic process alone at the same power density. The reason is that the DL process has the ability to hold the cell potential, which allows the faradaic process to deliver some energy even beyond the power at which the faradaic process alone would fail. These results are consistent with those shown in Fig. 2A, 4A, and 4B, which indicate that the energy loss at the larger current (based on relative utilization) is 20, 44, and 37% for the DL process alone, faradaic process alone, and combined DL and faradaic processes, respectively. Although there is always a trade-off between the energy and power densities, a capacitor with both DL and faradaic processes can store more energy and deliver more power compared with that obtained from either the DL or faradaic processes alone.

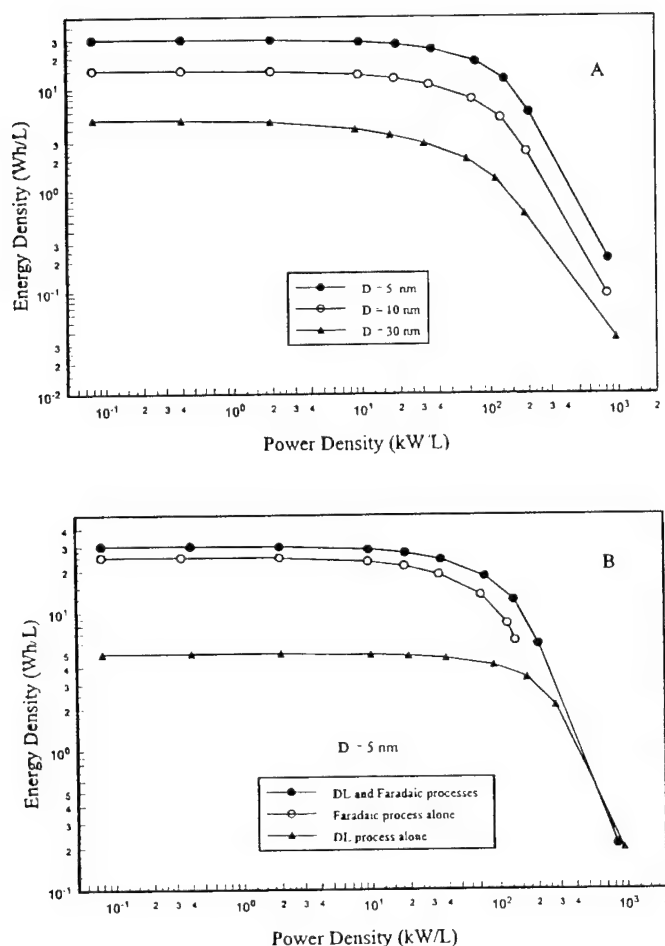


**Figure 7.** Ragone plots: (A) for the combined DL and faradaic processes for three  $\text{RuO}_2 \cdot x\text{H}_2\text{O}$  particle sizes and (B) for the DL process alone, faradaic process alone, and combined DL and faradaic processes with 5 nm diam  $\text{RuO}_2 \cdot x\text{H}_2\text{O}$  particles.

In this study, it is also assumed that the faradaic reaction takes place only at the surface of the particle with one-electron exchange between 0 and 1 V (SCE). In practice, however, the inner layers within a particle may also participate in the redox reaction through a proton diffusion mechanism;<sup>3,10</sup> other authors<sup>35</sup> have suggested a faradaic reaction of RuO<sub>2</sub> with a two-electron exchange. As a result, the faradaic charge of a fully oxidized electrode can double according to Eq. 27, which means that the energy density from the faradaic process can also double. Nevertheless, the power density may decrease because of slow proton diffusion in the innerlayers of the solid phase. In addition, in this study the electronic conductivity of the matrix is taken as 105 S/cm, which is 3-4 orders of magnitude higher than the value suggested by some researchers<sup>36</sup> based on boundary effects associated with powder materials<sup>37</sup> and less crystallinity<sup>38</sup> in hydrous RuO<sub>2</sub>. However, if the conductivity is taken as this lower value, the simulated results will not be affected much because the limiting conductivity is in the solution.

### Conclusions

A mathematical model of an electrochemical capacitor comprised of hydrous ruthenium oxide (RuO<sub>2</sub>·xH<sub>2</sub>O) electrodes, including both DL and surface faradaic processes, was developed to predict the behavior of the capacitor under the conditions of galvanostatic charge and discharge. A comparison of various numerical solutions from the model with analytical ones for the DL process alone revealed that the numerical simulations were accurate up to the fourth digit. The results show that the energy density can be increased by decreasing the particle size, whereas the power density can only be increased by increasing the cell current density. However, there is always a trade-off between the energy and power densities. The results also indicate that a capacitor with both DL and faradaic processes has higher energy densities compared with the DL process alone and higher power densities compared with the faradaic process alone. The model predicts that the faradaic process increases significantly the energy per unit volume of the capacitor for power densities of 100 kW/L or less.

### Acknowledgments

The authors are grateful for the financial support provided in part by the U.S. Army Research Office under grant no. DAAH04-96-1-0421 and in part by the U.S. Department of Energy under Cooperative Agreement no. DE-FC02-91ER75666.

The University of South Carolina assisted in meeting the publication costs of this article.

### List of Symbols

$A$	cross-sectional area of the electrode, cm <sup>2</sup>
$C_d$	DL capacitance per unit surface area, F/cm <sup>2</sup>
$D$	diameter of the RuO <sub>2</sub> ·xH <sub>2</sub> O particles, cm
$E$	local electrode potential, $\Phi_1$ - $\Phi_2$ , V
$E^*$	dimensionless local potential, $E/2V_0$
$f$	$F/RT$ , V <sup>-1</sup>
$F$	Faraday's constant, 96487 C/equiv
$h$	length of the crystal lattice on the RuO <sub>2</sub> ·xH <sub>2</sub> O surface, cm
$i_0$	exchange current density for the faradaic reaction, A/cm <sup>2</sup>
$i_1$	superficial current density in the matrix phase, A/cm <sup>2</sup>
$i_2$	superficial current density in the electrolyte phase, A/cm <sup>2</sup>
$i_c$	DL current per unit volume of the electrode, A/cm <sup>3</sup>
$i_{cell}$	applied cell current density, A/cm <sup>2</sup>
$I_{cell}$	total cell current, A
$i_c^*$	dimensionless DL current, $i_c L/i_{cell}$
$i_{cell}^*$	dimensionless cell current, $i_{cell} L/(\kappa_p + \sigma)/(\kappa_p \sigma V_0)$
$i_f$	faradaic current per unit volume of the electrode, A/cm <sup>3</sup>
$j_f$	faradaic transfer current density, A/cm <sup>2</sup>
$i_f^*$	dimensionless faradaic current, $i_f L/i_{cell}$
$L$	thickness of the electrode, $L = L_+ = L_-$ , cm
$L_A$	Avogadro's number, $6.0226 \times 10^{23}$ mol <sup>-1</sup>
$L_s$	thickness of the separator, cm
$Q_f$	faradaic charge per unit volume of the electrode, C/cm <sup>3</sup>
$Q_{f,oxd}$	faradaic charge per unit volume of the fully oxidized electrode, C/cm <sup>3</sup>
$Q_{f,red}$	faradaic charge per unit volume of the fully reduced electrode, C/cm <sup>3</sup>
$R$	universal gas constant, 8.3143 J/mol K
$S_v$	specific surface area per unit volume of the electrode, cm <sup>2</sup> /cm <sup>3</sup>
$t$	time, s

$t_d$	discharge time, s
$T$	temperature, K
$U_1$	equilibrium potential for the faradaic reaction, V (vs. SCE)
$V_{cell}$	volume of the cell, cm <sup>3</sup>
$V_0$	initial potential before charge, 0.5 V (vs. SCE)
$x$	position coordinate, cm
Greek	
$\alpha_a$	anodic transfer coefficient of the faradaic reaction
$\alpha_c$	cathodic transfer coefficient of the faradaic reaction
$\delta$	state of charge in the faradaic reaction
$\epsilon$	electrode porosity
$\epsilon_s$	separator porosity
$\Phi_1$	potential in the matrix phase, V
$\Phi_2$	potential in the electrolyte phase, V
$\Phi_{ave}$	average cell potential, V
$\Phi_{cell}$	cell potential or the matrix potential difference between the two current collectors, V
$\Phi_{cell}^*$	dimensionless cell potential, $\Phi_{cell}/2V_0$
$\kappa_0$	ionic conductivity of the bulk electrolyte, S/cm
$\kappa_p$	ionic conductivity of the electrolyte inside the pores of the electrode, S/cm
$\kappa_s$	ionic conductivity of the electrolyte inside the pores of the separator, S/cm
$\theta$	fraction of oxidized species in the faradaic reaction
$\sigma$	electronic conductivity of the matrix phase, S/cm
$\tau$	DL time constant, s
$\tau^*$	dimensionless time, $t/\tau$
$\xi$	dimensionless position coordinate, $x/L$

### References

- B. E. Conway, *J. Electrochem. Soc.*, **138**, 1539 (1991).
- B. E. Conway, in *Third International Seminar on Double Layer Capacitors and Similar Energy Storage Devices*, Vol. 3, Florida Educational Seminar, Inc., Boca Raton, FL (1993).
- S. Trasatti and P. Kurzweil, *Platinum Metals Rev.*, **38**, 46 (1994).
- S. Sarangapani, B. V. Tilak, and C. P. Chen, *J. Electrochem. Soc.*, **143**, 3791 (1994).
- I. D. Raistrick, in *Electrochemistry of Semiconductors and Electrodes*, J. McHardy and F. Ludwig, Editors, pp. 297-355, Noyes Publications, Park Ridge, NJ (1992).
- H. Shi, *Electrochim. Acta*, **41**, 1633 (1996).
- M. Aoki, K. Sato, and Y. Kobayashi, *IEICE Trans. Fundam.*, **E77-A**, 208 (1994).
- S. T. Mayer, R. W. Pekala, and J. L. Kaschmitter, *J. Electrochem. Soc.*, **140**, 446 (1993).
- I. Tanahashi, A. Yoshida, and A. Nishino, *Carbon*, **29**, 1033 (1991).
- J. P. Zhang, P. J. Cygan, and T. R. Jow, *J. Electrochem. Soc.*, **142**, 2699 (1995).
- K. C. Liu and M. A. Anderson, *J. Electrochem. Soc.*, **143**, 124 (1996).
- V. Srinivasan and J. W. Weidner, *J. Electrochem. Soc.*, **144**, L210 (1997).
- C. Lin, J. A. Ritter, and B. N. Popov, *J. Electrochem. Soc.*, **145**, 4091 (1998).
- F. A. Posey and T. Morozumi, *J. Electrochem. Soc.*, **113**, 176 (1966).
- A. M. Johnson and J. Newman, *J. Electrochem. Soc.*, **118**, 510 (1971).
- W. Tiedemann and J. Newman, *J. Electrochem. Soc.*, **122**, 70 (1975).
- V. Srinivasan, C. Lin, J. A. Ritter, and J. W. Weidner, in *Electrochemical Capacitors II*, F. M. Delnick, D. Ingersoll, X. Andrieu, and K. Naoi, Editors, PV 96-25, p. 153, The Electrochemical Society Proceedings Series, Pennington, NJ (1996).
- C. J. Farahmandi, in *Electrochemical Capacitors II*, F. M. Delnick, D. Ingersoll, X. Andrieu, and K. Naoi, Editors, PV 96-25, p. 167, The Electrochemical Society Proceedings Series, Pennington, NJ (1996).
- B. Pillay and J. Newman, *J. Electrochem. Soc.*, **143**, 1806 (1996).
- O. S. Ksenzhek, *Russ. J. Phys. Chem.*, **37**, 1089 (1963).
- S. Sarangapani, B. V. Tilak, and C.-P. Chen, *J. Electrochem. Soc.*, **143**, 3791 (1996).
- M. Doyle, T. F. Fuller, and J. Newman, *J. Electrochem. Soc.*, **140**, 1526 (1993).
- J. Newman and W. Tiedemann, *AIChE J.*, **21**, 25 (1975).
- P. De Vidts and R. E. White, *J. Electrochem. Soc.*, **144**, 1343 (1997).
- T. R. Jow and J. P. Zhang, *J. Electrochem. Soc.*, **145**, 49 (1998).
- T. Yeu and R. E. White, *J. Electrochem. Soc.*, **137**, 1327 (1990).
- R. E. White, S. E. Lorimer, and R. Dardy, *J. Electrochem. Soc.*, **130**, 1123 (1983).
- M. E. Davis, *Numerical Methods and Modeling for Chemical Engineers*, John Wiley & Sons, New York (1984).
- J. S. Newman, *Electrochemical Systems*, 2nd ed., Prentice-Hall, Inc., Englewood Cliffs, NJ (1991).
- K. Kimoshita, *Carbon: Electrochemical and Physicochemical Properties*, John Wiley & Sons, New York (1988).
- F. H. Pollak and W. E. O'Grady, *J. Electrochem. Soc.*, **132**, 2385 (1985).
- S. Trasatti and G. Lodi, in *Electrodes of Conductive Metallic Oxides-Part A*, p. 301, S. Trasatti, Editor, Elsevier, New York (1980).
- H. E. Darling, *J. Chem. Eng. Data*, **9**, 421 (1964).
- S. Levine and A. L. Smith, *Disc. Faraday Soc.*, **52**, 290 (1971).
- D. Michell, D. J. A. Rand, and W. Woods, *J. Electrochem. Soc.*, **89**, 11 (1978).
- S. Pizzini, G. Buzzanca, C. Mari, L. Rossi, and S. Torchio, *MRS Bull.*, **7**, 449 (1972).
- S. Trasatti, *Electrochim. Acta*, **36**, 225 (1991).
- W.-C. Shin and S.-G. Yoon, *J. Electrochem. Soc.*, **144**, 1055 (1997).

## Correlation of Double-Layer Capacitance with the Pore Structure of Sol-Gel Derived Carbon Xerogels

Chuan Lin,<sup>a</sup> James A. Ritter,<sup>\*z</sup> and Branko N. Popov<sup>\*</sup>

Department of Chemical Engineering, Swearingen Engineering Center, University of South Carolina, Columbia, South Carolina 29208, USA

Nine different sol-gel derived carbon xerogels were prepared with different pore structures by varying the carbonization temperature (in flowing N<sub>2</sub>) and activation time (in 5% CO<sub>2</sub> in N<sub>2</sub>). For each of these carbon xerogels, mesopore and micropore size distributions and cumulative surface areas were extracted from a density functional theory analysis. Increasing the carbonization temperature caused a decrease in the number of micropores in the 6 Å range but had little effect on the mesopore size distribution and thus mesopore cumulative surface area. Increasing the CO<sub>2</sub> activation time caused an increase in the number of both micro- and mesopores where pores in the 6 Å width range eventually became pores in the 12 Å width range. The electrochemical double-layer capacitance (DLC) of the carbon xerogels was found to correlate well with changes in the pore structure, and it was determined that pores less than about 8 Å in width did not contribute to the DLC.

© 1999 The Electrochemical Society. S0013-4651(98)12-091-8. All rights reserved.

Manuscript submitted December 28, 1998; revised manuscript received June 1, 1999.

Research on carbon-based electrochemical double-layer capacitors (EDLCs) has focused on developing new and improved carbon materials with high surface areas and suitable pore structures.<sup>1-5</sup> Both of these characteristics have been shown to control the energy and power densities of EDLCs.<sup>6</sup> However, the role of microporosity, *i.e.*, pores having diameters less than 20 Å, in the performance of an EDLC is still not very clear. In other words, what pore size is too small for the electrolyte to access, hence preventing it from forming a double layer?

Most of the studies in the literature have attempted to correlate the double-layer capacitance (DLC) simply in terms of the total Brunauer-Emmett-Teller (BET) surface area of a carbon material, with limited success.<sup>7-9</sup> Some other studies have had better success by correlating the DLC in terms of the micropore and mesopore surface areas.<sup>10-12</sup> However, none of these studies has been able to identify the pore sizes that may not contribute to the DLC. Yet this information is crucial to understanding the performance of an EDLC from a molecular level and to designing better carbon-based EDLCs by tailoring the pore structure for optimum performance.

The main reason for this lack of quantification lies in the techniques that have been employed to determine the surface areas of carbon materials.<sup>7-9</sup> The commonly used techniques are global in that they only provide information on the total surface area, which is sometimes divided into the total micropore and mesopore surface areas. These techniques are incapable of providing information on the pore size distributions (PSDs) and corresponding surface area distributions. However, a very promising technique, which has not been explored much in the characterization of EDLCs, is the use of density function theory (DFT) to determine the mesopore size distribution and the corresponding cumulative surface area of carbon materials.<sup>10</sup>

Therefore, the objectives here are to demonstrate the use of DFT in determining the PSD and cumulative surface area of carbon materials that are being evaluated as EDLCs, and to show how this information can be used to identify the pore sizes that are contributing to the DLC. The carbon material chosen for this purpose is a carbonized resorcinol-formaldehyde (R-F) resin derived from a sol-gel process. This material has been receiving considerable attention in the recent literature.<sup>1,6,11-17</sup> In this study, the DLCs of a series of carbon xerogels fabricated from R-F resins, carbonized at different temperatures and CO<sub>2</sub>-activated to different extents, are correlated with their corresponding PSDs and cumulative surface areas determined

from DFT. The contribution to the DLC of various pore sizes is revealed, including the pore size range that does not contribute to the DLC of these carbon materials. Qualitative explanations for the inactivity of these small pores are offered and contrasted with the correlation proposed by Shi.<sup>10</sup>

### Experimental

The sol-gel synthesis procedure used to obtain the carbon xerogels is reported in detail elsewhere.<sup>13,17</sup> It suffices to state that solutions containing 5 w/v % solids were prepared, in which the R-F mole ratio (R/F) was fixed at 1:2. Sodium carbonate was used as a catalyst and the resorcinol/sodium carbonate mole ratio (R/C) was fixed at 50. For the carbonization study, the carbon xerogels were formed by pyrolysis of the dried gels at the desired temperature for 3 h in a flowing N<sub>2</sub> atmosphere. For the CO<sub>2</sub> activation study, the carbon xerogels were formed by pyrolysis of the dried gels at 1050°C for 3 h in flowing N<sub>2</sub> and then at the same temperature for the desired time in flowing N<sub>2</sub> containing 5 vol % CO<sub>2</sub>.

A typical three-electrode test cell was used to carry out the electrochemical measurements. The working electrode contained about 5 mg of the carbon xerogel together with 5 wt % Teflon binder. It was hand-pressed into a disk 8.5 mm in diam and 150 μm thick. The disk was sandwiched between two tantalum rods, with one rod used as a current collector and the other rod used as a support, which was physically separated from the disk using a porous glass fiber filter. This assembly was placed in a cell containing 30 wt % H<sub>2</sub>SO<sub>4</sub> as the electrolyte. A saturated calomel electrode and platinum gauze were used as the reference and counter electrodes, respectively. Cyclic voltammetry (CV) was performed between 0 and 1 V (vs. saturated calomel electrode) with a sweep rate of 5 mV/s using a potentiostat (EG&G 273A). The experiments were conducted at room temperature.

The DLC of a single carbon xerogel electrode was calculated from the CV using

$$C = \frac{i}{sm} \quad [1]$$

where  $C$  is the specific DLC,  $i$  is the anodic current recorded at 0.5 V,  $s$  is the potential sweep rate, and  $m$  is the mass of the active electrode material. The PSD,  $f(w)$ , was calculated from the adsorption integral equation

$$n(P) = \int_{w_{\min}}^{w_{\max}} f(w) \rho(P, w) dw \quad [2]$$

where  $n(P)$  is the experimentally measured adsorption isotherm in terms of the number of moles of N<sub>2</sub> adsorbed at 77 K as a function

<sup>\*</sup> Electrochemical Society Active Member.

<sup>a</sup> Present address: Department of Chemical Engineering, Center for Advanced Engineering Fibers and Films, Clemson University, Clemson, South Carolina 29634, USA.

<sup>z</sup> E-mail: ritter@enr.sc.edu.



of pressure  $P$ ,  $w_{\min}$  and  $w_{\max}$  are the widths of the smallest and largest pores in the material, and  $\rho(P, w)$  is the local adsorption isotherm in terms of the molar density of  $N_2$  at 77 K and pressure  $P$  in a pore of width  $w$ . By definition,  $f(w) = dv/dw$ , where  $v$  is the pore volume. The experimental adsorption isotherm for each of the carbon xerogels was measured using a Coulter Omnisorp 610,<sup>17</sup> and the local adsorption isotherms were predicted from nonlocal DFT as described in detail elsewhere.<sup>18-21</sup> With the above experimental and theoretical adsorption isotherms, the PSD for each carbon xerogel was obtained by solving Eq. 2 using a regularization technique.<sup>22,23</sup> The cumulative surface area ( $S_c$ ) was then estimated from Eq. 3 by assuming a slit pore model for the carbon xerogels

$$S_c = \int_{w_{\min}}^{w_{\max}} \frac{2f(w)}{w} dw \quad [3]$$

### Results and Discussion

The effects of the carbonization temperature and the  $CO_2$  activation time on the PSDs of the carbon xerogels is shown in Fig. 1A and 1B, respectively. According to IUPAC nomenclature,<sup>24</sup> micropores are less than 20 Å in diam, mesopores are between 20 and 500 Å in diam, and macropores are greater than 500 Å in diam. Figure 1A shows that in the micropore region, all of the samples exhibited a peak with a mean pore width of about 6 Å. The height of this peak decreased with an increase in the carbonization temperature, clearly indicating the loss of microporosity. Three of the samples also exhibited a peak between pore widths of 10 and 20 Å. This peak was relatively small at 600°C, disappeared at 750 and 900°C, and reappeared at 1050 and 1200°C with a slight shift toward smaller pore

sizes, indicating the destruction and creation of microporosity with increasing carbonization temperature. In the mesopore region, a broad but small peak appeared with a mean pore width of around 200 Å; however, this peak did not change much with the carbonization temperature.

In contrast to the effect of the carbonization temperature, Fig. 1B shows that the effect of  $CO_2$  activation time on the PSDs of the carbon xerogels was much more pronounced. All of the samples exhibited a peak with a mean pore width of about 6 Å, which increased with time up to 2.5 h, and then decreased slightly after 3 h. All of the samples also exhibited a peak with a mean pore width of about 13 Å, which increased consistently with time. Some peaks with pore widths between 20 and 100 Å also appeared and grew with time; however, the peak with a mean pore width of ~200 Å changed little with time. These trends show very clearly the creation and destruction of small micropores in the 6 Å range with increased  $CO_2$  activation time, some of which became large micropores in the 12 Å range and small mesopores in the 30 Å range with the further burn-off of carbon. Moreover, these results, along with evidence in the literature,<sup>11</sup> which showed that these carbon xerogels are composed of carbon nanoparticles on the order of 10 to 20 nm in diam, also suggest that the larger mesopores (200 Å range) were derived from the voids between the carbon particles, the sizes of which were not affected by the carbonization temperature or  $CO_2$  activation time, and that the smaller mesopores (30 Å range) and all of the micropores were derived from pores within the nanoparticles, the distributions of which were greatly affected by both the carbonization temperature and  $CO_2$  activation time.

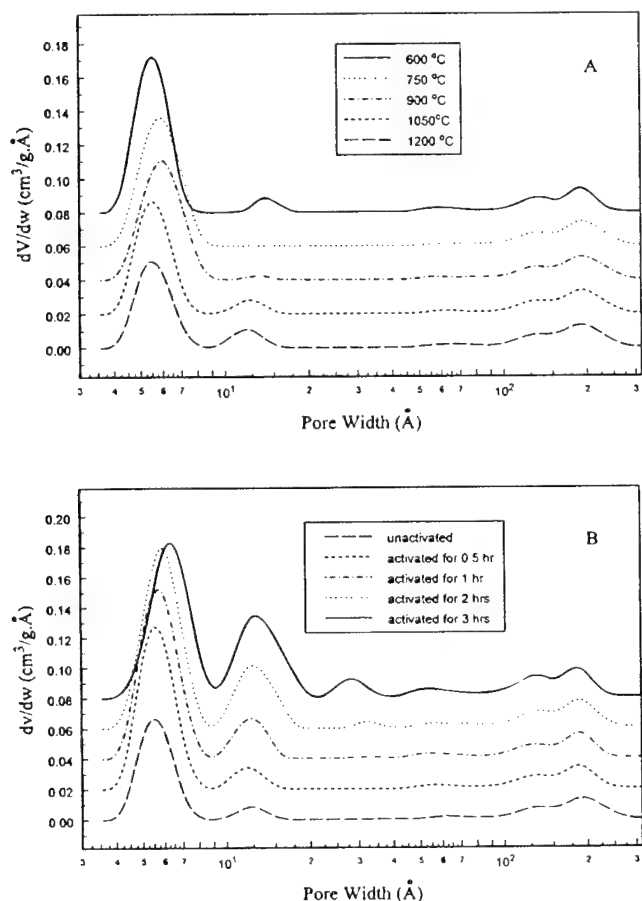


Figure 1. Effect of the carbonization temperature (A, top) and  $CO_2$  activation time (B, bottom) on the PSDs of the carbon xerogels. The curves are offset from each other by  $dv/dw = 0.02$ .

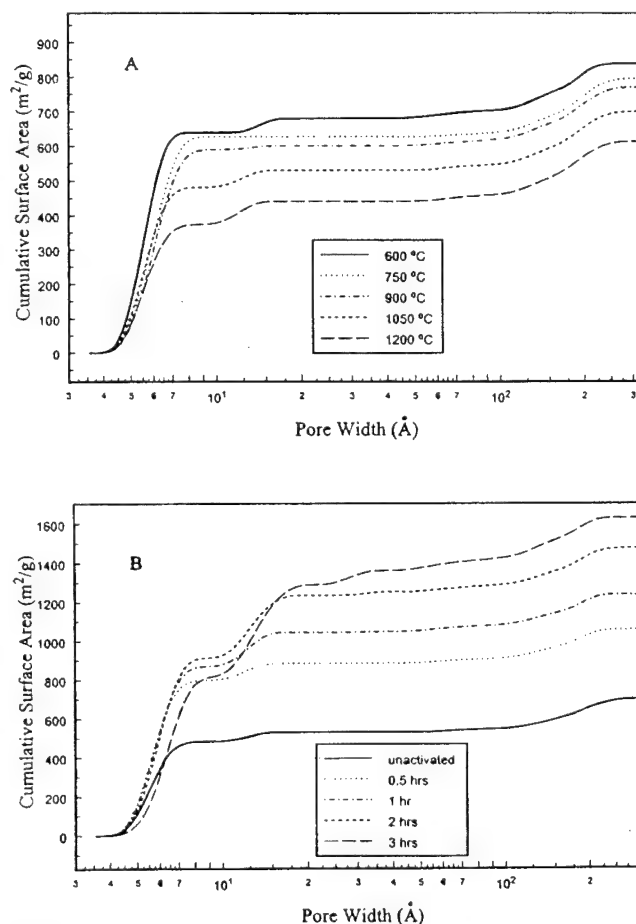


Figure 2. Effect of the carbonization temperature (A, top) and  $CO_2$  activation time (B, bottom) on the cumulative surface areas of the carbon xerogels.



The PSDs shown in Fig. 1A and B were used to determine the total ( $S_{\text{tot}}$ ), micropore ( $S_{\text{mi}}$ ), and mesopore ( $S_{\text{me}}$ ) surface areas, as described above and based on the cumulative surface areas shown in Fig. 2A and B, respectively, for the carbonization temperature and  $\text{CO}_2$  activation time studies. For the carbonization temperature study, the DLC and  $S_{\text{tot}}$ ,  $S_{\text{mi}}$ , and  $S_{\text{me}}$  are shown in Fig. 3A and B, all as a function of the carbonization temperature.  $S_{\text{tot}}$  was 840  $\text{m}^2/\text{g}$  for the carbon xerogel carbonized at 600°C, then it decreased almost linearly with an increase in temperature and finally dropped to 610  $\text{m}^2/\text{g}$  at 1200°C. However, the DLC of the carbon xerogel carbonized at 600°C was surprisingly almost zero. AC impedance tests indicated that this material had a very high ohmic resistance of  $\sim 500 \text{ k}\Omega$ , which indicates that it was not converted into an electrically conductive carbon material at such a low temperature. Excluding the sample at 600°C, the DLC exhibited a similar trend to  $S_{\text{tot}}$ . A maximum capacitance of 185 F/g was obtained at 750°C, then the capacitance decreased with an increase in temperature down to 98 F/g at 1200°C.

The origin of this decrease in the DLC with the carbonization temperature is revealed clearly in Fig. 3B and is related to a decrease in  $S_{\text{mi}}$ .  $S_{\text{mi}}$  decreased almost linearly with an increase in the carbonization temperature from 630  $\text{m}^2/\text{g}$  at 750°C to 440  $\text{m}^2/\text{g}$  at 1200°C; however,  $S_{\text{me}}$  remained nearly unchanged at about 170  $\text{m}^2/\text{g}$  and was independent of the carbonization temperature. These results suggest that pores less than 20 Å in width contributed to the DLC, which is consistent with that reported elsewhere.<sup>10,25</sup> However, the question that remains is what is the smallest pore size that can still contribute to the DLC? This question is addressed later.

For the  $\text{CO}_2$  activation study, the DLC and  $S_{\text{tot}}$ ,  $S_{\text{mi}}$ , and  $S_{\text{me}}$  are shown in Fig. 4A and B, all as a function of the  $\text{CO}_2$  activation time.  $S_{\text{tot}}$  was around 700  $\text{m}^2/\text{g}$  for the unactivated carbon xerogel, and it

increased with an increase in the  $\text{CO}_2$  activation time up to about 1630  $\text{m}^2/\text{g}$  after 3 h of activation; however, the rate of increase in  $S_{\text{tot}}$  decreased with time, as did  $S_{\text{mi}}$ . In contrast, the rate of increase in  $S_{\text{me}}$  increased with time. This result indicated that the activation process, which burns off carbon to create more pores and surface area, took place mainly within the carbon particles. In other words, the initial high rate of formation of micropores slowed at the expense of converting micropores into mesopores with increasing  $\text{CO}_2$  activation time. These results certainly impacted the DLC of these materials, as shown in Fig. 4A.

The DLC was 112 F/g for the unactivated carbon xerogel, and it increased with an increase in the  $\text{CO}_2$  activation time up to 170 F/g after 3 h of activation. The rate of increase in the DLC after 0.5 h also began to increase with time, *i.e.*, the slope was convex to the abscissa. The same trend was exhibited by  $S_{\text{me}}$  shown in Fig. 4B, whereas  $S_{\text{mi}}$  exhibited the opposite trend. This result indicates that the increase in  $S_{\text{me}}$  with time may have been controlling the increase in the DLC, a surprising result because the micropore surface areas were all significantly larger than the mesopore surface areas. For example,  $S_{\text{mi}}$  and  $S_{\text{me}}$  of the unactivated carbon xerogel were 530 and 170  $\text{m}^2/\text{g}$ , respectively, and they became 1290 and 340  $\text{m}^2/\text{g}$  after 3 h of  $\text{CO}_2$  activation, respectively. These trends suggested that some of the micropores were not contributing to the DLC. An analysis to determine the sizes of these inactive pores follows.

The unactivated but carbonized sample at 750°C gave rise to a DLC of 23.1  $\mu\text{F}/\text{cm}^2$ , based on the total surface area obtained from DFT. This value was slightly higher, however, than the ideal value that has been used to describe the DLC of clean graphite, which is about 20  $\mu\text{F}/\text{cm}^2$ .<sup>26</sup> This slightly higher DLC was probably due to pseudocapacitance caused by the presence of surface functional groups. Kinoshita<sup>26</sup> has shown that a minimum pyrolysis tempera-

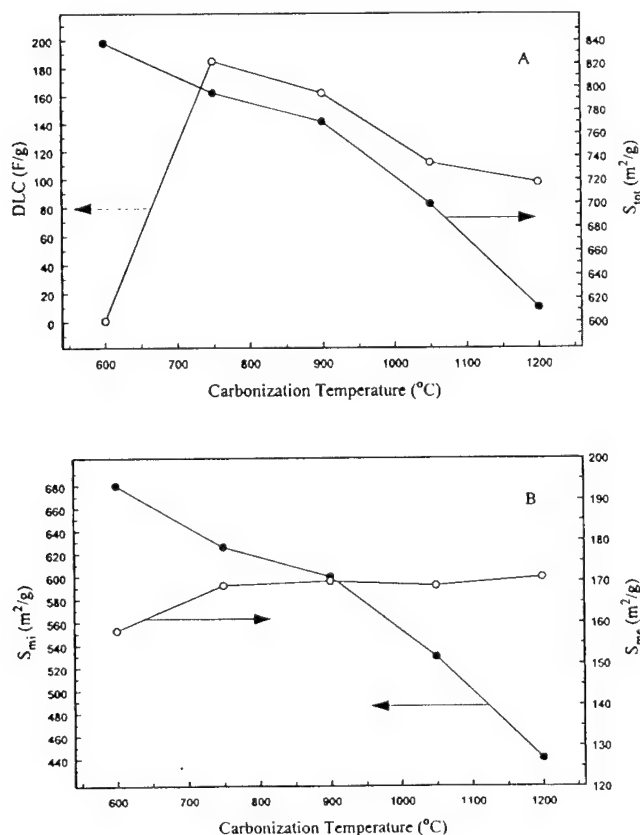


**Figure 3.** Effect of the carbonization temperature on the DLC and total surface area,  $S_{\text{tot}}$ , (A, top), and (B, bottom) micropore,  $S_{\text{mi}}$ , and mesopore,  $S_{\text{me}}$ , surface areas of the carbon xerogels.

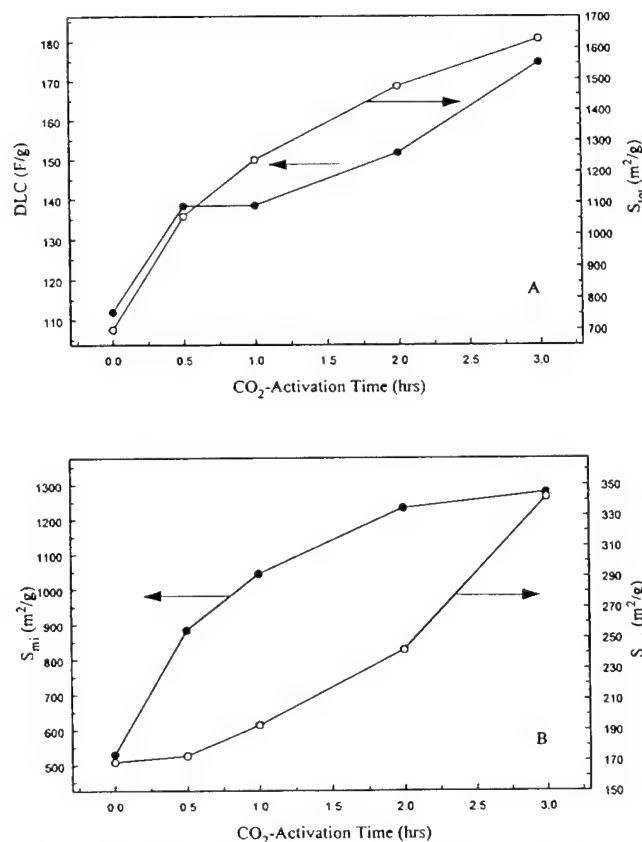


**Figure 4.** Effect of the  $\text{CO}_2$  activation time on the DLC and total surface area, (A, top)  $S_{\text{tot}}$ , and (B, bottom) micropore,  $S_{\text{mi}}$ , and mesopore,  $S_{\text{me}}$ , surface areas of the carbon xerogels.

**Table I. Minimum pore size that contributed to the DLC of the carbon xerogels.**

Conditions	DLC (F/g)	Total surface area (m <sup>2</sup> /g)	Active surface area (m <sup>2</sup> /g)	Inactive surface area (m <sup>2</sup> /g)	Minimum pore size Å
Carbonization temperature (°C)					
750	185.0	795.1	925.0	-129.9	— <sup>a</sup>
900	162.0	769.9	810.0	-40.1	— <sup>a</sup>
1050	112.0	698.8	560.0	138.8	5.1
1200	97.9	612.5	489.5	123.0	5.2
CO <sub>2</sub> activation time (h)					
0	112.0	698.8	560.0	138.8	5.1
0.5	138.3	1056.9	691.5	365.4	5.5
1	138.4	1237.2	692.0	545.2	6.0
2	151.7	1476.0	758.5	717.5	6.6
3	174.7	1629.4	873.5	755.9	7.8

<sup>a</sup> The minimum pore size was not discernible in this sample because of a pseudocapacitance contribution to the measured electrochemical capacitance.

ture of 1000°C is needed to destroy the residual surface functional groups (*e.g.*, OH and COOH) that are known to exist on these kinds of synthetic carbon materials. Therefore, the DLC of 20  $\mu\text{F}/\text{cm}^2$  was used as a benchmark to determine if a consistent trend could be found between the measured DLC of all of the samples and a characteristic pore size which indicated the minimum pore size that was contributing to these measured DLCs. For example, using this value of 20  $\mu\text{F}/\text{cm}^2$  for the sample carbonized at 1050°C resulted in an active surface area of 560 m<sup>2</sup>/g and an inactive surface area of 138.8 m<sup>2</sup> for a DLC of 112 F/g. According to the cumulative surface area for this sample shown in Fig. 2A, this cumulative inactive surface area corresponded to all of the pores less than 5.1 Å in width. Table I presents similar analyses for the eight electrochemically active samples from both the carbonization temperature and CO<sub>2</sub> activation time studies. Some very interesting trends were observed.

The two samples carbonized at 750 and 900°C resulted in higher active surface areas than their corresponding total surface areas, which correspondingly gave negative values for their inactive surface areas. As a result, no minimum pore size was reported for these two materials. Nevertheless, these results are consistent with the earlier statement about the effect of the presence of residual surface functional groups within the pores of carbon materials carbonized below 1000°C. These residual surface functional groups most likely produced a pseudocapacitance in these samples<sup>26</sup> that necessarily caused an overestimation in the active surface area, relative to the assumed ideal DLC of 20  $\mu\text{F}/\text{cm}^2$ . For the sample carbonized at 750°C, this pseudocapacitance amounted to about 3  $\mu\text{F}/\text{cm}^2$  or about 15% of the measured capacitance. For the samples carbonized at temperatures higher than 1000°C, the pseudocapacitance contribution was considered to be negligible; and thus, the measured DLCs of these materials were considered to represent the actual DLC of these materials, with no contribution from pseudocapacitance. For these six samples, this analysis consistently indicated that pore widths smaller than about 5 Å for the carbonized samples and between 5 and 8 Å for the CO<sub>2</sub> activated samples were not contributing to the DLC of these carbon xerogels. Within the error of this analysis, these results were considered to be consistent and show that the smaller micropores in these carbon materials, *e.g.*, those pores less than about 8 Å in diam, were not contributing significantly to the DLC.

It is interesting to compare the above analysis on synthetic carbon xerogels with a different analysis carried out by Shi<sup>10</sup> on both activated carbon microbeads and activated carbon fibers; however, this comparison is restricted to the activated carbon fibers, since they

are typically made from carbonized resins, similarly to the carbon xerogels. Shi<sup>10</sup> assumed that the DLC of a micropore surface is different than that of a mesopore surface, and from a simple linear correlation obtained capacitances of 14.5 and 7.5  $\mu\text{F}/\text{cm}^2$  for the micropore and mesopore surfaces of activated carbon fibers, respectively. When applied to the carbon xerogels, Shi's<sup>10</sup> correlation did not produce a linear relationship. However, the DLC of the six carbon xerogels carbonized above 1000°C correlated fairly linearly with the total surface area, as shown in Fig. 5. The slope of this linear correlation corresponded to a DLC of 6.54  $\mu\text{F}/\text{cm}^2$ , which was quite low compared to the ideal DLC of 20  $\mu\text{F}/\text{cm}^2$ , because this value also included the inactive surface area. A plot of the DLC vs. only the active surface area ( $S_{\text{act}}$ ) produced a straight line with a slope of 20  $\mu\text{F}/\text{cm}^2$ , as also shown in Fig. 5. An intriguing feature of these results is the fact that the DLC of the activated carbon fibers studied by Shi<sup>10</sup> also correlated fairly linearly with their total surface area, with a corresponding slope of 7.2  $\mu\text{F}/\text{cm}^2$ .

The point to be made here is that these low and similar values for the DLC of the activated carbon fibers and carbon xerogels, compared to the ideal value of 20  $\mu\text{F}/\text{cm}^2$ , can be accounted for in two ways. One way is to assume that the DLC of micropore and mesopore surfaces are different as done by Shi.<sup>10</sup> The other way is to assume that they are the same (at 20  $\mu\text{F}/\text{cm}^2$ ) and then assume that some of the smaller micropores are inactive as done in this study. It is quite clear that the behavior observed by Shi<sup>10</sup> by the activated carbon fibers can also be explained equally well by assuming that a minimum pore size exists, that below which does not contribute to the DLC. It is not clear at this time which assumption is correct, especially because both analyses produce physically realistic results. However, it suffices to state that the correlation of Shi<sup>10</sup> does not seem to apply to all microporous carbon materials. In contrast, the current analysis, based on a minimum active pore size, does apply to all microporous carbon materials.

### Conclusions

This work demonstrated very convincingly the ability of DFT to extract pore structure information from the physical adsorption isotherm. This information was used to follow the evolution of the micropore and mesopore structures in carbon xerogels during controlled, structure-altering experimentation with the carbonization temperature and CO<sub>2</sub> activation time. Careful analysis of the results from DFT coupled with the DLC of these materials revealed that pores less than about 8 Å in width were not contributing to the DLC in these carbon xerogels. Moreover, the carbonization temperature study showed very clearly that the main contribution to the DLC was from the larger micropores between 8 and 20 Å in width, and for these carbon xerogels a temperature of about 700°C appeared to be optimum. This work also showed that the CO<sub>2</sub> activation time can be

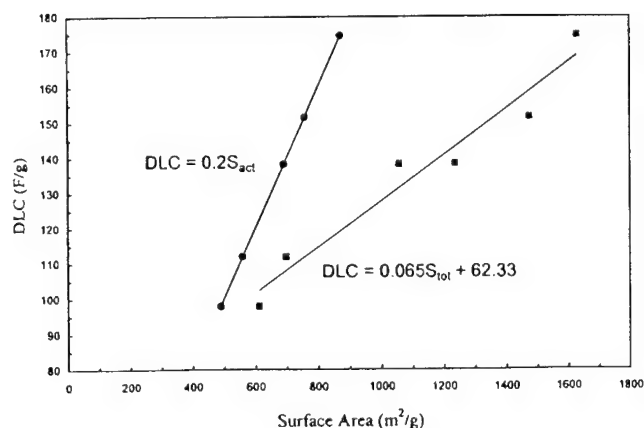


**Figure 5.** Linear correlations of the DLC with the total surface area,  $S_{\text{tot}}$ , and active surface area,  $S_{\text{act}}$ , of the carbon xerogels carbonized above 1000°C.

used to further optimize the performance of these carbon xerogels with respect to maximizing the number of micropores in the most active size range, i.e., in the 8 to 20 Å range. Overall, the results from this work should provide valuable insight into the design of better microporous carbon materials for use in EDLCs and other applications.

#### Acknowledgments

This material is based upon work supported in part by the U.S. Army Research Office under grant no. DAAH04-96-1-0421 and in part by the U.S. Department of Energy under cooperative agreement no. DE-FC02-91ER75666.

#### References

1. S. T. Mayer, J. L. Kaschmitter, and R. W. Pekala, in *New Sealed Rechargeable Batteries and Supercapacitors*, B. M. Barnett, G. Halpert, E. Dowgiallo, Y. Matsuda, and Z.-i. Takehara, Editors, PV 93-23, p. 38, The Electrochemical Society Proceedings Series, Pennington, NJ (1993).
2. M. Aoki, K. Sato, and Y. Kobayashi, *IEICE Trans. Fund.*, **E77-A**, 208 (1994).
3. T. C. Murphy and W. E. Kramer, in *Proceedings of the 37th Power Sources Symposium*, Cherry Hill, NJ, June, IEEE (1996).
4. E. J. Dowgiallo and J. E. Hardin, *IEEE AES Systems magazine*, p. 26 (Aug 1995).
5. P. Kurzweil and G. Dietrich, in *Proceedings of the 2nd International Seminar on Double Layer Capacitors*, Florida Educational Seminars, Inc., Deerfield Beach, FL (Dec 1992).
6. S. T. Mayer, R. W. Pekala, and J. L. Kaschmitter, *J. Electrochem. Soc.*, **140**, 446 (1993).
7. I. Tanahashi, A. Yoshida, and A. Nishino, *Bull. Chem. Soc. Jpn.*, **63**, 3611 (1990).
8. I. Tanahashi, A. Yoshida, and A. Nishino, *Bull. Chem. Soc. Jpn.*, **63**, 2755 (1990).
9. I. Tanahashi, A. Yoshida, and A. Nishino, *J. Electrochem. Soc.*, **137**, 3052 (1990).
10. H. Shi, *Electrochim. Acta*, **41**, 1633 (1996).
11. R. Saliger, U. Fischer, C. Herta, and J. Fricke, *J. Non-Cryst. Solids*, **225**, 81 (1998).
12. G. Reichenauer, A. Emmerling, J. Fricke, and R. W. Pekala, *J. Non-Cryst. Solids*, **225**, 210 (1998).
13. C. Lin and J. A. Ritter, *Carbon*, **35**, 1271 (1997).
14. D. W. Schaefer, R. W. Pekala, and G. Beaucage, *J. Non-Cryst. Solids*, **186**, 159 (1995).
15. R. W. Pekala, S. T. Mayer, J. L. Kaschmitter, and F. M. Kong, *Sol-Gel Processing and Applications*, Y. A. Attia, Editors, Plenum Press, New York (1994).
16. R. W. Pekala, C. T. Alviso, and J. D. Lemay, *Chemical Processing of Advanced Materials*, L. L. Hench and J. K. West, Editors, John Wiley & Sons, Inc., New York (1992).
17. C. Lin and J. A. Ritter, *Carbon*, In press (1999).
18. N. A. Seaton, J. P. R. B. Walton, and N. Quirke, *Carbon*, **27**, 853 (1989).
19. P. Braure, H. -R. Poosch, M. V. Szombathely, and M. Heuchel, *Studies in Surface Science and Catalysis*, Vol. 80, p. 67 (1993).
20. C. Lastoskie, K. E. Gubbins, and N. Quirke, *J. Phys. Chem.*, **97**, 4789 (1993).
21. B. P. Russell and M. D. LeVan, *Carbon*, **32**, 845 (1994).
22. M. V. Szombathely, P. Brauer, and M. Jaroniec, *J. Comput. Chem.*, **13**, 17 (1992).
23. J. Jagiello, *Langmuir*, **10**, 2778 (1994).
24. K. S. W. Sing, D. H. Everett, R. A. W. Haul, L. Moscou, R. A. Pierotti, J. Rouquerol, and T. Siemieniowska, *Pure Appl. Chem.*, **57**, 603 (1985).
25. I. Tanahashi, A. Yoshida, and A. Nishino, *Carbon*, **29**, 1033 (1991).
26. K. Kinoshita, *Carbon: Electrochemical and Physicochemical Properties*, John Wiley & Sons, Inc., New York (1988).

## Studies on the Capacitance of Nickel Oxide Films: Effect of Heating Temperature and Electrolyte Concentration

Venkat Srinivasan\* and John W. Weidner\*\*<sup>z</sup>

Department of Chemical Engineering, University of South Carolina, Columbia, South Carolina 29208, USA

Nickel oxide films were prepared by electrochemically precipitating the hydroxide and heating it in air to form the oxide. The resulting oxide films behave as a capacitor. The capacitance of the oxide depends on the heating temperature, showing a maximum at 300°C. The mechanism of charge storage was studied by measuring the capacitance and surface area as a function of heating temperature, and the capacitance in different electrolytes and potential windows. The charge-storage mechanism is believed to be a surface redox reaction involving adsorbed hydroxyl ions.  
 © 2000 The Electrochemical Society. S0013-4651(99)07-034-2. All rights reserved.

Manuscript submitted July 8, 1999; revised manuscript received October 26, 1999.

With the increasing interest in high-power devices (e.g., for acceleration in electric vehicles), electrochemical capacitors (ECs) have been studied extensively in recent years (see, for example, Ref. 1-3). Most commercially available ECs make use of the double layer formed at the electrode/electrolyte interface to store energy. As the double-layer capacitance is typically less than 40  $\mu\text{F}/\text{cm}^2$ ,<sup>4</sup> high-surface-area materials such as activated carbon are usually used. However, as much as 90% of the available surface area is not utilized in activated carbon due to the presence of micropores (<2 nm), which cannot be wetted by the electrolyte.<sup>5</sup> Another strategy for increasing the energy stored in these devices is the use of faradaic pseudocapacitors, which exhibit current-potential responses similar to that of double-layer capacitors. Transition metal oxides like  $\text{RuO}_2$ <sup>6,7</sup> and  $\text{IrO}_2$ <sup>7</sup> exhibit faradaic pseudocapacitance with capacitance reported to be as large as 760 F/g.<sup>6</sup> (Note that all capacitance values reported in this paper are for a single electrode excluding the mass of the separator, electrolyte, and current collectors.) However, the high cost of ruthenium and iridium has stimulated research for identifying other materials that exhibit similar behavior.

Recently Liu and Anderson<sup>8-11</sup> reported the pseudocapacitance of nickel oxide (i.e., NiO) films that were made by heating sol-gel-derived nickel hydroxide [i.e.,  $\text{Ni}(\text{OH})_2$ ] in air at 300°C. We investigated similar nickel oxide films, the only difference being that the nickel hydroxide was produced via electrochemical deposition.<sup>12</sup> Both groups reported a specific capacitance as high as 260 F/g. The films also maintain high utilization at high power densities and have excellent cycle life.<sup>12</sup> Even though the specific capacitance is comparable to that of activated carbon,<sup>5</sup> the ability to make thin films makes NiO attractive for high-power devices.

What is not known though is how heating temperature, electrolyte environment, or the potential range of operation affect the capacitance of nickel oxide. Therefore, in order to understand the mechanism of charge storage in these materials, the specific (i.e., capacitance per mass of material) and intrinsic (i.e., capacitance per surface area) capacitance are reported as a function of heating temperature (25-450°C), electrolyte environment (3-40 wt % KOH, and 1 N  $\text{H}_2\text{SO}_4$ ), and potential window of operation (-0.55 to 0.45 V vs. SCE). This insight can be used to guide electrode development, which may enable NiO to be a commercially viable electrode in ECs.

### Experimental

Thin films of nickel hydroxide were deposited on gold foils masked with a sealant (Silicone<sup>TM</sup>) so as to expose an area of 1.0  $\text{cm}^2$ . The films studied here were deposited at room temperature in a bath containing 1.8 M  $\text{Ni}(\text{NO}_3)_2$  and 0.075 M  $\text{NaNO}_3$  in a solvent of 50 vol % ethanol in a procedure described in detail elsewhere.<sup>13,14</sup> A cathodic current density of 5.0  $\text{mA}/\text{cm}^2$  was applied for

25 min, which according to these previous deposition studies should result in 350  $\mu\text{g}$  films with a capacity of 277 mC (i.e., 790 C/g). The expected capacity was confirmed by performing cyclic voltammetry on nickel hydroxide in 3 wt % KOH and integrating the area under the reduction peak of a stable cyclic voltammogram (CV).

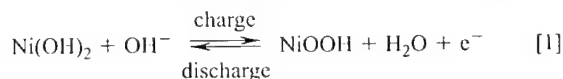
For subsequent studies in KOH, the cycled nickel hydroxide films were again rinsed in deionized (DI) water, heated to the desired temperature at a rate of 5°C per min, maintained at that temperature for 3 h, and subsequently cooled at 5°C per min to room temperature. The oxide films were then cycled in the electrolyte for approximately 25 cycles, and the steady-state capacitances were measured. Prior to conducting an experiment at a different KOH concentration, the films were rinsed in DI water and immersed in the new solution where it was allowed to equilibrate for 15 min. CVs were again performed to measure the capacity once steady state was reached. Studies in  $\text{H}_2\text{SO}_4$  were conducted by heating the as-deposited film to 300°C as described, but without first cycling in 3 wt % KOH.

A saturated calomel electrode (SCE) and a platinum mesh were used as the reference and counter electrode, respectively, in all experiments. Deposition and cyclic voltammetry studies were conducted on a computer-controlled EG&G Princeton Applied Research M273 potentiostat/galvanostat using the M270 software. The capacitance of the films was estimated by integrating the area under the CVs using the software.

Chemically precipitated nickel hydroxide was prepared by adding the nickel nitrate solution described previously into a beaker containing 3 wt % KOH using a dropper. The KOH solution was stirred continuously, thus finely dispersing the precipitated nickel hydroxide. Additional KOH was added to the solution to maintain the pH at 13.0. The resulting nickel hydroxide was filtered using a vacuum arrangement and repeatedly washed in order to remove the KOH from the material. The active material was dried at 80°C for 24 h prior to surface area measurements using the Brunauer-Emmett-Teller (BET) technique. The material was heated to the desired temperature using the same heating regime described and the surface-area measured. The surface-area measurements were performed using a Micromeritics Pulse Chemisorb 2700 analyzer using  $\text{N}_2$ .

### Results and Discussion

**Effect of the heating temperature on nickel hydroxide.**—Figure 1 shows the CVs of three nickel hydroxide films at a sweep rate of 5 mV/s. The CV of the as-deposited material cycled between -0.80 and 0.55 V vs. SCE shows a set of redox peaks corresponding to the nickel oxidation/reduction reaction, often ideally represented as



which involves the intercalation/deintercalation of protons. The large anodic currents positive of 0.5 V correspond to the oxygen evo-

\* Electrochemical Society Student Member.

\*\* Electrochemical Society Active Member.

<sup>z</sup> E-mail: weidner@cengr.sc.edu

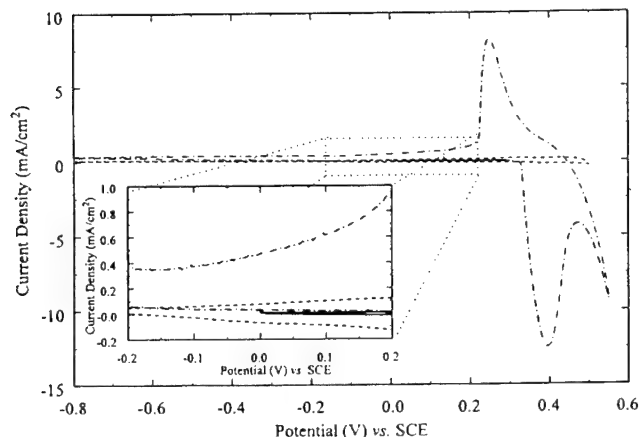
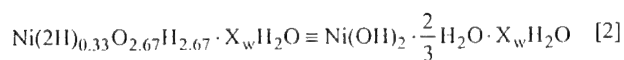


**Figure 1.** Cyclic voltammetry on: (---) an as-deposited film of nickel hydroxide cycled between  $-0.8$  and  $0.55$  V vs. SCE; (···) a film heated to  $300^{\circ}\text{C}$  and cycled between  $-0.8$  and  $0.50$  V; and (—) an as-deposited film cycled between  $0.0$  and  $0.3$  V. The sweep rate was  $5$  mV/s, the electrolyte was  $3$  wt % KOH, and the cathodic currents are positive.

lution reaction. When the film is heated to  $300^{\circ}\text{C}$ , the capacity decreases significantly and the current-potential response changes from battery behavior to capacitor behavior. That is, the peaks are no longer visible, and the anodic and cathodic current-potential responses are symmetric about the zero-current axis. This latter point is seen more clearly in the inset to Fig. 1. The response of the as-deposited material cycled between  $-0.80$  and  $0.55$  V is not symmetric about this axis, even in the potential window between  $-0.20$  to  $0.20$  V. However, if the as-deposited material is cycled between  $0.0$  and  $0.30$  V, below the potential where the oxidation of  $\text{Ni(OH)}_2$  occurs, the current-potential responses are symmetric about the zero-current axis. Therefore, the as-deposited material behaves as a capacitor as long as Reaction 1 is avoided.

In order to quantify the capacitance of the active material as a function of temperature, CVs were performed in a potential window where Reaction 1 was avoided. For materials heated to  $275^{\circ}\text{C}$  or less, the films were cycled between  $0$  and  $0.3$  V, and for materials heated to  $300^{\circ}\text{C}$  and above, the films were cycled between  $0.0$  and  $0.35$  V. Four of these steady-state CVs are shown in Fig. 2 in order to confirm that the capacitor behavior is achieved for materials heated between  $25$  and  $400^{\circ}\text{C}$ . Although the current-potential response is relatively symmetric about the zero-current axis, the capacitance of each film is potential dependent. For example, in the material heated to  $300^{\circ}\text{C}$ , the current, and hence the capacitance, at  $0.30$  V is twice that at  $0.10$  V. An ideal capacitor, on the other hand, would exhibit a potential-independent current (*i.e.*, capacitance). Also evident from Fig. 2 is that the capacitance increases when the material is heated from  $25$  to  $300^{\circ}\text{C}$  but decreases when heated above  $300^{\circ}\text{C}$ . Therefore, Fig. 2 indicates that there is an optimal heating temperature. However, plotting the capacitance rather than the specific capacitance vs. temperature may be misleading, since the mass of the film is also changing with temperature. Therefore, the change in structure, and hence the mass, of the active material upon heating is discussed so that the specific capacitance can be estimated.

The electrochemically deposited nickel hydroxide films are very defective, with  $25\%$  of the nickel lattice sites containing protons rather than nickel ions.<sup>15,16</sup> This material can be represented stoichiometrically as<sup>17</sup>



where  $X_w$  is the moles of water. This water can be structurally bound to the crystal<sup>18</sup> or in the film between the crystallites. In contrast, the  $\text{H}_2\text{O}$  in the " $2/3$   $\text{H}_2\text{O}$ " is not molecular water but rather two protons sitting on a nickel vacancy with an oxygen atom associated with it.<sup>17</sup>

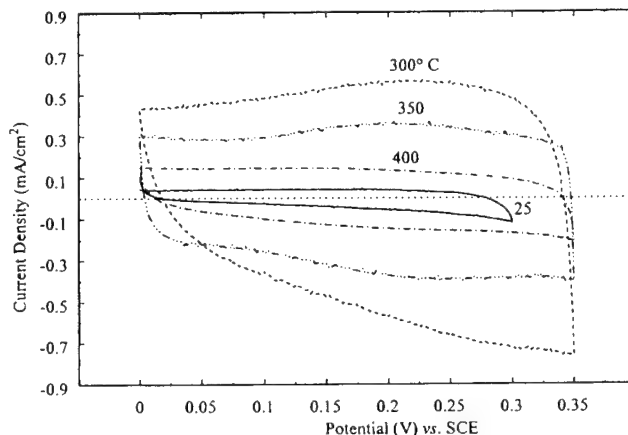
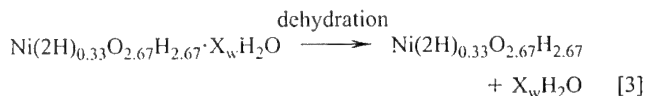


**Figure 2.** Cyclic voltammetry on nickel hydroxide films that were previously heated to different temperatures. The sweep rate was  $20$  mV/s, the electrolyte was  $3$  wt % KOH, and the cathodic currents are positive. (···) Zero current.

The redox behavior of this material is well studied as it is the positive electrode in nickel-based batteries and is represented in Reaction 1. Previous studies on heating this material have indicated a three-step weight-loss mechanism based on thermogravimetric analysis (TGA) and differential scanning calorimeter (DSC) results.<sup>18,19</sup> The first two occur when nickel hydroxide is heated to at least  $200^{\circ}\text{C}$ . At this temperature, molecular water is lost from the active material according to the following reaction



As shown previously, the dehydrated materials retained the electrochemical signatures of the as-deposited material.<sup>12</sup> Studies on the defect nature of nickel hydroxide have shown that the water content of these films ( $X_w$ ) is approximately  $1$  mol of water per mole Ni,<sup>20</sup> which corresponds to a  $16\%$  loss in mass via Reaction 3. Therefore, films heated to  $200^{\circ}\text{C}$  have  $84\%$  of the mass of the as-deposited material. Note that as  $X_w$  contains both structural water and the water between crystallites, one would realistically expect two weight losses, one at  $\sim 100^{\circ}\text{C}$  and the other at  $\sim 200^{\circ}\text{C}$  as observed by previous researchers.<sup>18,19</sup> However, due to difficulty in separating the two phenomenon, it is assumed that a single weight loss occurs at  $200^{\circ}\text{C}$ .

When the film is heated to  $\sim 300^{\circ}\text{C}$  or above, the hydroxide is converted to the oxide<sup>18,19</sup> according to the reaction



and the film becomes stoichiometric NiO. The conversion at  $\sim 300^{\circ}\text{C}$  has been shown previously to lead to a significant improvement in the cycle life<sup>12,19</sup> of these materials and a decrease in the optical response.<sup>19</sup> The assumption that the material at  $300^{\circ}\text{C}$  is stoichiometric NiO is reasonable considering the rapid decrease in the level of defects in NiO even at modest heat-treatment conditions.<sup>21</sup> Reaction 4 indicates a further loss of  $24\%$  of the mass. Therefore, at or above  $300^{\circ}\text{C}$  the mass of the film is  $60\%$  of the as-deposited mass.

The specific capacitance of the active material as a function of heating temperature is plotted in Fig. 3. The specific capacitance of the material was estimated from the CVs by integrating the area under the current-potential curve and then dividing by the sweep rate, the mass of the film, and the potential window according to the equation

$$C = \frac{1}{mv(V_a - V_c)} \int_{V_c}^{V_a} I(V) dV \quad [5]$$

For reasons discussed previously, films heated to  $200^{\circ}\text{C}$  were taken to have the mass of the as-deposited material. Films heated above

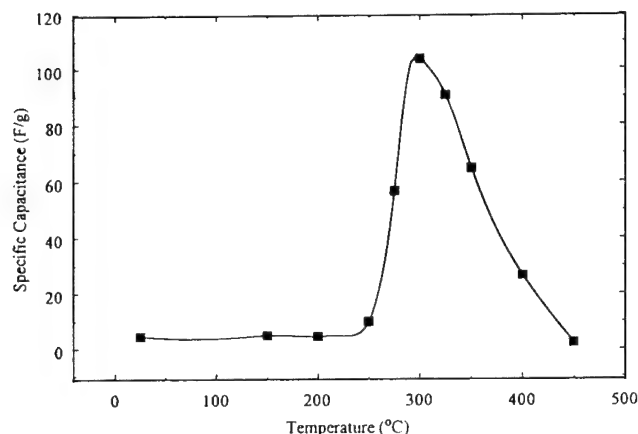


**Figure 3.** Specific capacitance of nickel hydroxide films that were previously heated to different temperatures. The capacitances were measured using CVs, four of which are shown in Fig. 2. (—) A curve fit through the data points.

200 but less than 300°C were taken to have 84% of the mass of the as-deposited material, and films heated at or above 300°C were taken to have 60% of the mass of the as-deposited material.

Although an as-deposited nickel hydroxide film exhibits a capacitor-like response when cycled between 0 and 0.30 V vs. SCE (see Fig. 2), it does not have a significant specific capacitance (4.7 F/g). As the material is heated, the specific capacitance remains fairly constant until the temperature reaches 300°C. At this temperature, the specific capacitance increases 22 times, to 104 F/g. This dramatic increase in capacitance at 300°C corresponds to the conversion of the hydroxide to the oxide according to Reaction 4. As the film is heated further, the specific capacitance of the oxide reduces until at 450°C the electrode does not store any useful capacity.

The significant change in the specific capacitance on heating can be caused by either (i) the formation of a high-surface-area material at ~300°C or (ii) pseudocapacitance due to oxide formation. In order to ascertain the cause of the dramatic increase in capacitance at 300°C, BET studies were conducted on bulk precipitated hydroxides at 150, 200, 275, 300, 350, and 400°C. The precipitation was conducted chemically as opposed to electrochemically since it is difficult to deposit electrochemically the requisite quantity of material needed for BET analysis. This is not to argue that the chemical and electrochemical methods yield identical materials, but rather to determine qualitatively how the surface area depends on the heating temperature.

The resulting surface area and intrinsic capacitance (*i.e.*, specific capacitance divided by the surface area) are shown in Fig. 4. The results show that heating the material from 150 to 200°C has a negligible effect on the surface area and intrinsic capacitance of the material. The intrinsic capacitance at these two heating temperatures was estimated to be 4.0  $\mu\text{F}/\text{cm}^2$ , a value consistent with charge storage across a double layer.<sup>4</sup> As the material is heated from 200 to 300°C, a 12% increase in surface area is observed, but the intrinsic capacitance increases by a factor of 17, to 68  $\mu\text{F}/\text{cm}^2$ . Further heating from 300 to 400°C causes the surface area to decrease from 153 to 86  $\text{m}^2/\text{g}$  (a 44% decrease) and the intrinsic capacitance to decrease from 68 to 31  $\mu\text{F}/\text{cm}^2$  (a 57% decrease).

The effect of the heating temperature on the surface area and the intrinsic capacitance suggests that the dramatic capacitance change at 300°C is due to the formation of NiO. Since the intrinsic capacitance of the NiO is too large to be explained by energy stored across the double layer, its capacitance must arise from the  $\text{Ni}^{2+}$  to  $\text{Ni}^{3+}$  redox reaction given by

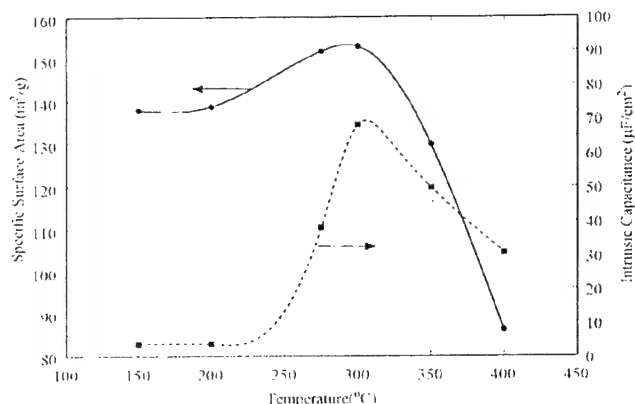
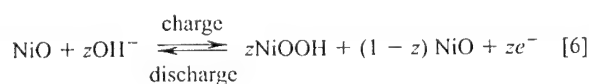


**Figure 4.** Specific surface area and intrinsic capacitance of nickel hydroxide that was previously heated to different temperatures. The surface area was measured from chemically precipitated material using BET. The lines are a curve fit through the data points.

Reaction 6 suggests that only a fraction of the nickel sites,  $z$ , are involved in the redox reaction (*i.e.*, when  $z$  equals 1.0 all the nickel sites have been oxidized/reduced reversibly).

The value of  $z$  can be estimated from the specific capacitance of the oxide film by the following relationship

$$z = \frac{CM\Delta V}{F} \quad [7]$$

Using Eq. 7, a potential window of 0.30 V, a molecular weight of 74.7 g/mol, and the specific capacitance from Fig. 3 gives a  $z$  value of 0.024 and 0.0062 at 300 and 400°C, respectively. In other words, at these respective temperatures only 2.5 and 0.62% of the nickel atoms participate in the reaction that produces the currents in Fig. 2.

These low values of  $z$  suggest that Reaction 6 is occurring only at the surface of NiO, with little bulk interaction. Unlike nickel hydroxide, where  $\text{H}^+$  intercalation into the active material is the mechanism of charge storage, the mechanism in the oxide seems to involve adsorption and reaction of  $\text{OH}^-$  ions at the surface. Considering the difference in size of  $\text{H}^+$  and  $\text{OH}^-$ , it is not surprising that there is little bulk interaction due to the diffusion of  $\text{OH}^-$  ions into the material. This is consistent with studies on cobalt oxide<sup>23</sup> and anodically deposited NiO,<sup>22</sup> which concluded that these materials involve predominantly surface redox sites. In contrast, a study conducted on hydrous ruthenium oxide<sup>6</sup> has concluded that this material exhibits significant bulk interactions, with a  $z$  value of approximately 0.85.

If, however, the decrease in specific capacitance above 300°C is only a BET surface-area phenomena, then the intrinsic capacitance shown in Fig. 4 would level off. Since this quantity is also decreasing, the fraction of surface sites participating in Reaction 6 must also be decreasing. In order to quantify this effect, the fraction of nickel atoms that reside on the surface of the active material,  $\xi$ , can be calculated from the following formula<sup>23</sup>

$$\xi = \frac{sM}{h^2L_A} \quad [8]$$

For NiO, the length of the crystal lattice,  $h$ , is 4.137 Å.<sup>24</sup> At 300 and 400°C,  $s = 153$  and 86  $\text{m}^2/\text{g}$  (see Fig. 4) resulting in  $\xi = 0.11$  and 0.062, respectively. Therefore, at 300 and 400°C, only 11 and 6.2% of the nickel atoms, respectively, are at the surface, and of those only 23 and 10%, respectively, are accessed during the CVs shown in Fig. 2 (*i.e.*,  $z/\xi = 0.23$  and 0.10, respectively). That the decrease is the percentage of surface sites accessed with temperature means that the electrochemically active surface area decreases at a greater rate than the BET surface area. This is probably due to the isolation of micropores that are no longer accessible to the electrolyte.

The optimum heating temperature of 300°C seen in Fig. 3 occurs when all the hydroxide is converted to oxide but before the electro-



chemically active surface area can be reduced due to sintering of the oxide particles. This optimum is independent of the subsequent cycling conditions (e.g., KOH concentration, potential window) since the predominant changes in microstructure occur during the heating process itself. The heating environment or heating rate, however, could influence the measured capacitance of the material by affecting the surface area or the extent of conversion of the hydroxide to the oxide. Liu and Anderson studied the capacitance of sol-gel-derived NiO films heated in different atmospheres<sup>8</sup> and concluded that air-fired samples show only a slightly higher capacitance compared to heating in pure nitrogen or oxygen. We performed selected experiments at a heating rate of 15°C/min, and no measurable difference in the capacitances or surface areas was detected. In addition, incomplete conversion of the hydroxide to the oxide is easy to detect by the presence of redox peaks in the CV due to Reaction 1. No such peaks were observed at heating temperatures of 300°C and above, indicating complete oxide conversion.

**Effect of the electrolyte concentration on the capacitance.**—The speculation that the charge-storage mechanism of the nickel-oxide film is due to redox Reaction 6 indicates that the significant capacitance should exist only in basic electrolytes. To confirm this hypothesis, experiments were conducted in sulfuric acid and the results compared to those conducted in potassium hydroxide. Figure 5 shows the CVs of two nickel hydroxide films heated to 300°C, one cycled in 3 wt % KOH and the other in 1 N H<sub>2</sub>SO<sub>4</sub>. The graph clearly indicates the enhanced charge-storage mechanism in basic electrolytes. The capacitance of the material cycled in sulfuric acid (16 F/g) was estimated to be one-sixth the value of the one cycled in KOH (155 F/g). Based on the surface area at 300°C (i.e., 153 m<sup>2</sup>/g), an intrinsic capacitance of 10.5 μF/cm<sup>2</sup> is obtained in sulfuric acid, a value consistent with double-layer capacitance.<sup>4</sup> Although previous studies on cycling single crystals of NiO in H<sub>2</sub>SO<sub>4</sub> have been reported to exhibit redox peaks due to the oxidation of Ni<sup>2+</sup> to Ni<sup>3+</sup> and Ni<sup>4+</sup>,<sup>25,26</sup> no such peaks are evident in Fig. 5. On longer cycles (~50 cycles), a redox peak grows in the CV shown in Fig. 5, consistent with the results of Tench and Yeager.<sup>26</sup> Note that the as-deposited film rapidly dissolves in sulfuric acid, while the film heated to 300°C has no apparent degradation, consistent with the results of Yohe *et al.*<sup>25</sup>

Reaction 6 also suggests that the charge-storage capacity of the film would increase with an increase in the concentration of OH<sup>-</sup> ions in solution. To test this hypothesis, CVs from -0.05 to 0.2 V vs. SCE were recorded over a wide range of KOH concentrations ranging from 0.5 wt % (0.09 M) to 40 wt % (7.1 M) KOH. The limit of

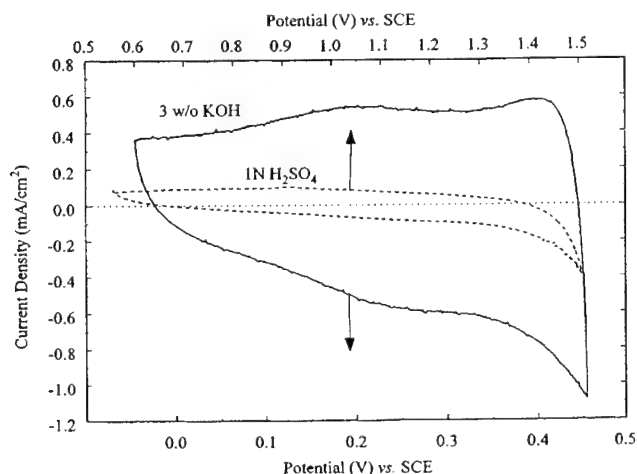
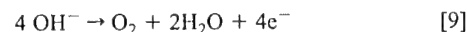


**Figure 5.** Cyclic voltammetry on nickel oxide films in: (—) 3 wt % KOH and (---) 1 N H<sub>2</sub>SO<sub>4</sub>. The oxide films were formed by heating nickel hydroxide to 300°C. The sweep rate was 5 mV/s, and the cathodic currents are positive. (····) Zero current.

0.2 V was chosen based on the fact that the oxygen evolution reaction according to



occurs at ~0.25 V in 40 wt % KOH (see Fig. 8). Note that there is a 50 mV decrease in the equilibrium potential of the oxygen evolution reaction when the KOH concentration increases from 0.5 to 40 wt %, as predicted using the Nernst equation for Reaction 9.

Figure 6 shows the specific capacitance as a function of the KOH concentration calculated from the CVs in conjunction with Eq. 5. In Fig. 6, the open circles represent the first set of experiments, where the capacity of the film was estimated at successively increasing concentrations from 0.5 to 40 wt % KOH. The triangles represent the data when the concentration was successively decreased from 40 to 0.5 wt % KOH on the same film. The data points shown in the figure are an average of four experiments on four different films. A clear hysteresis is observed between the two sets of data, indicating that some irreversible changes occurred in the film as the concentration was increased. However, subsequent experiments, involving both increasing and decreasing the concentration on the same film, resulted in capacities within 5% of that obtained in the second data set (i.e., triangles in Fig. 6). Therefore, the second data set also represents the reversible capacity vs. concentration data. Note that the capacitance at 3 wt % KOH (i.e., 0.54 M) reported in Fig. 6 is lower than the 300°C data reported in Fig. 3 due to the potential-dependent capacitance of the material. The smaller potential window used to generate the data in Fig. 6 results in a small capacitance.

From Reaction 6, one can formulate a rate expression of the form<sup>27</sup>

$$r = k_f[\text{NiO}]^a[\text{OH}^-]^b - k_b[\text{NiOOH}]^c \quad [10]$$

Assuming that the number of available nickel sites is independent of the OH<sup>-</sup> concentration, differentiating the rate with respect to [OH<sup>-</sup>] yields

$$\frac{dr}{d[\text{OH}^-]} = k_f b [\text{NiO}]^a [\text{OH}^-]^{b-1} \quad [11]$$

Since the specific capacitance data in Fig. 7 were obtained over a fixed time interval (i.e., potential window divided by the sweep rate), they are related to the rate of reaction by the expression

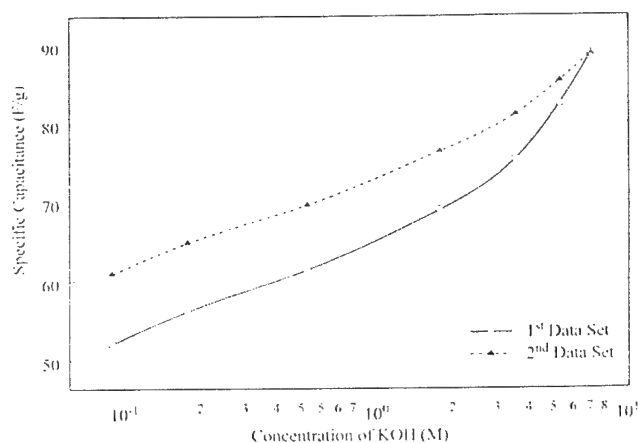


**Figure 6.** Specific capacitance of nickel oxide films as a function of KOH concentration. The oxide films were formed by heating nickel hydroxide to 300°C. The data points are an average of four experiments on four different films. The first data set is the specific capacitance on films when the concentration was increased consecutively from 0.5 to 40 wt % KOH (i.e., 0.09–7.1 M KOH). The second data set is the specific capacitance when the concentration was decreased from 40 to 0.5 wt % KOH on the same film. Subsequent experiments, involving both increasing and decreasing the concentration on the same film, resulted in capacities within 5% of that represented by the triangles. The lines are a curve fit through the data points.

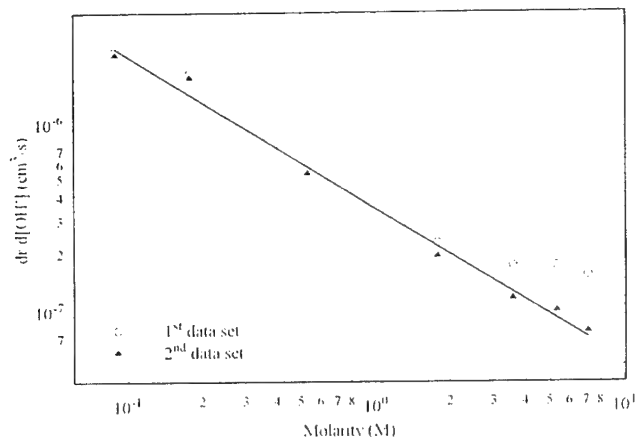


**Figure 7.** The derivative in the nickel redox reaction rate with respect to the KOH concentration as a function of KOH concentration. The rate data were derived by combining the capacitance data in Fig. 6 with Eq. 12. The derivative was calculated at each KOH concentration using finite differences. The data points are an average of four data sets. The line is the best fit of Eq. 11 through the second data set. The slope of the line gives  $b = 0.2$ .

$$r = \frac{C_{vm}}{F} \quad [12]$$

with the assumption that one electron is transferred for every mole of nickel reacted. Therefore, the specific capacitance in Fig. 6 is converted to rate using Eq. 12, and the slope,  $dr/d[\text{OH}^-]$ , is calculated at each KOH concentration using finite differences.<sup>28</sup> A plot of the logarithm of  $dr/d[\text{OH}^-]$  vs. the logarithm of the KOH concentration is shown in Fig. 7. The circles and triangles correspond to the first and second data sets shown in Fig. 6. The line is the best fit through the triangular data points. The slope of the line is  $(b-1)$ , which gives the reaction order with respect to the  $\text{OH}^-$  concentration of 0.2. The intercept is related to the rate constant of the forward reaction, the order with respect to the NiO sites, the number of sites, and the order with respect to  $\text{OH}^-$ .

The best fit of Eq. 11 through the data is the same for both data sets as long as the three highest concentrations for the first data are ignored. The straight line through the data in Fig. 7 suggests that the total number of Ni sites available for reaction is independent of the  $\text{OH}^-$  concentration. It is possible that at high KOH concentrations the number of Ni sites increases for the first data set, which results in the deviation of the points from the straight line. Such an increase in the number of Ni sites could result from an increase in the surface area of the film at high KOH concentrations, a change that can be expected to be irreversible. However, this irreversible change in structure has no effect on the order of the reaction, which is evident from the relatively constant slope between the two experiments. Once the material has been cycled in high KOH concentrations, the capacitance vs. concentration appears to be reversible and follows a straight line represented by the triangles.

**Effect of the potential window on electrode operation.**—The fact that only 23% of the surface sites are used when the material is heated to 300°C and cycled in 3 wt % KOH is due in part to the limited potential window used. If the anodic limit of the potential window is increased from 0.30 to 0.45 V, the specific capacitance increases from 103 to 132 F/g. This translates into an increase in the percentage of surface sites accessed from 23 to 30%. If the anodic limit of the potential window is decreased to 0.20 V, the specific capacitance decreases to 62 F/g (see triangle at 0.54 M KOH in Fig. 6), and only 14% of the surface sites are accessed. Therefore, increasing the anodic potential limit, holding the electrolyte concentration constant, increases the capacitance.

In addition, the data in Fig. 6 indicates that increasing the KOH concentration, holding the anodic potential limit constant, increases

the capacitance. In practice, however, these two variables are coupled. Lower KOH concentrations result in an increase in the anodic potential limit of the electrode, since oxygen evolution occurs at more positive potentials. This increase would enhance the energy-storage capability of the positive electrode, since the capacitance increases with potential and the energy of a capacitor scales as the square of the potential. In order to demonstrate how the KOH concentration and potential window are coupled, CVs were generated with a fixed cathodic limit of  $-0.55$  V but with an anodic limit adjusted to limit the oxygen evolution current at  $\sim 1$  mA/cm<sup>2</sup>. Figure 8 shows the CVs at three different concentrations on a film heated to 300°C. By placing a limit on the amount of oxygen generated, an increase in the KOH concentration results in a decrease in the anodic potential limit and a resulting decrease in the specific capacitance. For example, using only the most positive 0.30 V in Fig. 8, a specific capacitance of 142 F/g is obtained in 3 wt % KOH compared to 130 F/g in 40 wt % KOH. The lower KOH concentrations enable us to access the higher capacitances that are seen at higher potentials. Figure 8 also demonstrates that NiO is best suited as a positive electrode. For example, in 3 wt % KOH the capacitance of NiO is five times larger in the potential window 0.0 to 0.45 V vs. SCE compared to the potential window  $-0.5$  to 0.0 V vs. SCE.

The effect of the KOH concentration on the overall potential window of the device depends on the choice of the negative electrode, and subsequently, the sensitivity of hydrogen evolution kinetics to KOH concentration. Another factor that must be considered when determining the optimum KOH concentration for a device is the power density. Higher KOH concentrations have greater conductivity (the conductivity of KOH is a maximum at 33 wt %) and hence lead to higher power densities.

### Conclusion

Nickel oxide films were fabricated by electrochemically precipitating the hydroxide and heating it to form the oxide. While nickel hydroxide cycled to 0.45 V vs. SCE behaves as a battery material due to the proton intercalation reaction, the hydroxide cycled to 0.30 V or the oxide cycled to 0.45 V behaves as a capacitor. The specific capacitance (capacitance per unit mass) of the films was measured as a function of the heating temperature in 3 wt % KOH and over a potential window where no proton intercalation occurs. A negligible increase in specific capacitance was observed as the heating temperature was increased from 25 to 200°C. However, when the heating temperature was increased to 300°C, the specific capacitance increased by a factor of 22.

The large rise in capacitance at 300°C corresponds to the temperature at which the hydroxide is converted to the oxide. Heating to

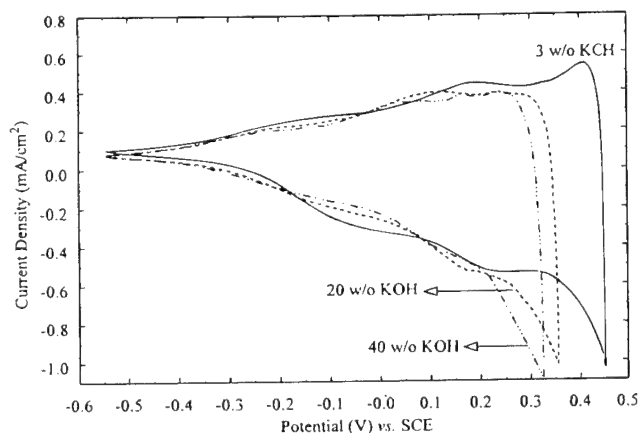


**Figure 8.** Cyclic voltammetry on a nickel oxide film in different KOH concentrations. The oxide film was formed by heating nickel hydroxide to 300°C. The voltammograms were reversed at the anodic potential limit when the current reached  $\sim 1$  mA/cm<sup>2</sup>. The sweep rate was 20 mV/s. (---) Zero current.

temperatures above 300°C results in a decrease in the BET surface area and a decrease in the intrinsic capacitance (capacitance per unit BET surface area) of the nickel oxide. Since the intrinsic capacitance decreases with heating temperature, electrochemically active surface area is decreasing faster than the BET surface area. This is probably due to the isolation of micropores that are no longer accessible to the electrolyte.

The large intrinsic capacitance for the oxide suggests that the charge storage is due to a surface redox reaction (*i.e.*, pseudocapacitance), probably involving the adsorption of hydroxyls rather than from a double layer. This was confirmed by cycling the material in different electrolyte environments. In 1 N H<sub>2</sub>SO<sub>4</sub>, pseudocapacitance was not observed. In KOH, the pseudocapacitance increased with concentration with an estimated reaction order of 0.2, while holding the potential window constant.

Finally, the capacitance of nickel oxide was found to be a strong function of the potential window of operation. Its capacitance was five times larger in the potential window 0.0 to 0.45 V vs. SCE compared to the potential window -0.5 to 0.0 V vs. SCE, thus making the material best suited as a positive electrode in devices. The potential-dependent capacitance also resulted in a capacitance that decreased with KOH concentration when a fixed oxygen evolution rate was used to determine the anodic potential limit rather than a fixed potential.

#### Acknowledgments

The authors gratefully acknowledge financial support from the U.S. Department of Energy under Cooperative Agreement no. DE-FC02-91ER75666 and the U.S. Department of Defense under grant no. DAAH04-96-1-0421. Discussions with Professor Bahne Cornilsen (Michigan Technological University) on the structure and chemistry of nickel hydroxide are gratefully acknowledged.

The University of South Carolina assisted in meeting the publication costs of this article.

#### List of Symbols

$a$	order of reaction with respect to NiO
$b$	order of reaction with respect to KOH
$c$	order of reaction with respect to NiOOH
$C$	specific capacitance, F/g
$F$	Faraday constant, 96,487 C/equiv
$h$	length of crystal lattice, cm
$I$	current, A
$k_b$	reverse reaction rate constant for Reaction 6, cm s <sup>-1</sup> (mol/cm <sup>3</sup> ) <sup>1-c</sup>
$k_f$	forward reaction rate constant for Reaction 6, cm s <sup>-1</sup> (mol/cm <sup>3</sup> ) <sup>1-a-b</sup>
$L_A$	Avogadro number, 6.023 × 10 <sup>23</sup> mol <sup>-1</sup>
$m$	mass of the film, g
$M$	molecular weight, g/mol
$r$	rate of reaction, mol/cm <sup>3</sup> s
$s$	specific surface area, cm <sup>2</sup> /g
$V$	potential, V
$V_a$	anodic potential limit in a CV, V
$V_c$	cathodic potential limit in a CV, V

$z$	fraction of nickel atoms involved in the redox process
$\Delta V$	potential window, V
Greek	
$\nu$	sweep rate, V/s
$\xi$	fraction of nickel atoms on the surface

#### References

1. B. E. Conway, *J. Electrochem. Soc.*, **138**, 1539 (1991).
2. S. Trassati and P. Kurzweil, *Platinum Met. Rev.*, **38**, 46 (1994).
3. S. Sarangapani, B. V. Tilak, and C.-P. Chen, *J. Electrochem. Soc.*, **143**, 3791 (1996).
4. A. J. Bard and L. R. Faulkner, *Electrochemical Methods: Fundamentals and Applications*, John Wiley & Sons, Inc., New York (1980).
5. S. T. Mayer, R. W. Pekela, and J. L. Kaschmitter, *J. Electrochem. Soc.*, **140**, 446 (1993).
6. J. P. Zheng, P. J. Cygan, and T. R. Jow, *J. Electrochem. Soc.*, **142**, 2699 (1995).
7. B. E. Conway, in *Electrochemical Capacitors*, F. M. Delnick and M. Tomkiewicz, Editors, PV 95-29, p. 15, The Electrochemical Society Proceedings Series, Pennington, NJ (1995).
8. K.-C. Liu and M. A. Anderson, in *Electrochemical Capacitors*, F. M. Delnick and M. Tomkiewicz, Editors, PV 95-29, p. 68, The Electrochemical Society Proceedings Series, Pennington, NJ (1995).
9. K.-C. Liu and M. A. Anderson, *J. Electrochem. Soc.*, **143**, 124 (1996).
10. K.-C. Liu and M. A. Anderson, in *Electrochemical Capacitors II*, F. M. Delnick, D. Ingersoll, X. Andrieu, and K. Naoi, Editors, PV 96-25, p. 97, The Electrochemical Society Proceedings Series, Pennington, NJ (1996).
11. K.-C. Liu and M. A. Anderson, in *Electrochemical Capacitors II*, F. M. Delnick, D. Ingersoll, X. Andrieu, and K. Naoi, Editors, PV 96-25, p. 85, The Electrochemical Society Proceedings Series, Pennington, NJ (1996).
12. V. Srinivasan and J. W. Weidner, *J. Electrochem. Soc.*, **144**, L210 (1997).
13. C. C. Streinz, A. P. Hartman, S. Motupally, and J. W. Weidner, *J. Electrochem. Soc.*, **142**, 1084 (1995).
14. C. C. Streinz, S. Motupally, and J. W. Weidner, *J. Electrochem. Soc.*, **143**, 4051 (1995).
15. P. L. Loyselle, P. J. Karjala, and B. C. Cornilsen, in *Electrochemical and Thermal Modeling of Battery: Fuel Cell and Photocenergy Conversion Systems*, R. J. Selman and H. C. Maru, Editors, PV 86-12, p. 114, The Electrochemical Society Proceedings Series, Pennington, NJ (1986).
16. B. Cornilsen, X. Cai, R. Tanbug, and G. Meitzner, in *Aqueous Batteries*, P. D. Bennett and S. Gross, Editors, PV 96-16, p. 88, The Electrochemical Society Proceedings Series, Pennington, NJ (1997).
17. Z. Xu, B. C. Cornilsen, and G. Meitzner, in *Selected Battery Topics*, G. Halpert, M. L. Gopikanth, K. M. Abraham, W. R. Cieslak, and W. A. Adams, Editors, PV 98-15, p. 1, The Electrochemical Society Proceedings Series, Pennington, NJ (1999).
18. M. Mani and J. P. deNeufville, *J. Electrochem. Soc.*, **135**, 800 (1988).
19. C. Natarajan, H. Motsumoto, and G. Nagomi, *J. Electrochem. Soc.*, **144**, 121 (1997).
20. V. Srinivasan, B. C. Cornilsen, and J. W. Weidner, in *Selected Battery Topics*, G. Halpert, M. L. Gopikanth, K. M. Abraham, W. R. Cieslak, and W. A. Adams, Editors, PV 98-15, p. 31, The Electrochemical Society Proceedings Series, Pennington, NJ (1999).
21. D. A. Wruck and M. Rubin, *J. Electrochem. Soc.*, **140**, 1097 (1993).
22. S. Cordoba-Torres, A. Hugot-Le Goff, and S. Joiret, *J. Electrochem. Soc.*, **138**, 1554 (1991).
23. C. Lin, J. A. Ritter, and B. N. Popov, *J. Electrochem. Soc.*, **145**, 4097 (1998).
24. *CRC Handbook of Chemistry and Physics*, CRC Press, Inc., Boca Raton, FL (1979).
25. D. Yohe, A. Riga, R. Greef, and E. Yeager, *Electrochim. Acta*, **13**, 1351 (1968).
26. D. M. Tench and E. Yeager, *J. Electrochem. Soc.*, **120**, 164 (1973).
27. O. Levenspiel, *Chemical Reaction Engineering*, John Wiley & Sons, Inc., New York (1972).
28. S. C. Chapra and R. P. Canale, *Numerical Methods for Engineers*, 2nd ed., McGraw-Hill, Inc., New York (1988).

# Ni-Composite Microencapsulated Graphite as the Negative Electrode in Lithium-Ion Batteries

## I. Initial Irreversible Capacity Study

P. Yu,\* J. A. Ritter,\*\* R. E. White,\*\*\* and B. N. Popov\*\*\*<sup>‡</sup>

Center for Electrochemical Engineering, Department of Chemical Engineering, University of South Carolina, Columbia, South Carolina 29208, USA

A novel approach for suppressing the solvated lithium intercalation in graphite was developed by microencapsulating graphite with nanosized Ni-composite particles. The Ni-composite graphite showed great improvement in charge-discharge performance, coulomb efficiency, and cycling behavior when used as the negative electrode in a Li-ion cell with propylene carbonate (PC)-based electrolyte. For example, a 10 wt % Ni-composite coating increased the initial charge-discharge coulomb efficiency of SFG75 graphite (75  $\mu\text{m}$ , Timcal America) from 59 to 84% and the reversible capacity by 30–40 mAh/g. The Ni-composite coating consisted of nanosized particles distributed over the surface of the graphite particle, which effectively blocked some of the edge surfaces exposed to the electrolyte. This minimized solvated lithium intercalation at these edge sites, which subsequently minimized the PC reduction within the graphite and the exfoliation of the graphene layers, and also gas evolution. Corresponding improvements in both the charge-discharge performance and safety of the negative electrode in a rechargeable Li-ion cell resulted. © 2000 The Electrochemical Society. S0013-4651(99)08-113-6. All rights reserved.

Manuscript submitted August 27, 1999; revised manuscript received November 22, 1999.

Since Sony introduced the first commercial cell in 1990 that used a carbon material in lieu of lithium metal as the negative electrode,<sup>1</sup> rechargeable Li-ion batteries have become readily available worldwide. Of various carbon materials, graphite is favored because it exhibits a high specific capacity, a most desirable charge potential profile, and superior cycling behavior. However, the irreversible reactions that take place with lithium during the first cycle have been one of the very persistent problems associated with the use of graphite. In commercial Li-ion cells, the loss of lithium due to these irreversible reactions is normally compensated for by using excess cathode material, however, this leads to a decrease in the specific energy density and thus an increase in the cell cost.<sup>2,3</sup> These irreversible reactions can also cause gas evolution, which may result in some very serious safety issues, such as cell can buckling, cell venting, electrolyte spillage, and even fire.<sup>2,4</sup>

It is widely known<sup>2–5</sup> that the irreversible capacity can originate from electrolyte decomposition followed by the formation of a solid electrolyte interface (SEI) film on the external surface of the graphite. However, it can also arise from solvated lithium intercalation between the graphene layers and subsequent reduction of the solvent,<sup>6–7</sup> because the formation of a solvated lithium/graphite compound like  $\text{Li}_x(\text{sol})\cdot\text{C}_6$  is more favorable than the formation of  $\text{Li}_x\text{C}_6$  during insertion.<sup>6</sup> The irreversible capacities in both cases are largely dependent on the external surface area of the electrode,<sup>6</sup> because the exposed surface is where the irreversible reactions take place. In fact, it has been shown that the irreversible capacity associated with the edge surfaces of graphite is substantially larger than that associated with the basal plane surfaces due to solvent cointercalation into the layer spacing.<sup>7</sup>

The irreversible capacity associated with the use of graphite also varies considerably with different electrolytes, and especially with different solvents. It has been shown<sup>7–9</sup> that the irreversible reactions are worse in propylene carbonate (PC)-based electrolyte than in ethylene carbonate (EC)-based electrolyte, and PC alone can cause severe degradation of the graphite structure by a process called “exfoliation.”<sup>7–11</sup> The results by Ogumi *et al.*<sup>12</sup> indicated that PC begins to decompose at *ca.* 1 V vs.  $\text{Li/Li}^+$  and continues to decompose during the remainder of the intercalation process. It has further been suggested that this decomposition occurs continuously without forming

a stable passive SEI layer on the edge surfaces of the graphite particles.<sup>7–11</sup> The net effect is that the PC solvent continuously cointercalates with Li-ions into the graphene layers and subsequently reduces, which gives rise to a large irreversible capacity during cycling.<sup>9,11</sup> Nevertheless, PC is still attractive for use as an electrolyte in Li-ion batteries, especially for low-temperature operation, because of its high salt solubility and low melting point ( $-55^\circ\text{C}$ ).

Recently, some attempts to suppress the irreversible solvated lithium intercalation into graphite have been made by adding inorganic agents such as  $\text{CO}_2$ ,<sup>13</sup>  $\text{NO}_2$ ,<sup>14</sup> and  $\text{SO}_2$ ,<sup>15</sup> or organic agents such as crown ethers to the electrolyte.<sup>12,16</sup> These additives contribute to the formation of a less permeable SEI film which effectively decreases the diffusion of solvated lithium ions through the surface of the graphite, but these additives still induce some irreversible capacity in the first cycle because they also react with lithium. Another approach that has been reported<sup>17</sup> is to electrochemically reduce EC on the external surface of the graphite particles to cover them with an effective SEI film prior to use in the PC electrolyte. With these works in mind, this two-part series reports on the development of a novel Ni-composite-coated graphite material that minimizes the initial irreversible capacity in a Li-ion cell.

Three types of graphite materials were coated with Ni-composite particles using a microencapsulation technique. In Part I of this series, the effect of the Ni coating on reducing the initial irreversible capacity is revealed, based on using galvanostatic, cyclic voltammetry, scanning electron microscopy (SEM) and Brunauer-Emmett-Teller (BET) surface area results obtained with both bare and Ni-coated graphite materials. Part II of this series reports on electrochemical impedance and self-intercalation studies with the same materials.

## Experimental

Three types of synthetic graphite, G1 (1  $\mu\text{m}$  Aldrich), KS10 (10  $\mu\text{m}$  Timcal America), and SFG75 (75  $\mu\text{m}$  Timcal America), were used as received. The microencapsulation of these graphites with Ni composite was carried out at 85–90°C for 0.5 h in a plating bath containing sodium hypophosphite as a reducing agent. The procedure has been described in detail elsewhere.<sup>18</sup> After deposition, the concentration of nickel in the plating solution was analyzed by ethylenediaminetetraacetic acid (EDTA) complexometric titration.<sup>19</sup> In this work, 3, 5, 8, 10, and 25 wt % Ni composites were deposited on KS10 graphite, while 10 wt % Ni composites were deposited on G1 and SFG75 graphites. Following the deposition process, the graphites were washed with deionized water and dried at 90°C overnight in a vacuum oven.

\* Electrochemical Society Student Member.

\*\* Electrochemical Society Active Member.

\*\*\* Electrochemical Society Fellow.

<sup>‡</sup> E-mail: popov@engr.sc.edu

The electrochemical characterizations were carried out in Swagelok three-electrode T-cells. A typical graphite negative electrode was prepared by mixing graphite powder with 6 wt % poly(vinylidene fluoride) (PVDF, Aldrich) powder and 1-methyl-2-pyrrolidinone solvent. The resulting slurry was roller pressed onto a stainless steel current collector and dried under vacuum at 150°C for 12 h. The resulting pellet was approximately 95  $\mu\text{m}$  thick and weighed about 10 mg. The counter and reference electrodes were made of Li foil (99.9%, Aldrich), and a sheet of Whatman glass fiber membrane (Baxter Diagnostics Co.) was used as a separator. The electrolyte used consists of 1 M  $\text{LiPF}_6$  in a 1:1:3 mixture of PC/EC/dimethyl carbonate (DMC) with less than 15 ppm  $\text{H}_2\text{O}$  and 80 ppm HF (EM, Inc.). Also, an electrolyte consisting of 1 M  $\text{LiPF}_6$  in a 1:1 mixture of EC/DMC with less than 15 ppm  $\text{H}_2\text{O}$  and 80 ppm HF (EM, Inc.) was used for comparison and also as received. The procedure for the fabrication of the electrodes and the Li-ion cells are described in detail elsewhere.<sup>20</sup> The charge-discharge behavior of each T-cell was investigated using an Arbin Battery Test (BT-2043) system at a current of 0.5 mA (C/8 rate) with cutoff potentials of 0.005 and 2 V vs.  $\text{Li/Li}^+$ . Cyclic voltammograms (CVs) were obtained using a scan rate of 0.05 mV/s. The surface images of the bare KS10 graphite and Ni-composite KS10 prior to any charge-discharge cycles were taken using a Hitachi S-2500 Delta scanning electron microscope. A Micromeritics Pulse Chemisorb 2700 was used to obtain the specific surface areas based on the single-point, BET method. Each sample was dried in a flowing stream of argon at 200°C for 1 h prior to the BET measurement.

## Results and Discussion

**Initial Charge-Discharge Behavior of KS10 in 1 M  $\text{LiPF}_6$ /EC/DMC and 1 M  $\text{LiPF}_6$ /PC/EC/DMC electrolytes.**—To identify the contribution of the PC solvent to the initial irreversible capacity, especially the irreversible capacity related to solvated lithium intercalation, bare KS10 was cycled in 1 M  $\text{LiPF}_6$ /EC/DMC and 1 M  $\text{LiPF}_6$ /PC/EC/DMC electrolytes separately. The first cycle charge-discharge curves are given in Fig. 1.

Although the deintercalation capacities for KS10 are about the same in both electrolytes (approximately 300 mAh/g), the first lithium intercalation capacity in the PC/EC/DMC electrolyte is much larger at 742 mAh/g compared to that in EC/DMC electrolyte at 399.7 mAh/g. Moreover, the capacities between 0.56 and 0.2 V vs.  $\text{Li/Li}^+$ , which correspond to solvated lithium intercalation,<sup>6</sup> are 338.3 and 55.2 mAh/g in PC/EC/DMC and EC/DMC electrolytes, respectively. Although a quantitative comparison is not possible, because of the different amounts of EC/DMC used in each electrolyte, it is clear that the large irreversible capacity in the PC/EC/DMC electrolyte is caused by PC reduction, with a minor contribution from EC decomposition. Therefore, the remaining experiments were

all carried out in 1 M  $\text{LiPF}_6$ /PC/EC/DMC electrolyte to investigate the effect of microencapsulating graphite particles with Ni-composite on the initial irreversible capacity arising from both PC and EC.

**Initial charge-discharge behavior of Ni-composite KS10.**—The galvanostatic first discharge-charge cycles for bare and Ni-composite KS10 were carried out using a current of 0.5 mA (rate of C/8) with the cutoff potential range set between 0.005 and 2 V vs.  $\text{Li/Li}^+$ . Note that the capacity was based on the total weight of the negative electrode. Figure 2a and b illustrate the first cycle discharge-charge curves for bare KS10 and KS10 containing different amounts of Ni composite. Three discontinuities, denoted by points A, B, and C in Fig. 2a, are observed in the intercalation profile for bare KS10 at 0.71, 0.56, and 0.2 V vs.  $\text{Li/Li}^+$ , respectively. The curves above and below these points exhibit different slopes, which indicates that different electrochemical reactions are taking place within these potential ranges. According to Winter's classification,<sup>6</sup> the region AB between 0.56 and 0.71 V vs.  $\text{Li/Li}^+$  corresponds to electrolyte decomposition/SEI film formation, the region BC between 0.2 and 0.56 V vs.  $\text{Li/Li}^+$  is mainly related to solvated lithium intercalation and reduction, and the region CD below 0.2 V vs.  $\text{Li/Li}^+$  is associated with lithium-graphite intercalation compound (Li-GIC) formation. The capacities arising from electrolyte decomposition and solvated lithium intercalation are irreversible and cannot be recovered during subsequent cycles. For bare KS10, about 35 mAh/g of initial intercalation capacity is produced in region AB, while 338 mAh/g of capacity is produced in region BC, reflecting that 4.7 and 45.6% of the total intercalation capacity of 740.4 mAh/g are consumed by SEI film for-

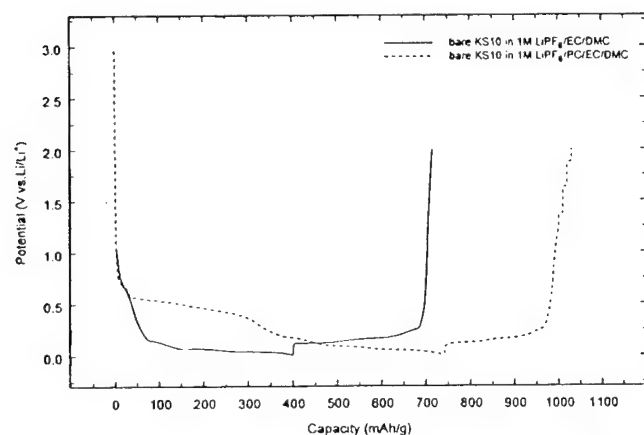


Figure 1. Initial charge-discharge profiles for bare KS10 graphite in PC/EC/DMC (ratio of 1:1:3) and EC/DMC (ratio of 1:1) electrolytes (C/8 charge-discharge rate).

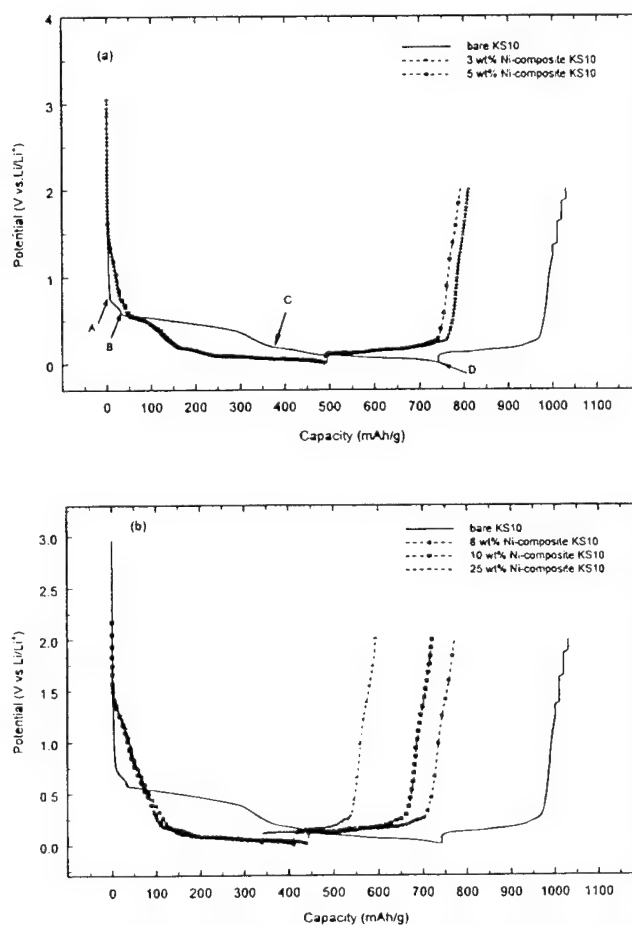
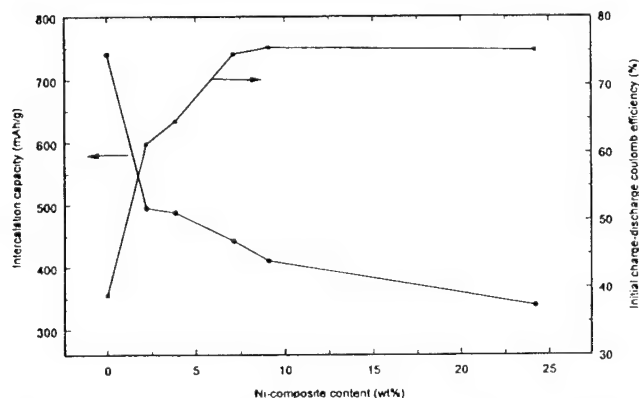


Figure 2. Galvanostatic first cycle discharge-charge curves for bare KS10 graphite and KS10 graphite coated with different amounts of Ni composite in 1 M  $\text{LiPF}_6$ /PC/EC/DMC electrolyte (C/8 charge-discharge rate).

mation and solvated lithium intercalation, respectively. Clearly, in this case, the main irreversible capacity arises from solvated lithium intercalation inside the graphite layers rather than electrolyte decomposition on the external surface. In fact, the huge solvated lithium intercalation capacity produced in KS10 may be due to the large edge surface area of KS10.<sup>6</sup> When 3 or 5 wt % Ni composite is deposited on KS10, the plateau observed between 0.2 and 0.56 V vs.  $\text{Li/Li}^+$  of the first intercalation curve is decreased dramatically, but can still be observed in Fig. 2a. However, Fig. 2b shows that after 8 wt % Ni-composite is deposited on KS10, the plateau totally disappears on the first intercalation curve, with essentially the same behavior exhibited by the 10 and 25 wt % Ni-composites. These results reveal that microencapsulation of Ni composite on graphite is favorable for reducing the solvated lithium intercalation inside graphite. This is shown very clearly in Fig. 3, which displays the initial intercalation capacity ( $C_{\text{int}}$ ) and initial discharge-charge coulomb efficiencies, both as functions of the Ni-composite content.

With a 3 wt % Ni-composite coating on KS10, the initial intercalation capacity of KS10 substantially decreases from 740.4 to 494.6 mAh/g and the initial intercalation-charge coulomb efficiency increases from 38.8 to 61.3%. These marked improvements result from the decreased solvated lithium intercalation as shown in Fig. 2. When the Ni-composite coating increases from 3 to 10 wt %, more of the solvated lithium intercalation reaction is suppressed and hence the initial intercalation capacity continues decreasing while the initial discharge-charge efficiency continues increasing. However, after a 10 wt % Ni-composite coating is deposited, the initial charge-discharge efficiency curves level off, while the initial intercalation capacity continues to decrease. The leveling off of the coulomb efficiency indicates that a 10 wt % Ni-composite coating is sufficient to cover the graphite surface and suppress the solvated lithium intercalation. In contrast, the continuously decreasing initial intercalation capacity indicates a decrease in the amount of useful material for reversible Li intercalation in the Ni-composite KS10 graphite. Thus, the optimum coating is obtained with the 10 wt % Ni-composite coating on KS10 graphite, which exhibits a maximum discharge-charge coulomb efficiency of about 76% with a corresponding intercalation capacity of 410 mAh/g.

To further investigate the effect of Ni composite on the irreversible capacity of different graphites, two other types of graphite with different particle sizes and shapes were each coated with a 10 wt % Ni composite. The particle sizes of the G1 and SFG75 graphites are 1 and 75  $\mu\text{m}$ , respectively. The G1 graphite particles are also round, whereas the SFG75 graphite particles are flat and flaky.<sup>6</sup> The initial charge-discharge profiles of the 10 wt % Ni-composite G1 and SFG75 are depicted in Fig. 4a and b, respectively. Both the bare G1 and SFG75 exhibit plateaus between 0.22 and 0.62 V vs.  $\text{Li/Li}^+$ , which were shown previously to be associated with solvated lithium intercalation.



**Figure 3.** Initial intercalation capacities and charge-discharge coulomb efficiencies extracted from Fig. 2 as a function of the Ni-composite content of the KS10 graphite.

Since there are more edge surfaces in G1 than in SFG75,<sup>6</sup> the irreversible capacity corresponding to the plateau region between 0.22 and 0.62 V vs.  $\text{Li/Li}^+$  in the G1 graphite is larger than that in the SFG75 graphite. However, these plateau regions are clearly depressed when G1 and SFG75 graphite are microencapsulated with Ni composite, and as expected, lowering the irreversible capacity associated with solvated lithium intercalation also gives rise to the improved discharge-charge coulomb efficiency. The initial charge-discharge coulomb efficiencies for bare G1 and SFG75 are 35 and 59%, respectively, while the efficiencies for Ni-composite G1 and SFG75 are increased to 59 and 84%, respectively. Therefore, even for three different types of graphite, a Ni-composite coating significantly reduces or suppresses the initial irreversible reactions, which greatly improves the initial discharge-charge performance compared to the bare graphite precursors.

Note that a small plateau appears at 1.5 V vs.  $\text{Li/Li}^+$  in Fig. 2, 3, and 4 for all Ni-composite coated graphites. This plateau is located in the potential region corresponding to water reduction. Since microencapsulation of the graphite with Ni-composite was carried out in an aqueous solution, the coated graphite possibly contains a trace amount of water that cannot be removed by moderate heating. The reduction of trace water during the first intercalation process has been confirmed by Christie and Vincent.<sup>21</sup> Their results show that the reduction of trace water occurs at 1.44 V vs.  $\text{Li/Li}^+$ , which is close to the plateaus observed in Fig. 2a and Fig. 4. The water reduction was also observed by Dautzenberg *et al.*<sup>22</sup> and Pletcher *et al.*<sup>23</sup>

**Cyclic voltammograms.**—To further illustrate how the Ni-composite coating affects graphite performance, cyclic voltammetry was

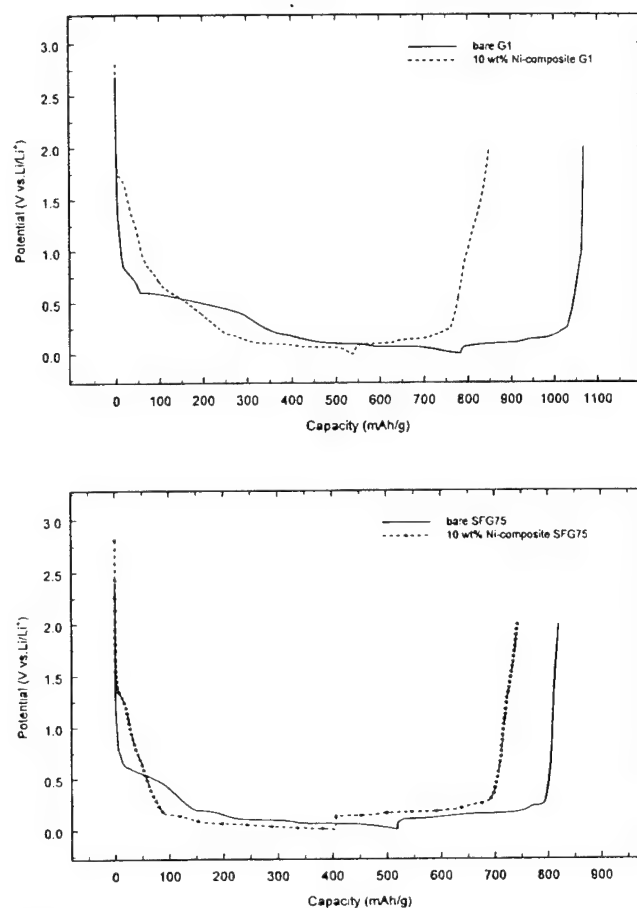


**Figure 4.** Initial charge-discharge profiles for (a, top) bare G1 graphite and Ni-composite G1 graphite and (b, bottom) bare SFG75 graphite and Ni-composite SFG75 graphite (C/8 charge-discharge rate).



performed on bare and Ni composite KS10 with the same samples as in Fig. 2. Figure 5a shows the CVs for the first cycle which were obtained using a scan rate of 0.05 mV/s with the cutoff potentials set between 0.005 and 1.5 V. In Fig. 5a, two reduction peaks for the bare KS10 are observed in the cathodic curve at 0.2–0.6 V and at 0.6–0.9 V vs.  $\text{Li/Li}^+$ . These peaks do not appear in the anodic curve, indicating that irreversible reactions are taking place in these two potential ranges. They are also in the same potential ranges as the plateaus in Fig. 2, confirming that the irreversible reactions occur during the initial intercalation process. The intercalation capacities

of bare KS10 corresponding to these two peaks are 309.8 and 36.9 mAh/g, respectively. These values are comparable to the values obtained in Fig. 2 for bare KS10. In other words, the intercalation capacity associated mainly with solvated lithium intercalation is 8.4 times larger than the intercalation capacity corresponding to the irreversible reactions occurring on the external surface. Moreover, bare KS10 clearly fails in inhibiting the solvated lithium intercalation. However, with a 3 wt % Ni-composite coating on KS10, the peak between 0.2 and 0.6 V vs.  $\text{Li/Li}^+$  (Fig. 5b) decreases dramatically. When increasing the Ni-composite content even further from 3 to 8 wt %, this peak gradually disappears and does not return even for Ni-composite contents up to 25 wt % (Fig. 5c). These results again suggest that around a 10 wt % Ni-composite coating is sufficient to suppress the solvated lithium intercalation reaction. The capacities corresponding to these potential ranges are summarized in Table I. Comparing the bare KS10 with the 3 wt % Ni-composite KS10 shows that the capacity associated with solvated lithium intercalation decreases from 309.8 to 144.2 mAh/g; this corresponds to recovering or saving 53.4% of the lost capacity. This trend of recovering more of the lost capacity continues with increasing Ni-composite content, up to recoveries slightly higher than 85%.

One point that must be mentioned is that there was no gas evolution in the T-cells using 10 wt % Ni-composite KS10 or 10 wt % Ni-composite SFG75, while there was always gas evolution in the T-cells using bare KS10 or bare SFG75. Since gas evolution is mainly caused by electrolyte reduction, especially solvent reduction, the absence of gas evolution is a strong indication that the irreversible reactions, especially solvent reduction, are suppressed by Ni-composite microencapsulation. Therefore, a Ni-composite coating on graphite has the potential to even improve the safety of a Li-ion cell. The question that remains to be answered is, what is the mechanism associated with the Ni-composite coating that reduces irreversible capacity and improves both performance and safety? To address this issue, the bare and Ni-composite KS10 were physically characterized using SEM imaging and BET surface area analysis to develop a cause and effect relationship.

**SEM images and BET surface areas.**—Figure 6 shows the SEM images of KS10 graphite before (Fig. 6a) and after encapsulation with Ni composite (Fig. 6b). The bright spots in Fig. 6b were identified as containing Ni composite using energy-dispersive X-ray analysis (EDAX). This image shows very clearly that the Ni composite is evenly distributed over the surface of KS10, and that the sizes of the Ni-composite particles are on the order of nanometers or tens of nanometers. It is clear that the nanometer-sized Ni-composite particles appear to decrease the exposed surface of the graphite particles by depositing within the surface depressions. The specific surface areas of the bare and 10 wt % Ni-composite KS10, G1, and SFG75 are given in Table II (note that they are reported in terms of the net mass of graphite in the material to examine how the Ni-composite coating decreases the surface area relative to the bare graphite). A 5 wt % Ni-composite coating on KS10 causes the surface area to decrease from 14.5 to 12.4  $\text{m}^2/\text{g}$ , and it continues to decrease slightly upon increasing the Ni-composite content. These results corroborate very well with the SEM findings. Coating G1 and SFG75

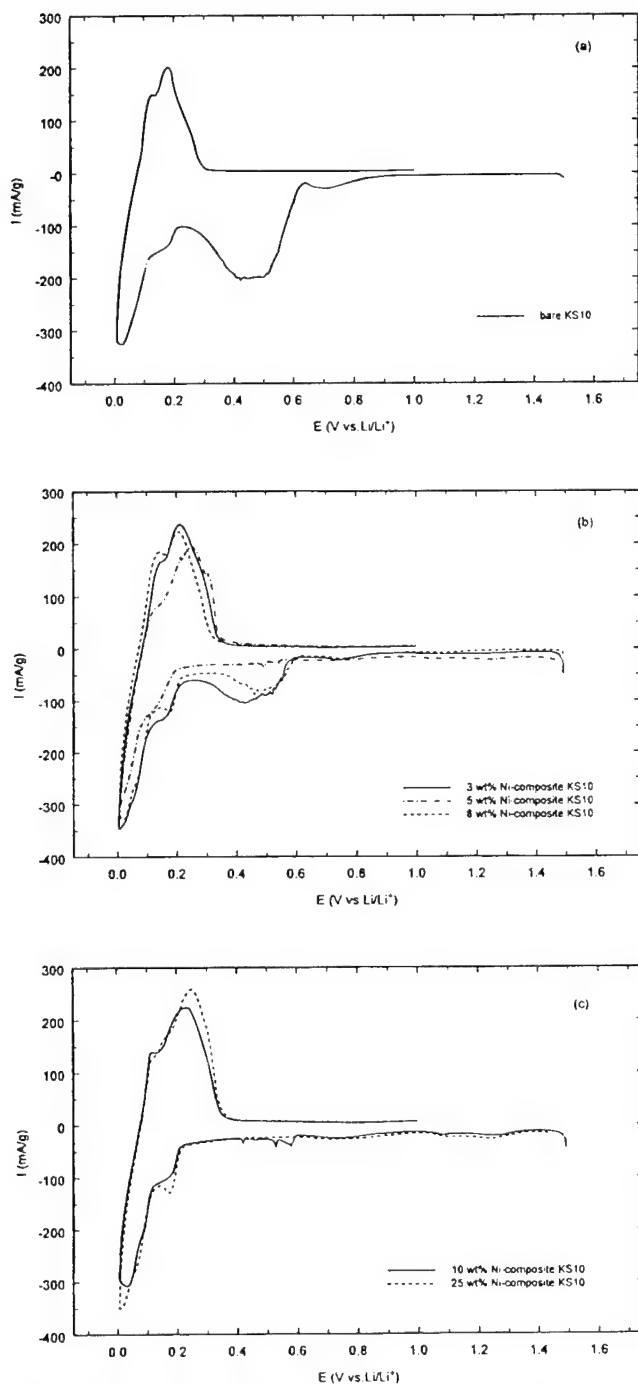


Figure 5. Cyclic voltammograms for bare KS10 graphite and KS10 graphite coated with different amounts of Ni composite in 1 M  $\text{LiPF}_6/\text{PC}/\text{EC}/\text{DMC}$  electrolyte (0.05 mV/s scan rate).

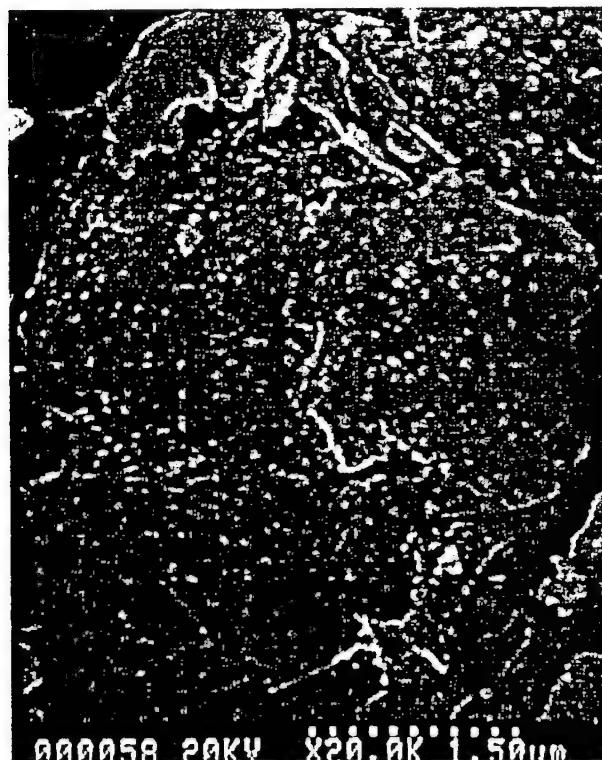
Table I. Capacities obtained from Fig. 5 in the potential range between 0.2 and 0.6 V vs.  $\text{Li}^+/\text{Li}$ .

Sample	Capacity (mAh/g)	Capacity saved (%)
Bare KS10	309.8	0
3 wt % Ni-composite-coated KS10	144.2	53.4
5 wt % Ni-composite-coated KS10	108.9	64.8
8 wt % Ni-composite-coated KS10	54.3	82.5
10 wt % Ni-composite-coated KS10	54.5	82.4
25 wt % Ni-composite-coated KS10	42.8	86.1

with Ni composite also causes a decrease in the surface areas of the bare G1 and SFG75.



(a)



(b)

Figure 6. SEM images of (a) bare KS10 graphite and (b) 10 wt % Ni-composite KS10 graphite.

To identify how the Ni-composite coating improves the first discharge-charge behavior, the initial irreversible capacity was analyzed with respect to the surface area. The initial irreversible capacity  $C_{irr}$  was calculated by subtracting the first intercalation capacity from the first deintercalation capacity. The relative values of the initial irreversible capacity  $C_{irr}/C_{int}$  as a function of the surface area are presented in Table II. The KS 10 values of  $C_{irr}/C_{int}$  decreased from 1.6 to 0.3 with a decrease of the surface area from 14.5 to 11.9 m<sup>2</sup>/g. The same trend was observed for G1 and SFG75.

In order to identify other factors which may contribute to the occurrence of the irreversible capacity, the irreversible capacity was normalized with surface area ( $C_{irr}/SA$ ) and is presented in Table II. If the irreversible capacity depends on surface area only, the normalized value  $C_{irr}/SA$  should be a constant value for each type of graphite before and after encapsulation with Ni composite. As shown in Table II, the values of  $C_{irr}/SA$  change from 31.2 to 7.1 mAh/m<sup>2</sup> for KS10, from 44.4 to 23.6 mAh/m<sup>2</sup> for G1, and from 65.2 to 20.3 mAh/m<sup>2</sup> for SFG75. Clearly there is a large variation in  $C_{irr}/SA$  for each type of graphite. Also, the  $C_{irr}/SA$  values decreased by increasing the amount of Ni composite. The results indicate that other factors beside the surface area contribute to the decreased irreversible capacity. Since the Ni-composite coating consisted of 10-15 nm particles that are larger than the graphene layer space of 0.3354 nm,<sup>6</sup> one cannot expect insertion of nickel composite in the layer to narrow down the layer space. In addition, the graphite particle size is essentially the same before and after encapsulation because of a small thickness of the Ni composite coating, approximately 3.4 nm (calculated). Therefore, there is no change in the graphite structure or particle size that may contribute to the variation of the irreversible capacity.

The results can be explained, however, by taking into account the fact that the solvated lithium intercalation takes place mainly on the edge surfaces of graphite rather than on the basal planes of graphite. Thus, the decreased irreversible capacity with increasing Ni-composite content suggests that the Ni-composite particles may be deposited on the edge surfaces of the graphite. This reduces the edge surfaces exposed to the electrolyte and may make the surface less permeable to the rather large solvated lithium ion. The net effect is to suppress solvated lithium intercalation at the edge sites and subsequent reduction of the solvent within the graphene layers, which substantially decreases the first cycle irreversible capacity as shown in Table II. Also increasing the amount of Ni composite covering the graphite surface narrows further the interstitial space between the nickel composite particles, which further decreases the solvated lithium intercalation and reduction in graphite.

**Cycling behavior.**—Bare and 10 wt % Ni-composite KS10 were galvanostatically cycled at C/8, C/4, C/2.5, and C/8, rates for 20, 10, 10, and 20 cycles, respectively. The cycling performance is presented in Fig. 7 in terms of the deintercalation capacity. The deintercalation capacities of the Ni-composite KS10 and bare KS10 both decrease with increasing deintercalation rate. However, at the same rate the deintercalation capacities of the Ni-composite KS10 are generally 30-40 mAh/g higher than those of the bare KS10. Again, this improved cycling ability is most likely due to Ni-composite suppressing PC solvent intercalation into and subsequent solvent reduction within the graphite, which often leads to destruction of the graphene layers by exfoliation. The increased deintercalation capacity associated with the Ni-composite KS10 may also result from enhanced kinetics, since Ni-composite graphite exhibits an improved conductivity. Based on an impedance study, Part II of this research illustrates these features.<sup>24</sup>

### Conclusions

Three types of graphite were microencapsulated with Ni-composite nanoparticles by a novel encapsulation deposition technique. These Ni-composite graphites were investigated as the negative electrode in a Li-ion cell with PC-based electrolyte. They showed a marked improvement in discharge-charge performance, coulomb

Table II. BET surface areas and the initial irreversible capacities of bare and Ni-composite graphites.<sup>a</sup>

Type of graphite	BET surface area (m <sup>2</sup> /g)	$C_{irr}/C_{int}$	$C_{irr}/SA$ (mAh/m <sup>2</sup> )
Bare KS10 (10 μm)	14.5	1.6	31.2
5 wt % Ni-composite-coated KS10	12.4	0.6	14.8
10 wt % Ni-composite-coated KS10	12.3	0.3	8.2
25 wt % Ni-composite-coated KS10	11.9	0.3	7.1
Bare G1 (1 μm)	11.2	1.8	44.4
10 wt % Ni-composite-coated G1	9.2	0.7	23.6
Bare SFG75 (75 μm)	3.3	0.7	65.3
10 wt % Ni-composite-coated SFG75	3.1	0.2	20.3

<sup>a</sup> The BET surface area is based on the mass of graphite only.

efficiency, and cycling behavior compared to the bare graphite precursors. For example, a 10 wt % Ni-composite coating on SFG75 graphite increased the initial discharge-charge coulomb efficiency from 59 to 84% and the reversible deintercalation charge capacity by 30-40 mAh/g. The Ni-composite coating consisted of nanosized particles distributed over the surface of the graphite particle, which effectively filled in some of the surface depressions and thus blocked some of the edge surfaces exposed to the electrolyte. This minimized solvated lithium intercalation at these edge sites, which subsequently minimized PC reduction within and exfoliation of the graphene layers, it also minimized gas evolution from the cell during cycling. In conclusion, a Ni-composite graphite negative electrode, made from a novel microencapsulation technique, has the potential to significantly improve both the performance and safety of the Li-ion cell relative to that of the bare graphite precursor.

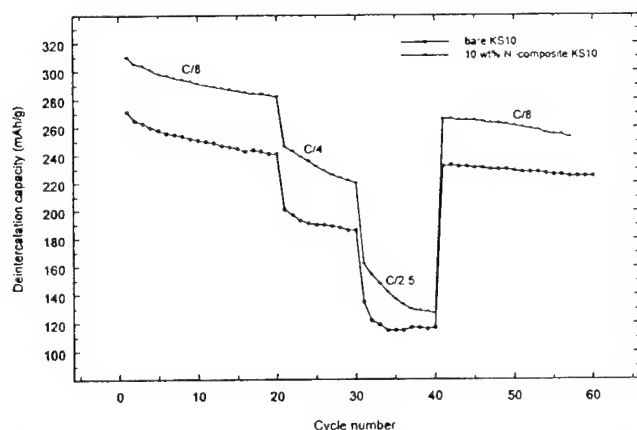


Figure 7. Cycling behavior of bare KS10 graphite and 10 wt % Ni-composite KS10 graphite at various charge-discharge rates.

## Acknowledgments

Financial supports provided in part by the DOE Division of Chemical Sciences, Office of Basic Energy Sciences, G. M. De-FG02-96ER 146598, in part by the Office of Research and Development, CIA, C/O no. 93-F148100-100.

The University of South Carolina assisted in meeting the publication costs of this article.

## References

1. K. Ozawa, *Solid State Ionics*, **69**, 212 (1994).
2. P. Arora, R. E. White, and M. Doyle, *J. Electrochem. Soc.*, **145**, 3647 (1998).
3. W. Xing and J. R. Dahn, *J. Electrochem. Soc.*, **144**, 1195 (1997).
4. T. Osaka, T. Momma, Y. Matsumoto, and Y. Uchida, *J. Electrochem. Soc.*, **144**, 1709 (1997).
5. F. Kong, J. Kim, X. Song, M. Inaba, K. Kinoshita, and F. McLarnon, *Electrochem. Solid-State Lett.*, **1**, 39 (1998).
6. M. Winter, P. Novak, and A. Monnier, *J. Electrochem. Soc.*, **145**, 428 (1998).
7. G. Chung, S. Jun, K. Lee, and M. Kim, *J. Electrochem. Soc.*, **146**, 1664 (1999).
8. A. N. Dey and B. P. Sullivan, *J. Electrochem. Soc.*, **117**, 222 (1970).
9. M. Arakawa and J. Yamaki, *J. Electroanal. Chem.*, **219**, 273 (1987).
10. R. Fong, U. von Sacken, and J. R. Dahn, *J. Electrochem. Soc.*, **137**, 2009 (1990).
11. T. Osaka, T. Momma, T. Tajima, and Y. Matsumoto, *J. Electrochem. Soc.*, **142**, 1057 (1995).
12. Z. Ogumi, M. Inaba, Y. Kawatate, A. Funabiki, and T. Abe, Abstract 73, Vol. 98-1, The Electrochemical Society Meeting Abstracts, San Diego, CA, May 3-8, 1998.
13. O. Chusid, Y. Ein-Eli, and D. Aurbach, *J. Power Sources*, **43-44**, 47 (1993).
14. J. O. Besenhard, M. W. Wagner, A. D. Jannakoudakis, P. D. Jannakoudakis, and E. Theodoridou, *J. Power Sources*, **43-44**, 413 (1993).
15. Y. Ein-Eli, S. R. Thomas, and V. R. Koch, *J. Electrochem. Soc.*, **143**, L195 (1996).
16. Z. X. Shu, R. S. McMillan, J. J. Murraro, and J. Davidson, *J. Electrochem. Soc.*, **142**, L161 (1995).
17. D. Billaud, A. Naji, and P. Willmann, *J. Chem. Soc., Chem. Commun.*, 1867 (1995).
18. F. A. Lowenheim, *Electroplating*, p. 402, McGraw-Hill Book Co., New York, (1978).
19. P. W. Wild, *Modern Analysis for Electroplating*, Finishing Publications, Ltd., Hapton Hill, Middlesex, England (1974).
20. P. Yu, B. N. Popov, J. A. Ritter, and R. E. White, *J. Electrochem. Soc.*, **146**, 8 (1999).
21. A. M. Christie and C. A. Vincent, *J. Appl. Electrochem.*, **26**, 255 (1996).
22. G. Dautzenberg, F. Croce, S. Passerini, and B. Scrosati, *Chem. Mater.*, **5**, 1268 (1993).
23. D. Pletcher, J. F. Rohan, and A. G. Ritchie, *Electrochim. Acta*, **39**, 1369 (1994).
24. P. Yu, J. A. Ritter, R. E. White, and B. N. Popov, *J. Electrochem. Soc.*, To be published.

# Ni-Composite Microencapsulated Graphite as the Negative Electrode in Lithium-Ion Batteries

## II. Electrochemical Impedance and Self-Discharge Studies

P. Yu,\* J. A. Ritter,\*\* R. E. White,\*\*\* and B. N. Popov\*\*\*,z

Center for Electrochemical Engineering, Department of Chemical Engineering, University of South Carolina, Columbia, South Carolina 29208, USA

Electrochemical impedance and self-discharge studies were carried out to investigate lithium intercalation into bare and Ni-coated KS10 graphite. Values of the charge-transfer resistances, exchange current densities, surface film resistances, and lithium-ion diffusion coefficients as functions of the state of charge (SOC) all favored the 10 wt % Ni composite KS10 graphite over bare KS10 graphite when these materials were used as the negative electrode in a Li-ion cell with mixed organic electrolyte. The charge-transfer resistances were always lower and gave rise to between 26 and 27% larger exchange current densities, which increased from 137 to 614 mA/g as the SOC increased. The surface film resistances for Ni composite KS10 were between 0.02 and 0.05  $\Omega$  g, slightly smaller than those of 0.03 to 0.08  $\Omega$  g for bare KS10, and both surface film resistances decreased with increasing SOC. The lithium-ion diffusion coefficients were always slightly larger, ranging between  $1.09 \times 10^{-9}$  and  $6.7 \times 10^{-9}$  cm<sup>2</sup>/s. Results from the self-discharge study also favored the 10 wt % Ni composite KS10, which exhibited less capacity loss over a 10 day period compared to bare KS10.

© 2000 The Electrochemical Society. S0013-4651(99)09-057-6. All rights reserved.

Manuscript submitted September 16, 1999; revised manuscript received February 1, 2000.

A considerable amount of research has been carried out to develop carbonaceous materials for the lithium-ion battery that have a high reversible capacity and to investigate the structural changes that take place during lithium intercalation into these carbonaceous materials. However, relatively few studies have focused on kinetic aspects, such as determination of the electrochemical exchange current density and the lithium-ion diffusion coefficient, despite their importance in battery charge/discharge characteristics.<sup>5-7</sup> The exchange current density characterizes the electrocatalytic activity of the electrode, which controls the kinetics of the charge-transfer reaction occurring at the electrode/electrolyte interface. In contrast, the lithium-ion diffusion coefficient determines the charge/discharge performance, particularly at high charge/discharge rates, because the diffusion of lithium-ions into and out of the carbon structure are the rate-determining steps during charge and discharge, in most cases.<sup>8</sup> Clearly, the determination of these kinetic parameters is essential for predicting and optimizing the performance of new carbonaceous materials being developed for use in the lithium-ion battery.

Part I of this work<sup>9</sup> reported on the development of a novel electrodeless deposition procedure for making Ni composite graphite materials for use as the anode (negative electrode) in the lithium-ion battery. These materials significantly suppressed solvated lithium intercalation into the graphite in propylene carbonate (PC)-based electrolyte, decreased the irreversible capacity in the first cycle, and exhibited 30–40 mAh/g higher discharge capacities (delithiation) compared to bare graphite at the same rate. However, as mentioned above, a superior anode material must also exhibit good kinetics. Therefore, the objective of Part II of this work is to report on the kinetic effects due to the presence of a Ni composite coating on graphite. To reveal these effects, electrochemical charge-transfer resistances, exchange current densities, surface film resistances, and lithium-ion diffusion coefficients are determined for the 10 wt % Ni composite KS10 graphite developed in Part I and also for the bare KS10 graphite precursor. The self-discharge behavior of these two materials is also investigated to determine the role of the Ni composite coating.

### Experimental

The microencapsulation of the graphite KS10 (10  $\mu$ m, Timcal) with Ni composite was carried out between 85 and 90°C in a plating

bath containing sodium hypophosphite as a reducing agent. The nickel composite coating consisted of nanosized particles distributed over the surface of the graphite particle.<sup>9</sup> The thickness of the Ni composite coating was calculated to be approximately 3.4 nm.<sup>9</sup> Therefore, there was no marked change in the graphite structure or the particle size of KS10 (10  $\mu$ m) after microencapsulation. However, the Brunauer-Emmett-Teller (BET) surface area of the 10 wt % Ni composite KS10 decreased slightly from 14.5 m<sup>2</sup>/g (estimated for bare KS10) to 12.3 m<sup>2</sup>/g. In this work, 10 wt % Ni composite KS10 and bare KS10 graphites were electrochemically characterized to obtain various kinetic parameters.

The electrochemical characterizations of these materials were carried out using a Swagelok three-electrode T-cell. A typical graphite negative electrode was prepared by mixing graphite powder with 6 wt % poly(vinylidene fluoride) (PVDF, Aldrich) powder and 1-methyl-2-pyrrolidinone solvent. The resulting slurry was spread onto a stainless steel current collector and dried under vacuum at 150°C for 12 h. The pellet was approximately 95  $\mu$ m in thickness, 1.26 cm in diameter, and contained about 9 mg of material. Because Markovsky *et al.*<sup>10</sup> showed that both the kinetics and impedance of the composite electrode were affected by the amount of binder, particle size and orientation, and electrode thickness, the kinetic behavior of bare and Ni composite KS10 was studied using electrode pellets prepared with approximately the same thickness, weight, and amount of binder. Taking into account that the properties of KS10 graphite particles are similar to those of KS6 (6  $\mu$ m), which was found to be highly oriented,<sup>10</sup> the above preparation procedure yields a horizontal orientation of the particles with their basal planes parallel to the current collector. This horizontal orientation of the KS10 particles was observed in scanning electron microscopy (SEM) images.<sup>9</sup>

The counter and reference electrodes were made from lithium foil (99.9%, Aldrich), and a sheet of Whatman glass fiber membrane (Baxter Diagnostics Co.) was used as a separator. The electrolyte consisted of 1 M LiPF<sub>6</sub> in a 1:1:3 mixture of propylene carbonate/ethylene carbonate/dimethyl carbonate (PC, EC, DMC) with less than 15 ppm H<sub>2</sub>O and 80 ppm HF from (EM Inc.).

Electrochemical impedance spectroscopy (EIS) was carried out at different states of charge at room temperature. Before the EIS experiments were performed, each T-cell was initially charged and discharged between 0.005 and 1.0 V vs. Li<sup>+</sup>/Li for three cycles using a constant current density of 0.5 mA/cm<sup>2</sup> to stabilize the system and to avoid the influence of any irreversible phenomena occurring during the first cycle. The electrochemical impedance data were gener-

\* Electrochemical Society Student Member.

\*\* Electrochemical Society Active Member.

\*\*\* Electrochemical Society Fellow.

z E-mail: popov@engr.sc.edu

ated in the frequency range of 100 kHz to 0.005 Hz with a low ac voltage amplitude of 5 mV to minimize perturbation of the system. Self-discharge behavior was examined using the following procedure. Each T-cell was first cycled three times, then charged at C/8 rate to 0.005 V vs. Li<sup>+</sup>/Li, held under open-circuit conditions for a period of time, and finally discharged at the same rate (C/8) to 2 V vs. Li<sup>+</sup>/Li. The discharge capacity after storage was measured, and the percent retained was determined by the ratio of this discharge capacity to the initial discharge capacity. All experiments were carried out at 25°C using an EG&G PAR potentiostat/galvanostat model 273A and SI 1255 frequency response analyzer driven by the CorrWare software system from Scribner Associates, Inc. Also, the electrical conductivities of the materials were measured by pressing about 0.7 g of powder into a pellet 0.8 cm in diameter and 6 mm thick at 65,000 psi and then measuring the electric resistance of the pellet using a digital multimeter.

### Results and Discussion

Figures 1a and b display the Nyquist plots obtained from the EIS experiments for bare KS10 and 10 wt % Ni composite KS10 at various states of charge (SOC), respectively. All of the spectra for both materials exhibit at least one semicircle and most exhibit two semicircles, which are associated with nondiffusive impedance. The impedance is explained in Fig. 2 in terms of a generalized equivalent

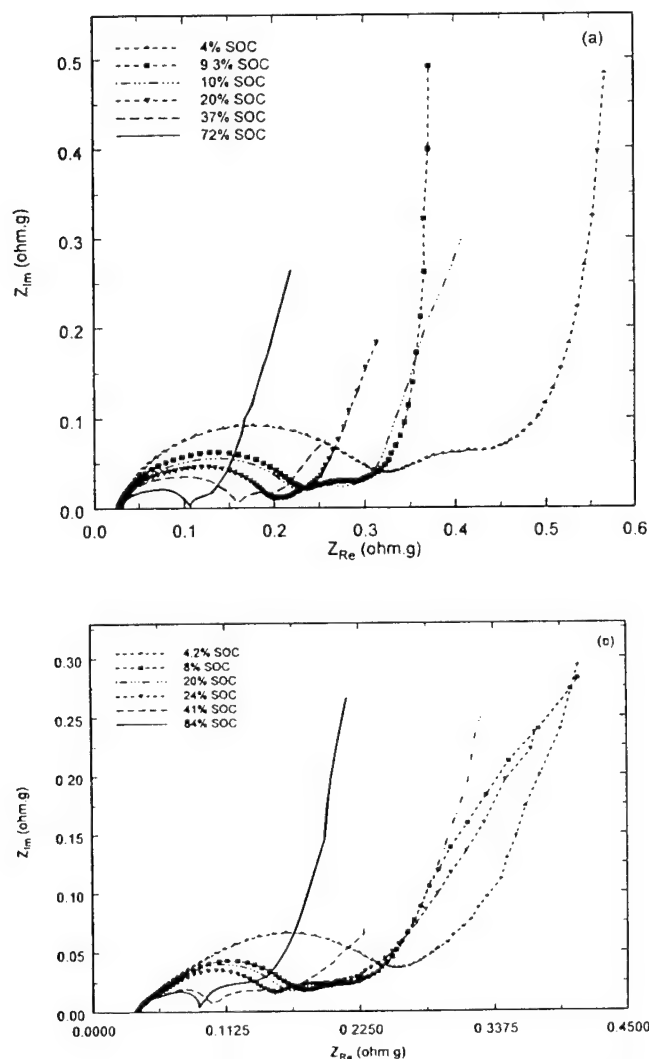


Figure 1. Nyquist plots for (a) bare KS10 and (b) 10 wt % Ni composite KS10 at various SOC.

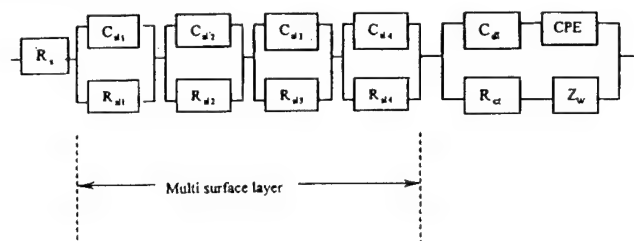


Figure 2. Equivalent circuit based on the impedance spectra in Fig. 1.

circuit. The first semicircle occurring in the high-frequency region is a combination of R/C circuits in series and represents the migration of Li ions through the passivation films.<sup>10</sup> The surface species are precipitated in a gradual reduction process at the active reductive electrode surface. Thus, the passivation films have a multilayer structure due to the variation of composition of the surface passivating species with distance from the active electrode material.<sup>11</sup> The R/C circuits in series are used to characterize this phenomenon with the total resistance  $R_{sl}$  and total capacitance  $C_{sl}$ .<sup>10,12</sup> The second semicircle in the medium-frequency region is attributed to an interfacial charge transfer of Li<sup>+</sup>/Li with a resistance  $R_{ct}$  and double-layer capacitance  $C_{dl}$ . The capacitive component, denoted as a constant-phase element (CPE), is introduced into the circuit to describe the depressed nature of the semicircle. In addition,  $R_s$  accounts for the ionic resistance of the electrolyte in the generalized electric circuit. It is interesting that for both materials the sizes of the semicircles decrease with an increase in the SOC. This behavior is indicative of a decrease in the nondiffusive impedance as more lithium intercalates into the graphite.

The low-frequency spectra beyond the semicircles are attributed to Li<sup>+</sup> diffusion impedance. The 45° slope in the initial parts of these spectra corresponds to semi-infinite diffusion, which is denoted by the Warburg impedance  $Z_w$  and included in the equivalent circuit in series with the charge transfer. Spectra at the very low frequencies, with slopes steeper than 45° and in some cases even approaching 90° (vertical spectra), are associated with finite diffusion. The region between the finite diffusion and semi-infinite diffusion regions, i.e., the transition region, has been used very effectively to obtain the diffusion coefficient,<sup>11,12</sup> as shown below.

The equivalent circuit depicted in Fig. 2 was regressed to the impedance data using Solatron impedance software, Zview™ (Scribner Associates, Inc.), to obtain the different resistances and capacitances as a function of the SOC. The resulting surface film resistances  $R_{sl}$  at various SOC are presented in Fig. 3 for both bare KS10 and for 10 wt % Ni composite KS10. For both materials,  $R_{sl}$  decreases slightly with increasing SOC. The values of  $R_{sl}$  for bare KS10 range from 0.08 to 0.3 Ω g, or from 11.2 to 42 Ω cm<sup>2</sup>. The evaluation of the resis-

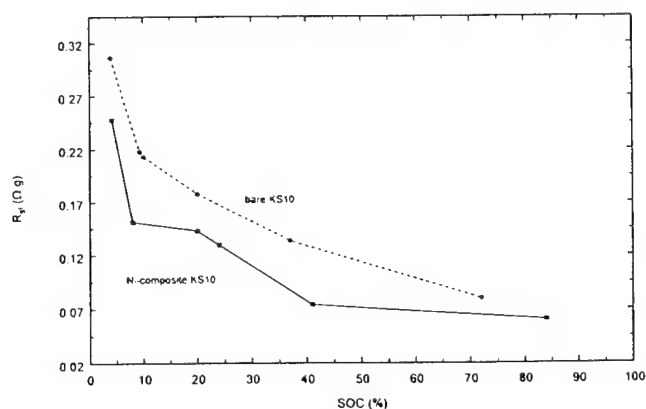


Figure 3. Surface film resistance extracted from the data in Fig. 1 as a function of SOC for bare KS10 and 10 wt % Ni composite KS10.

tance was based on the geometric surface area of 1.26 cm<sup>2</sup> or on the pellet weight of 9 mg. The observed surface film resistances are comparable to those reported in the literature for lithium metal (7 to 49 Ω cm<sup>2</sup>).<sup>13</sup> The  $R_{si}$  values evaluated for Ni composite KS10 varied between 0.02 and 0.05 Ω cm<sup>2</sup>. These values are consistently smaller than those observed for bare KS10. These results indicate that the presence of Ni composite particles on KS10 graphite reduces the surface film resistance of bare KS10. The observed decrease in the surface film resistance may arise from the enhanced ionic conductivity of the surface film around grain boundaries due to the Ni composite coating because nickel metal has a larger conductivity [ $1.44 \times 10^5$  (Ω cm<sup>-1</sup>)] than graphite [ $7.34 \times 10^4$  (Ω cm<sup>-1</sup>)].<sup>14</sup>

In addition, the Ni composite coating on KS10 significantly suppresses solvated lithium intercalation and reduction.<sup>9</sup> Thus, a smaller amount of electrolyte is reduced on the Ni composite KS10 resulting in a thinner surface film when compared to the bare graphite; this leads to a lower surface film resistance.

The dependence of the charge-transfer resistance  $R_{ct}$  on SOC is plotted in Fig. 4 for both bare KS10 and 10 wt % Ni composite KS10. For both materials,  $R_{ct}$  decreases slightly with increasing SOC, i.e., as more lithium-ions intercalate into the graphite. However,  $R_{ct}$  for bare KS10 is consistently higher. For example,  $R_{ct}$  for bare KS10 ranged between 0.065 and 0.246 Ω g, or between 9.4 and 35.7 kΩ cm<sup>2</sup> based on a specific surface area (BET) of 14.5 m<sup>2</sup>/g for bare KS10.<sup>9</sup> These values are larger than those reported in the literature at relatively high SOC for a natural graphite.<sup>7</sup>  $R_{ct}$  values for the 10 wt % Ni composite KS10 were between 0.056 and 0.173 Ω g, or between 6.8 and 21.3 kΩ cm<sup>2</sup> based on a BET surface area of 12.3 m<sup>2</sup>/g for 10 wt % Ni composite KS10.<sup>9</sup>

These results indicate that the presence of a 10 wt % Ni composite coating on KS10 graphite reduces the charge-transfer resistance compared to bare KS10 at all SOC. The charge-transfer resistances in Fig. 4 are also used to determine the exchange current density  $i_0$ , which characterizes the electrocatalytic activity of the negative electrode.

According to a linearized version of the Butler-Volmer equation at low overpotentials,<sup>15</sup>  $i_0$  is determined from

$$R_{ct} = \frac{RT}{F i_0} \quad [1]$$

where  $T$  is the absolute temperature (298 K),  $R$  is the universal gas constant, and  $F$  is Faraday's constant. The corresponding exchange current densities for bare KS10 and 10 wt % Ni composite KS10 are plotted as a function of the SOC in Fig. 5. Because of the inverse relation between  $R_{ct}$  and  $i_0$ , the decreasing charge-transfer resistance noted in Fig. 5 produces an increasing exchange current density with increasing SOC; similarly, because  $R_{ct}$  is larger for bare KS10,  $i_0$  is

smaller. For example,  $i_0$  ranges between 148 and 454 mA/g for 10 wt % Ni composite KS10 and only between 104 and 391 mA/g for bare KS10.

These consistently higher values of  $i_0$  for the 10 wt % Ni composite KS10 are consistent with  $R_{ct}$  depending strongly on the composition of the surface.<sup>16</sup> These results also indicate that the electrocatalytic activity of the KS10 graphite surface coated with Ni composite is more favorable toward the Li<sup>+</sup>/Li charge-transfer reaction than the bare KS10 graphite surface. The charge-transfer reaction rate is also affected by and decreases with an increase in the electrical resistance of the electrode material, which is about 14% higher for bare KS10 (3.3 Ω) compared to 10 wt % Ni composite KS10 (2.9 Ω). This result illustrates that the electrical conductivity and thus the charge-transfer reaction rate both increase by coating KS10 graphite with 10 wt % Ni composite. This improvement is most likely due to the higher conductivity of Ni metal compared to graphite, as shown above. Due to the higher charge-transfer reaction rate associated with the higher conductivity, a higher reversible capacity is also manifest in the 10 wt % Ni composite KS10 during long-time cycling, as illustrated in Part I of this series.<sup>9</sup>

The lithium-ion diffusion in graphite is a very important transport step among a series of processes that take place sequentially during charging.<sup>17</sup> For example, lithium-ions (i) must diffuse through the electrolyte, (ii) migrate through the SEI film, (iii) electrochemically react via charge transfer on the surface, and (iv) diffuse through and intercalate between the graphene layers within the graphite structure. Therefore, it is critical to determine the lithium-ion diffusion coefficient with some degree of accuracy. Different techniques have been explored for obtaining the lithium-ion diffusion coefficient; the advantages and disadvantages of each have been presented in the previous paper.<sup>11</sup> Based on some previous work by the authors,<sup>11,12</sup> the slopes of the impedance spectra in the transition regions of the Nyquist plots (Fig. 1a and b) were analyzed with the assistance of the following equations

$$Z(\omega) = \frac{\partial \eta_R}{\partial I} + \frac{(1-i)\sigma}{\sqrt{\omega} \{ \coth[(1+j)\psi] - (1-j)\psi \}^{1/2}} \quad [2]$$

$$\frac{d(Z_{im})}{d(Z_{re})} = \frac{(S_3 S_5 + S_4 S_7 - S_1 S_6 + S_2 S_8) T_4 - 2 T_3 (S_4 S_3 + S_2 S_1)}{(S_3 S_6 + S_4 S_8 - S_1 S_5 + S_2 S_7) T_4 - 2 T_5 (S_4 S_3 + S_2 S_1)} \quad [3]$$

$$T_3 = (S_4 S_5 - S_2 S_6); \quad T_4 = (S_4^2 + S_2^2); \quad T_5 = (S_4 S_6 + S_2 S_5) \quad [4]$$

$$S_1 = S_5 S_6; \quad S_2 = 2\psi - S_5; \quad S_3 = 2 \coth(\psi) \cot(\psi) (1 - \psi S_6) - 2\psi S_5 + S_8 \quad [5]$$

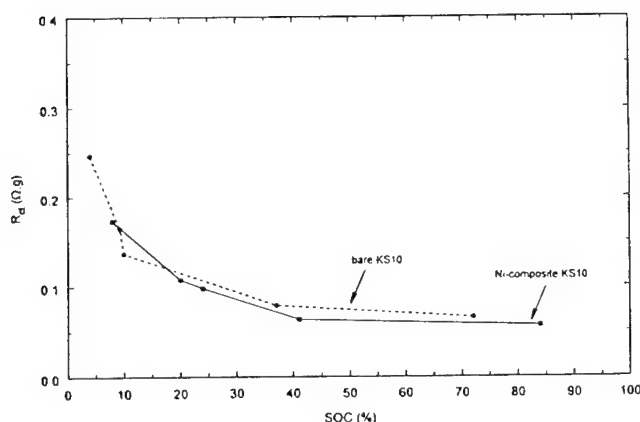


Figure 4. Charge-transfer resistance extracted from the data in Fig. 1 as a function of SOC for bare KS10 and 10 wt % Ni composite KS10.

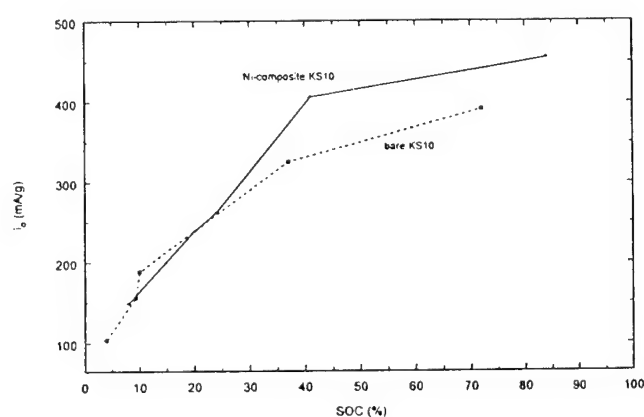


Figure 5. Exchange current density calculated as a function of SOC for bare KS10 and 10 wt % Ni composite KS10.



$$S_4 = 2\psi \coth(\psi) \cot(\psi) - S_6; \quad S_5 = \coth(\psi) - \cot(\psi) \quad [6]$$

$$S_6 = \coth(\psi) + \cot(\psi); \quad S_7 = 2 - S_1; \quad S_8 = \cot(\psi)^2 + \coth(\psi)^2 \quad [7]$$

$$\psi = \sqrt{\frac{\omega R_p^2}{2D}} \quad [8]$$

where  $Z(\omega)$  is the complex electrochemical impedance that includes  $\partial\eta_R/\partial I$  as the nondiffusion impedance (*i.e.*, the charge-transfer resistance and the surface film resistance) and  $(1-j)\sigma/\omega[\coth(1+j)\psi - (1-j)\psi]^{1/2}$  as the diffusion impedance.  $\sigma$  is the modified Warburg prefactor,  $j$  is  $\sqrt{-1}$ ,  $D$  is the lithium-ion diffusion coefficient in graphite,  $\omega$  is the angular frequency, and  $R_p$  is the particle radius (5  $\mu\text{m}$  for KS10). The resulting diffusion coefficients for bare KS10 and 10 wt % Ni composite KS10 are presented in Fig. 6 as a function of SOC.

The lithium-ion diffusion coefficients obtained for both bare KS10 and 10 wt % Ni composite KS10 are comparable to each other and vary similarly with SOC. In most cases, however, the lithium-ion diffusion coefficient is slightly higher for the 10 wt % Ni composite KS10 with values ranging from  $1.3 \times 10^{-9}$  to  $7.1 \times 10^{-9} \text{ cm}^2/\text{s}$ , the corresponding values for bare KS10 range from  $1.1 \times 10^{-9}$  to  $6.7 \times 10^{-9} \text{ cm}^2/\text{s}$ . These values are comparable to those reported by Guyomard and Tarascon<sup>18</sup> for petroleum coke ( $1.0 \times 10^{-9}$  to  $1.8 \times 10^{-8} \text{ cm}^2/\text{s}$ ) using the potential intermittent titration technique (PITT). These results show very clearly that the 10 wt % Ni composite coating on KS10 graphite does not hinder the diffusion of lithium-ions into the graphite structure, and in most cases it has a beneficial effect.

It is also interesting that for both materials the lithium-ion diffusion coefficients exhibit minimum values at about 20% SOC. In other words, at low SOC the lithium-ion diffusion coefficient decreases with increasing SOC, which is in agreement with that reported for other carbonaceous materials.<sup>18-20</sup> However, at SOC above 20%, the lithium-ion diffusion coefficient begins to increase with SOC. An increase in the lithium-ion diffusion coefficient at higher SOC has been reported by Funabiki *et al.*<sup>7</sup> for a natural graphite and by Julien<sup>21</sup> for fluorographite  $\text{CF}_{1.13}$ . This phenomenon can be attributed to the formation of different staged compounds, *i.e.*, different graphite intercalation compounds (GICs), as the lithium-ion insertion process continues.

The dependence of the lithium-ion diffusion coefficient on the staged structure of graphite can be ascribed<sup>7</sup> to differences in the in-plane and out-of-plane Li-GICs, because stage 1 and stage 2 phases (high SOC) are known to have an in-plane superstructure,<sup>22</sup> whereas stage 2, stage 3, and stage 4 phases (medium SOC) do not.<sup>7</sup> As expected, the transport of lithium ions in an in-plane structure is much more rapid than in an out-of-plane structure. Moreover, it has

also been shown<sup>21</sup> that local strains are greatly reduced by the coinsertion of fluorine and lithium-ions into the host graphite structure, which is beneficial to the enhanced in-plane diffusion coefficients. In addition, the graphene layer undergoes a large expansion in the  $c$  axis direction during the formation of the stage 1 compounds (high SOC). In contrast, much less expansion occurs during the formation of stage 3 compounds (medium SOC).<sup>8</sup> This large expansion of the graphene layer, corresponding to an enlarged layer spacing, most likely gives rise to the increased lithium-ion diffusion coefficients at high SOC as the diffusion of lithium-ions takes place in the direction parallel to the graphene layer. These three features described above most likely contribute to the increased lithium ion diffusion coefficients observed for both bare KS10 and 10 wt % Ni composite KS10 at higher SOC.

In addition, the abrupt variation of the diffusion coefficient exhibited at about 20% SOC for both bare KS10 and 10 wt % Ni composite KS10 was previously observed by Funabiki *et al.*<sup>7,26</sup> This sharp change in the diffusion coefficient occurs in the region of the coexistence of stage 4 and dilute stage 1 biphasic.<sup>7</sup> The lithium kinetics at the biphasic state are believed to be governed by the displacement rate of the biphasic interface and not by the Fickian diffusion process.

Self-discharge processes normally take place during a highly charged state of the electrode and are caused by the highly oxidizing and reducing character of the electrode materials and the electrolyte, respectively.<sup>18</sup> Self-discharge is also mainly associated with the performance of the negative electrode, although it can be associated with the positive electrode, but to a much lesser extent.<sup>23</sup> Therefore, self-discharge of a Li-ion cell is largely attributed to the loss of capacity in the graphite electrode, in which reversible delithiation takes place in conjugation with irreversible solvent reduction.<sup>23,24</sup> In other words, the self-discharge process can be indicative of the stability of the electrolyte solution toward the graphite electrode. It is generally observed that Li-ion cells comprised of a negative electrode/electrolyte system that produces a poor solid electrolyte interphase (SEI) film on the electrode surface, often gives rise to the highest rate of self-discharge or largest capacity loss.<sup>23</sup>

To investigate the stability of the SEI film formed on the surfaces of both bare KS10 and 10 wt % Ni composite KS10, the self-discharge behavior of these materials was tested by determining the discharge capacity retained after different storage times. Figure 7 shows the percentage of the discharge capacity retained for both materials after storing them for 1, 3, and 10 days. After 1 day of storage, 2 to 3% of the capacity was lost, after 3 days of storage 5 to 6% of the capacity was lost, and after 10 days of storage 8 to 10% of the capacity was lost. However, in all cases, the higher lost capacity percentages are associated with the bare KS10 graphite. In other words, the capacity losses due to self-discharge are reduced by coating KS10

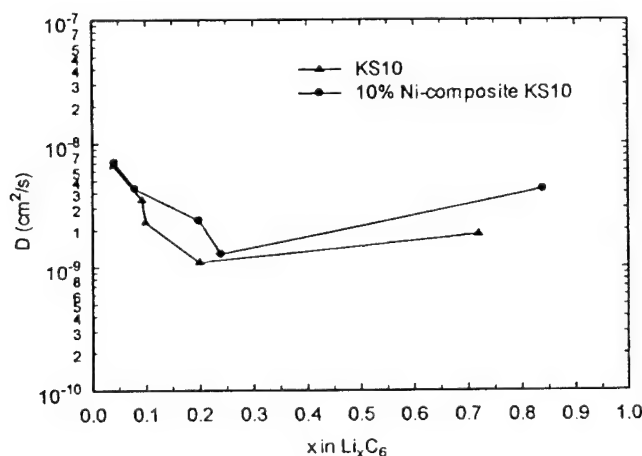


Figure 6. Lithium-ion diffusion coefficients extracted from the data in Fig. 1 as a function of SOC for bare KS10 and 10 wt % Ni composite KS10.

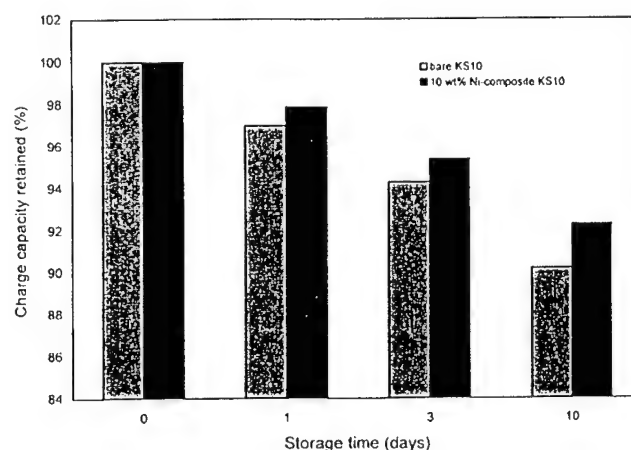


Figure 7. Self-discharge behavior of bare KS10 and 10 wt % Ni composite KS10.

graphite with 10 wt % Ni composite. This slightly lower self-discharge rate associated with the 10 wt % Ni composite KS10 may be attributed to the formation of a more stable, but not more resistant, SEI film (see Fig. 5).

### Conclusions

Part I of this series reported on the development of a novel electrodeless deposition technique for making Ni composite KS10 graphite. When investigated as the negative electrode in a Li-ion cell with PC based electrolyte, a 10 wt % Ni composite KS10 graphite exhibited a marked improvement in the charge-discharge performance, coulombic efficiency and cycling behavior compared to the bare precursor graphites. In the present study, *i.e.*, Part II of this series, electrochemical impedance and self-discharge studies were carried out to investigate kinetic effects associated with coating KS10 graphite with 10 wt % Ni composite. Charge-transfer resistances, exchange current densities, surface film resistances, and lithium-ion diffusion coefficients as functions of the SOC were extracted from impedance spectra obtained for bare KS10 and 10 wt % Ni composite KS10. The charge-transfer resistances obtained for the 10 wt % Ni composite KS10 were always lower than those obtained for the bare KS10, and gave rise to between 26 and 27% larger exchange current densities for the 10 wt % Ni composite KS10, which increased from 137 to 614 mA/g as the SOC increased. This result indicated that a 10 wt % Ni composite coating is favorable for the lithium-ion charge-transfer reaction. The surface film resistances for Ni composite KS10 were between 0.02 and 0.05  $\Omega$  g, slightly smaller than those of 0.03 to 0.08  $\Omega$  g for bare KS10, and both surface film resistances decreased with increasing SOC. This result suggested that the 10 wt % Ni composite coating on KS10 graphite possibly enhanced the lithium-ion conduction in the surface film. The lithium-ion diffusion coefficients extracted from the transition diffusion region in the Nyquist plots were always slightly larger for the 10 wt % Ni composite KS10 compared to the bare KS10, ranging between  $1.1 \times 10^{-9}$  and  $6.7 \times 10^{-9}$  cm<sup>2</sup>/s, and  $1.28 \times 10^{-9}$  and  $7.1 \times 10^{-9}$  cm<sup>2</sup>/s, respectively. These results show very clearly that the 10 wt % Ni composite coating on KS10 graphite did not hinder the diffusion of lithium ions into the graphite structure, and in most cases it had a beneficial effect. Both materials also exhibited an increase in the lithium-ion diffusion coefficient at higher SOC's; this behavior was explained in terms of the formation of a graphite-intercalation compound Li-GIC in-plane superstructure, lower local strains between the graphene layers, and larger expansion of the graphene layers, as more lithium-ions intercalated into the graphite. Results from a self-discharge study also favored the 10 wt % Ni composite KS10, which exhibited less capacity loss over a 10 day period compared to bare KS10. This result was attributed to the formation of a more stable, but not more resistant, SEI film on the surface of the KS10 coated with 10 wt % Ni composite.

### Acknowledgments

Financial support provided in part by the DOE Division of Chemical Sciences, Office of Basic Energy Sciences, G. M. De-FG02-96ER 146598, in part by the Office of Research and Development, C/O no. 93-F148100-100 and in part by the Army Research Office, grant no. DAAH04-96-1-0421 are gratefully acknowledged.

The University of South Carolina assisted in meeting the publication costs of this article.

### List of Symbols

$C_{dl}$	double-layer capacitance, $\mu$ F
$C_{sl}$	surface film capacitance, $\mu$ F
$D$	lithium ion diffusion coefficient in graphite, cm <sup>2</sup> /s
$F$	Faraday's constant, 96,487 C/equiv
$I$	current, A
$j$	imaginary number, $\sqrt{-1}$
$R$	gas constant, 8.314 J/mol K
$R_p$	radius of spherical particle, cm
$R_{ct}$	charge-transfer resistance, $\Omega$ g
$R_s$	electrolyte ionic resistance, $\Omega$ g
$R_{sl}$	surface film resistance, $\Omega$ g
$x$	Li <sub>x</sub> C <sub>6</sub> stoichiometric parameter, mole
$Z_{im}$	imaginary impedance, $\Omega$ g
$Z_{re}$	real impedance, $\Omega$ g
$Z_w$	Warburg impedance, $\Omega$ g
$\omega$	angular frequency s <sup>-1</sup>
$\sigma$	modified Warburg prefactor, $\Omega$ s <sup>1/2</sup>
$\eta_R$	particle surface overpotential ( $r = R$ ), V
$\psi$	defined by Eq. 8
$\partial\eta_R/\partial I$	nondiffusion impedance, $\Omega$

### References

- H. Shi, J. Barker, M. Y. Saidi, and R. Koksang, *J. Electrochem. Soc.*, **143**, 3466 (1996).
- J. R. Dahn, R. Fong, and M. J. Spoon, *Phys. Rev. B*, **42**, 6424 (1990).
- R. Yazami and M. Deschamps, *Bull. Electrochem.*, **12**, 206 (1996).
- T. D. Tran, J. H. Feikert, X. Song, and K. Kinoshita, *J. Electrochem. Soc.*, **142**, 3297 (1995).
- S. R. Narayanan, D. H. Shen, and G. Halpert, *J. Electrochem. Soc.*, **140**, 1854 (1993).
- J. Xu and G. C. Farrington, *J. Electrochem. Soc.*, **142**, 3303 (1995).
- A. Funabiki, M. Inaba, and Z. Ogumi, *J. Electrochem. Soc.*, **145**, 172 (1998).
- K. Kinoshita, *Carbon Electrochemical and Physicochemical Properties*, John Wiley & Sons Inc., New York (1988).
- P. Yu, J. A. Ritter, R. E. White, and B. N. Popov, *J. Electrochem. Soc.*, **147**, 1280 (2000).
- B. Markovsky, M. D. Levi, and D. Aurbach, *Electrochim. Acta*, **43**, 2287 (1998).
- P. Yu, B. N. Popov, J. A. Ritter, and R. E. White, *J. Electrochem. Soc.*, **146**, 8 (1999).
- B. Haran, B. N. Popov, and R. E. White, *J. Power Sources*, **75**, 56, (1998).
- K. Naoi, M. Mori, Y. Naruoka, W. M. Lamanna, and R. Atanasoski, *J. Electrochem. Soc.*, **146**, 462 (1999).
- Handbook of Chemistry and Physics*, 52nd ed., R. C. Weast, Editor, The Chemical Rubber Co., Cleveland, OH (1971).
- A. J. Bard and L. R. Faulkner, *Electrochemical Methods-Fundamentals and Applications*, John Wiley & Sons Inc., New York (1980).
- J. S. Newman, *Electrochemical Systems*, 2nd ed., Prentice Hall International, Englewood Cliffs, NJ (1991).
- H. Kanoh, Q. Feng, Y. Miyai, and K. Ooi, *J. Electrochem. Soc.*, **142**, 702 (1995).
- D. Guyomard and J. M. Tarascon, *J. Electrochem. Soc.*, **139**, 937 (1992).
- N. Takami, A. Satoh, M. Hara, and T. Ohsaki, *J. Electrochem. Soc.*, **142**, 371 (1995).
- T. Uchida, Y. Morikawa, H. Ikuta, and M. Wakihara, *J. Electrochem. Soc.*, **143**, 2606 (1996).
- C. Julien and G. Nazri, *Solid State Batteries: Materials Design and Optimization*, p. 392, Kluwer Academic Publishers, Boston, MA (1994).
- M. S. Dresselhaus and G. Dresselhaus, *Adv. Phys.*, **30**, 139 (1981).
- M. C. Smart, B. V. Ratnakumar, and S. Surampudi, *J. Electrochem. Soc.*, **146**, 486 (1999).
- P. Arora, B. N. Popov, and R. E. White, *J. Electrochem. Soc.*, **145**, 807 (1998).
- S. Shiraishi, K. Kanamura, and Z. Takehara, *J. Electrochem. Soc.*, **146**, 1633 (1999).
- N. Takami, A. Satoh, T. Ohsaki, and M. Kanda, *J. Electrochem. Soc.*, **145**, 478 (1998).



# Carbonization and activation of sol–gel derived carbon xerogels

Chuan Lin, James A. Ritter\*

*Department of Chemical Engineering, Swearingen Engineering Center, University of South Carolina, Columbia, SC 29208, USA*

Received 15 March 1999; accepted 2 August 1999

## Abstract

The effects of the carbonization temperature (in  $N_2$ ) and  $CO_2$ -activation time (in 5%  $CO_2$  in  $N_2$ ) on the pore structure of carbon xerogels, derived from the sol–gel polymerization of resorcinol–formaldehyde resins, were studied in detail. As the carbonization temperature increased, the number of micropores in the 0.6 nm range decreased, with essentially no effect on the pores in the mesopore range, and the cumulative surface areas and pore volumes both decreased, but only marginally. As the  $CO_2$ -activation time increased, the number of micropores and mesopores both increased, where pores in the 0.6 nm range eventually became pores in the 0.13 nm range, and the cumulative surface areas and pore volumes both increased significantly. The skeletal densities also increased significantly, approaching that of graphite, with an increase in both the carbonization temperature and  $CO_2$ -activation time, but the nanoparticle size was largely unaffected. Weight loss was nearly independent of the carbonization temperature at about 50%, but it was strongly dependent on the  $CO_2$ -activation time with a maximum weight loss of about 75%. © 2000 Elsevier Science Ltd. All rights reserved.

**Keywords:** A. Carbon xerogels. Resins; B. Carbonization. Activation; D. Porosity

## 1. Introduction

Organic aerogels and xerogels, derived from the polycondensation of resorcinol with formaldehyde, have been receiving considerable attention in the literature [1–9] since their introduction by Pekala in 1989 [1]. The increasing popularity of these organic materials is largely due to their unique and controllable properties, which in turn are attributed to the reaction mechanism being akin to the sol–gel process [1]. The sol–gel process is quickly becoming one of the most promising material synthesis techniques because it readily allows for control of the texture, composition, homogeneity and structural properties of the resulting materials [10].

Organic aerogels, which are made by removing the solvent from the gel structure by drying supercritically with carbon dioxide, have been characterized extensively in terms of their structural properties as an organic resin [1,6–8,11,12]. Some of these organic resins have also been carbonized or pyrolyzed in an inert atmosphere such as nitrogen to produce a carbon aerogel, with uniquely different properties compared to the uncarbonized organic

aerogels. In contrast, organic xerogels, which are made by removing the solvent from the gel structure by drying conventionally with nitrogen or air under normal conditions, have not been characterized nearly as much as their organic aerogel counterparts. This is also true for carbonized organic xerogels, which produce so called carbon xerogels.

In this study, the evolution of the pore structure of carbon xerogels derived from resorcinol–formaldehyde (R–F) resins is followed while carbonizing at increasingly higher temperatures and activating with  $CO_2$  for increasingly longer times. The relatively new and very powerful density function theory (DFT) method is used, along with more traditional characterization techniques, to obtain pore structural information. The effects of carbonization temperature and  $CO_2$ -activation time on the pore size distribution, particle morphology, cumulative surface area, cumulative pore volume, skeletal density and thermogravimetric analysis are disclosed and discussed.

## 2. Experimental

The synthesis procedure for the carbon xerogels was similar to that reported elsewhere [4,9]. A solution containing 5 wt.% solids in 100 ml of solution was prepared,

\*Corresponding author. Tel.: +1-803-777-3590; fax: +1-803-777-8265.

E-mail address: [ritter@enr.sc.edu](mailto:ritter@enr.sc.edu) (J.A. Ritter).

in which the R–F mole ratio was fixed at 1:2. Sodium carbonate was used as the catalyst, and the R–C (resorcinol–sodium carbonate) mole ratio was fixed at 50. Based on previous work [9], the initial pH of the solution was set at 6.0 using dilute  $\text{HNO}_3$ . The solution was sealed in a flask and magnetically stirred for 30 min, followed by 1 week of curing in an oven at  $85^\circ\text{C} \pm 3^\circ\text{C}$  (no stirring). After curing, the gel was washed with acetone for 3 days. Fresh solvent was replaced daily after vacuum filtration. Then the washed gel was dried under nitrogen in a tube-furnace. Using a heating rate of  $0.5^\circ\text{C min}^{-1}$ , it was heated to  $65^\circ\text{C}$  and held there for 5 h; it was then heated to  $110^\circ\text{C}$  and held there for another 5 h. For the carbonization study, the carbon xerogels were formed by pyrolysis of the dried gels at the desired temperature for 3 h in  $\text{N}_2$ . For the  $\text{CO}_2$ -activation study, the carbon xerogels were formed by pyrolysis of the dried gels at  $1050^\circ\text{C}$  for 1 h in  $\text{N}_2$ , then at the same temperature for the desired time in  $\text{N}_2$  containing 5 vol.%  $\text{CO}_2$  and finally at the same temperature for another 2 h in  $\text{N}_2$ . In both cases the heating and cooling rates were set at  $5^\circ\text{C min}^{-1}$ .

The PSD,  $f(w)$ , was calculated from the adsorption integral equation

$$n(P) = \int_{w_{\min}}^{w_{\max}} f(w) \rho(P, w) dw \quad (1)$$

where  $n(P)$  is the experimentally measured adsorption isotherm in terms of the specific moles of  $\text{N}_2$  adsorbed at 77 K as a function of pressure  $P$ .  $w_{\min}$  and  $w_{\max}$  are the widths of the smallest and largest pores in the material, and  $\rho(P, w)$  is the local adsorption isotherm in terms of the molar density of  $\text{N}_2$  at 77 K and pressure  $P$  in a pore of width  $w$ . By definition,  $f(w) = dV/dw$ , where  $V$  is the pore volume. The experimental adsorption isotherm for each of the carbon xerogels was measured using a Coulter Omnisorp 610 in the static fixed-dose mode. The samples were dried in air at 420 K and then outgassed under vacuum for several hours at 520 K until the pressure fell below  $5 \times 10^{-6}$  Torr. All of the powdery samples received an intermediate helium purge to minimize fluidization during evacuation. The first data point on the isotherm was obtained at  $5 \times 10^{-6}$  Torr, with more than 200 data points collected between this pressure and a relative pressure of unity (i.e.,  $P/P^0 = 1.0$ ). The dead space in the sample chamber was calibrated with helium after each isotherm was obtained.

The local adsorption isotherms were predicted from non-local DFT as described in detail elsewhere [13–17]. With the above experimental and theoretical adsorption isotherms, the PSD for each carbon xerogel was obtained by solving Eq. (1) using a regularization technique that has also been described in detail elsewhere [17–19]. The cumulative pore volume ( $V_c$ ) was estimated from the following equation

$$V_c = \int_{w_{\min}}^w f(w) dw \quad (2)$$

and the cumulative surface area ( $S_c$ ) was estimated from Eq. (3) by assuming a slit pore model for the carbon xerogels.

$$S_c = \int_{w_{\min}}^w \frac{2f(w)}{w} dw \quad (3)$$

Transmission electron micrographs were obtained with a Hitachi H-8000 transmission electron microscope (TEM), and skeletal densities were measured using a Quantachrome Ultrapycnometer 1000. A Perkin-Elmer thermogravimetric analyzer (TGA-7) was used to follow the weight loss of the carbon xerogels during carbonization and  $\text{CO}_2$ -activation. The conditions were the same as those used within the tube furnace.

### 3. Results and discussion

#### 3.1. Effect of carbonization temperature

The effect of the carbonization temperature on the pore structure of the carbon xerogels is shown in Figs. 1–5. Fig. 1(A) displays the  $\text{N}_2$  adsorption isotherms for the different carbonization temperatures that ranged from 600 to  $1200^\circ\text{C}$ ; Fig. 1(B) shows the corresponding PSDs. Note that in both figures the data points (over 200 per isotherm and PSD) have been removed for clarity. All of the adsorption isotherms in Fig. 1(A) were similarly shaped and typical of a material that contains both microporosity and mesoporosity [20]. The rectangular shape at very low relative pressures was indicative of the presence of microporosity and the very gradual increase in the amount adsorbed over a wide range of relative pressures was indicative of the presence of some mesoporosity. The sharp increase in the amount adsorbed as the relative pressure approached 1.0 was caused by condensation most likely in the large mesopores within and between the carbon xerogel particles, which were typically 15–20 nm in diameter as shown in Fig. 2. Although these adsorption isotherms hardly differed from each other, except for a slight decrease in the amount adsorbed with increasing carbonization temperature, DFT analysis of the PSDs revealed some interesting and subtle features.

According to IUPAC nomenclature [21], micropores are less than 2 nm in diameter, mesopores are between 2 nm and 50 nm in diameter, and macropores are greater than 50 nm in diameter. Fig. 1(B) shows that in the micropore region all of the samples exhibited a peak with a mean pore width of about 0.6 nm. The height of this peak decreased with an increase in the carbonization temperature, clearly indicating the loss of microporosity. Three of

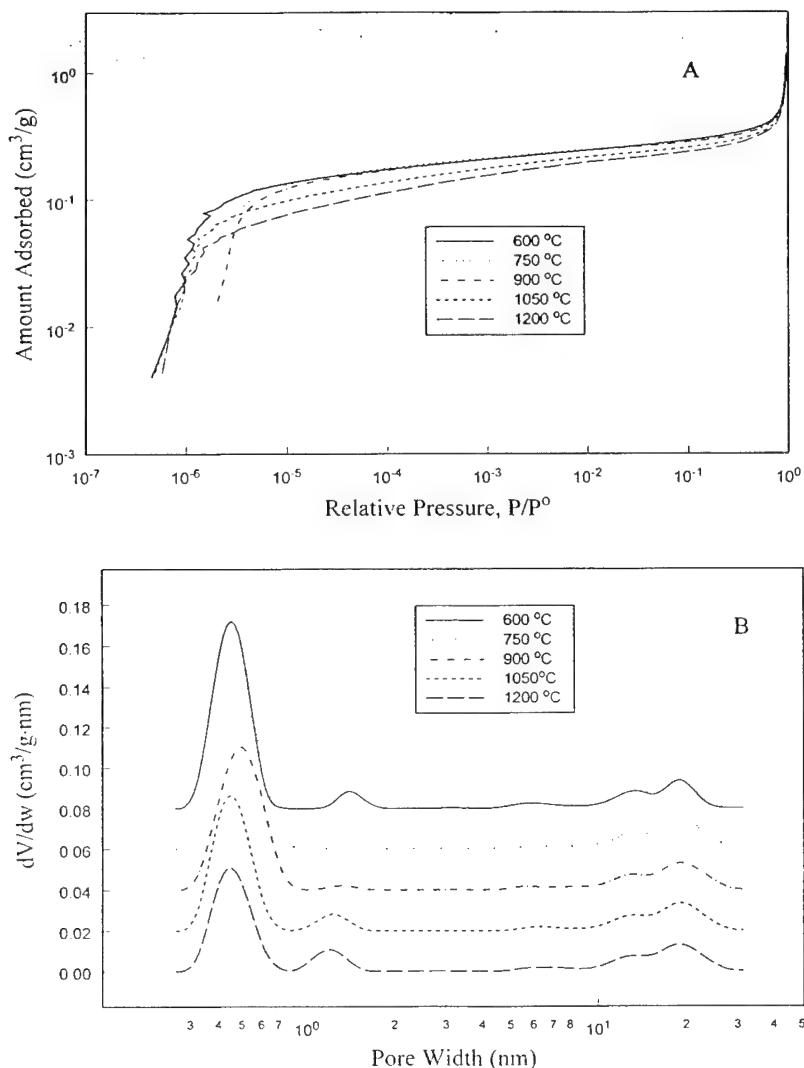


Fig. 1. Effect of the carbonization temperature on: (A) the experimental nitrogen adsorption isotherms at 77 K in terms of the volume of liquid nitrogen adsorbed per gram of adsorbent; and (B) the corresponding PSDs from DFT for the carbon xerogels.

the samples also exhibited a peak between pore widths of 1 and 2 nm. This peak was relatively small at 600°C, disappeared at 750 and 900°C, and reappeared at 1050 and 1200°C with a slight shift toward smaller pore sizes, indicating the destruction and creation of microporosity with increasing carbonization temperature. In the mesopore region, a broad but small peak appeared with a mean pore width of around 20 nm; however, this peak did not change much with the carbonization temperature. The cumulative pore volumes shown in Fig. 3(A,B), in terms of the absolute volumes and percentages, exhibited very similar trends, as expected from the adsorption isotherms and PSDs shown in Fig. 1.

The total pore volume, ranging from 1.4 to 1.6 cm<sup>3</sup> g<sup>-1</sup>, decreased slightly with an increase in the carbonization

temperature, except for the one carbonized at 600°C, which had the smallest pore volume compared to the other carbon xerogels. However, this carbon xerogel had the largest micropore volume. The cumulative pore volume corresponding to pore widths of less than 0.7 nm was about 0.18 cm<sup>3</sup> g<sup>-1</sup>, which accounted for about 12% of the total pore volume. As the carbonization temperature increased, however, the volume of the pores in this size range decreased to about 0.1 cm<sup>3</sup> g<sup>-1</sup> for the carbon xerogel carbonized at 1200°C. Then, for all of the carbon xerogels, the cumulative pore volume corresponding to pore widths ranging from 0.7 to 10 nm increased only very slightly, indicating that few pores in this size range existed. Finally, for all of the carbon xerogels, the cumulative pore volume increased sharply at around 10 nm and levelled off at

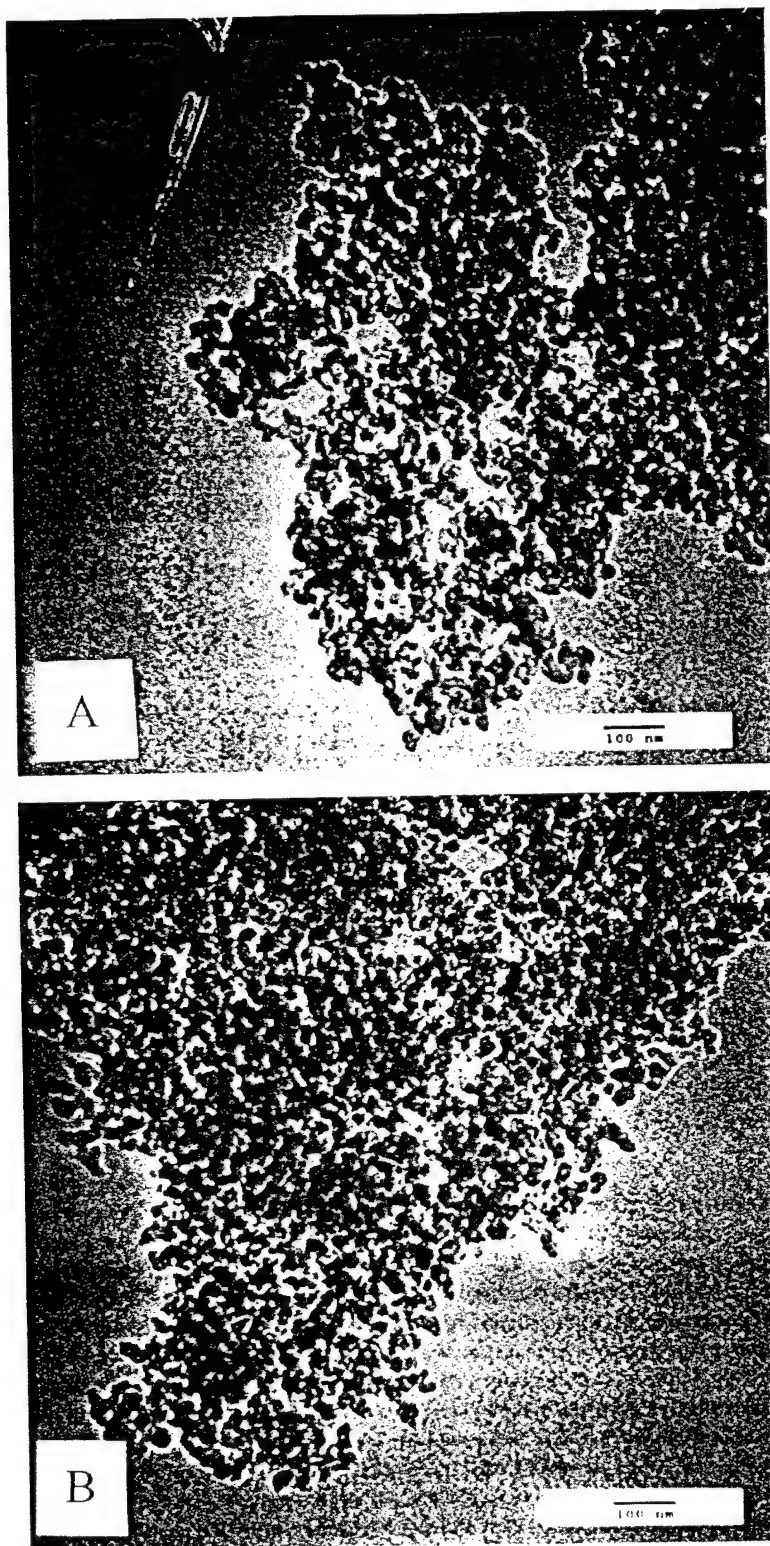


Fig. 2. TEM micrographs of the carbon xerogels carbonized at: (A) 600°C; and (B) 1200°C.



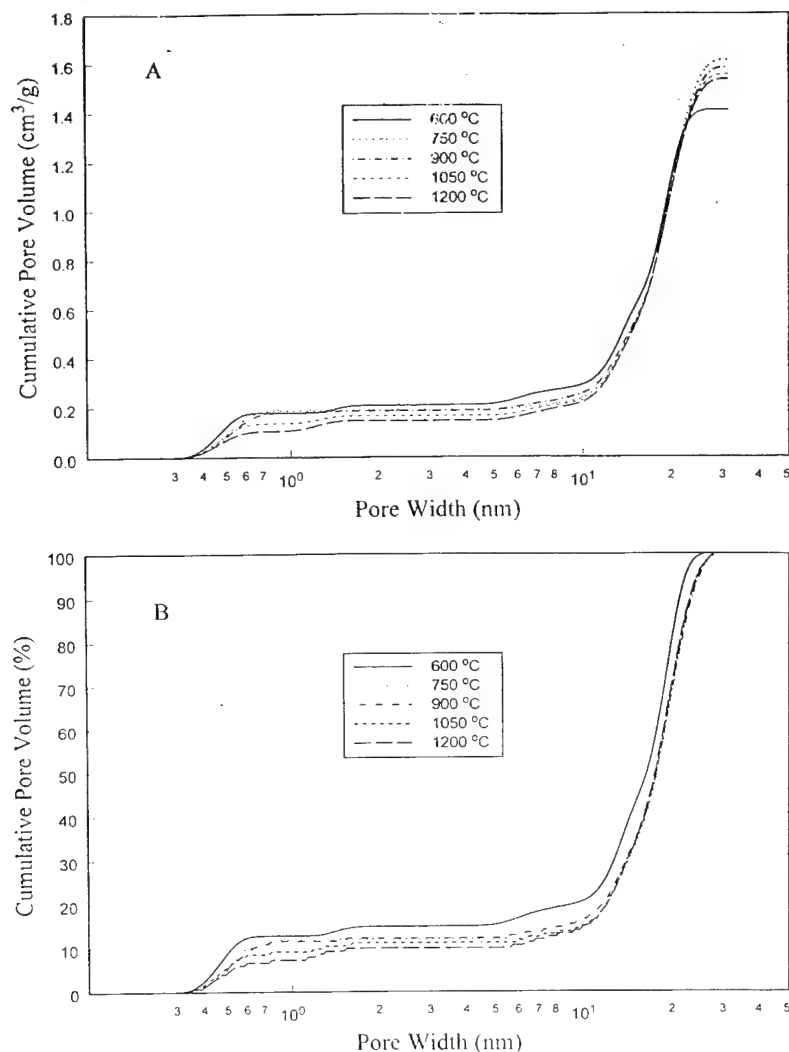


Fig. 3. Effect of the carbonization temperature on the cumulative pore volumes of the carbon xerogels in terms of: (A) absolute volumes; and (B) percentages.

around 25 nm. The pore volumes in this size range were about  $1.3 \text{ cm}^3 \text{ g}^{-1}$  and accounted for about 90% of the total pore volume in these carbon xerogels. The cumulative surface areas shown in Fig. 4(A,B), in terms of absolute values and percentages, revealed even more detailed information about the variation in pore structure with the carbonization temperature.

The total surface area decreased from  $850$  to  $600 \text{ m}^2 \text{ g}^{-1}$  as the carbonization temperature increased from  $600$  to  $1200^\circ\text{C}$ . Much of this surface area was lost from the effect of the carbonization temperature on the pores in the micropore range ( $<2 \text{ nm}$ ). Pore widths of less than  $0.7 \text{ nm}$  accounted for a significant portion of the total surface area, ranging from about  $60$  to  $75\%$  in order of decreasing carbonization temperature. The larger pores with widths

ranging from  $10$  to  $25 \text{ nm}$  accounted for only  $20$ – $30\%$  of the total surface area. Again, the cumulative surface area did not change much over a broad range of pore widths ranging from  $1.5$  to  $10 \text{ nm}$ , indicating that few pores existed in this range. However, a slight increase in the cumulative surface area was observed due to the pores with widths ranging from  $0.7$  to  $1.5 \text{ nm}$ , which accounted for about  $5$ – $10\%$  of the total surface area and was consistent with the PSD results. It was also interesting that  $10$ – $15\%$  of the pore volume in the micropore range accounted for  $70$ – $80\%$  of the surface area. Clearly, the effect of the carbonization temperature on the pore structure of these carbon xerogels was manifest through a loss in the number of micropores in the  $0.4$ – $0.7 \text{ nm}$  range. This was also the case for the carbon xerogel carbonized at

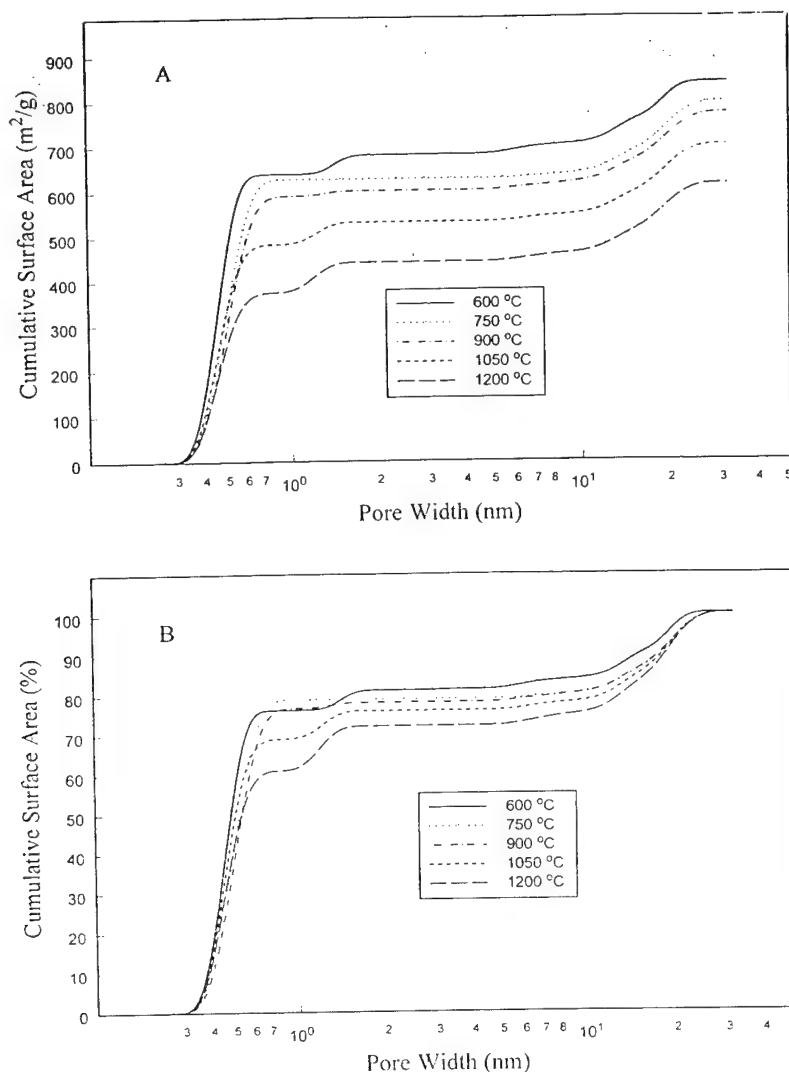


Fig. 4. Effect of the carbonization temperature on the cumulative surface areas of the carbon xerogels in terms of: (A) absolute volumes; and (B) percentages.

600°C, as seen from Fig. 2(A). An explanation for this behavior was obtained from the skeletal densities and TGAs shown in Fig. 5(A).

As the carbonization temperature increased, the skeletal density also increased significantly up to 1050°C; it then levelled off at  $2.1 \text{ g cm}^{-3}$ , which was just below the theoretical density of graphite ( $2.25 \text{ g cm}^{-3}$ ) [22]. Moreover, the TGAs shown in Fig. 5(B), after exhibiting a 50% weight loss essentially independent of the carbonization temperature above 750°C, exhibited very little weight loss between 750 and 1200°C, indicating that only structural changes were taking place during carbonization in this temperature range. This TGA coupled with the skeletal densities suggested that the micropores were disappearing due to densification of the carbon xerogels, most likely due

to C–C bond formation at the expense of C–H bond breakage. The micrographs in Fig. 2 indicated that this densification process was very subtle because the carbon xerogel particle size decreased only slightly when carbonized at 1200°C compared to that at 600°C. The results also suggested that the initial increase in the total pore volume in going from the carbon xerogel carbonized at 600°C to the one carbonized at 750°C [Fig. 3(A)] was most likely caused by the removal of surface functional groups, because the TGAs showed that this change was accompanied by a weight loss of about 7%.

Similar effects of the carbonization temperature have also been reported in the literature for the mesopore structure of R–F carbon aerogels. Tamon et al. [7] showed that the mesopore volume decreased with an increase in

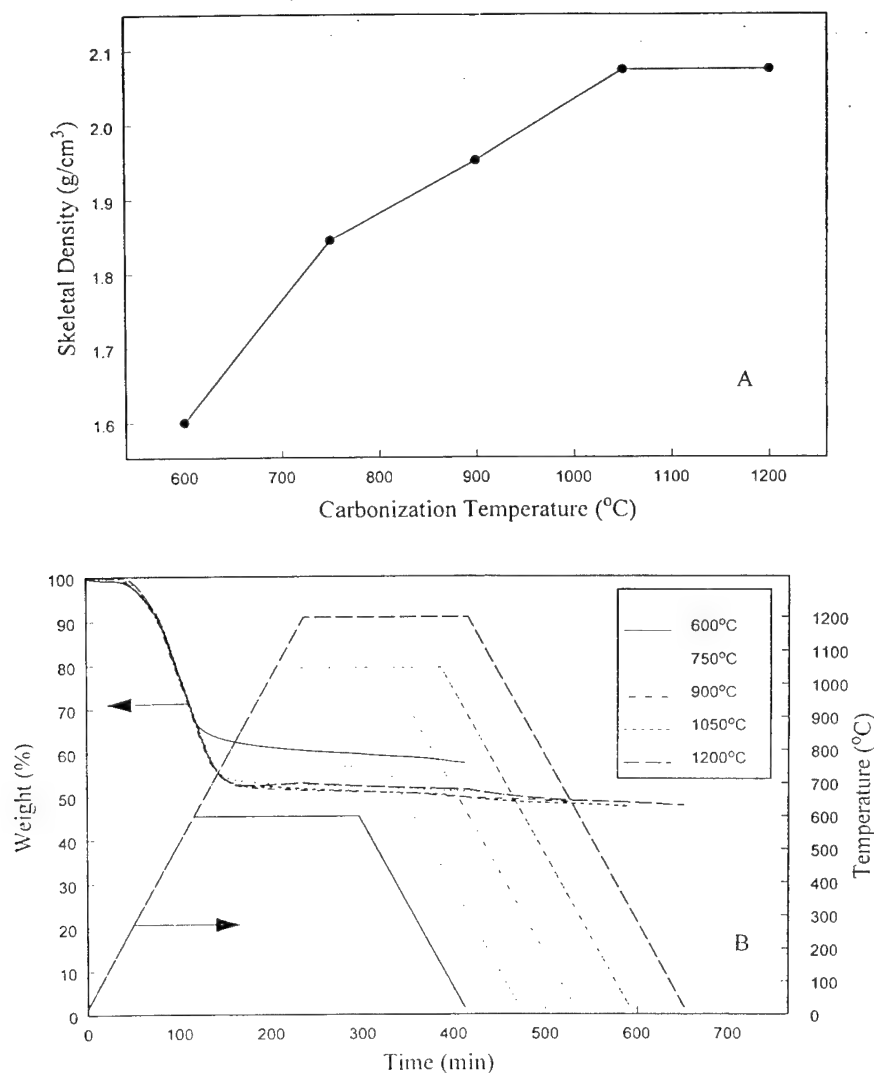


Fig. 5. Effect of the carbonization temperature on the: (A) skeletal densities; and (B) TGAs of the carbon xerogels.

the carbonization temperature, with little effect on the peak pore size. The same effects were observed here with the R-F carbon xerogels, but in the micropore size range instead of the mesopore size range.

### 3.2. Effect of CO<sub>2</sub>-activation time

The effect of the CO<sub>2</sub>-activation time on the pore structure of the carbon xerogels is shown in Figs. 6–10. Fig. 6(A) displays the N<sub>2</sub> adsorption isotherms for the different extents of CO<sub>2</sub>-activation that ranged from no activation to 3 h; Fig. 6(B) shows the corresponding PSDs. Again, note that the data points (over 200 per isotherm and PSD) have been removed for clarity. All of the adsorption isotherms in Fig. 6(A) were similarly shaped and once again typical of a material that contains both microporosity

and mesoporosity [21]. However, as the CO<sub>2</sub>-activation time increased, very distinct changes occurred in both the slope of the isotherm after the initial sharp rise at very low relative pressures and the amount adsorbed. An increase in the slope of the isotherm over a very broad relative pressure range was indicative of the creation of larger pores with increasing CO<sub>2</sub>-activation time. The PSDs in Fig. 6(B) show the sizes of the pores that were actually created.

All of the samples exhibited a peak with a mean pore width of about 0.6 nm, which increased with time up to 2.5 h, and then decreased slightly after 3 h. All of the samples also exhibited a peak with a mean pore width of about 1.3 nm, which increased consistently with time. Some peaks with pore widths between 2 and 10 nm also appeared and grew with time; however, the peak with a mean pore width

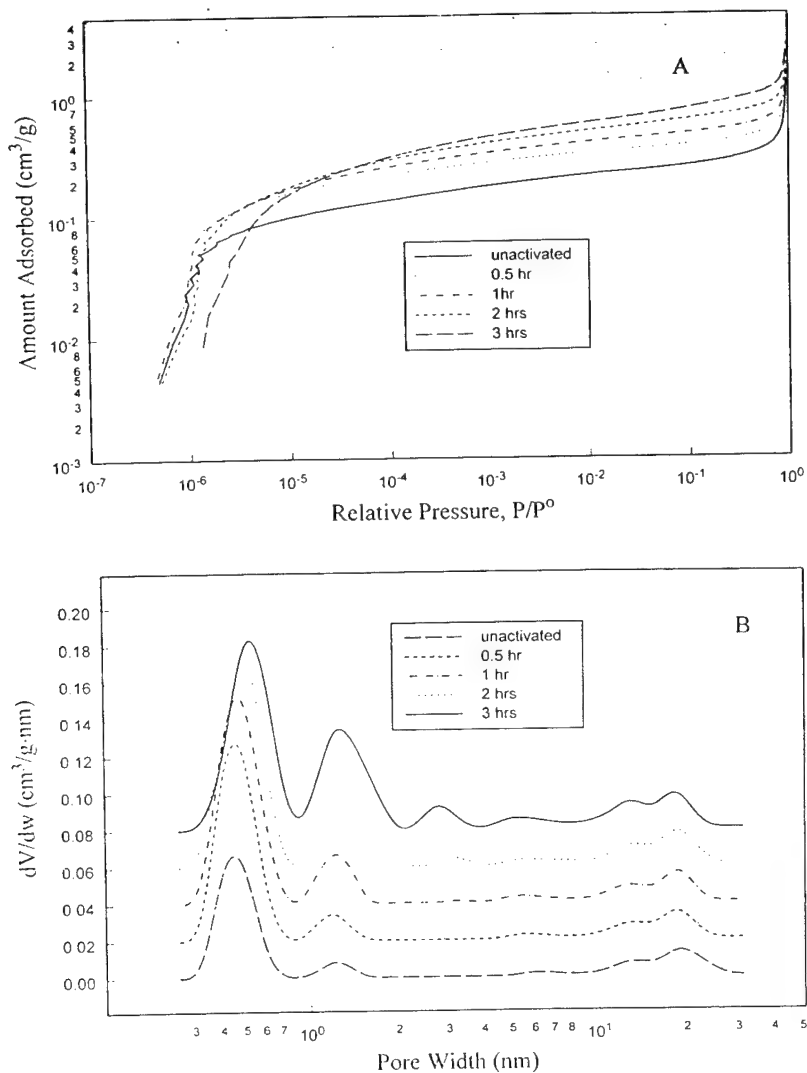


Fig. 6. Effect of the CO<sub>2</sub>-activation time on the: (A) experimental nitrogen adsorption isotherms at 77 K in terms of the volume of liquid nitrogen adsorbed per gram of adsorbent; and (B) the corresponding PSDs from DFT for the carbon xerogels.

of around 20 nm changed little with time. These trends show very clearly the creation and destruction of small micropores in the 0.6 nm range with increased CO<sub>2</sub>-activation time, some of which became large micropores in the 1.3 nm range and small mesopores in the 3 nm range with further burn-off of carbon. Moreover, the micrographs in Fig. 7 show that these xerogels were composed of carbon nanoparticles of the order 10–20 nm in diameter, and thus the larger mesopores (20 nm range) were derived from the voids between the carbon particles, the sizes of which were not affected by the CO<sub>2</sub>-activation time. These micrographs also indicated that the smaller mesopores (3 nm range) and all of the micropores were derived from pores within the nanoparticles, the distributions of which were greatly affected by the CO<sub>2</sub>-activation time, as

discussed above. The cumulative pore volumes shown in Fig. 8(A,B), in terms of absolute values and percentages, also show these marked effects of CO<sub>2</sub>-activation time.

In general, as the CO<sub>2</sub>-activation time increased, larger pores were created, some in the micropore size range 1–2 nm, some in the smaller mesopore size range 2–10 nm and some even in the larger mesopore size range 10–20 nm. These effects were reflected in the total pore volume increasing significantly from 1.5 to 2.5 cm<sup>3</sup> g<sup>-1</sup> with an increase in the CO<sub>2</sub>-activation time. For the unactivated carbon xerogel, the micropores accounted for about 10%, the smaller mesopores accounted for about 5%, and the larger mesopores accounted for about 85% of the total pore volume. In contrast, for the carbon xerogel CO<sub>2</sub>-activated for 3 h, the micropores accounted for about 20%, the

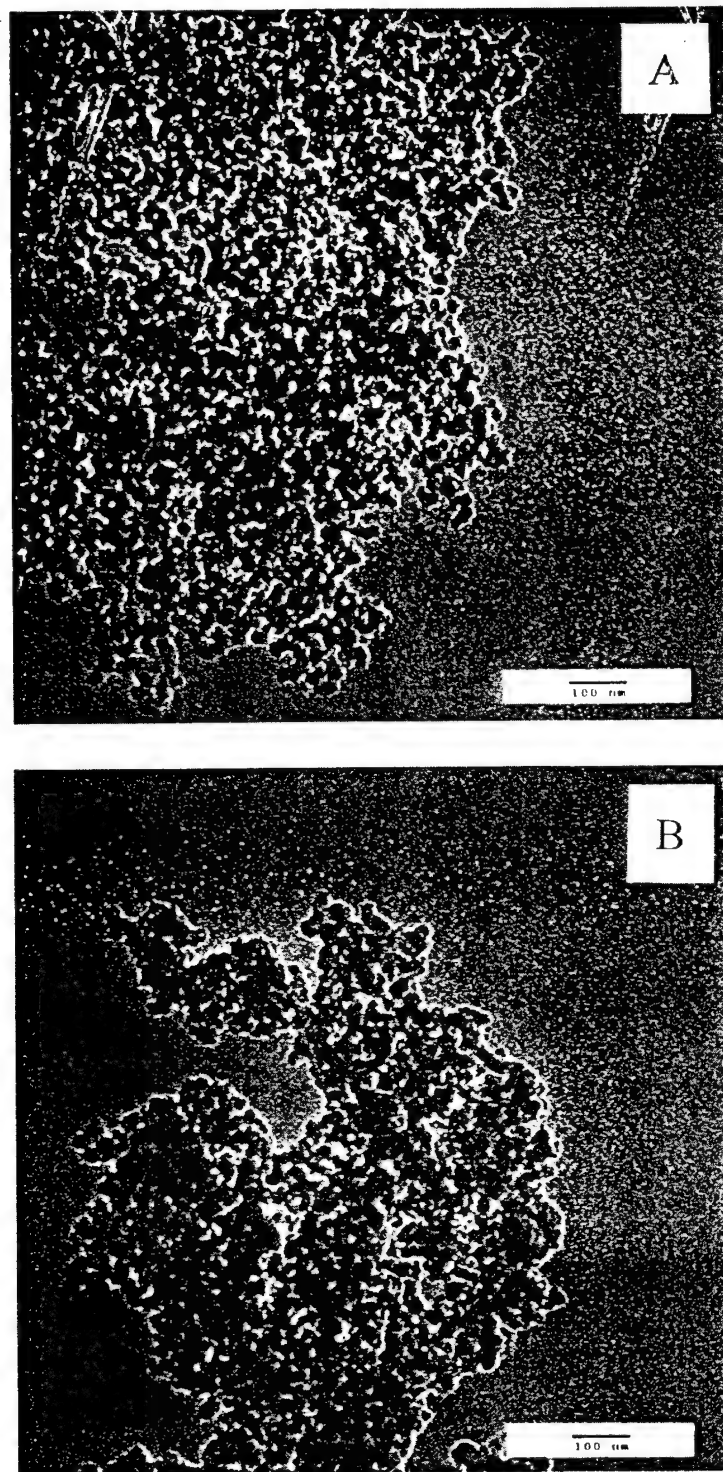


Fig. 7. TEM micrographs of the carbon xerogels  $\text{CO}_2$ -activated for: (A) 1 h; and (B) 3 h.

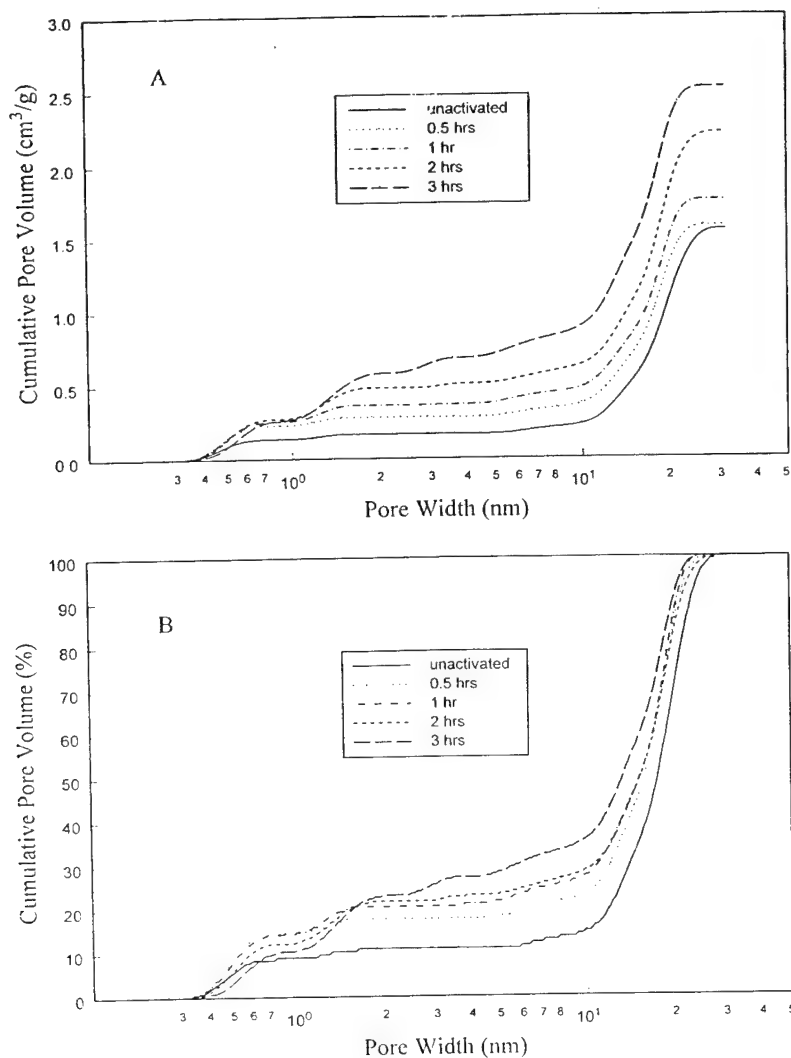


Fig. 8. Effect of the CO<sub>2</sub>-activation time on the cumulative pore volumes of the carbon xerogels in terms of: (A) absolute volumes; and (B) percentages.

smaller mesopores accounted for about 15% and the larger mesopores accounted for about 65% of the total pore volume. This large change in the micropore and smaller mesopore volumes had a significant impact on the cumulative surface areas.

The cumulative surface areas shown in Fig. 9(A,B), in terms of absolute values and percentages, show that the total surface area increased from 600 to 1600 m<sup>2</sup> g<sup>-1</sup> with an increase in the CO<sub>2</sub>-activation time from 0 to 3 h. The cumulative surface area corresponding to pore widths of less than 0.7 nm was about 450 m<sup>2</sup> g<sup>-1</sup> for the unactivated carbon xerogel. It consistently increased with the CO<sub>2</sub>-activation time to about 800 m<sup>2</sup> g<sup>-1</sup> for the carbon xerogel CO<sub>2</sub>-activated for 2.5 h, but then decreased to about 500 m<sup>2</sup> g<sup>-1</sup> for the carbon xerogel CO<sub>2</sub>-activated for 3 h. The cumulative surface area corresponding to pore widths

ranging from 0.7 to 10 nm, however, increased consistently with the CO<sub>2</sub>-activation time with much of the increase caused by an increase in the number of larger micropores. In contrast, the cumulative surface area corresponding to pore widths between 10 and 25 nm changed little with activation time. In terms of percentages, excluding the unactivated carbon xerogel, the cumulative surface area for pore widths of less than 0.7 nm decreased from about 70 to 35% with an increase in the activation time. However, the cumulative surface area for the pore widths between 0.7 and 2 nm increased with an increase in the activation time from about 20 to 45%. Except for the carbon xerogel activated the longest, about 20% of the surface area was due to pore widths in the 20–30 nm range, with little contribution coming from the 2–10 nm pores. For the carbon xerogel activated the longest, a 10%



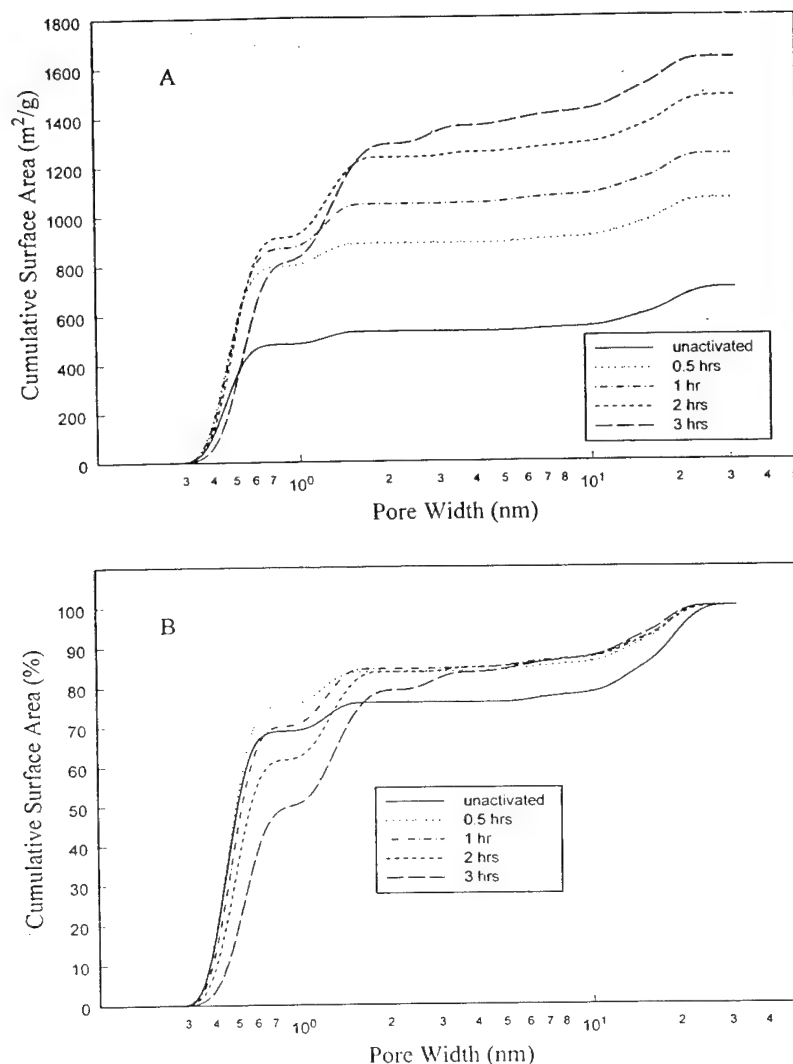


Fig. 9. Effect of the CO<sub>2</sub>-activation time on the cumulative surface areas of the carbon xerogels in terms of: (A) absolute volumes; and (B) percentages.

contribution to the surface area came from both pore size ranges. These results also showed that in general 10–20% of the pore volume contained within the micropores accounted for 75–85% of the surface area.

Clearly the effect of the CO<sub>2</sub>-activation time on the pore structure of these carbon xerogels was much more pronounced compared to the effect of carbonization temperature, and it was manifest through radical changes in both the sizes and the quantities of micropores and small mesopores. Fig. 10(A) shows that these changes were also accompanied by a slight densification of the carbon xerogels with an increase in the activation time up to very near the theoretical density of graphite (2.25 g cm<sup>-3</sup>) [22] after 2 h of activation. Once again, however, the changes occurred with hardly any change in the particle size of the

carbon xerogels, as shown in Fig. 7. These results, along with the TGA shown in Fig. 10(B), indicated that the activation process, which essentially removed surface functional groups and carbon, thereby creating more pores and surface area, took place mainly within the carbon xerogel particles. The weight loss due to activation was also significant, where 75% of the carbon xerogel was lost after 3 h. It was interesting that this weight loss occurred simultaneously with densification, which suggested that some of the loss in micropores that must have occurred due to densification, as demonstrated in the carbonization study, was overwhelmed by the effect of the activation, with the net effect being the creation of more of the larger micropores and small mesopores. But remember that the number of smaller micropores increased and then de-

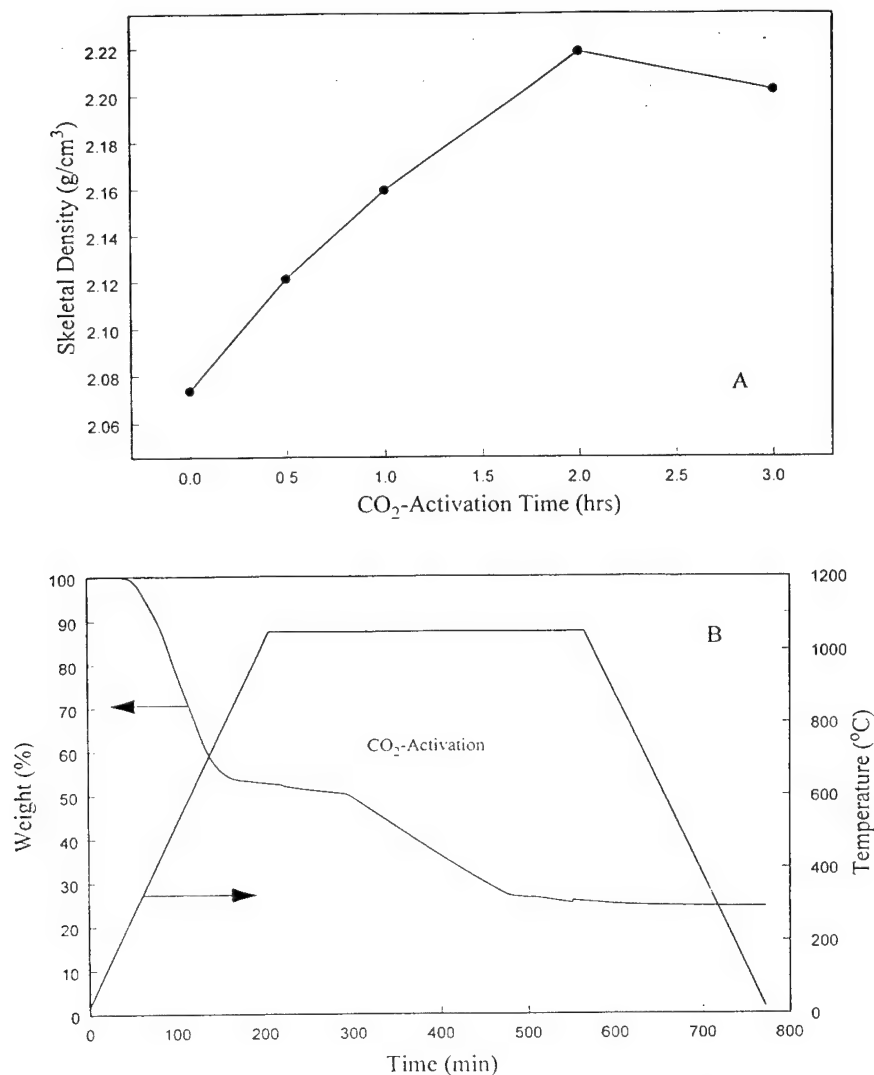


Fig. 10. Effect of the CO<sub>2</sub>-activation time on the: (A) skeletal densities; and (B) TGAs of the carbon xerogels.

creased with an increase in the CO<sub>2</sub>-activation time. Some of this decrease may have been due partly to densification, similar to the effect of carbonization, and it may have also been due partly to carbon burn-off where smaller pores became larger pores.

The effect of activation on R-F carbon aerogels was also briefly investigated by Pekala et al. [5]. They showed a marked increase in the BET surface area and total pore volume for a CO<sub>2</sub>-activated carbon aerogel compared to an unactivated one. Moreover, there was essentially no effect of activation on the medium mesopores. Both of these results are consistent with the trends observed here for the effect of CO<sub>2</sub>-activation on the pore structure of these carbon xerogels. Once again, however, the carbon aerogels were largely mesoporous materials, whereas the carbon xerogels contained a large fraction of micropores.

#### 4. Conclusions

The pore structure of carbon xerogels derived from resorcinol-formaldehyde resins was modified significantly during controlled, structure-altering experimentation with the carbonization temperature and CO<sub>2</sub>-activation time. Extensive characterization of these materials, based mostly on pore size information obtained from nitrogen adsorption isotherms coupled with density functional theory analysis revealed some very interesting effects and trends. Increasing the carbonization temperature caused a decrease in the number of micropores in the 0.6 nm range, but it had little effect on the mesopore size distribution and thus mesopore cumulative pore volumes and surface areas. In contrast, increasing the CO<sub>2</sub>-activation time caused an increase in the number of both micropores and mesopores, where

pores in the 6 Å range eventually became pores in the 1.3 nm range, and the cumulative surface areas and pore volumes both increased significantly, indicative of the creation of more pores with further carbon burn-off. The skeletal densities also increased significantly, approaching that of graphite, with an increase in both the carbonization temperature and the CO<sub>2</sub>-activation time, but the nanoparticle size was largely unaffected. These results indicated that significant intraparticle restructuring occurred that was mainly due to the removal of surface functional groups and/or the elimination of smaller micropores. Weight loss was nearly independent of the carbonization temperature at about 50%, but it was strongly dependent on the CO<sub>2</sub>-activation time with a maximum loss of about 75%. Overall, this study is thought to lend much insight into the development of unique synthetic carbon materials having a controlled pore structure.

### Acknowledgements

This material is based upon work supported in part by the US Army Research Office under Grant No. DAAH04-96-1-0421 and in part by the US Department of Energy under Cooperative Agreement No. DE-FC02-91ER75666. Many thanks to Dr. Jacek Jagiello of the Westvaco Charleston Research Center for measuring the nitrogen adsorption isotherms and calculating the PSDs from a DFT analysis.

### References

- [1] Pekala RW. *J Mat Sci* 1989;24:3221.
- [2] Pekala RW, Alviso CT, Lemay JD. In: Hensch LL, West JK, editors. *Chemical processing of advanced materials*. New York: John Wiley, 1992.
- [3] Mayer ST, Kaschmitter JL, Pekala RW. *Proc Symp on New Sealed Rechargeable Batteries and Supercapacitors*, PV 93-23, Electrochemical Society, Kyoto, Japan, 1993.
- [4] Mayer ST, Pekala RW, Kaschmitter JL. *J Electrochem Soc* 1993;140:446.
- [5] Pekala RW, Mayer ST, Kaschmitter JL, Kong FM. In: Attia YA, editor. *Sol-gel processing and applications*. New York: Plenum Press, 1994.
- [6] Tamon H, Ishizaka H, Mikami M, Okazaki M. *Carbon* 1997;35:791.
- [7] Tamon H, Ishizaka H, Araki T, Okazaki M. *Carbon* 1998;36:1257.
- [8] Tamon H, Ishizaka H. *Carbon* 1998;36:1397.
- [9] Lin C, Ritter JA. *Carbon* 1997;35:1271.
- [10] Brinker CJ, Scherer GW. *Sol-gel science*. San Diego, CA: Academic Press, 1990.
- [11] Ruben GC, Pekala RW, Tillotson TM, Hrubesh LW. *J Mat Sci* 1992;27:4341.
- [12] Ruben GC, Pekala RW. *J Non-Cryst Solids* 1995;186:219.
- [13] Seaton NA, Walton JPRB, Quirke N. *Carbon* 1989;27:853.
- [14] Brauer P, Poosch H-R, Szombathely MV, Heuchel M, Jaroniec M. In: Suzuki M, editor. *Fundamentals of adsorption*. New York: Elsevier Science, 1993.
- [15] Lastoskie C, Gubbins KE, Quirke N. *J Phys Chem* 1993;97:4789.
- [16] Russell BP, LeVan MD. *Carbon* 1994;32:845.
- [17] Jagiello J, Tolles D. In: Meunier F, editor. *Fundamentals of adsorption*. Paris: Elsevier Science, 1998.
- [18] Szombathely MV, Brauer P, Jaroniec M. *J Comput Chem* 1992;13:17.
- [19] Jagiello J. *Langmuir* 1994;10:2778.
- [20] Gregg SJ, Sing KSW. *Adsorption, surface area and porosity*. New York: Academic Press, 1982.
- [21] Sing KSW, Everett DH, Haul RAW, Moscou L, Pierotti RA, Rouquerol J, Siemieniowska T. *Pure and Appl Chem* 1985;57:603.
- [22] West RC, Astle MJ. *CRC handbook of chemistry and physics*, 62nd ed., CRC Press, Boca Raton, FL, 1981–1982.

**A NONSTOICHIOMETRIC STRUCTURAL MODEL TO CHARACTERIZE CHANGES IN THE  
NICKEL HYDROXIDE ELECTRODE DURING CYCLING**

Venkat Srinivasan,<sup>1,\*</sup> Bahne C. Cornilsen<sup>2,\*\*</sup> and John W. Weidner<sup>1,\*\*</sup>

1. Department of Chemical Engineering  
University of South Carolina  
Columbia, SC 29208

2. Department of Chemistry  
Michigan Technological University  
1400 Townsend Drive, Houghton, MI 49931

*Manuscript Submitted to  
The Journal of The Electrochemical Society  
as a Technical Paper*

June 20, 2000

---

\* Electrochemical Society student member

\*\* Electrochemical Society active member

## **Abstract**

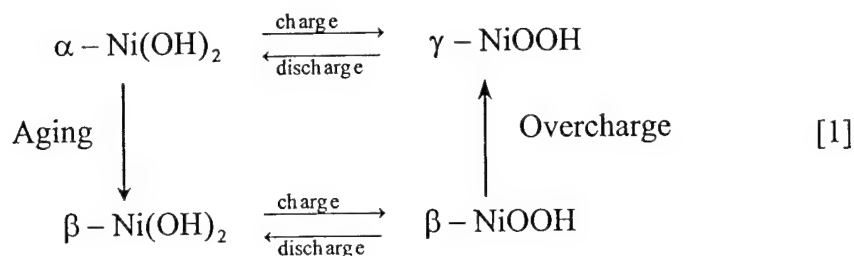
A procedure is developed whereby experimental changes in capacity and mass can be correlated with the nonstoichiometry and point defect structure of nickel hydroxide thin films. The capacity and mass of the films are simultaneously monitored using an electrochemical quartz crystal microbalance (EQCM). This information is used as input into the point defect-containing structural model to track the changes that occur during short term cycling. Pure nickel hydroxide films have been chosen as the test material. The loss in capacity on cycling is explained based on incomplete incorporation of potassium ions in (or near) the nickel vacancy during charge, as additional protons are then allowed to occupy the vacant lattice site. The model and methodology developed in this paper can be used to correlate electrochemical signatures with material microstructure.

## Introduction

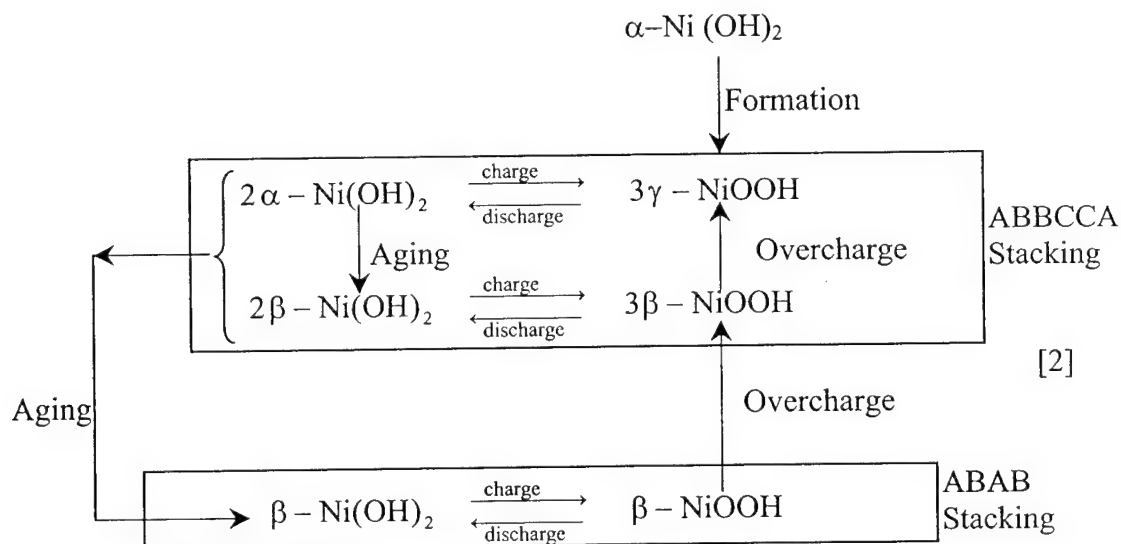
Nickel hydroxide is the positive electrode in a number of battery systems, namely, the Ni-Cd, Ni-MH and Ni-H<sub>2</sub> cells.<sup>1</sup> In addition, the material finds applications in electrochromic devices for use as “smart windows”.<sup>2,3</sup> The active material preparation often involves precipitation of the hydroxide from a nitrate salt solution, either by chemical or electrochemical techniques.<sup>4</sup> Depending on the preparation conditions, the electrochemical signatures of the active material are known to vary.<sup>5,6</sup> In addition, variations in capacity and voltage are also seen on cycling.<sup>7-9</sup> All these variations have been attributed to differences in the structures of these materials.<sup>5</sup>

Bode and coworkers described the reactions occurring in the solid active material in terms of four phases, namely (i) an anhydrous phase termed  $\beta$ -Ni(OH)<sub>2</sub>, (ii) a hydrated phase termed  $\alpha$ -Ni(OH)<sub>2</sub>, and (iii) two oxidized phases, termed  $\beta$ -NiOOH or  $\gamma$ -NiOOH.<sup>10</sup> Oxidation of  $\beta$ -Ni(OH)<sub>2</sub> resulted in the formation of  $\beta$ -NiOOH while oxidation of  $\alpha$ -Ni(OH)<sub>2</sub> resulted in  $\gamma$ -NiOOH. The  $\beta$  phase could convert to the  $\gamma$  phase on overcharge, taking the material to the  $\alpha$ - $\gamma$  cycle, and the  $\alpha$  phase could transform to the  $\beta$  phase in concentrated alkali, returning the electrode to the  $\beta$ - $\beta$  cycle. This reaction scheme can be schematically represented as<sup>10</sup>





However, over the past decade, Raman spectroscopic studies on the active material have indicated that the four electrochemically active materials are of the same nonclose-packed crystal structure (...ABBCCA... stacking), with the close-packed phase (...ABAB... stacking) being electrochemically unstable,<sup>11-15</sup> with little change in the Raman spectrum upon cycling and upon aging in hot concentrated alkali.<sup>20</sup> This was represented in the form of a modified Bode diagram (see Cornilsen<sup>16</sup>) as



Since the  $2\alpha$ - $3\gamma$  and the  $2\beta$ - $3\beta$  cycles involve materials that are nonclose-packed, there is no phase transition involved in going from one cycle to the other. On the other hand, aging from the  $2\alpha$  to the  $\beta$  involves a structural change as the  $\beta$  material is close-packed.

Loyselle *et al.*<sup>11</sup> used a point defect approach to describe the active material and proposed that the difference between the two Barnard cycles<sup>5</sup> (the two reactions represented in the upper rectangle) was the level of nickel vacancies,  $V_{Ni}$ , not the crystal structures. For example, the  $2\alpha-3\gamma$  cycle was observed to have 25% nickel defects (*i.e.* 25% nickel vacancies), while the  $2\beta-3\beta$  cycle has 11% nickel defects.<sup>11</sup> These vacancies may either be occupied by protons, by potassium ions, or left vacant. This approach was used to explain some of the phenomena unique to the nickel electrode (*e.g.*, existence of a maximum oxidation state of 3.67).<sup>15</sup> The modified Bode diagram, as defined relative to Bode's 2 cycles, suggests a finite number of distinct reactions within the ...ABBCCA... structure. In reality, this point defect approach argues that any reaction within this ...ABBCCA... structure is part of a continuum that depends on the concentrations of protons, alkali cations, Ni vacancies, and oxygens present in the lattice.

In this paper, we demonstrate this continuum of reactions as shown in the modified Bode diagram and with respect to the point-defect model. We also show how changes in capacity and mass are related to changes in the point defect parameters, and which parameter changes are consistent with experimental observations cited in the literature. Finally, we correlate changes in mass and capacity during cycling to changes in the point defect parameters. This detailed analysis of cycling provides insight into the microscopic changes that occur in the active material as the as-deposited nickel hydroxide is subjected to short-term cycling (*i.e.*, nine cycles).

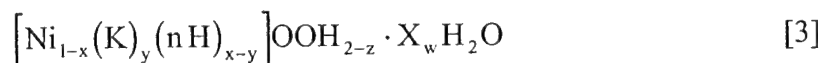
## Experimental

Films of nickel hydroxide were deposited electrochemically on a  $0.196\text{ cm}^2$  gold substrate sputtered on a quartz crystal in a procedure described in detail elsewhere.<sup>17, 18</sup> Prior to deposition, the crystals were immersed for a few seconds in a freshly prepared 3:1 mixture of concentrated sulfuric acid and hydrogen peroxide (Piranha reagent) and then rinsed of reagents using deionized water (resistivity  $18\text{ M}\Omega\text{-cm}$ ). The films were deposited at room temperature in a bath containing  $1.8\text{ M Ni(NO}_3)_2$  and  $0.075\text{ M NaNO}_3$  in a solvent of 50 v/o ethanol using a cathodic current of  $1.0\text{ mA}$  ( $5.1\text{ mA/cm}^2$ ). The mass of the film was monitored using an EQCM (EG&G model QA-917), and the current was switched off once the mass reached  $67\text{ }\mu\text{g}$ . It was observed that deposition continued as a result of the alkaline pH at the electrode surface. Once the mass change was negligible, the deposition solution was quickly drained from the cell and the deposited film was washed in deionized water. This procedure resulted in films of mass  $69.1\pm0.01\text{ }\mu\text{g}$ . In order to determine the moles of Ni in a film, five films were stripped with  $1.0\text{ ml}$  of dilute nitric acid ( $\text{pH}=1.0$ ) and further flushed with  $3.0\text{ ml}$  of degassed, deionized water. The resulting  $4.0\text{ ml}$  of solution was injected into an ion-chromatograph (DIONEX) and the moles of nickel were determined from the concentration and volume of solution. Dividing the mass of the film by the moles of nickel gave an average molecular weight for the five films of  $121\pm6$  grams of as-deposited material per mole of nickel. Films cycled in 3% KOH for 25 cycles were found to have a similar nickel content, indicating no loss of nickel on cycling.

For galvanostatic charge/discharge experiments, 3% KOH solution was placed in the EQCM cell containing a nickel hydroxide film. The cell also contained a SCE reference and a platinum counter electrode. An EG&G M273 potentiostat/galvanostat was used to control the current, and the mass was monitored by the EQCM. Experiment control and data acquisition were achieved using the M270 software.

### Defect Model Development

The nickel hydroxide active material deposited using the cathodic precipitation technique produces porous films<sup>19</sup> with a considerable amount of electrolyte incorporated in the pores.<sup>18</sup> Therefore, the film can be considered as a collection of crystallites in a porous matrix, as seen in the schematic shown in Figure 1. Based on the spectroscopic evidence and chemical analyses, this material is seen to have considerable nonstoichiometry and can be represented using point defect notation as<sup>10-15</sup>



That is, a fraction,  $x$ , of the nickel lattice sites are vacant. The potassium ions occupy a fraction  $y$  of these nickel vacancies and the remaining vacancies are occupied by  $n$  protons. When there are no protons on the nickel vacancy (*i.e.*,  $n=0$ ) the empty Ni site will be represented by the notation  $V_{\text{Ni}}$ . In addition, there are two oxygen sites and two interlamellar proton sites per Ni lattice site in the unit cell. The occupation of the proton sites varies, depending on the state of charge of the material. For example, in the fully discharged state there will be two interlamellar protons ( $z=0$ ), and in the fully charged

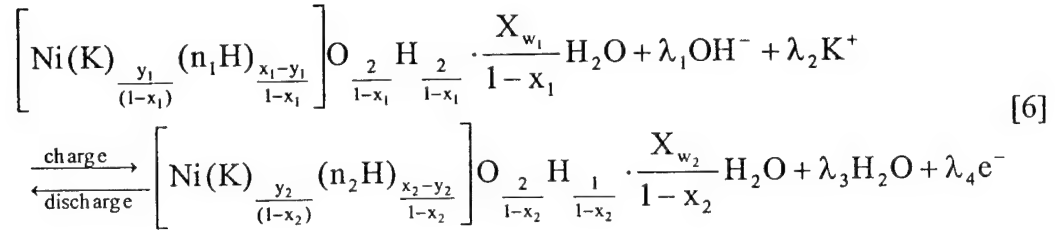
material there will be only one interlamellar proton ( $z=1$ ). Intermediate values of  $z$  between 0 and 1 represent intermediate states of charge. In addition, water molecules can be present either as interlamellar water or between the crystallites, and are represented by  $X_w$ .

Equations 4 and 5 relate the film oxidation state (Ox) and molecular weight (M) to the defect parameters defined in equation 3.

$$Ox = \left[ \frac{(2 + z) - y - n(x - y)}{1 - x} \right] \quad [4]$$

$$M = 58.69 + \frac{39.1y + n(x - y) + 33 + z}{1 - x} + 18 \frac{X_w}{1 - x} \quad [5]$$

During charging, the mechanisms that occur at the electrode/electrolyte interface are sketched in Figure 1. Protons in the solid matrix diffuse to the surface of the crystallite and combine with hydroxyl ions to form water. Simultaneously, a potassium ion may intercalate into the crystallite and reside in or near the nickel vacancy.<sup>10</sup> During this process, the oxidation state of nickel increases as an electron is ejected into the external circuit. The reverse of this process occurs on discharge. Using the notation established in equation 3, these reaction sequences can be combined to give the following overall reaction on a per nickel basis



where,

$$\lambda_1 = \left[ \frac{n_1(x_1 - y_1) - 2}{(1 - x_1)} - \frac{n_2(x_2 - y_2) - 3}{(1 - x_2)} \right] \tag{7}$$

$$\lambda_2 = \left[ \frac{y_2}{(1 - x_2)} - \frac{y_1}{(1 - x_1)} \right] \tag{8}$$

$$\lambda_3 = \left[ \frac{n_1(x_1 - y_1)}{(1 - x_1)} - \frac{n_2(x_2 - y_2) - 1}{(1 - x_2)} \right] + \frac{X_{w_1}}{1 - x_1} - \frac{X_{w_2}}{1 - x_2} \tag{9}$$

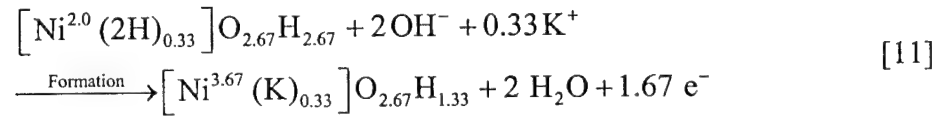
$$\lambda_4 = \left[ \frac{3 - y_2 - n_2(x_2 - y_2)}{(1 - x_2)} - \frac{2 - y_1 - n_1(x_1 - y_1)}{(1 - x_1)} \right] \tag{10}$$

The subscripts  $i=1$  and  $i=2$  on  $x$ ,  $y$ ,  $n$  and  $X_w$  represent the fully discharged and fully charged states, respectively. Therefore, reaction 6 is written to represent the defect structure of the two end-point materials upon discharge and charge (*i.e.*,  $z=0$  and  $z=1$ , respectively). An equation analogous to equation 6 can be written for intermediate oxidation states by including  $z$  as a variable. In this study, it is assumed that only data that has undergone complete charge or discharge is analyzed, and therefore  $z$  will be either 0 (completely discharged) or 1 (completely charged). However, because a shortage of interlamellar protons has the same effect on the charged capacity and the mass change



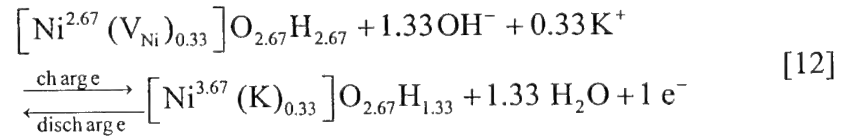
as the addition of vacancy protons, a change in  $n$  can have the same effect as a change in  $z$ . Distinguishing between these two types of protons is not possible in this work.

Reaction 6 can be used to represent specific reactions shown in the modified Bode diagram. For example, the  $\alpha$  to  $3\gamma$  reaction (termed “formation” in reaction 2) can be obtained by substituting  $x_1=x_2=y_2=0.25$ ,  $n_1= 2$  and  $y_1=0$  into reaction 6. The resulting equation is<sup>15</sup>



The superscripts on the Ni define the nickel oxidation state. When the material is charged, one interlamellar proton per Ni site is removed for equation 3 (1.33 interlamellar protons per  $\text{Ni}_{\text{Ni}}$ , where  $\text{Ni}_{\text{Ni}}$  are the nickel sites filled with nickel cations and equal to 1 in equation 11), and all the protons on the nickel vacancies are replaced by potassium ions (*i.e.* ,  $y_2=x_2$ ). Since none of the nickel vacancies are occupied by protons, the value of  $n_2$  is irrelevant.

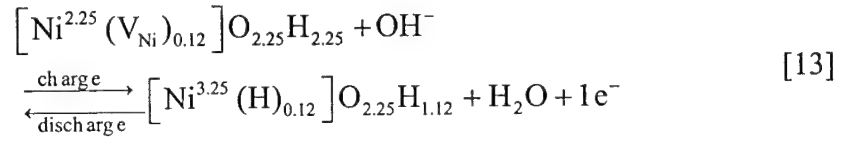
After the formation, the  $2\alpha$ - $3\gamma$  reaction can be obtained by substituting  $x_1=x_2=y_2=0.25$ ,  $n_1= 0$  and  $y_1=0$  as shown in eqn. 12.<sup>15</sup>



The discharge of the  $3\gamma$  material involves the incorporation of interlamellar protons, and the release of potassium ions from the nickel vacancies. However, the discharged material does not contain protons on the nickel vacancies as did the as-deposited material

(see the left-hand side of equation 11). Consequently, the oxidation state of the  $2\alpha$  material is 2.67 rather than the 2.0 of the  $\alpha$  material.

Similarly, the  $2\beta$ – $3\beta$  cycle is considered to exhibit a defect content of 0.11<sup>15</sup> and this reaction is obtained by substituting  $x_1=x_2=0.11$ ,  $n_1=0$ ,  $y_1=y_2=0$  and  $n_2=1$  as shown in eqn. 13. In contrast to the  $2\alpha$ – $3\gamma$  cycle, each vacancy in the  $2\beta$ – $3\beta$  cycle exchanges a proton rather than a potassium ion.



However, it is important to keep in mind that reactions 11-13 are in reality three examples of what is really a continuum of reactions, all of which are represented by reaction 6.

While Kim *et al.*<sup>7</sup> also used the defect model developed by Loyselle *et al.*<sup>11</sup> to analyze their data, they assumed that all variations in capacity occurred due to incomplete removal of interlamellar protons on charge (*i.e.*,  $z < 1$ ). They also assumed that the discharged material contained one proton per nickel vacancy (*i.e.*,  $n_1=1$ ,  $y_1=0$ ,  $x_1=0.25$ ), and on charge this proton was replaced with a potassium ion (*i.e.*,  $y_2=x_2=0.25$ ). The limitation of their assumptions is that changes in mass and capacity are linked through a single parameter,  $z$ . In addition, this does not enable them to explain the large capacity seen during the first charge (*i.e.*, formation) since  $n_1$  is equal to 1. Finally, using  $n_1=1$  with a defect content of 0.25 obtained from spectroscopic data,<sup>11</sup> the maximum oxidation state for nickel is limited to 3.33, which is well below the reported value of 3.67.<sup>7, 20-22</sup>

## Effect of Defect Parameters on the Capacity of the Active Material

In this section, the capacity of the active material (*i.e.*, the number of electrons transferred) during successive charge/discharge cycles is calculated from equation 10 for different values of the defect parameters  $x$ ,  $y$ , and  $n$ . The results of these calculations are compared with five experimental observations that are reported in the literature. The comparison provides insight into which parameters are most likely to change as nickel hydroxide films are cycled. The five observations are: (a) 1.67 electrons per nickel are transferred in the first charge<sup>22</sup>; (b) 1.0 electrons per nickel are transferred during the subsequent discharge and charge;<sup>22</sup> (c) the charge and discharge capacity decreases with cycling<sup>8,23</sup>; (d) the total mass of the film increases with cycling,<sup>24</sup> and (e) the mass of the film increases on charge and decreases on discharge.<sup>7, 23, 24</sup> Although the last two phenomena deal with mass and not capacity, these provide insight into how the defect parameters may change on cycling.

Although one could study numerous combinations of the six defect parameters (three each in the charged and discharged state), we present five scenarios, listed in Table 1, that provide insight into how the six parameters affect capacity. These scenarios also reflect the theories postulated in the literature to explain the observed capacity and mass change with cycling. The effect of varying some of the parameters within each scenario is also discussed. Using the defect parameters listed in the table, the number of electrons transferred as a function of cycle number are calculated from equation 10. For illustrative purposes, the parameters that vary in a given scenario are assumed to change linearly with cycle number. The number of electrons transferred per nickel *vs* cycle

number for scenarios 1-3 are plotted in Figure 2 and that for scenarios 4 and 5 are plotted in Figure 3.

Scenario 1 describes a  $2\alpha-3\gamma$  cycle (*i.e.*,  $x = 0.25$ ), where  $K^+$  is inserted on charge and progressively more of the potassium ions remain on the Ni vacancies during discharge (*i.e.*,  $y_1$  increases from 0 to 0.25). Scenario 2 describes the conversion of the material from the  $2\alpha-3\gamma$  to the  $2\beta-3\beta$  cycle (*i.e.*,  $x$  decreases from 0.25 to 0.11). For illustrative purposes, the decrease in defect content is assumed to occur on the discharge while on charge the defect content is unchanged. As the defect content of the film decreases with cycling, so does the amount of potassium exchanged. On discharge, two protons replace the potassium ions on the nickel vacancies (*i.e.*,  $n_1 = 2$ ). Scenario 3 describes a film converting from the  $2\beta-3\beta$  to the  $2\alpha-3\gamma$  cycle (*i.e.*,  $x$  increases from 0.11 to 0.25). Again, the increase in  $x$  has been taken to occur on the discharge, with  $x$  unchanged on charge. However, unlike scenario 2, no protons replace the potassium ions on discharge (*i.e.*,  $n_1 = 0$ ). Scenario 4 describes a  $2\alpha-3\gamma$  cycle (*i.e.*,  $x = 0.25$ ), where progressively less of the potassium ions are incorporated onto the Ni vacancies during charge (*i.e.*,  $y_2$  decreases from 0.25 to 0.11). The vacancies not filled with potassium are instead filled with two protons (*i.e.*,  $n_2 = 2$ ). Scenario 5 is a combination of scenarios 2 and 4, where the material is converting from the  $2\alpha-3\gamma$  to the  $2\beta-3\beta$  cycle with two protons replacing potassium ions on the Ni vacancy during charge. Note that the potassium ion content decreases at a greater rate than the decrease in the defect content. All five scenarios involve incorporation of potassium ions into the Ni vacancy on charge, which is consistent with observation (e) (*i.e.*, a mass increase is observed on charge).

Figure 3 reveals that scenario 1 results in a 1.67 electron transfer per nickel in the first charge and a  $\approx 1.0$  electron transfer in the subsequent discharge, consistent with observations (a) and (b). However, this scenario results in an increase in capacity on cycling, which is inconsistent with observation (c). As progressively less potassium is exchanged, the change in the oxidation state of nickel increases. Therefore, one can conclude that the increase in mass on cycling, observation (d), is not due to an increase in the amount of potassium ions remaining on the Ni vacancy, as suggested by previous researchers.<sup>24</sup>

While scenario 1 shows an increase in capacity on cycling, scenario 2 exhibits a decrease in capacity, consistent with observation (c). However, this decrease in capacity with cycling occurs steadily from 1.67 to 1.25 electrons per nickel, which is inconsistent with observation (b). The large electron transfer is due to the replacement of potassium ions with two protons on discharge. Since  $n_1 = 2$ , the oxidation state of the discharged material is 2.0 after each cycle. The oxidation state of the charged material decreases steadily from 3.67 to 3.25. If  $n_1$  was set equal to 1 rather than 2, the number of electrons transferred would decrease from 1.3 to 1.1 for cycles 2-9, and if  $n_1=0$  a 1.0 electron transfer would occur during each cycle. These results are in opposition to observations (b) and (c), respectively.

In contrast to scenarios 1 and 2, scenario 3 predicts a slight decrease in the discharge capacity on cycling as the number of electrons transferred decreases from 0.95 to 0.94. However, the first charge results in a 1.25 electron transfer as opposed to the 1.67 electron transfer noted in observation (a). This is a consequence of starting with a

defect content of  $x = 0.11$ . The only way to achieve a 1.67 electron transfer on the first charge is to start with a defect content of  $x = 0.25$ .

While scenarios 1-3 show results that are inconsistent with one or more of experimental observations (a)-(d), scenarios 4 and 5, shown in Figure 4, are consistent with all these observations. The reason these scenarios are consistent with the experimental observations is that progressively less of the potassium ions are incorporated onto the Ni vacancies during charge. Filling a nickel vacancy with two protons in the charged state rather than a potassium ion results in a decrease in the oxidation state of the charged material in order to compensate for the extra positive charge. In scenario 4, the oxidation state of the discharge material remains at 2.67, and therefore the number of electrons transferred decreases.

Scenario 5 is similar to scenario 2 in that both result in a decrease in capacity on cycling. The major qualitative difference between these two scenarios, though, is that scenario 2 shows a steady decrease in capacity with cycling while scenario 5 shows a sharp capacity decrease between cycles 1 and 2. The discontinuity in scenario 5 is due to the fact that there are no protons in the discharged material past the as-deposited state. This means 1.67 electrons are removed on the first charge but only 1.0 electrons are reinserted on the subsequent discharge. In contrast, scenario 2 always has two protons reintercalated into the defects after each discharge, thus allowing 1.67 electrons to be reinserted during the first discharge.

Although both scenarios show a steady decrease in capacity during cycles 2-9, this decrease occurs for different reasons. In scenario 2, the oxidation state of the



discharged material is always 2.0 because  $y_2 = 0$  and  $n_2 = 2$ , but the oxidation state of the charged material decreases because the defect content decreases. In scenario 5, both the oxidation state of the charged and discharged material decreases as  $x$  decreases. However, the oxidation state of the charged material decreases faster than the discharged material resulting in a net decrease in the number of electrons transferred. This greater decrease in the charged state is caused by  $y_2$  being less than  $x_2$ . If  $y_2$  were equal to  $x_2$  then the number of electrons transferred would be 1.0 for each cycle except for the first charge. The greater the difference between  $y_2$  and  $x_2$ , the larger the decrease in capacity. Note that intercalation of three protons rather than two in scenarios 4 and 5 would also show a decrease in capacity with cycle number, but the decrease would be even greater. The incorporation of additional protons ( $n > 1$ ) into the nickel vacancy, as postulated in scenarios 4 and 5, can also be thought of as incomplete removal of the interlamellar protons (*i.e.*, incomplete charging with  $z < 1$ ), with the nickel vacancy left vacant. As mentioned earlier, irrespective of the position of the proton (interlamellar or in the vacancy), the oxidation state and molecular weight are the same, and hence the capacity and mass changes are as well.

The decrease in capacity seen in scenarios 4 and 5 can also be achieved by setting  $x_1 = 0.25$  and  $n_1 = 0$ . This would fix the oxidation state of the discharge material at 2.67. Then if  $x_2$  progressively decreased on each cycle, with  $y_2 = x_2$ , the oxidation state of the charged material would decrease, thus decreasing the capacity. However, it seems unlikely that the defect content of the material would increase and decrease every charged-discharge cycle and hence this is not considered a likely scenario.

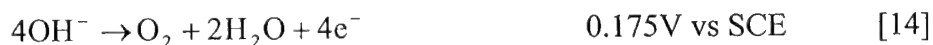
From these five different scenarios, some broad conclusions can be drawn on the possible ways to explain the experimental observations of cycled nickel hydroxide.

1. The 1.67 electron transfer on the first charge can only be achieved by starting with a defect content of  $x = 0.25$  and removing a net positive charge from each Ni vacancy. The net result is a nickel oxidation state of 3.67 after the first charge. Coupling this with a mass increase on charge, observation (e), it is most likely that the removal of a positive charge from the Ni vacancy occurs via the exchange of 2 protons with one  $K^+$  as opposed to removing one proton with no potassium exchange.
2. The 1.0 electron transfer in the first discharge is only possible by having an empty vacancy on discharge (*i.e.*,  $n_1=0$  and  $y_1 = 0$ ). Although a 1.0 electron transfer would occur regardless of the value for  $x$ , taking observations (a) and (b) together means  $x = 0.25$  and the oxidation state of nickel on the first discharge goes from 3.67 to 2.67.
3. The decrease in capacity of the active material below 1.0 electrons transferred per nickel can be achieved by (i) increasing the oxidation state of the discharged phase above 2.67 and/or (ii) decreasing the oxidation state of the charged phase below 3.67. A nickel oxidation state greater than 2.67 in the fully discharged material (*i.e.*,  $z = 0$ ) can only occur if  $x > 0.25$ . However, a defect content above 0.25 has never been observed experimentally. Therefore, item (i) is negated as a possible cause for observation (c). The capacity decrease appears to be caused by a decrease in the oxidation state of the charged material. This decrease could occur by either progressively filling the Ni vacancy with more than one charge-compensating ion (*i.e.*, two or more  $K^+$  or  $H^+$ ) or by decreasing  $x_2$  with cycling while keeping  $x_1$

constant. This later scenario seems unlikely since the defect content would be increasing and decreasing significantly during each charge/discharge cycle. It is unlikely that this repeated expanding and contracting of the lattice could occur on the time scale of each cycle. This oscillating defect content would also put undue stress on the crystal lattice. Therefore, the steady decrease in the oxidation state of the discharged material is most likely due to the filling of the Ni vacancy with more than one charge-compensating ion. The size of a potassium ion makes it improbable that two of these cations can be accommodated on one vacancy. It is more likely that an increasing number of vacancies are filled with more than one proton (*i.e.*,  $n_2 > 1$ ) on cycling. For this to occur,  $y_2$  has to decrease and /or  $n_2$  has to increase with cycling.

### Experimental Capacity and Mass-Change Data

Figure 4 shows the potential profiles for the first two charge and discharge cycles for a 69.1  $\mu\text{g}$  nickel hydroxide film. On charge, the oxidation of nickel is the main reaction between the 0.30 and 0.33 V vs SCE. However, at these voltages a fraction of the current is also going into the oxygen evolution reaction



As the nickel becomes fully oxidized (*i.e.*,  $z \rightarrow 1$ ), more of the current goes into reaction 14 and the voltage rises. At approximately 0.425 V, the material is fully charged and oxygen evolution becomes the sole reaction. Figure 4 also shows the potential profiles on discharge. The sharp drop in potential corresponds to the end of discharge (*i.e.*,  $z = 0$ ).

Potential profiles similar to those shown in Figure 4 were used to calculate the capacity transferred to or removed from the film. The capacity is the time required to fully charge or discharge the material,  $\tau$ , designated by  $\times$  on Figure 4, multiplied by the applied current. The resulting capacity on charge and discharge over 9 cycles is shown in Figure 5, where the symbols are a mean of 3-4 data sets and the error bars represent the high and low values. The larger error bars on the charge compared to the discharge is due to the larger error in identifying the end of charge as this point is not as well defined. The greater capacity on charge is due to the increased oxygen evolution compared to discharge.

The following equation is used to convert the capacity in Figure 5 to electrons transferred per nickel

$$\lambda_4 = \frac{\epsilon Q M_1^0}{F} \quad [15]$$

where  $M_1^0$  is the molecular weight of the film in the as-deposited state (121 g/mole Ni) and  $\epsilon$  is the fraction of the applied current that has gone into the nickel reaction during the course of the charge or discharge and is given by

$$\epsilon = 1 - \frac{\int_0^{\tau} i_{ox} dt}{Q} \quad [16]$$

The oxygen current at each time (*i.e.*, voltage) is given by the following Tafel expression

$$i_{ox} = i_{o,ox} \exp\left(\frac{\alpha nF(E - U_{ref,ox})}{RT}\right) \quad [17]$$

where,  $U_{ref,ox}$  is the equilibrium potential of the oxygen evolution reaction (0.175 V vs SCE in 3% KOH).<sup>25</sup>

The exchange current density for the oxygen evolution reaction,  $i_{o,ox}$ , was determined from equation 17 for each charge by setting  $\alpha n$  to 0.75,<sup>26</sup>  $E$  to the voltage of the second charge plateau, and  $i_{ox}$  to the applied current. This value of  $i_{o,ox}$  was used in Equation 17 to get  $i_{ox}$  as a function of  $E$  on the charge and the subsequent discharge. These oxygen currents were substituted into a discretized form of equation 16 to obtain  $\epsilon$ . This procedure was repeated for each of the films for the 1<sup>st</sup>, 6<sup>th</sup> and 9<sup>th</sup> cycle. It was found that the charges were approximately 17-20% inefficient, and the discharges were only 0.6-2% inefficient. Accounting for this inefficiency, it was seen that the charge and discharge capacities were within 2% of each other. Therefore, past the 1<sup>st</sup> cycle the capacity of the film on charge is the same as the capacity on the subsequent discharge. The electrons transferred per nickel are shown in Figure 6. Again, the symbols are a mean of 3-4 data sets and the error bars represent the high and low values. These data are consistent with the three previous experimental observations discussed earlier: (a)  $\approx 1.67$  electrons per nickel are transferred in the first charge<sup>22</sup>; (b) 1.0 electrons per nickel are transferred during the subsequent discharge and charge<sup>22</sup>; and (c) the charge and discharge capacity steadily decreases with cycling.<sup>8, 23</sup>

Using the average number of electrons transferred and assuming that the as-deposited material has an oxidation state of 2.0, the change in oxidation state can be

calculated on cycling as shown in Figure 7. As the material is cycled, the discharged state reaches a steady value close to 2.6. The charged material, on the other hand, starts with an oxidation state of 3.63 and on cycling the oxidation state reduces to 3.39 by the ninth cycle in a manner consistent with Figure 6 (*i.e.*, number of  $e^-$ ).

Using the EQCM, the mass change of the film was also monitored during charge and discharge. The results from the first two cycles are shown in Figure 8 as a function of time. Consistent with previous results, and observation (e), the mass of the film increased on charge and decreased on discharge.<sup>7, 8, 23, 24</sup> In addition, the mass change is negligible at the end of the charge as the oxygen evolution reaction does not result in a mass change. The total change in mass following complete charge and discharge is shown in Figure 9 for the first 9 cycles and is represented as the change in molecular weight (weight change divided by number of moles of Ni). Again, the symbols are a mean of 3-4 data sets and the error bars represent the high and low values. The magnitude of the mass change is more on charge than on the discharge, which is seen clearly in Figure 8. This is true for all cycles, and it results in an overall increase in the mass of the film on cycling, which is consistent with the observation (d).<sup>24</sup> Although the total mass of the film increases with cycling, the mass change from cycle to cycle decreases. For example, the mass reduction during the first discharge was approximately 5.3 g/mole Ni, but that for the ninth discharge was only 3.3 g/mole Ni.



## Extracting Defect Parameters from Experimental Data

The four defect parameters in the charged and discharged state ( $x$ ,  $y$ ,  $n$ , and  $X_w$ ) are evaluated sequentially by coupling the data in Figures 6 and 8 with equations 4, 5 and 10. The defect parameters in the as-deposited material are fully defined by using the molecular weight of the as-deposited material (*i.e.*, 121 g/mol) and the following three assumptions.

1. The as-deposited material has a nickel oxidation state of 2.0.
2. Nickel vacancies in the as-deposited material are void of potassium (*i.e.*,  $y_1=0$ ).

Coupled with assumption 1 this means that  $n_1 = 2$ .

3. There are 0.25 nickel vacancies per nickel lattice site (*i.e.*,  $x_1=0.25$ ).<sup>11</sup> Further, the number of nickel vacancies does not change appreciably during the first nine cycles (*i.e.*,  $x_1=x_2=0.25$  in all cycles).

Based on the molecular weight and these three assumptions, the water content of the as-deposited material,  $X_{w1}^0$ , is 0.69 moles of water per mole of nickel. Note that this water is different from the 0.67 H<sub>2</sub>O reported by Barnard *et al.*<sup>5</sup> for the 'activated'  $\alpha$  phase material. While the water reported by Barnard *et al.* is two protons on a nickel vacancy with an oxygen atom associated with it,<sup>16</sup>  $X_w$  is molecular water present in the lattice and/or between the crystallites and is in excess of the 0.67 H<sub>2</sub>O reported by Barnard *et al.*

Assumption 3 fixes  $x$ , and the three remaining defect parameters after the first charge must be determined from two pieces of information-the capacity and mass-change data. Since a unique set of parameters is not possible, two cases are examined here,  $n_2=2$

and  $n_2=3$ . As seen from Figures 6 and 8, 1.63 electrons/mol and 6.74 g/mol, respectively, are exchanged on the first charge. Therefore, equations 10 and 5 are used to give  $y_2=0.22$  and  $X_{w2}=0.555$  for  $n_2=2$ , and  $y_2=0.23$  and  $X_{w2}=0.525$  for  $n_2=3$ . Using these parameters,  $n_1=0$ , and the capacity and mass-change data during the first discharge,  $y_1$  and  $X_{w1}$  are calculated for the two values of  $n_2$ . This sequential process is continued until  $y$  and  $X_w$  are determined for each charge and discharge cycle. This data is shown in Figures 10 and 11, respectively. Cycle '0' represents the as-deposited material in these figures.

As the material is charged, the potassium content increases and almost all the vacancies are filled with potassium ions. The vacancies not filled with potassium are instead filled with either two protons [case (i)] or three protons [case (ii)]. A material with three protons on the nickel vacancy is consistent with a material proposed by Barnard *et al.*<sup>27</sup> whose point defect representation has been shown to contain three protons on the Ni vacancy.<sup>11, 13</sup> However, the excess proton could reside interlamellar as opposed to being in the vacancy. As the material is cycled, the potassium content of the discharged phase ( $y_1$ ) attains a constant value and the charged state ( $y_2$ ) has increasingly less potassium ions intercalated, as is clear from the decrease in  $y_2$  with cycling. The difference between these two cases is in the calculated potassium content on charge. While case (i) results in a dramatic change in  $y_2$  over the ten cycles, case (ii) has a more moderate change. This is because in case (ii) we have more protons compared to case (i), and hence fewer vacancies are needed to achieve the requisite oxidation state change. As the lattice has excessive protons, the fraction of  $Ni^{4+}$  in the lattice decreases; hence, the average oxidation state of nickel in the charged state decreases as is seen in Figure 7.

The increase in the water content of the films can be seen from Figure 11 where the moles of water per mole of nickel is tracked as the film is cycled. We see that both cases produce the same qualitative effect in early cycles with water incorporation during discharge and expulsion during charge.<sup>28, 29</sup> However, case (i) predicts that this change would reverse on later cycles. This is because the potassium incorporation on charge decreases more rapidly in case (i) and the increase in mass on charge is accommodated by incorporating water into the lattice. However, both the cases predict a steady increase in water content on cycling the film. This increase in water content is the cause for the increase in the total mass of the film observed on cycling.<sup>24</sup>

The simulations described above were generated by setting  $x_1 = x_2 = 0.25$  and estimating  $y_2$  and  $y_1$  from the data. Alternatively, one could set  $y_1 = 0$  and estimate  $y_2$  and  $x$ , with  $x = x_1 = x_2$ . The result would be a slight decrease in  $x$  from 0.25 to 0.235 in the 1<sup>st</sup> cycle rather than the slight increase in  $y_1$  from 0 to 0.04 shown in Figure 10. The value for  $x$  would remain essential constant for cycles 2-9. The value for  $y_2$  would be essentially the same as that shown in Figure 10, and no qualitative differences would be seen in Figures 11. This reiterates that the decrease in capacity on cycling observed in Figure 6 is mainly due to the decrease in  $y_2$  shown in Figure 10.

## Conclusion

A methodology has been developed to correlate the changes in capacity and mass observed during cycling of nickel hydroxide films with the defect structure of the active material. The capacity and mass of the films were measured simultaneously

using an EQCM and used as input into the point-defect model. The methodology was used to study short term cycling of the nickel electrode. The following conclusions were drawn from these results (i) A cathodically deposited  $\alpha$  nickel hydroxide film has a defect content of 0.25. During the 1<sup>st</sup> charge, the two protons from the nickel vacancy de-intercalate and in turn a  $K^+$  ions occupies the vacancy resulting in a 1.67 electron transfer; (ii) During discharge, the  $K^+$  de-intercalates and the vacancy is left vacant resulting in a 1 electron transfer; (iii) with each successive charge, as the film is cycled, the potassium content decreases but the proton content in the lattice increases, thus leading to a lower oxidation state of Ni in the charged state and a drop in capacity; (iv) the water content of the film decreases on charge and increases on discharge and (v) The water content of the film appears to increase on cycling, thus leading to an increase in the total mass of the film.

### **Acknowledgements**

The authors gratefully acknowledge the financial support from the Office of Research and Development of the United States Central Intelligence Agency, the U.S. Department of Energy under Cooperative Agreement No. DE-FCO2-91ER75666, and the U.S. Department of Defense under grant No. DAAH04-96-1-0421.

## Notation

E	electrode potential, V
F	Faraday's constant, 96487 C/eq.
I	applied current, A
$i_{o,ox}$	exchange current for the oxygen reaction, A
$i_{ox}$	current expended to oxygen evolution, A
M	molecular weight
n	number of protons divided by number of Ni vacancies not occupied by $K^+$
$N_{Ni}$	number of moles of nickel, mol
Ox	oxidation state
R	universal gas constant, 8.314 J/mol·K
T	temperature, °C
t	time, sec
$U_{ref,ox}$	standard potential of the oxygen evolution reaction, V
W	weight of the active material, g
x	moles of vacancies per mole of lattice sites
$X_w$	moles of water per mole of lattice sites
y	moles of vacancies occupied by potassium ions per mole of lattice sites.
z	extend of the nickel oxidation/reduction reaction
$\Delta m$	mass change, g

## Greek

$\alpha$	transfer coefficient
----------	----------------------

$\varepsilon$	efficiency of the nickel reaction
$\lambda_1$	moles of $\text{OH}^-$ ions per mole Ni
$\lambda_2$	moles of $\text{K}^+$ ions per mole Ni
$\lambda_3$	moles of water per mole Ni
$\lambda_4$	number of electrons per mole Ni

#### **Subscript**

1	discharged state, nickel hydroxide
2	charged state, oxy-hydroxide

#### **Superscript**

0	as-deposited state
---	--------------------

## References

1. J. McBreen (Editor), *The Nickel Oxide Electrode*, Plenum Press, 1990.
2. P. Delichere, S. Joiret, A. Hugot-le Goff, K. Bange, and B. Hetz, *J. Electrochem. Soc.*, **135**, 1856 (1988).
3. M. K. Carpenter, R. S. Conell, and D. A. Corrigan, *Solar Energy Mater.*, **16**, 333 (1987).
4. S. Gross, *Review of Electrochemical Impregnation of Nickel Cadmium Cells*, Jet Propulsion Laboratory, Pasadena (1977).
5. R. Barnard, C. F. Randall, and F. L. Tye, *J. Appl. Electrochem.*, **10**, 109 (1980).
6. R. Barnard, C. F. Randall, and F. L. Tye, *J. Appl. Electrochem.*, **11**, 517 (1981).
7. M. Kim, T. Hwang, and K. Kim, *J. Electrochem. Soc.*, **144**, 1537 (1997).
8. M. Kim and K. Kim, *J. Electrochem. Soc.*, **145**, 507 (1998).
9. P. Timmerman, B. V. Ratnakumar, and S. Di Stefano, *Aqueous Batteries*, P. D. Bennet and S. Gross, eds., PV 96-16, p. 130, The Electrochemical Society Proceedings Series, Pennington, NJ (1996).
10. H. Bode, K. Dehmelt, and J. Witte, *Electrochim. Acta*, **11**, 1079 (1966).
11. P. L. Loyselle, P. J. Karjala, and B. C. Cornilsen, *Electrochemical and Thermal Modeling of Battery, Fuel Cell and Photoenergy Conversion Systems*, R. J.



Selman and H. C. Maru, eds., PV 86-12, p. 114, The Electrochemical Society Proceedings Series, Pennington, NJ (1986).

12. B. C. Cornilsen, P. J. Karjala, and P. L. Loyselle, *J. Power Sources*, **22**, 351 (1988).
13. B. C. Cornilsen, X. Shan, and P. L. Loyselle, *J. Power Sources*, **29**, 453 (1990).
14. B. C. Cornilsen, X. Shan, and P. L. Loyselle, *Proceedings on the Symposium on Nickel Hydroxide Electrodes*, D. A. Corrigan and A. H. Zimmerman, eds., PV 90-4, p. 82, The Electrochemical Society Proceedings Series, Pennington, NJ (1990).
15. B. Cornilsen, X. Cai, R. Tanbug, and G. Meitzner, *Aqueous Batteries*, P. D. Bennett and S. Gross, eds., PV 96-16, p. 88, The Electrochemical Society Proceedings Series, Pennington, NJ (1997).
16. Z. Xu, B. C. Cornilsen, and G. Meitzner, *Selected Battery Topics*, G. Halpert, M. L. Gopikanth, K. M. Abraham, W. R. Cieslak and W. A. Adams, eds., PV 98-15, p. 1, The Electrochemical Society Proceedings Series, Pennington, NJ (1999).
17. C. C. Streinz, S. Motupally, and J. W. Weidner, *J. Electrochem. Soc.*, **143**, 4051 (1995).
18. C. C. Streinz, A. P. Hartman, S. Motupally, and J. W. Weidner, *J. Electrochem. Soc.*, **142**, 1084 (1995).
19. E. E. Kalu, V. Srinivasan, T. Nwaoga, and J. W. Weidner, *Selected Battery Topics*, G. Halpert, M. L. Gopikanth, K. M. Abraham, W. R. Cieslak and W. A.

- Adams, eds., PV 98-15, p. 639, The Electrochemical Society Proceedings Series, Pennington, NJ (1999).
20. J. Desilvestro, D. A. Corrigan, and M. J. Weaver, *J. Electrochem. Soc.*, **135**, 885 (1988).
  21. W. E. O'Grady, K. I. Pandya, K. E. Swider, and D. A. Corrigan, *J. Electrochem. Soc.*, **143**, 1613 (1996).
  22. D. A. Corrigan and S. L. Knight, *J. Electrochem. Soc.*, **136**, 613 (1989).
  23. Y. Mo, E. Hwang, and D. A. Scherson, *J. Electrochem. Soc.*, **143**, 37 (1996).
  24. S. I. Cordoba-Torresi, C. Gabrielli, A. Hugot-Le Goff, and R. Torresi, *J. Electrochem. Soc.*, **138**, 1548 (1991).
  25. A. J. Bard and L. R. Faulkner, *Electrochemical methods: Fundamentals and applications*, John Wiley and sons Inc., (1980).
  26. M. Jain, S. Motupally, and J. W. Weidner, *Aqueous Batteries*, P. D. Bennet and S. Gross, eds., 96-16, p. 121, Pennington, NJ (1996).
  27. R. Barnard and C. F. Randall, *J. Appl. Electrochem.*, **12**, 27 (1982).
  28. G. T. Cheek and W. E. O'Grady, *J. Electroanal. Chem.*, **421**, 173 (1997).
  29. R. Kostecki and F. McLarnon, *J. Electrochem. Soc.*, **138**, 2527 (1997).

Name	$x_1$	$x_2$	$y_1$	$y_2$	$n_1$	$n_2$
<b>Scenario 1</b>	0.25	0.25	$0 \rightarrow 0.25$	$x_2$	0	N/A
<b>Scenario 2</b>	$0.25 \rightarrow 0.11$	$0.25 \rightarrow 0.11$	0	$x_2$	2	N/A
<b>Scenario 3</b>	$0.11 \rightarrow 0.25$	$0.11 \rightarrow 0.25$	0	$x_2$	0	N/A
<b>Scenario 4</b>	0.25	0.25	0	$0.25 \rightarrow 0.11$	0	2
<b>Scenario 5</b>	$0.25 \rightarrow 0.11$	$0.25 \rightarrow 0.11$	0	$0.25 \rightarrow 0$	0	2

**Table 1.** Different combinations of the defect parameters used to generate the number of electrons transferred in Figures 1 and 2. When  $y_2=x_2$ , none of the nickel vacancies are occupied by protons and therefore  $n_2$  is not applicable (N/A). The parameters that vary in a given scenario are assumed to change linearly with cycle number. For all five scenarios listed above, the number of protons on the nickel vacancies of the as-deposited material is 2.0 (i.e, the initial oxidation state is 2.0).

## List of Figures

**Figure 1.** Schematic of the nickel hydroxide active material deposited using the cathodic precipitation technique. The reactions occurring on charge are sketched in the figure.

**Figure 2.** Number of electrons transferred per nickel during charge and discharge for scenarios 1-3 shown in Table 1. The number of electrons transferred was calculated from equation 10.

**Figure 3.** Number of electrons transferred per nickel during charge and discharge for scenarios 4 and 5 shown in Table 1. The number of electrons transferred was calculated from equation 10.

**Figure 4.** First two constant current charge/discharges of a 70  $\mu\text{g}$  nickel hydroxide at 0.1 mA. The  $\times$  represents the point where the electrode was assumed to be fully charged or discharged and was used to generate Figure 5.

**Figure 5.** Capacity on charge and discharge vs cycle number for a 70  $\mu\text{g}$  nickel hydroxide electrode. The plot was generated using data similar to that shown in Figure 4. The symbols are the average of 3-4 data sets and the error bars represent the spread in the data.

**Figure 6.** Number of electrons transferred during charge and discharge of a 70  $\mu\text{g}$  nickel hydroxide film. The graph was generated using the charge/discharge curve in Figure 4 and correcting for the oxygen evolution reaction using equations 15, 16 and 17. The symbols are an average of 3-4 data sets and the error bars represent the spread in the data.

**Figure 7.** Average oxidation state during cycling of a 70  $\mu\text{g}$  nickel hydroxide film. The oxidation state was estimated assuming the oxidation state of the as-deposited material to be 2.0 and the number of electrons transferred are those given in Figure 6.

**Figure 8.** Mass change during charge/discharge of a 70  $\mu\text{g}$  nickel hydroxide film. The mass increases on charge and decreases on discharge and the change was measured using an EQCM. The current used was 0.1mA.

**Figure 9.** Change in molecular weight during charge/discharge of 70  $\mu\text{g}$  nickel hydroxide films. The mass increases on charge and decreases on discharge. The symbols are an average of 3-4 data sets and the error bars represent the spread in the data. The molecular weight of the as-deposited material is 121 g/Mole Ni.

**Figure 10.** Change in defect parameters on cycling nickel hydroxide films. The defect parameters were extracted using the model and the experimental capacity and mass change data (Figures 6 and 8).  $n_1$  was assumed to be 2 in the as-deposited film and 0 for the other cycles for both cases. The graph shows the values obtained for three values of  $n_2$ . While the values of  $y_1$  and  $x$  remain the same for all three cases, the differences in the values of  $y_2$  are shown.

**Figure 11.** Change in water content on cycling nickel hydroxide films. The water content was extracted using the model and the experimental capacity and mass change data (Figures 6 and 8).  $n_1$  was assumed to be 2 in the as-deposited film and 0 for the other cycles for both cases. The water content is plotted for  $n_2=2$  and 3. While the value is the same for both cases in the discharged material (solid line), the differences in the charged state (dotted line) are shown.

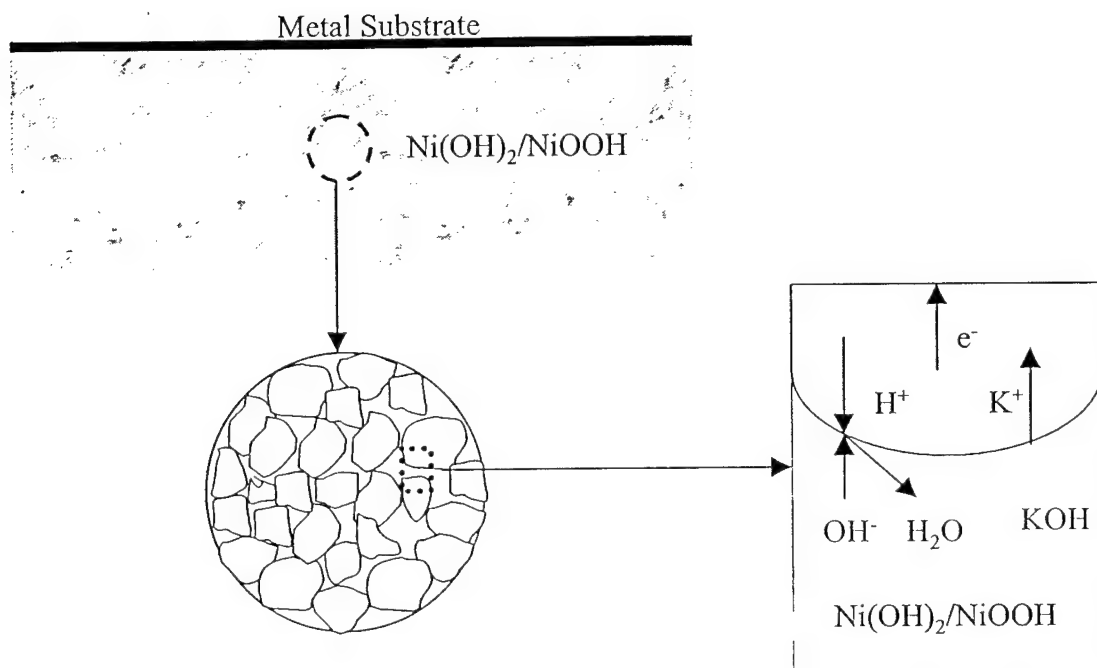


Figure 1. Schematic of the nickel hydroxide active material deposited using the cathodic precipitation technique. The reactions occurring on charge are sketched in the figure.

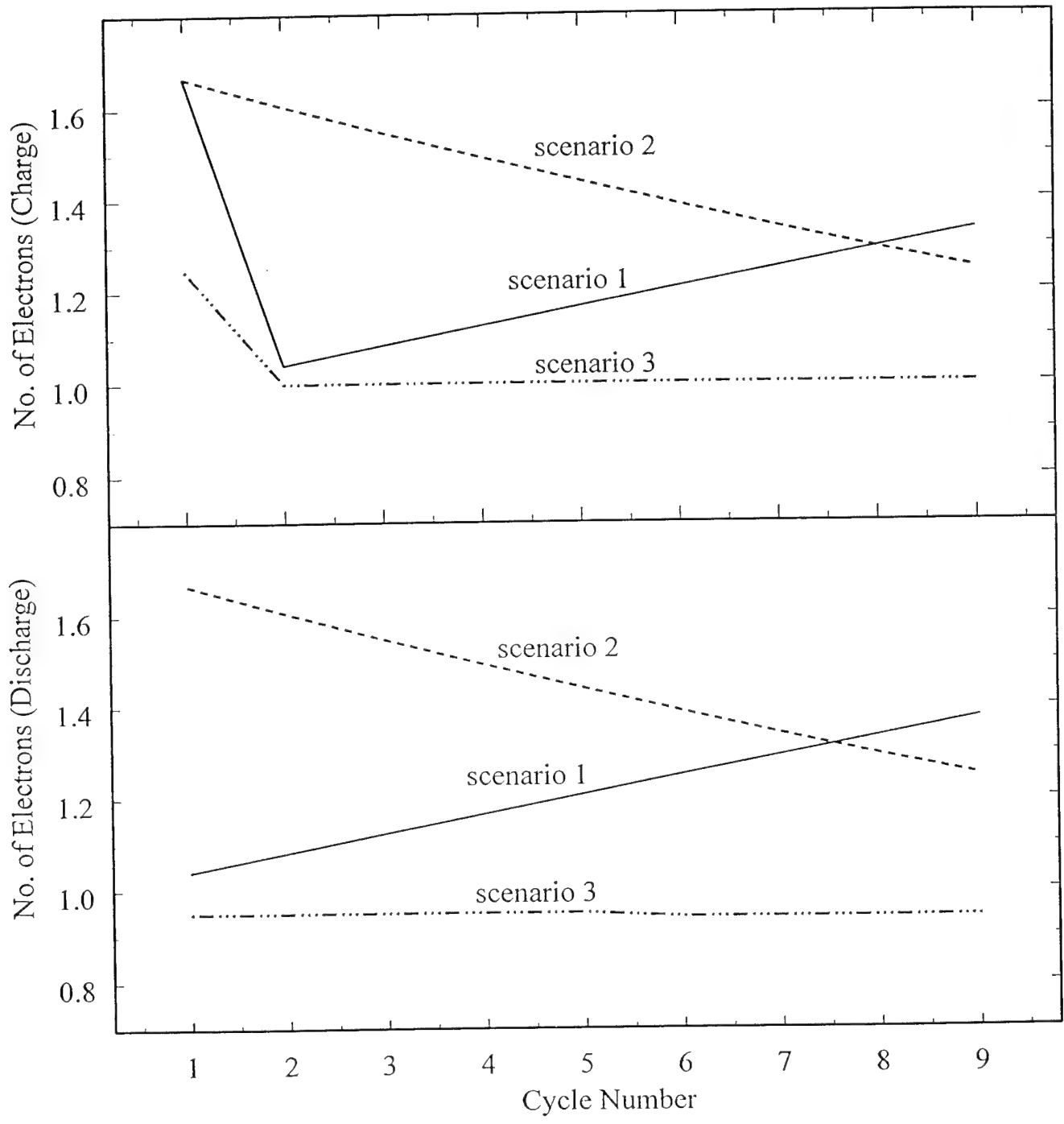


Figure 2. Number of electrons transferred per nickel during charge and discharge for scenarios 1-3 shown in Table 1. The number of electrons transferred was calculated from equation 10.



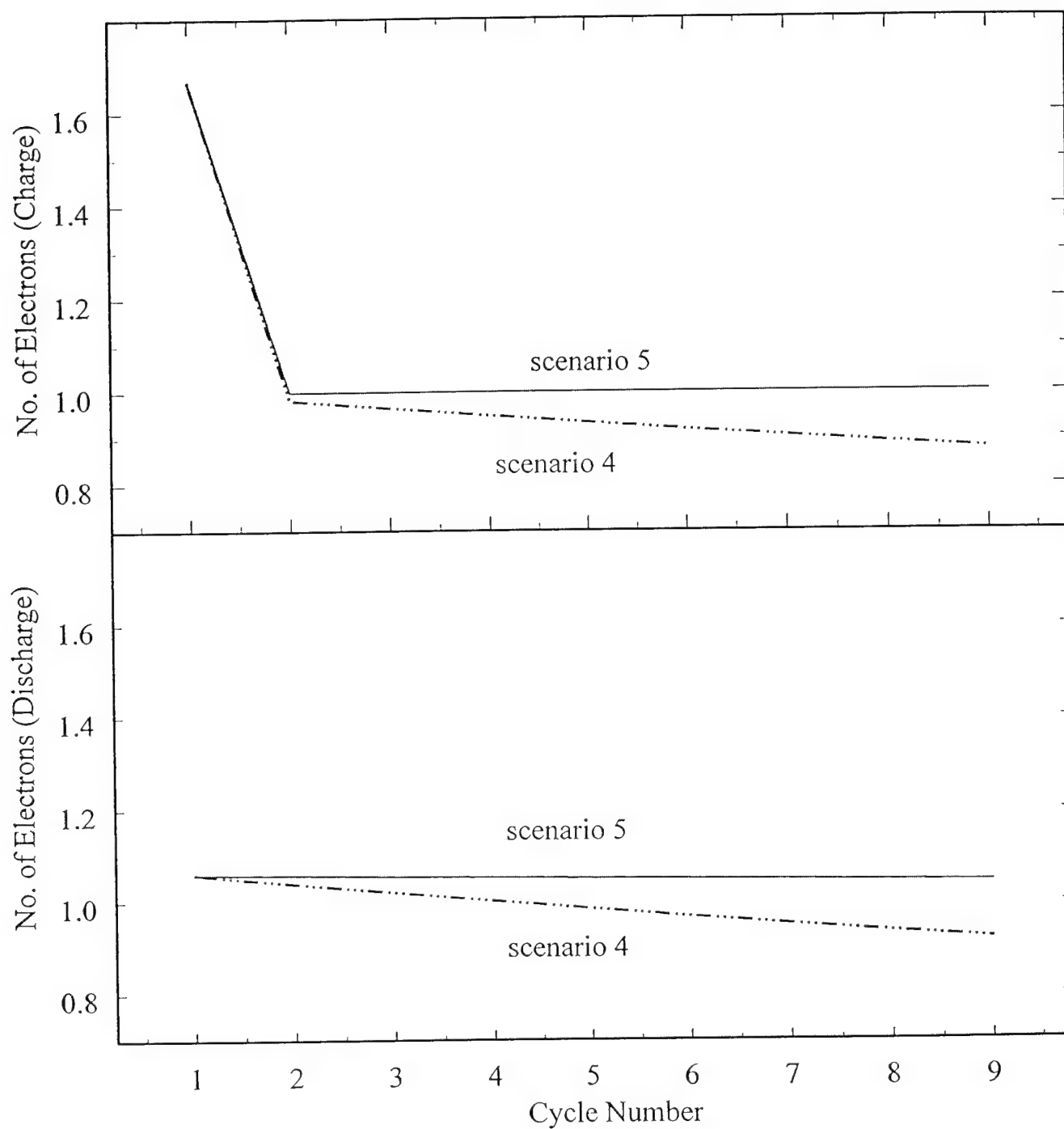


Figure 3. Number of electrons transferred per nickel during charge and discharge for scenarios 4 and 5 shown in Table 1. The number of electrons transferred was calculated from equation 10.

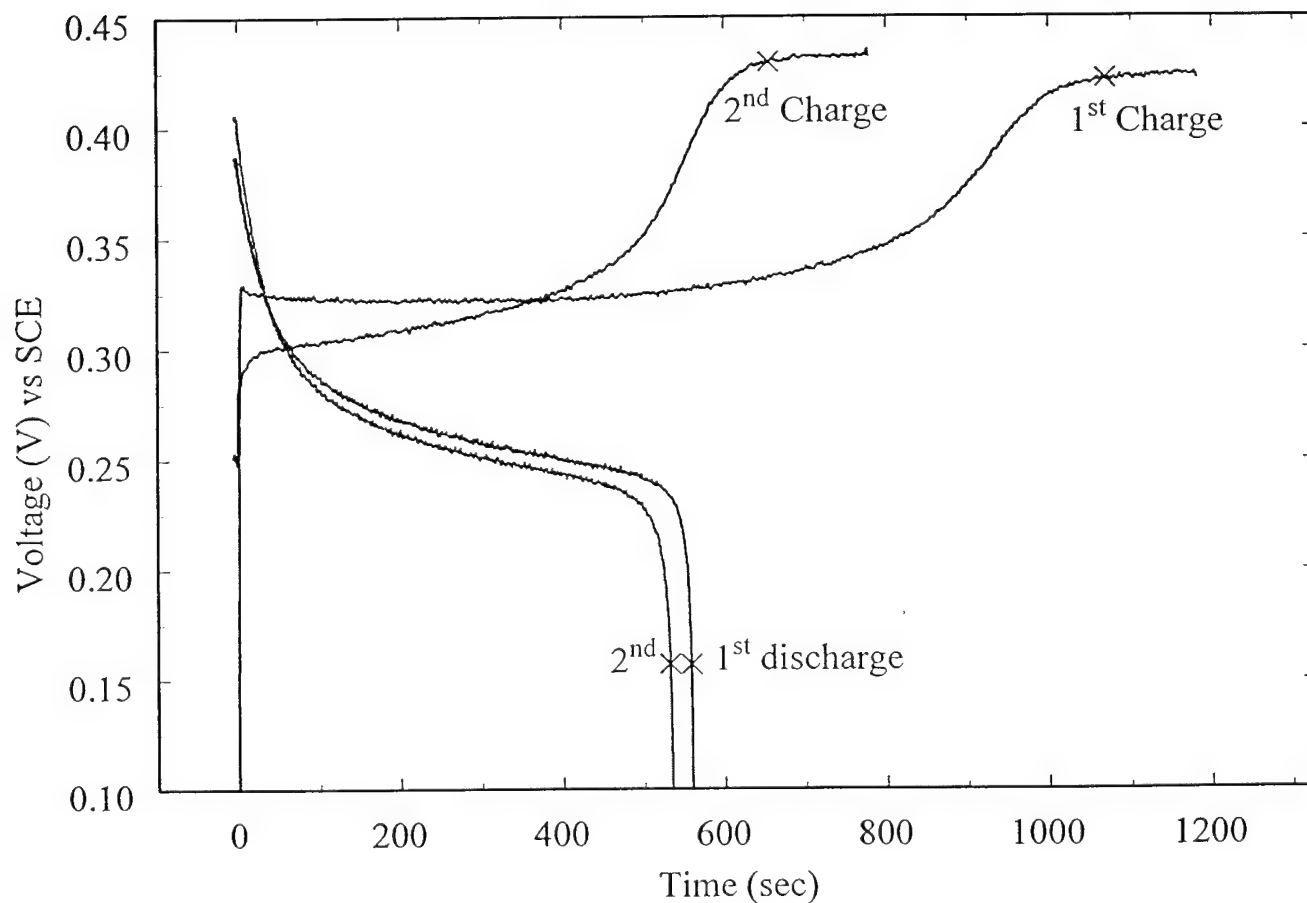


Figure 4. First two constant current charge/discharges of a 70 µg nickel hydroxide at 0.1 mA. The × represents the point where the electrode was assumed to be fully charged or discharged and was used to generate Figure 5.

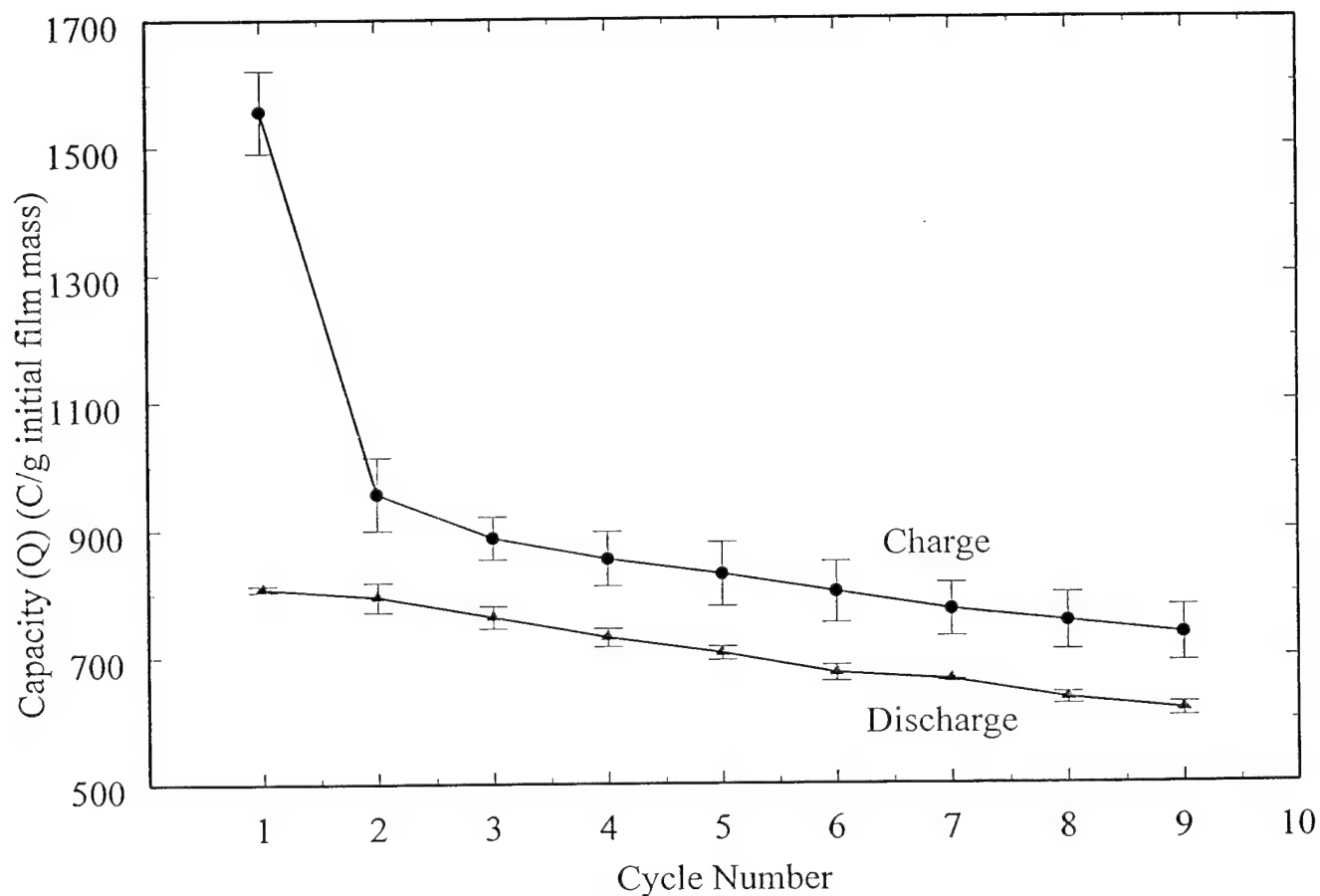


Figure 5. Capacity on charge and discharge vs cycle number for a 70  $\mu\text{g}$  nickel hydroxide electrode. The plot was generated using data similar to that shown in Figure 4. The symbols are the average of 3-4 data sets and the error bars represent the spread in the data.

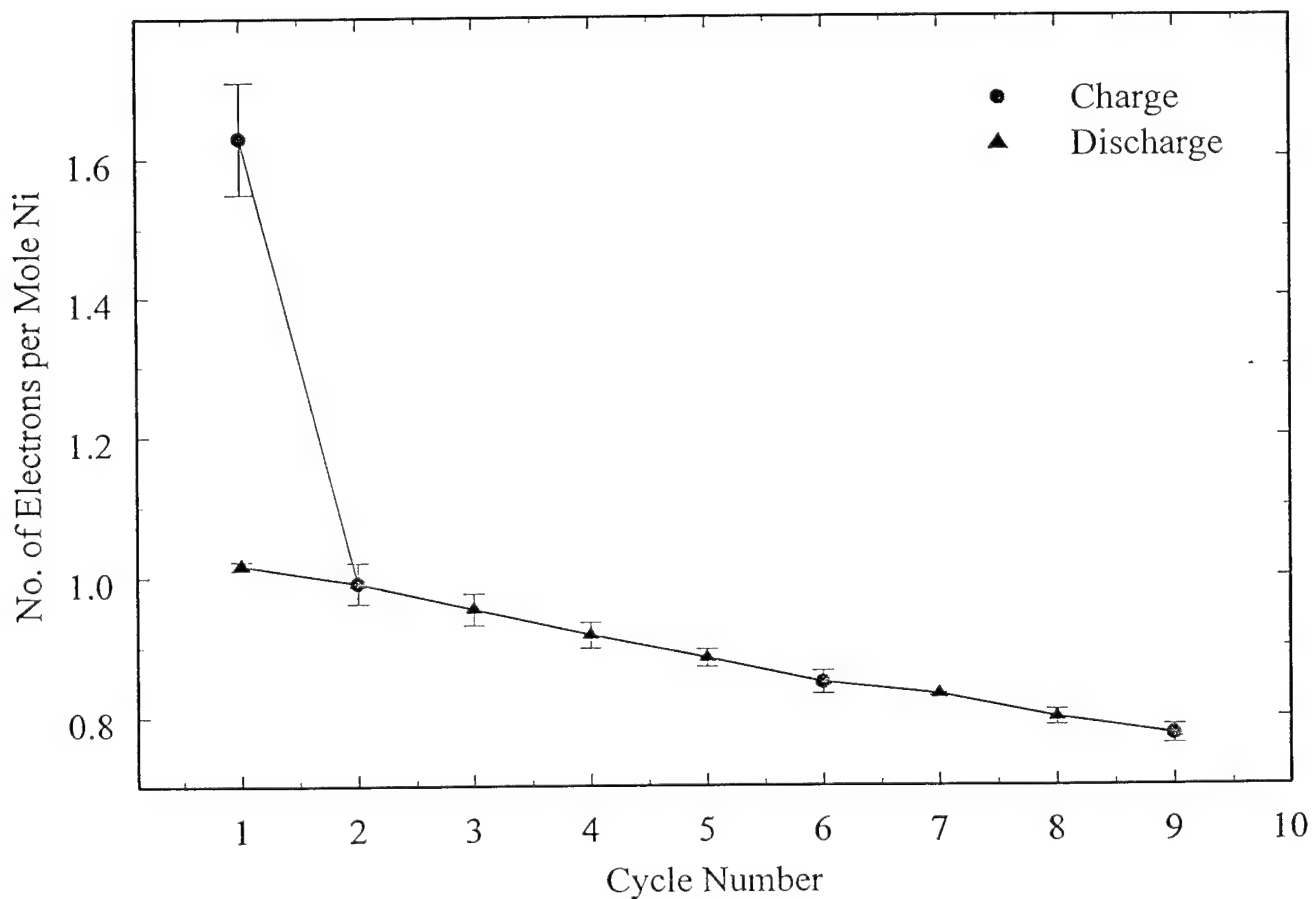


Figure 6. Number of electrons transferred during charge and discharge of a 70  $\mu\text{g}$  nickel hydroxide film. The graph was generated using the charge/discharge curve in Figure 4 and correcting for the oxygen evolution reaction using equations 15, 16 and 17. The symbols are an average of 3-4 data sets and the error bars represent the spread in the data.

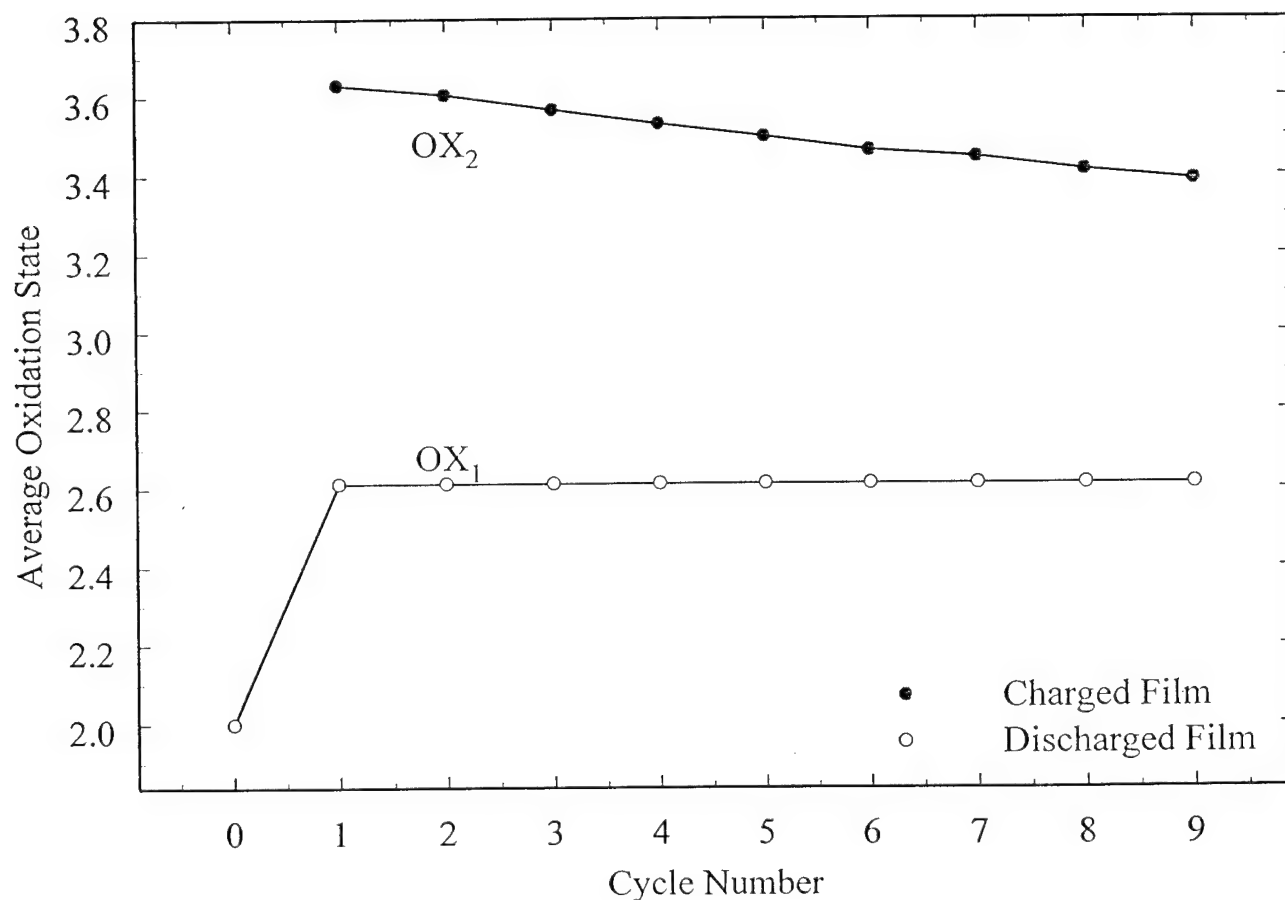


Figure 7. Average oxidation state during cycling of a 70  $\mu\text{g}$  nickel hydroxide film. The oxidation state was estimated assuming the oxidation state of the as-deposited material to be 2.0 and the number of electrons transferred are those given in Figure 6.

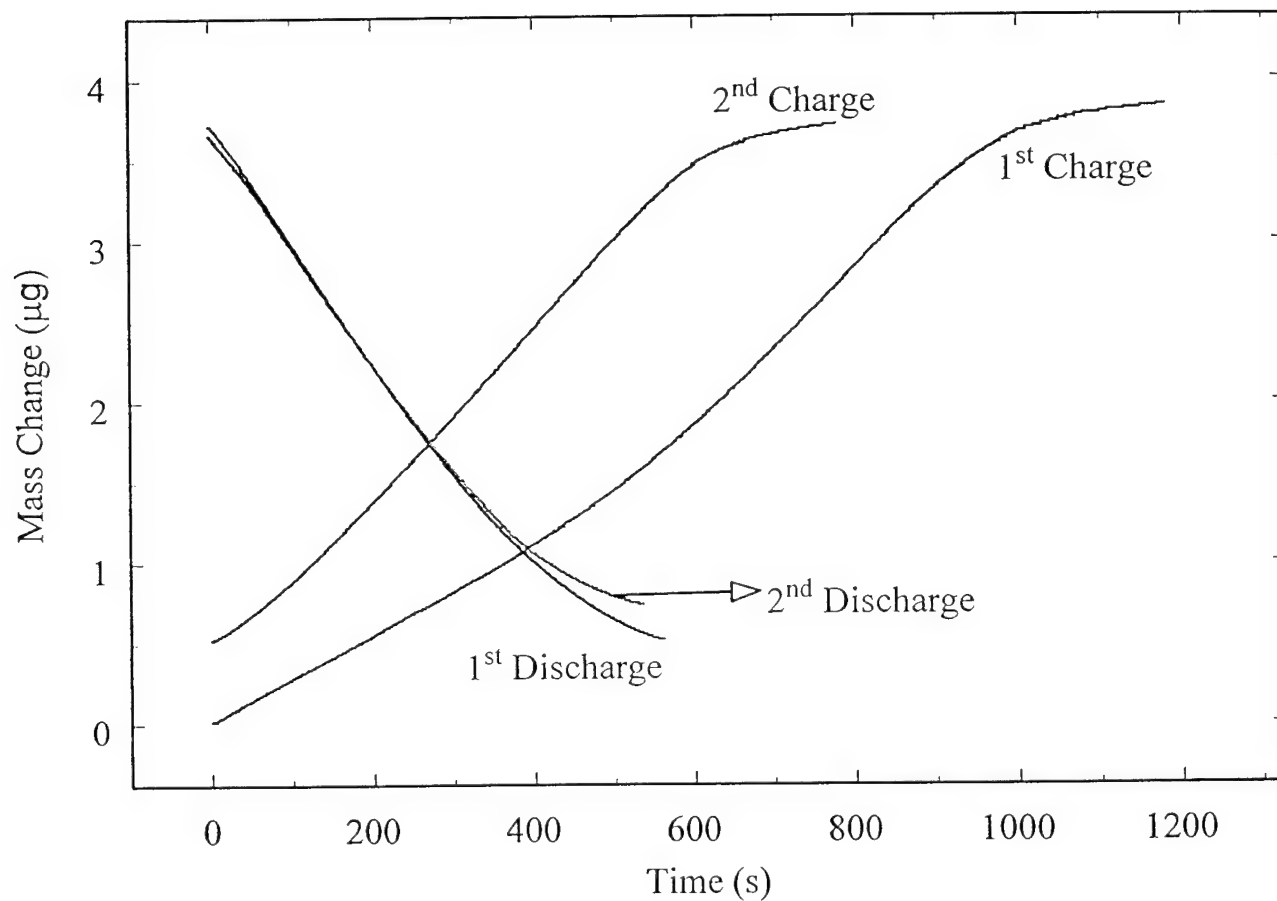


Figure 8. Mass change during charge/discharge of a 70  $\mu\text{g}$  nickel hydroxide film. The mass increases on charge and decreases on discharge and the change was measured using an EQCM. The current used was 0.1mA.

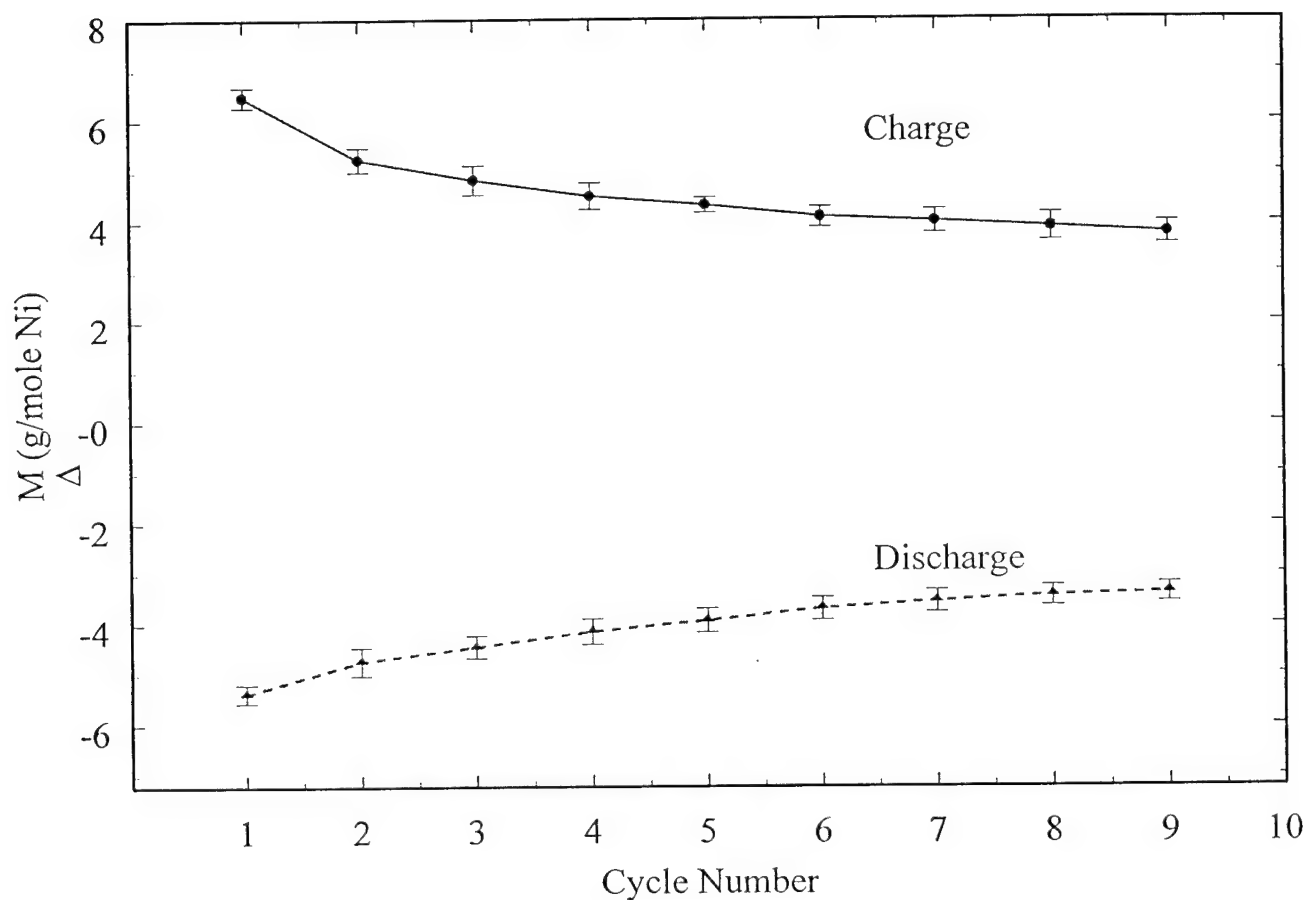


Figure 9. Change in molecular weight during charge/discharge of 70  $\mu\text{g}$  nickel hydroxide films. The mass increases on charge and decreases on discharge. The symbols are an average of 3-4 data sets and the error bars represent the spread in the data. The molecular weight of the as-deposited material is 121 g/Mole Ni.



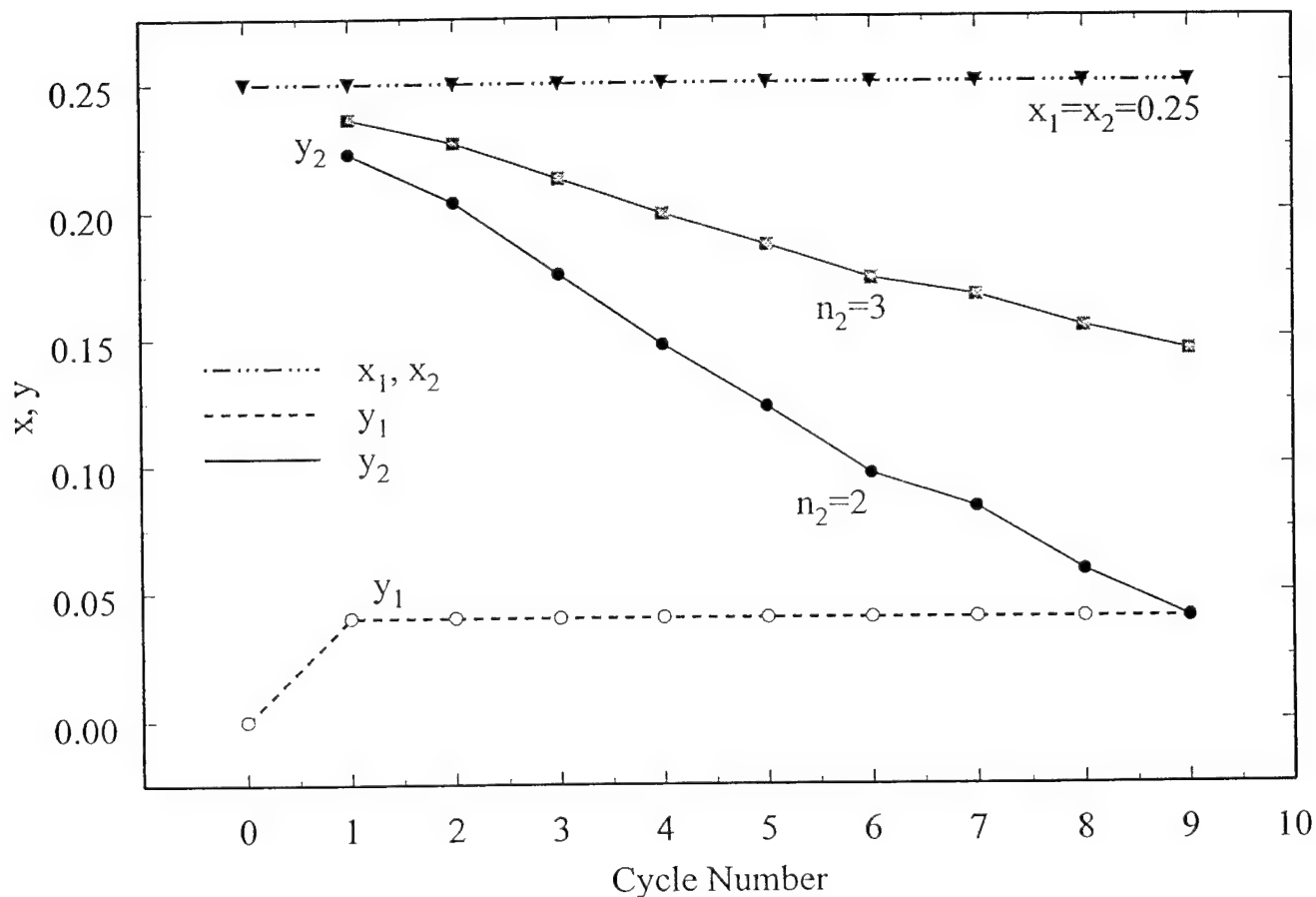


Figure 10. Change in defect parameters on cycling nickel hydroxide films. The defect parameters were extracted using the model and the experimental capacity and mass change data (Figures 6 and 8).  $n_1$  was assumed to be 2 in the as-deposited film and 0 for the other cycles for both cases. The graph shows the values obtained for three values of  $n_2$ . While the values of  $y_1$  and  $x$  remain the same for all three cases, the differences in the values of  $y_2$  are shown.

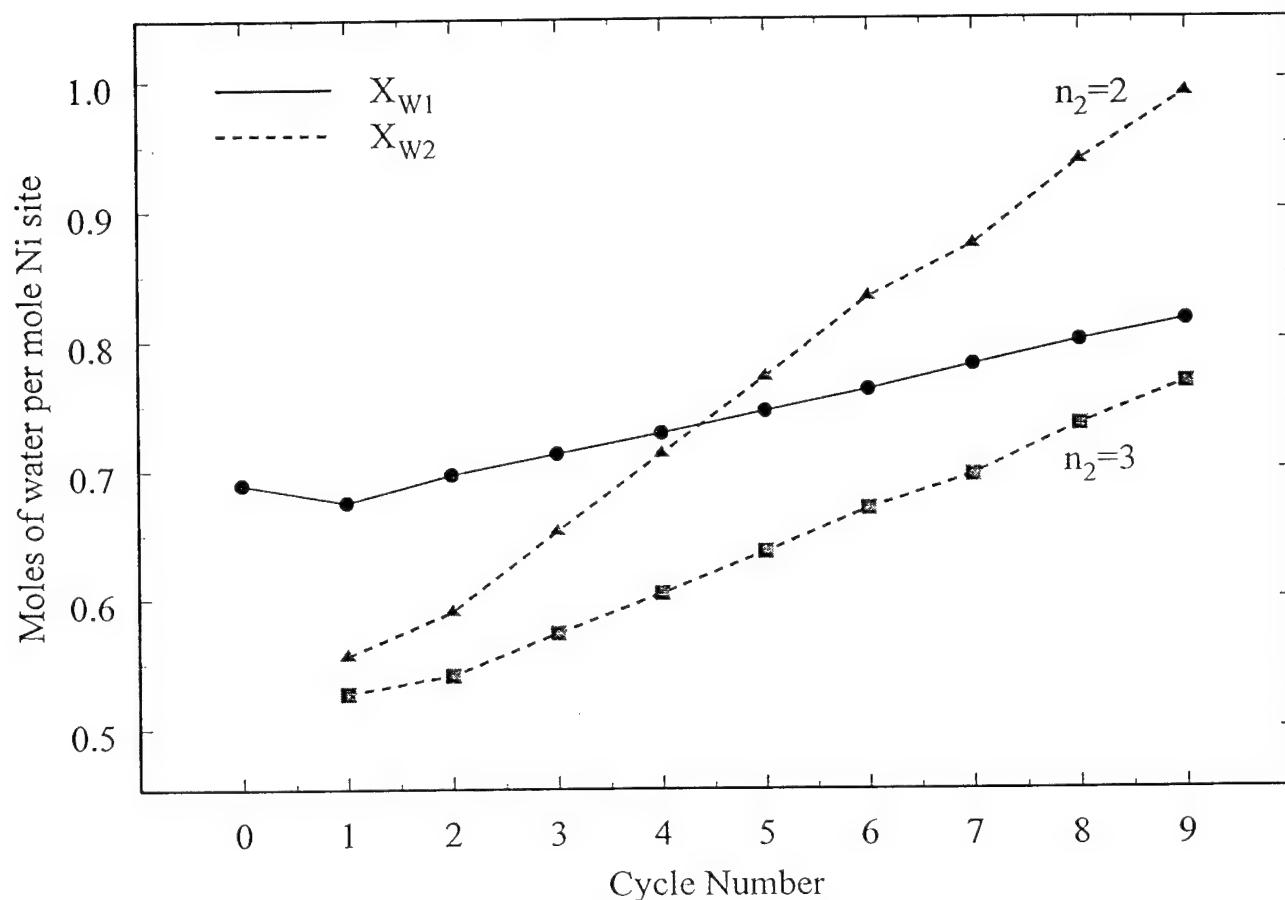


Figure 11. Change in water content on cycling nickel hydroxide films. The water content was extracted using the model and the experimental capacity and mass change data (Figures 6 and 8).  $n_1$  was assumed to be 2 in the as-deposited film and 0 for the other cycles for both cases. The water content is plotted for  $n_2=2$  and 3. While the value is the same for both cases in the discharged material (solid line), the differences in the charged state (dotted line) are shown

**Sol-Gel Derived Carbon Aerogels and Xerogels 1.  
Electrochemical Characterization from a Statistical Design Approach**

Emily J. Zanto, James A. Ritter\* and Branko N. Popov

Department of Chemical Engineering  
Swearingen Engineering Center  
University of South Carolina  
Columbia, SC 29208  
Voice: (803)-777-3590  
Fax: (803) 777-8265  
ritter@engr.sc.edu

A manuscript submitted to

***Carbon***

for review and consideration for publication.

September 2000

Keywords: carbonized resin, carbon aerogel, carbon xerogel, sol-gel

---

\* To whom all correspondence should be addressed.

## **Abstract**

Carbon gels were synthesized via the sol-gel polycondensation of resorcinol with formaldehyde using a sodium carbonate catalyst. A full  $2^4$  factorial design study was performed to study the effect of initial solution pH, wt% solids, pyrolysis temperature and gel type (aerogel or xerogel) on surface area, pore volume and electrochemical capacitance. It has been found that the gels showing the highest surface area also show the highest capacitance. These include the aerogels made with a high initial solution pH and a low pyrolysis temperature. Pore volume is also maximized with an aerogel and a high initial gel pH. Results also indicate there are interaction effects occurring between factors, especially between initial solution pH and gel type which make this factorial design approach an effective means of studying these materials.

## Introduction

Pekala [1] introduced organic aerogels derived from the polycondensation of resorcinol with formaldehyde through a reaction mechanism similar to the sol-gel processing of silica. The resulting organic gels were dried supercritically in CO<sub>2</sub> to produce the organic "aerogel". Since this initial work, numerous articles have been published on the properties and uses of these novel organic aerogel materials. [2-12] These materials have also been pyrolyzed in an inert atmosphere to produce carbon aerogels [5]. Much of the research from Pekala and co-workers has focused on developing a high energy density electrochemical capacitor [4,8] while others have focused on developing an electrosorption process for the reversible removal of ions from aqueous streams [6,10], both based on the unique properties of the carbon aerogel. It must be emphasized, however, that not all of these studies have been concerned with organic and carbon "aerogels"; they have also considered organic and carbon xerogels.

An aerogel is produced when the solvent contained within the voids of a gelatinous structure is removed supercritically (usually with CO<sub>2</sub>) in the absence of a vapor-liquid interface and thus without any interfacial tension. Ideally, this process leaves the gel structure unchanged with no shrinkage of the internal voids [13]. In contrast, a xerogel is produced when the solvent is removed by conventional methods such as evaporation under normal conditions. This process causes the internal gel structure to collapse due to the presence of the vapor-liquid interface, which causes tremendous interfacial tension especially in small voids or pores [13]. Most of the published properties on these materials have been based on the supercritically dried organic and carbon aerogels [5,11,12,14,15] with few exceptions [7,16]. Yet, one of the major applications of these materials, i.e. the electrosorption process, has been based on a conventionally dried xerogel even though it has been referred to as an aerogel. The point here is not terminology,

which can be readily clarified based on the experimental procedure. The point is that the physical and chemical properties of organic or carbon aerogels and xerogels are expected to be different. However, none of the aforementioned studies have addressed this issue. Therefore, the objective of this study is to illuminate the differences between carbon aerogels and xerogels using a statistical design of experiments approach. Four factors (parameters) were investigated: initial solution pH, weight percent solids, pyrolysis temperature and gel type (aerogel or xerogel). In this initial study, the three response variables of interest are the surface area, pore volume and electrochemical capacitance. Although these response variables have been studied in previous works, the experiments have been based on the typical, change one factor at a time approach, which does not allow for factor interactions to be understood. In contrast, this study shows not only how each factor affects the response variables of interest, but also how the factors interact with one another.

## Experimental

Resorcinol (ACS, 99+%, Alfa Aesar), formaldehyde (37% in water, Aldrich), sodium carbonate (anhydrous, ACS, Fisher), and acetone (optima, 99.6%, Fisher) were used as received. The synthesis procedure for these gels was developed based on the procedure for making carbon aerogels [3] and xerogels [7]. The solutions prepared contained either 5 or 20 w/v% solids, in which the R/F (resorcinol/formaldehyde) mole ratio was fixed at 1:2. Sodium carbonate was used as the catalyst, where the R/C (resorcinol/sodium carbonate) mole ratio was fixed at 50:1. Four, one liter batches of gel were made in a glove box under nitrogen atmosphere. These four batches included one with a low initial solution pH and low wt% solids, one with a high initial solution pH and low wt% solids, one with a low initial solution pH and high wt% solids, and one with a high initial solution pH and high wt% solids. These solutions were then poured into 100

ml glass containers and tightly sealed with caps. They were removed from the glove box and placed in an oven at 87 °C for one week to gel and cure.

When removed from the oven, each batch was divided into two parts. The first part, designated to be xerogel, was first washed with acetone for three days, replacing the acetone daily under vacuum filtration and then dried in a conventional oven under nitrogen flow. This drying procedure included first heating the gel to 65 °C with a heating rate of 5 °/min, holding it there for 5 hours, heating it to 110 °C with a heating rate of 5 °/min, holding it there for 3 hours, and then letting it cool gradually. The second part, designated to be aerogel, was first broken up into medium sized chunks. These chunks were placed in a dish of acetone inside a vacuum dessicator. The dessicator bottom was filled with Drierite and acetone. A dish of anhydrous  $\text{NaCO}_3$  was placed in the dessicator on the shelf. The dessicator was evacuated until the acetone began to boil at which time the dessicator was sealed to maintain the vacuum pressure. The dessicator was opened daily to replace the acetone in which the gel was sitting with fresh acetone and to exchange the saturated  $\text{NaCO}_3$  with dry  $\text{NaCO}_3$ . This procedure was followed for one week to ensure that all the water in the gel was replaced with acetone.

The acetone-exchanged gel was then transferred into a supercritical dryer at 10 °C which was subsequently filled with liquid  $\text{CO}_2$ . The gel remained in the  $\text{CO}_2$  for 24 hours with the  $\text{CO}_2$  replenished as needed to maintain the liquid level above the gel. In this way, the acetone in the gel was replaced with liquid  $\text{CO}_2$ . After 24 hours of soaking, the temperature of the supercritical dryer was increased until the liquid  $\text{CO}_2$  turned supercritical (~38 °C). The  $\text{CO}_2$  was then released slowly to prevent disruption of the gel structure. Once the pressure was released, the gels were removed from the drier and placed into the glove box until they were pyrolyzed.

The dried xerogel and aerogel resins were again separated into two parts. Half of each sample was pyrolyzed at 800 °C and the other half at 1050 °C in a tube furnace under 1 L/min nitrogen flow. In this way, the initial four batches of gel created 16 different carbonized materials.

A Micromeritics Pulse Chemisorb 2700 Analyzer was used to obtain the surface areas and pore volumes of both the carbon xerogels and aerogels using the single point BET method. An EG&G Potentiostat Model 273A was used to run constant current charge and discharge tests on the samples. From these tests, the capacitance was calculated using the following equation,

$$C = \frac{i \cdot \Delta t}{\Delta V \cdot m} \quad (1)$$

where  $i$  is the current,  $t$  is the time,  $V$  is the voltage, and  $m$  is the mass of the carbon pellet. For these tests, a constant current of 1mA was used. A small sample pellet was made by combining the carbonized gel powder with a Teflon binder in a 20:1 mass ratio. The pellet was regenerated at 150 °C for 1 hr and then soaked in 6 M KOH overnight before being tested.

## Results and Discussion

A full factorial design is an experimental arrangement in which a small integral number of levels,  $l$ , is chosen for each of the  $k$  factors, and all  $l^k$  combinations of these levels are run. Often, an  $l$  of 2 is chosen to represent a high value and a low value. The present research was performed using this arrangement and 4 factors, creating a full  $2^4$  design. Table 1 details the  $2^4$  factorial design carried out in this research. The four factors (initial solution pH, wt% solids, pyrolysis temperature, and gel type) and their high and low levels were chosen by reviewing the literature and determining the significant areas of variability in the production process that affect the outcome of the final carbon product [7,9,16,17]. For the methane adsorption capacity and



monolith density portion of this research, a  $2^3$  full factorial design study was completed using factors A – C from Table 1, maintaining the areogel gel type. For the storage of natural gas, carbon monoliths are more appropriate than carbon powders. For this reason, the aerogel gel type was studied.

Once the tests were complete, the experimental data was analyzed using Taguchi's statistical design methods [18]. This includes first completing a response table, calculating the effects, plotting the effects on a probability plot, and then from this plot, determining which effects are significant. The results of the surface area, pore volume, and capacitance tests are shown in Table 2. From the completed response tables, the effects for each factor and factor interaction were calculated for each response variable and plotted on separate probability plots using Minitab 11.11 for Windows. The analysis for the surface area is presented and discussed first.

Figure 1 shows the normal probability plot. From this plot, it can be seen that the only factors and factor interactions that do not fall near the straight line are the gel pH, pyrolysis temperature, gel type and the gel pH-gel type interaction. Using this analysis method, these results indicate that these are the only factors that significantly affect the surface area of the carbon gel. It is important to note that, with this analysis method, once an interaction has been identified as significant, it is no longer meaningful to look at the individual factors involved, rather, one must look only at the interaction. To do this an interaction plot is created. In the case of surface area, the gel pH-gel type interaction was plotted to determine the factor settings that maximize or minimize surface area. This plot is also shown in Figure 1. From the interaction plot, it can be seen that in order to maximize surface area, the high pH aerogel should be used, and because the two lines do not cross, the opposite factor settings should be used to minimize

the surface area. It can also be seen from the graph that although both lines have a positive slope, the xerogel (D2) is not as sensitive to changes in pH as the aerogel.

Using the information from this analysis, it was found that in order to maximize surface area, an aerogel with a high pH and a low pyrolysis temperature should be made. This factor level combination yields a predicted average surface area of  $882 \text{ m}^2/\text{g}$ . Within the range of this study, wt% solids did not affect surface area. To minimize surface area, the opposite settings should be used, leading to a predicted surface area of  $475 \text{ m}^2/\text{g}$ .

Figure 2 shows the normal probability plot for pore volume. This plot indicates that gel pH, gel type, and the gel pH-gel type interaction are significant. Due to the interaction, as mentioned above, it is only necessary to look at the interaction rather than the individual factors involved. To understand this effect, Figure 2 shows the interaction effect graphically. From this interaction plot it can be seen that to maximize pore volume, an aerogel with the high pH should be used. Wt% solids and pyrolysis temperature did not affect pore volume in the range of this study. Making an aerogel with the higher 7.0 pH will produce a product with the predicted average pore volume of  $1.24 \text{ m}^3/\text{g}$ . It is interesting to note that the pore volumes for the xerogels made in this study were not affected significantly by the factors being studied within the range of their settings.

Figure 3 shows the normal probability plot for electrochemical capacitance. This plot indicates that gel pH may be significant but all the effects seem to fall in a straight line, indicating no significant effects. The problem with this result is that any change in capacitance of about 20 F/g or more is in reality significant. For this reason, the data was transformed by taking the log of each response value. Figure 4 shows the resulting probability plot of the transformed capacitance data. The results of the probability plot indicate that gel pH, wt%

solids, and pyrolysis temperature signal as main effects and two interactions including gel pH-gel type and gel pH-wt% solids exist. Interaction plots for these are shown in Figure 5. From these plots, it can be seen that to maximize the double layer capacitance, an aerogel with the high gel pH should be used with the low wt% solids. By using these settings along with the low pyrolysis temperature, the predicted average double layer capacitance is 188 F/g.

### Acknowledgements

This material is based upon work supported in part by the U. S. Army Research Office under Grant No. DAAH04-96-1-0421, and in part by the U. S. National Science Foundation under Grant No. GER-9554556.

### References

1. R.W. Pekala, *J. Mater. Sci.*, 24 (1989) 3221.
2. G.C. Ruben, R.W. Pekala, T.M. Tillotson and L.W. Hrubesh, *J. Mater. Sci.*, 27 (1992) 4341.
3. R.W. Pekala, C.T. Alviso and J.D. Lemay, *Chemical Processing of Advanced Materials*, (L.L. Hench and F.K. West, eds.), John Wiley & Sons, Inc., New York (1992).
4. S.T. Mayer, R.W. Pekala and J.L. Kaschmitter, *J. Electrochem. Soc.*, 140 (1993) 446.
5. R.W. Pekala, S.T. Mayer, J.L. Daschmitter and F.M. Kong, *Sol-Gel Processing and Applications*, Plenum Press, New York (1994) 369.
6. J. C. Farmer, D. V. Fix, G. V. Mack, R. W. Pekala and J. F. Poco, *J. Applied Electrochem.*, 26 (1996) 1007.
7. C. Lin, J. A. Ritter, *Carbon*, 35 (1997) 1271.
8. J. M. Miller, B. Dunn, T. D. Tran and R. W. Pekala, *J. Electrochem. Soc.*, 144 (1997) L309.
9. H. Tamon, H. Ishizaka, M. Mikami and M. Okazaki, *Carbon*, 35 (1997) 791.

10. J. C. Farmer, S. M. Bahowick, J. E. Harrar, D. V. Fix, R. E. Martinelli, A. K. Vu and K. L. Carroll, *Energy and Fuels*, 11 (1997) 337.
11. H. Tamon and H. Ishizaka, *Carbon*, 36 (1998) 1397.
12. H. Tamon, H. Ishizaka, T. Araki and M. Okazaki, *Carbon*, 36 (1998) 1257.
13. C.J Brinker and G.W. Scherer, *Sol-Gel Science*, Academic Press, San Diego, CA (1990).
14. G. Reichenauer, A. Emmerling, J. Fricke and R.W. Pekala, *J. of Non-Crystalline Solids*, 225 (1998) 221.
15. R. Saliger, U. Fischer, C. Herta and J. Fricke, *J. of Non-Crystalline Solids*, 225 (1998) 81-85.
16. C. Lin, J. A. Ritter, *J. Electrochem. Soc.*, in press (2000).
17. W. Xing, J.S. Xue, T. Zheng, A. Gibaud and J.R. Dahn, *J. Electrochem. Soc.*, 143 (1996) 3482.
18. R.H Lochner and J.E. Matar, *Designing for Quality*, ASQC Quality Press, Milwaukee, 1990.
19. P.J. Davis, C.J. Brinker, D.M. Smith and R.A. Assink, *J. Non-Cryst. Solids*, 142 (1992) 197.
20. C. Lin and J.A. Ritter, *Fundamentals of Adsorption* (M.D. LeVan, ed.), Kluwer Academic Publishers, Boston (1996).
21. E.M. Rabinovich, in L.C. Klien (Eds.), *Sol-Gel Technology for Thin Films, Fibers, Preforms and Specialty Shapes*, Noyes, Park Ridge, NJ (1988).
22. W.F. Maier, I.C. Tilgner, W. Wiedron and H.C. Ko, *Advanced Materials*, 5 (1993) 726.
23. R.W. Pekala, *Mater. Res. Soc. Proc.*, 171 (1990) 285.
24. R.W. Pekala, C.T. Alviso, F.M. Kong, S.S. Hulsey, *J. Non-Cryst. Solids*, 145 (1992) 90.
25. R.W. Pekala and D.W. Schaefer, *Macromolecules*, 26 (1993) 5487.

26. F.M. Kong, S.R. Buckley, C.L. Giles, B.L. Haendler Jr., L.M. Hair, S.A. Letts, G.E. Overturf III, C.W. Price and R.C. Cook, UCRL-LR-106946-DE92-004848, LLNL, Livermore, CA, 1991.

Table 1.  $2^4$  Factorial Design Factor Settings

Factor	High Setting	Low Setting
A. Initial Solution pH	7.0	5.5
B. Weight % Solids	20%	5%
C. Pyrolysis Temperature	1050°C	800°C
D. Gel Type	Xerogel	Aerogel

Table 2. 2<sup>4</sup> Factorial Design Results for the Carbon Aerogels and Xerogels

Initial Solution pH	Weight % Solids	Pyrolysis Temperature °C	Gel Type	Surface Area m <sup>2</sup> /g	Pore Volume cm <sup>3</sup> /g	Capacitance F/g
5.5	5%	800	Aerogel	561	0.32	128
5.5	5%	800	Xerogel	569	0.36	161
5.5	5%	1050	Aerogel	508	0.3	68
5.5	5%	1050	Xerogel	521	0.28	105
5.5	20%	800	Aerogel	517	0.24	86
5.5	20%	800	Xerogel	493	0.26	63
5.5	20%	1050	Aerogel	474	0.23	<b>59</b>
5.5	20%	1050	Xerogel	<b>460</b>	0.25	74
7.0	5%	800	Aerogel	900	0.92	<b>179</b>
7.0	5%	800	Xerogel	591	<b>0.20</b>	113
7.0	5%	1050	Aerogel	753	1.32	142
7.0	5%	1050	Xerogel	540	0.40	106
7.0	20%	800	Aerogel	<b>929</b>	1.31	146
7.0	20%	800	Xerogel	586	0.44	124
7.0	20%	1050	Aerogel	804	<b>1.42</b>	144
7.0	20%	1050	Xerogel	515	0.44	104
<b>Mean</b>				<b>608</b>	<b>0.54</b>	<b>113</b>

Table 3. 2<sup>3</sup> Factorial Design Experimental Results for the Carbon Aerogels

Initial Solution pH	Weight % Solids	Pyrolysis Temperature °C	Surface Area m <sup>2</sup> /g	Pore Volume cm <sup>3</sup> /g	Capacitance F/g
5.5	5%	800	561	0.32	128
5.5	5%	1050	508	0.30	68
5.5	20%	800	517	0.24	86
5.5	20%	1050	<b>474</b>	<b>0.23</b>	<b>59</b>
7.0	5%	800	900	0.92	<b>179</b>
7.0	5%	1050	753	1.32	142
7.0	20%	800	<b>929</b>	1.31	146
7.0	20%	1050	804	<b>1.42</b>	144
		<b>Mean</b>	<b>681</b>	<b>0.76</b>	<b>119</b>



Table 4. 2<sup>3</sup> Factorial Design Experimental Results for the Carbon Xerogels

Initial Solution pH	Weight % Solids	Pyrolysis Temperature °C	Surface Area m <sup>2</sup> /g	Pore Volume cm <sup>3</sup> /g	Capacitance F/g
5.5	5%	800	569	0.36	<b>161</b>
5.5	5%	1050	521	0.28	105
5.5	20%	800	493	0.26	<b>63</b>
5.5	20%	1050	<b>460</b>	0.25	74
7.0	5%	800	<b>591</b>	<b>0.20</b>	113
7.0	5%	1050	540	0.40	106
7.0	20%	800	586	<b>0.44</b>	124
7.0	20%	1050	515	<b>0.44</b>	104
<b>Mean</b>			<b>534</b>	<b>0.33</b>	<b>106</b>

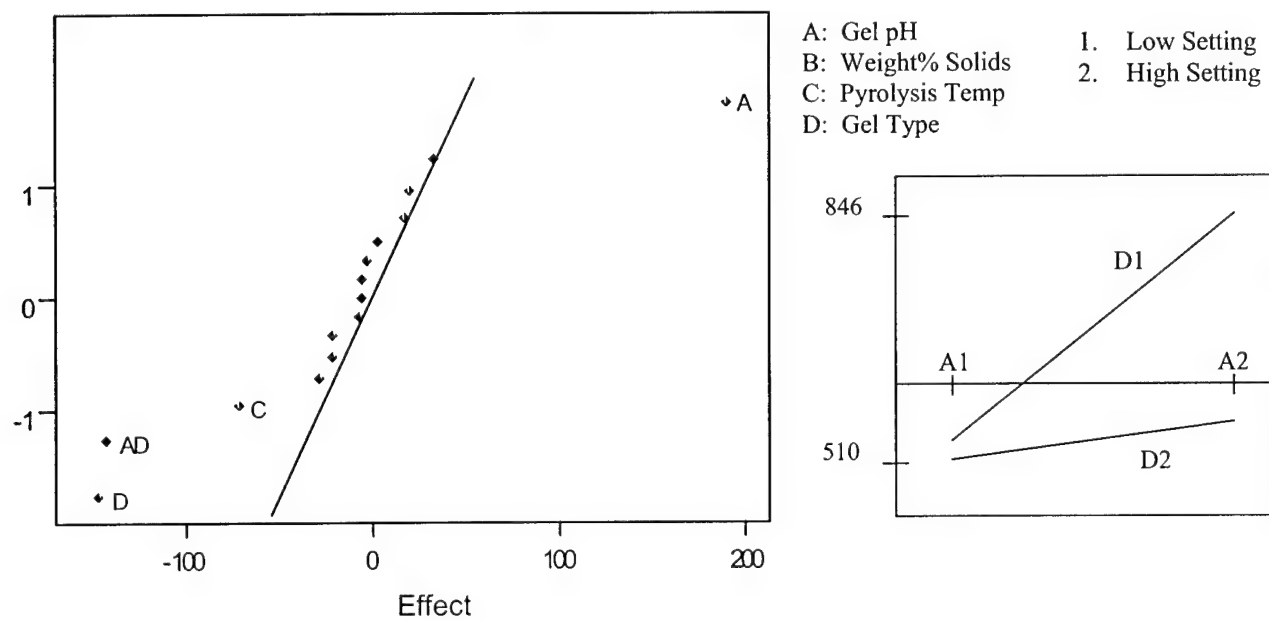


Figure 1. Surface area probability plot and Gel pH – Gel Type interaction plot.

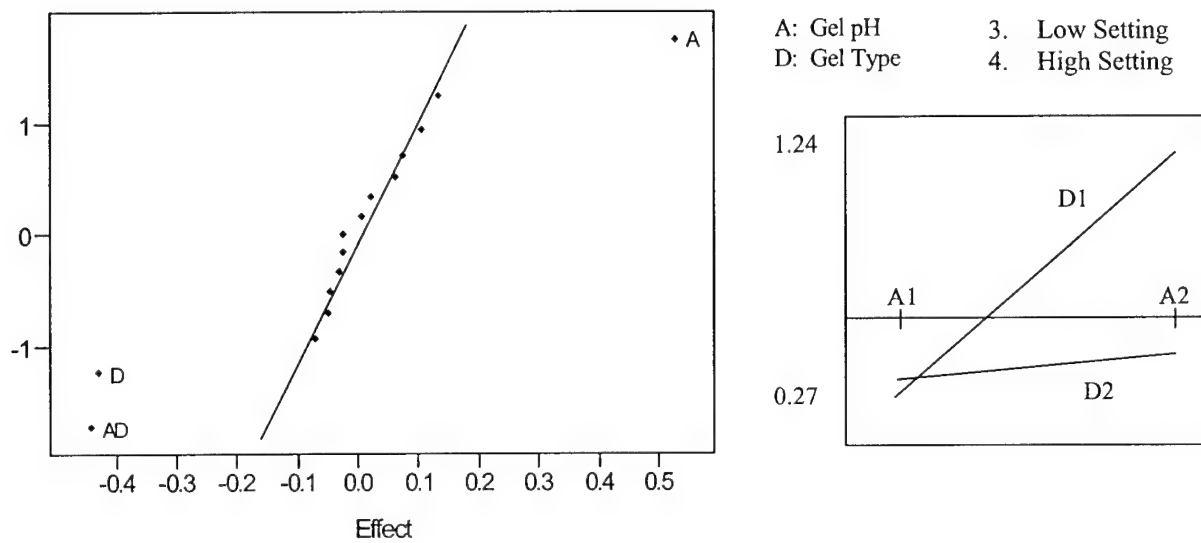


Figure 2. Pore volume probability plot and Gel pH – Gel Type interaction plot.

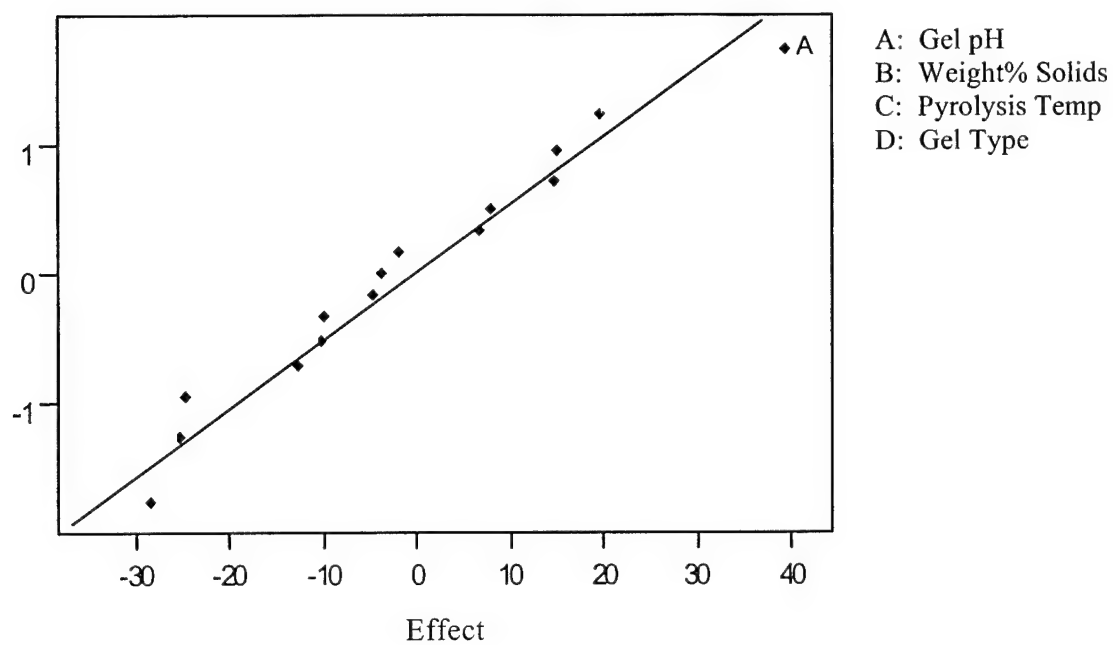


Figure 3. Double layer capacitance probability plot.

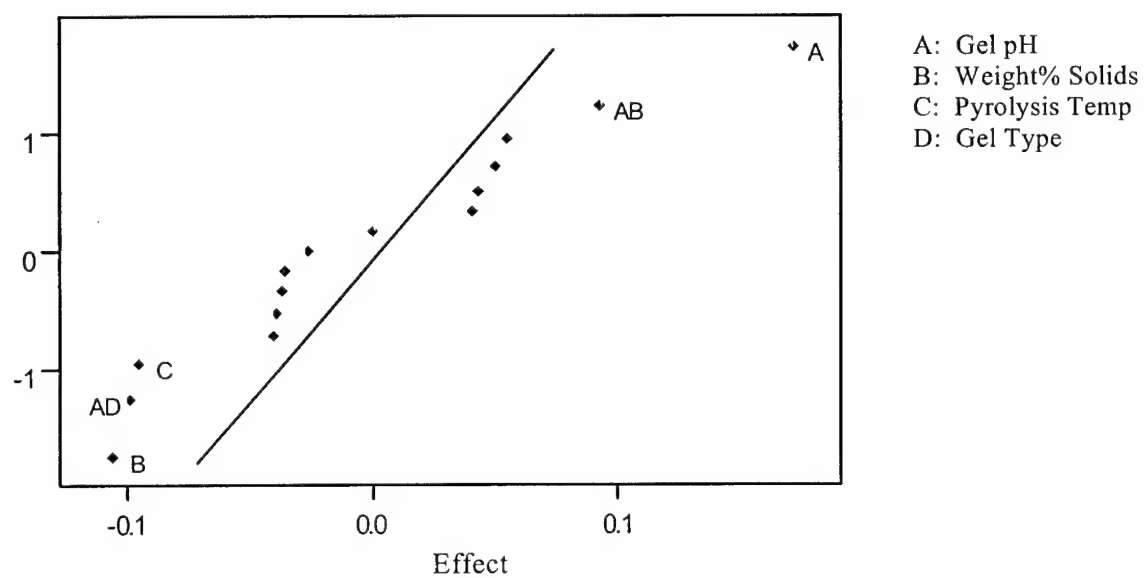


Figure 4. Double layer capacitance probability plot using transformed data.

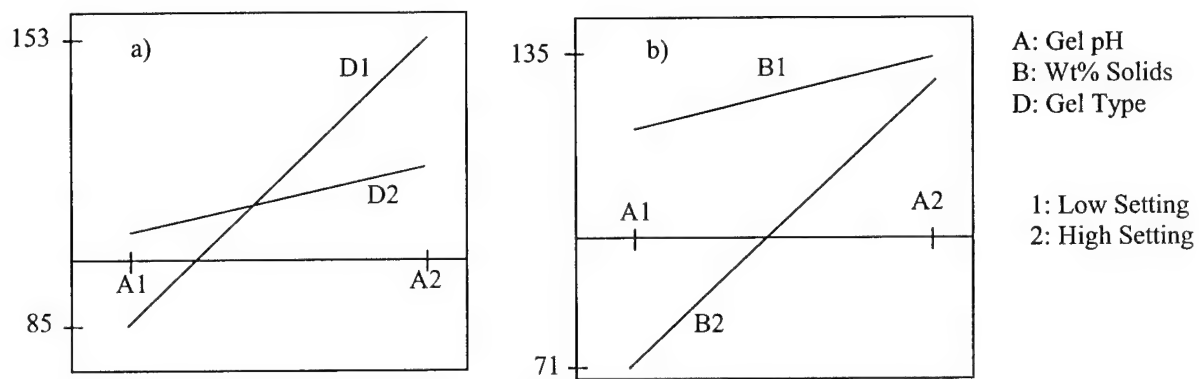


Figure 5. Double layer capacitance interaction plots for a) gel pH – gel type and b) gel type – wt% solids interactions.

**APPROXIMATE SOLUTIONS FOR  
GALVANOSTATIC DISCHARGE OF SPHERICAL PARTICLES -  
1. CONSTANT DIFFUSION COEFFICIENT**

Venkat R. Subramanian,<sup>\*</sup> James A. Ritter<sup>\*\*</sup> and Ralph E. White<sup>\*\*\*</sup>

Department of Chemical Engineering

University of South Carolina

Columbia, SC 29208.

September 1<sup>st</sup>, 2000

Submitted to

Dr. Paul A. Kohl

Editorial Office

Journal of The Electrochemical Society

10 South Main Street, Pennington, NJ 08534 – 2896 USA

<sup>\*</sup> Electrochemical Society Student member  
<sup>\*\*</sup> Electrochemical Society Member  
<sup>\*\*\*</sup> Electrochemical Society Fellow  
White@engr.sc.edu

## ABSTRACT

Approximate models are developed, based on second, fourth and sixth order polynomials, that describe the concentration profile of an electrochemically active species in a spherical electrode particle. Analytical expressions are obtained that describe how the concentration profiles, surface concentrations and electrode utilization change during the galvanostatic discharge of an electrode particle. Based on a comparison with an exact analytical model over a wide range of dimensionless current densities, all three approximate models performed extremely well in predicting these quantities. Quantitative criterion for the validity of these models is also developed and shows that the sixth order, four parameter approximate model is the best. These approximate models, or similarly developed models, should find extensive use in simplifying the modeling of complex electrochemical systems without sacrificing much accuracy.



## INTRODUCTION

The mathematical modeling of electrochemical systems, *e.g.*, batteries or electrochemical capacitors, involves the simultaneous solution of coupled partial differential and algebraic equations that describe among other things current, voltage and electrochemically active species distributions as functions of both time and position throughout the system<sup>1</sup>. Solution methodologies are therefore both complicated and time consuming. For this reason, approximations are continually sought that simplify the governing set of equations without imparting a significant error in the resulting solution. Moreover, many of these electrochemical systems require the modeling of electrodes comprised of roughly spherical particles, into or out of which an electrochemically active species must diffuse during charge and discharge.

This diffusion process is governed by a partial differential equation that describes how the concentration of the electrochemically active species in the particle changes in both time and position during charge and discharge. It is fortuitous that similar diffusion phenomena and hence equations arise in many areas of science and engineering, and in particular, in describing the uptake of a species in adsorbent or catalyst particles. In these two very much related areas, a considerable amount of work has been done on trying to simplify the governing equations by applying various approximations that a priori describe how the concentration profiles change in the spherical particles.

The most widely utilized approximations have been based on parabolic and higher order polynomial functions that describe the concentration profile in the particle,<sup>2-18</sup>

which all began with the work of Liaw *et al.*<sup>2</sup> The coefficients of these polynomials are generally time dependent. Nevertheless, they have been resolved in terms of known and constant system parameters by applying the governing initial and boundary conditions to them. In this way, the partial differential equation describing the concentration in both time and position inside the particle has been reduced to an ordinary differential equation describing how the volume-averaged concentration in the particle changes with time. This ordinary differential equation essentially describes the flux into or out of the particle; and in many cases, it has the form of a linear driving force, where the flux is proportional to a concentration difference.

In some cases, this equation has been integrated either numerically or analytically to describe the diffusion into or out of a particle, for example in batch adsorption or reaction systems. But, in most cases, it is coupled with other differential and algebraic equations, resulting in a simpler approximate solution to a more complex process. This later approach was also used in the modeling of an electrochemical system (batteries), wherein a parabolic species distribution was assumed to describe the distribution in a thin film coating surrounding a particle<sup>19</sup>; however, quantitative justification for such an approximation was not given. Moreover, in a related work,<sup>20</sup> a linear driving force flux relationship was assumed, again with little justification and no mention of whether a parabolic profile approximation leads to a linear driving force flux relation as it does in adsorption and catalytic systems. It is also interesting that when Doyle and Newman<sup>21</sup> simplified the analysis of the discharge process of a lithium ion battery under solid phase diffusion limitations by assuming a pseudo steady-state approximation for longer times or

slower rates, the concentration profile inside the particle became dependent on the square of the radial coordinate *i.e.*, it became inherently parabolic. But again this pseudo steady-state approximation was not quantitatively justified. In contrast, the accuracy of polynomial profile approximations in adsorption and catalytic systems has been shown to depend on many factors; and in many situations very accurate results have been obtained. Thus, these simple but effective polynomial profile approximations have been widely used in simplifying the modeling of adsorption and catalytic processes that involve diffusion into a spherical particle.

In this work, the utility of different polynomial approximations in describing the diffusion of an electrochemically active species out of a spherical electrode particle during galvanostatic discharge is demonstrated. Part 1 of this series deals with the constant diffusion coefficient case, whereas part 2 extends this work and deals with the concentration (state of charge) dependent diffusion coefficient case. Second, fourth and sixth order polynomials are examined. These respectively result in two, three and four parameter models that describe the concentration profiles inside the particle. Strengths and weaknesses of these different polynomial profile approximations are exposed, based on comparing the approximate predictions with those obtained from an exact analytical solution in terms of concentration profiles, surface concentrations and electrode utilization. Quantitative criteria for the validity of these various approximate models are established and their use in other more complex electrochemical systems and other boundary conditions (*e.g.*, cyclic voltametry) are suggested, and discussed in part 3 of this work.

## DIFFUSION MODEL

### 1. Parabolic Profile Model:

Consider a spherical electrode particle completely charged with a corresponding initial concentration  $c_0$ . The transient diffusion in the particle can be expressed as,

$$\frac{\partial c}{\partial t} = D_s \frac{1}{r^2} \frac{\partial}{\partial r} \left( r^2 \frac{\partial c}{\partial r} \right) \quad (1)$$

where  $c$  is the concentration of the diffusing species (*e.g.*, hydrogen), and  $D_s$  is the corresponding diffusion coefficient. In this case, the diffusion coefficient is constant and does not vary with concentration (*i.e.*, state of charge). With the electrochemical reaction taking place only at the surface of the particle, the initial and boundary conditions are given by

$$c = c_0 \quad \text{at } t = 0 \text{ and for } 0 \leq r \leq R_p \quad (\text{fully charged state}) \quad (2)$$

$$\frac{\partial c}{\partial r} = 0 \quad \text{at } r = 0 \text{ and for } t \geq 0 \quad (3)$$

and

$$D_s \frac{\partial c}{\partial r} = -\frac{i_a}{nF} \quad \text{at } r = R_p \text{ and for } t \geq 0 \quad (4)$$

where  $i_a$  is the applied current density at the surface of the particle,  $R_p$  is the radius of the particle,  $n$  is the number of electrons taking place in the electrochemical reaction and  $F$  is Faraday's constant. Introducing the following dimensionless variables,

$$C = \frac{c}{c_0}; \quad x = \frac{r}{R_p} \quad \text{and} \quad \tau = \frac{D_s t}{R_p^2} \quad (5)$$

simplifies the model to,

$$\frac{\partial C}{\partial \tau} = \frac{1}{x^2} \frac{\partial}{\partial x} \left( x^2 \frac{\partial C}{\partial x} \right) \quad (6)$$

with the corresponding initial and boundary conditions,

$$C = 1 \quad \text{at } \tau = 0 \text{ and for } 0 \leq x \leq 1 \quad (7)$$

$$\frac{\partial C}{\partial x} = 0 \text{ at } x = 0 \text{ and for } \tau \geq 0 \quad (8)$$

and

$$\frac{\partial C}{\partial x} = -\delta \text{ at } x = 1 \text{ and for } \tau \geq 0 \quad (9)$$

where  $\delta$  is the applied dimensionless current density defined as,

$$\delta = \frac{i_a R}{n F D_s c_0} \quad (10)$$

An exact analytical solution to this model can be obtained by the separation of variables<sup>22,23</sup> and given by<sup>24</sup>

$$C(x, \tau) = 1 - \delta \left[ 3\tau + \frac{1}{10} (5x^2 - 3) - 2 \frac{1}{x} \sum_{n=1}^{\infty} \frac{\sin(\lambda_n x)}{\lambda_n^2 \sin(\lambda_n)} \exp(-\lambda_n^2 \tau) \right] \quad (11)$$

with eigenvalues  $\lambda_n = \tan(\lambda_n)$ . The number of terms required for convergence of this series can be significant and depends strongly upon the dimensionless current density  $\delta$ .

A simpler solution to the same problem can be obtained by assuming that the concentration of the diffusing species inside the particle is described by a parabolic profile,

$$C = a(\tau) + b(\tau)x^2 \quad (12)$$

where  $a(\tau)$  and  $b(\tau)$  are functions of  $\tau$ . The boundary condition at the center (equation 8) is automatically satisfied. Applying equation 12 to the boundary condition at the surface (equation 9) gives,

$$\left. \frac{\partial C}{\partial x} \right|_{x=1} = 2b(\tau) = -\delta \quad (13)$$

According to equation 12, the volume-averaged concentration is given by,

$$\bar{C} = \int_{x=0}^1 C \cdot 3x^2 dx = a(\tau) + \frac{3}{5}b(\tau) \quad (14)$$

Both sides of equation 6 are now multiplied by  $3x^2$  and integrated from 0 to 1 using equation 12 for C in equation 6. This results in

$$\begin{aligned} \int_{x=0}^1 \frac{\partial C}{\partial \tau} \cdot 3x^2 dx &= \int_{x=0}^1 \frac{1}{x^2} \frac{\partial}{\partial x} \left( x^2 \frac{\partial C}{\partial x} \right) \cdot 3x^2 dx \\ \Rightarrow \quad \frac{d\bar{C}}{d\tau} &= 6b(\tau) = -3\delta \end{aligned} \quad (15)$$

an ordinary time-dependent differential equation in terms of the volume-averaged concentration. However, it is interesting that this analysis does not result in a linear driving force type expression, as it typically does in adsorption and catalytic systems. The solution to equation 15 with the initial condition given in equation 7 is

$$\bar{C} = 1 - 3\delta\tau \quad (16)$$

A comparison of equations 14 and 16 leads to,

$$a(\tau) = 1 - 3\delta\tau + \frac{3}{10}\delta \quad (17)$$

Hence, the concentration profile in the particle, based on the parabolic profile (PP) approximation, is given by,

$$\begin{aligned} C_{pp} &= 1 - 3\delta\tau + \frac{3}{10}\delta - \frac{\delta}{2}x^2 \\ &= 1 - \delta \left[ 3\tau + \frac{1}{10}(5x^2 - 3) \right] \end{aligned} \quad (18)$$

A comparison with the exact solution (equation 13) shows that the parabolic profile (PP) model does not yield the exponential terms and hence results in a much simpler solution. Note that for this case  $a(\tau)$  is a function of  $\tau$ , where as  $b(\tau)$  is a constant. In general, this is not always the case and the results may vary according to the boundary conditions and the initial governing equation.

In an electrode particle, the electrochemical behavior is determined completely by the concentration at the surface. The surface concentration from the exact solution is given by

$$C_{S_{\text{exact}}} = C_{x=1} = C(x,\tau) = 1-\delta \left[ 3\tau + \frac{2}{10} - 2 \sum_{n=1}^{\infty} \frac{1}{\lambda_n^2} \exp(-\lambda_n^2 \tau) \right] \quad (19)$$

and that from the PP solution is given by

$$C_{S_{\text{PP}}} = C_{\text{PP}, x=1} = 1-\delta \left[ 3\tau + \frac{2}{10} \right] \quad (20)$$

Utilization is also a very important property for any electrode particle. It is defined as the amount of active material reacted, according to

$$\begin{aligned} U &= \frac{\text{Initial concentration} - \text{concentration left in the particle after discharge}}{\text{Initial concentration}} \times (100) \\ &= \frac{1 - \int_{x=0}^1 C(x, \tau_{\text{disch}}) 3x^2 dx}{1} (100) \end{aligned} \quad (21)$$

where  $3x^2 dx$  is the differential volume element of the spherical particle, and  $\tau_{\text{disch}}$  is the dimensionless time taken for discharge, which is determined by setting the surface concentration to zero. Substitution of equation 11 (for the exact concentration) into equation (21) and integrating yields

$$U_{\text{exact}}(\%) = 3\delta\tau_{\text{disch,ex}}(100) \quad (22)$$

where  $\tau_{\text{disch,ex}}$  is the exact dimensionless time taken for complete discharge. This value is obtained by setting the left hand side of equation 19 to zero and solving for  $\tau$ . Note that the integral of the infinite series is zero as explained in reference 21. Similarly using the PP solution (equation 18) leads to

$$U_{\text{pp}}(\%) = 3\delta\tau_{\text{disch,PP}}(100) \quad (23)$$

where  $\tau_{\text{disch,PP}}$  is the dimensionless time taken for complete discharge which is obtained from equation 20 with the surface concentration set to zero. Accordingly,

$$U_{\text{pp}}(\%) = \left(1 - \frac{\delta}{5}\right)(100) \quad (24)$$

## 2. Higher Order Polynomial Profile Models:

Three and four parameter polynomial profile approximations can also be utilized to obtain simpler but potentially more accurate solutions to the governing equations (equations 1-4) for the concentration profile inside the electrode particle. For example, a fourth order, three parameter polynomial such as

$$C = a(\tau) + b(\tau)x^2 + d(\tau)x^4 \quad (25)$$

where  $a(\tau)$ ,  $b(\tau)$  and  $d(\tau)$  are functions of  $\tau$ , can be applied in the same way as equation 12. As before, the boundary condition at the center (equation 8) is automatically satisfied. Applying equation 25 to the boundary condition at the surface (equation 9) gives,

$$\left. \frac{\partial C}{\partial x} \right|_{x=1} = 2b(\tau) + 4d(\tau) = -\delta \quad (26)$$



According to equation 25, the volume-averaged concentration is given by,

$$\bar{C} = \int_{x=0}^1 C \cdot 3x^2 dx = a(\tau) + \frac{3}{5}b(\tau) + \frac{3}{7}d(\tau) \quad (27)$$

Both sides of equation 6 are now multiplied by  $3x^2$  and integrated from 0 to 1 using equation 25 for C in equation 6. This results in

$$\frac{d\bar{C}}{d\tau} = 6b(\tau) + 12d(\tau) = -3\delta \quad (28)$$

The solution to equation 28 with the initial condition given in equation 7 is

$$\bar{C} = a(\tau) + \frac{3}{5}b(\tau) + \frac{3}{7}d(\tau) = 1 - 3\delta\tau \quad (29)$$

Since in this case there are three constants ( $a(\tau)$ ,  $b(\tau)$  and  $d(\tau)$ ) to evaluate, three equations are needed. So, in addition to equations 26 and 29, the governing equation (equation 6) is evaluated at  $x = 1$ , *i.e.*,

$$\left. \frac{\partial C}{\partial \tau} \right|_{x=1} = \frac{1}{x^2} \frac{\partial}{\partial x} \left( x^2 \frac{\partial C}{\partial x} \right) \Big|_{x=1} \quad (30)$$

Substituting equation 25 into equation 30 leads to

$$\frac{da(\tau)}{d\tau} + \frac{db(\tau)}{d\tau} + \frac{dd(\tau)}{d\tau} = 6b(\tau) + 20d(\tau) \quad (31)$$

Solving equations 26, 29 and 31 gives the three constants as,

$$\begin{aligned} a(\tau) &= 1 - 3\delta\tau + \frac{3}{10}\delta - \frac{27}{140}\delta \exp(-35\tau) \\ b(\tau) &= -\frac{1}{2}\delta + \frac{1}{2}\delta \exp(-35\tau) \\ \text{and} \\ d(\tau) &= -\frac{1}{4}\delta \exp(-35\tau) \end{aligned} \quad (32)$$

These three parameters give the surface concentration as,

$$C_{S_{3p}} = 1 - \delta \left[ 3\tau + \frac{2}{10} \right] + \frac{2}{5} \delta \exp(-35\tau) \quad (33)$$

Similarly, one more parameter can be added to equation 25 in the form of the following sixth order polynomial

$$C = a(\tau) + b(\tau)x^2 + d(\tau)x^4 + e(\tau)x^6 \quad (34)$$

To solve for this fourth parameter  $e(\tau)$  another equation is needed and obtained by applying the limit,  $x = 0$ , to both sides of the governing equation, *i.e.*, equation 6. For this four parameter model, the following differential equations result and are solved simultaneously using the exponential matrix method<sup>25</sup> (which the authors refer to as the semi-analytical method<sup>26-28</sup>).

$$\frac{d\bar{C}}{d\tau} = 6b(\tau) + 12d(\tau) + 18e(\tau) = -3\delta \quad (35)$$

$$\frac{da(\tau)}{d\tau} + \frac{db(\tau)}{d\tau} + \frac{dd(\tau)}{d\tau} + \frac{de(\tau)}{d\tau} = 6b(\tau) + 20d(\tau) + 42e(\tau) \quad (36)$$

$$\frac{da(\tau)}{d\tau} = 6b(\tau) \quad (37)$$

This all leads to the following expression for the surface concentration:

$$C_{S_{4p}} = 1 - \delta \left[ 3\tau + \frac{2}{10} \right] + 0.1135\delta \exp(-100.123\tau) + 0.0864\delta \exp(-18.877\tau) \quad (38)$$

## RESULTS AND DISCUSSION

It is clear from the above analysis that the concentration profiles, surface concentrations and electrode utilization predicted from the approximate and exact models depend mainly on the magnitude of the dimensionless current density,  $\delta$ . Figures 1 and 2 compare the concentration profiles in the particle obtained from the approximate and exact models at different dimensionless times during discharge for low and high values of

$\delta$ , respectively. For both values of  $\delta$ , the exact and approximate models agree extremely well with each other, except at short dimensionless times approaching  $\tau = 0$ . The deviations are also larger for higher values of  $\delta$ , indicating that the polynomial profile approximations begin to break down at higher reaction rates, but only during the initial states of discharge. After an initial period of time the agreement between the approximate and exact models is nearly perfect for all three polynomial functions. This is not the case for the surface concentrations, however.

Figures 3 to 6 compare the dimensionless surface concentrations predicted from the exact and the three approximate models as a function of the state of discharge, for values of  $\delta$  equal to 0.1, 0.2, 2 and 5 respectively. Only the four parameter model is capable of predicting the surface concentration over a broad range of  $\delta$  with reasonable accuracy. In contrast, the two and three parameter models only do well at low values of  $\delta$ ; at higher values, they behave similarly and completely misrepresent the surface concentration at zero state of discharge where it should be unity. So, again at high reaction rates, the second and fourth order polynomial approximations breakdown, but not the sixth order polynomial approximation; and at low to moderate values of  $\delta$ , again all three approximate models agree reasonably well with the exact model. Similar results are realized in predicting the electrode utilization.

Figure 7 compares the utilization predicted from the exact and the three approximate models as a function of  $\delta$ . The four parameter model agrees extremely well with the exact solution over a brand range of  $\delta$  up to a  $\delta$  of about 2. In contrast, the two

and three parameter models begin to deviate from the exact model at a  $\delta$  of around 4, with the two parameter model deviating the most. Nevertheless, all three approximate models agree quite well with the exact solution in predicting the utilization of the electrode over a wide range of reaction rates.

As stated earlier, the surface concentration is one of the more important concentrations that governs the performance of electrochemical systems; and hence, it is worth quantifying the error in the prediction of the surface concentration from the three approximate models. For this purpose, a time-averaged percent error in the surface concentration is defined as

$$\varepsilon = \frac{\int_{\tau=0}^{\tau=\tau_{\text{disch.ex}}} C_{s,\text{exact}} d\tau - \int_{\tau=0}^{\tau=\tau_{\text{disch.app}}} C_{s,\text{approximate}} d\tau}{\int_{\tau=0}^{\tau=\tau_{\text{disch.ex}}} C_{s,\text{exact}} d\tau} (100) \quad (39)$$

These percent errors are plotted in Figure 7 as a function of  $\delta$ , for all three approximate models. The error in predicting the surface concentration from the two and three parameter models is very similar, with errors of less than 5% resulting for values of  $\delta$  less than 0.5 and 1.0 respectively. In contrast, the error in predicting the surface concentration from the four parameter model is much smaller, with values of  $\delta$  up to around 4 still only resulting in an error of less than 5%. Overall, the three approximate models provide a relatively accurate prediction of the surface concentration over a very broad and practical range of  $\delta$  and the four parameter model hardly deviates at all from the exact solution within this range.

Clearly, the solutions to the unsteady-state diffusion equation developed here (*i.e.*, equations 20, 33 and 38) are not only much simpler to use compared to the exact solution (equation 18), they also shed some light on the validity of other simplified analyses carried out on electrochemical systems in the literature.<sup>19-21</sup> For example, they provide a quantitative description of the error that may be incurred by applying a parabolic profile approximation to describe the concentration profile of an electrochemically active species in a thin film surrounding a spherical particle, as done by Wang *et al.*<sup>19</sup> In a similar manner, they provide a quantitative description of the parameter range over which the pseudo steady-state approximation may be applied, as done by Doyle and Newman.<sup>21</sup> In other words, the simple solutions developed here can be used to give a quantitative estimate of what longer times or slower rates really means in an electrochemical system, based on the magnitude of the dimensionless current density, for example. The solution methodologies developed here may also be of great use in simplifying the analyses of pseudo two dimensional problems.<sup>29</sup> For example, instead of integrating the exact solution (equation 19), one of the approximate solutions (equations 20, 33 or 38) can be easily integrated by applying Duhamel's superposition theorem.

## CONCLUSIONS

A common assumption used in simplifying the modeling of complex adsorption and catalytic systems is introduced here for simplifying the modeling of complex electrochemical systems. In particular, second, fourth and sixth order polynomial profile approximations, that describe the concentration profile of an electrochemically active species in a spherical electrode particle, are used to simplify the unsteady-state diffusion equation with a constant diffusion coefficient and describe the galvanostatic discharge of electrode particles. The resulting analytical expressions compare extremely well with the exact analytical solution in predicting the concentration profiles, surface concentrations and electrode utilization over a broad range of practical dimensionless current densities. Based on a quantitative criterion that is also developed, the sixth order, four parameter polynomial approximation gives the best results, with errors of less than 5% over a broad range of practical conditions. These relationships should thus be very useful in the design and analysis of electrochemical systems, and also in parameter estimation.

The methodology developed in this work should also be very useful in simplifying the analysis of other more complicated electrochemical systems, for example, in solving pseudo two-dimensional problems. Moreover, this methodology is readily extended to the case where the diffusion coefficient is a function of concentration (*i.e.*, state of charge), as will be shown in part 2 of this study. It is also amiable to time dependent and/or other nonlinear boundary conditions, and even impedance studies as will be shown in part 3 of this work. Therefore, it is anticipated that these polynomial

profile approximations will find considerable use in simplifying the modeling of complex electrochemical systems without sacrificing much accuracy.

#### Acknowledgements

This material is based upon work supported in part by the National Reconnaissance Organization (NRO) under contract #1999 I016400 000 000, and in part by the U. S. Army Research Office under Grant No. DAAH04-96-1-0421.

## REFERENCES

1. J. S. Newman, *Electrochemical Systems*, chapter 18, Prentice Hall, Englewood Cliffs, New Jersey (1991).
2. C. H. Liaw, J. S. P. Wang, R. H. Greenkorn, and K. C. Chao, *AIChE Journal*, **54**, 376-381 (1979).
3. N. Wakao, and S. Kaguei, *Heat and Mass transfer in Packed Beds*, Gordon & Breach, New York, USA (1982).
4. D. Do and R. Rice, *AIChE Journal*, **32**, 149 (1986).
5. J. H. Hills, *Chemical Engineering Science*, **11**, 2779 (1986).
6. D. Do, and P. L. J. Mayfield, *AIChE Journal*, **33**, 1397 (1987).
7. T. Tomida, and B. J. McCoy, *AIChE Journal*, **33**, 1908 (1987).
8. D. Do and T. Nguyen, *Chemical Engineering Communications*, **72**, 171 (1988).
9. M. A. Buzanowski, and R. T. Yang, *Chemical Engineering Science*, **44**, 2683 (1989).
10. D. H. Kim, *AIChE Journal*, **35**, 343 (1989).
11. M. Goto, J. M. Smith, and B. J. McCoy, *Chemical Engineering Science*, **45**, 443 (1990).
12. C. C. Lai and C. S. Tan, *AIChE Journal*, **37**, 461 (1991).
13. M. Goto, and T. Hirose, *Chemical Engineering Science*, **48**, 443 (1993).
14. C. Yao, and C. Tien, *Chemical Engineering Science*, **48**, 187 (1993).
15. R. Zhang, and J. A. Ritter, *Chemical Engineering Science*, **52**, 3161 (1997).
16. G. Carta and A. Cincotti, *Chemical Engineering Science*, **53**, 3483 (1998).



17. G. G. Botte, R. Zhang, and J. A. Ritter, *Chemical Engineering Science*, **53**, 4135 (1998).
18. G. G. Botte, R. Zhang, and J. A. Ritter, *Adsorption*, **5**, 375 (1999).
19. W. B. Gu, C. Y. Wang, and B. Y. Liaw, *Journal of Electrochemical Society*, **145**, 3407 (1998).
20. W. B. Gu, C. Y. Wang, and B. Y. Liaw, *Journal of Electrochemical Society*, **145**, 3418 (1998).
21. M. Doyle, and J. Newman, *Journal of Applied Electrochemistry*, **27**, 846, (1993).
22. V.R. Subramanian and R.E. White, *Separation of Variables for Diffusion in Composite Electrodes with Flux Boundary Conditions, on Tutorials in Electrochemical Engineering*, R.F. Savinell and A.C. West (Ed.,) The Electrochemical Society, Inc., Pennington, New Jersey (1999).
23. V.R. Subramanian and R.E. White, *New Separation of Variables Method for Composite Electrodes with Galvanostatic Boundary Conditions, Journal of Power Sources* (submitted August, 2000).
24. H. S. Carslaw and J. C. Jaeger, *Conduction of Heat in Solids*, Oxford University Press, London (1973), p. 112.
25. A. Varma and M. Morbidelli, *Mathematical Methods in Chemical Engineering*, Oxford University Press, New York (1997).
26. P. De Vidts and R.E. White, *Computers and Chemical Engineering*, **16**, 1007 (1992).
27. V. R. Subramanian and R.E. White, *Journal of the Electrochemical Society*, **147**, 1636, (2000).

28. V. R. Subramanian and R.E. White, *Symbolic Solutions for Boundary Value Problems Using Maple, Computers and Chemical Engineering*, (in press).
29. M. Doyle, T. F. Fuller and J. Newman, *Journal of the Electrochemical Society*, **140**, 1526, (1993).

## NOMENCLATURE

$a(\tau)$	time dependent constant (dimensionless)
$b(\tau)$	time dependent constant (dimensionless)
$d(\tau)$	time dependent constant (dimensionless)
$c$	concentration, moles/cm <sup>3</sup>
$c_0$	initial concentration moles/cm <sup>3</sup>
$c_s$	surface concentration moles/cm <sup>3</sup>
$i$	applied current density, A/cm <sup>2</sup>
$C$	dimensionless concentration
$C_s$	dimensionless surface concentration
$D$	diffusion coefficient, cm <sup>2</sup> /sec
$I$	applied current, A/g
$R_p$	radius of the electrode particle, cm
$U$	utilization (dimensionless)

Greek:

$\delta$	dimensionless current density at the surface
$\tau$	dimensionless time

## KEYWORDS

Dimensionless current density

Parabolic Profile (PP) solution

Maple V<sup>®</sup>

Utilization

## FIGURE CAPTIONS

1. Approximate and exact dimensionless concentration profiles inside a spherical electrode particle for  $\delta = 0.1$ .
2. Approximate and exact dimensionless concentration profiles inside a spherical electrode particle for  $\delta = 0.5$ .
3. Approximate and exact dimensionless surface concentrations at the surface of a spherical electrode particle as a function of the state of discharge for  $\delta = 0.1$  (low value of  $\delta$ ).
4. Approximate and exact dimensionless surface concentrations at the surface of a spherical electrode particle as a function of the state of discharge for  $\delta = 1$  (moderate value of  $\delta$ ).
5. Approximate and exact dimensionless surface concentrations at the surface of a spherical electrode particle as a function of the state of discharge for  $\delta = 2$  (high value of  $\delta$ ).
6. Approximate and exact dimensionless surface concentrations at the surface of a spherical electrode particle as a function of the state of discharge for  $\delta = 5$  (extremely high value of  $\delta$ ).
7. Approximate and exact predictions of the electrode utilization in a spherical electrode particle as a function of the dimensionless current density  $\delta$ .
8. Error in predicting the dimensionless surface concentration at the surface of a spherical electrode particle from the approximate models as a function of the dimensionless current density  $\delta$ .

Figure 1. Subramanian *et al.*

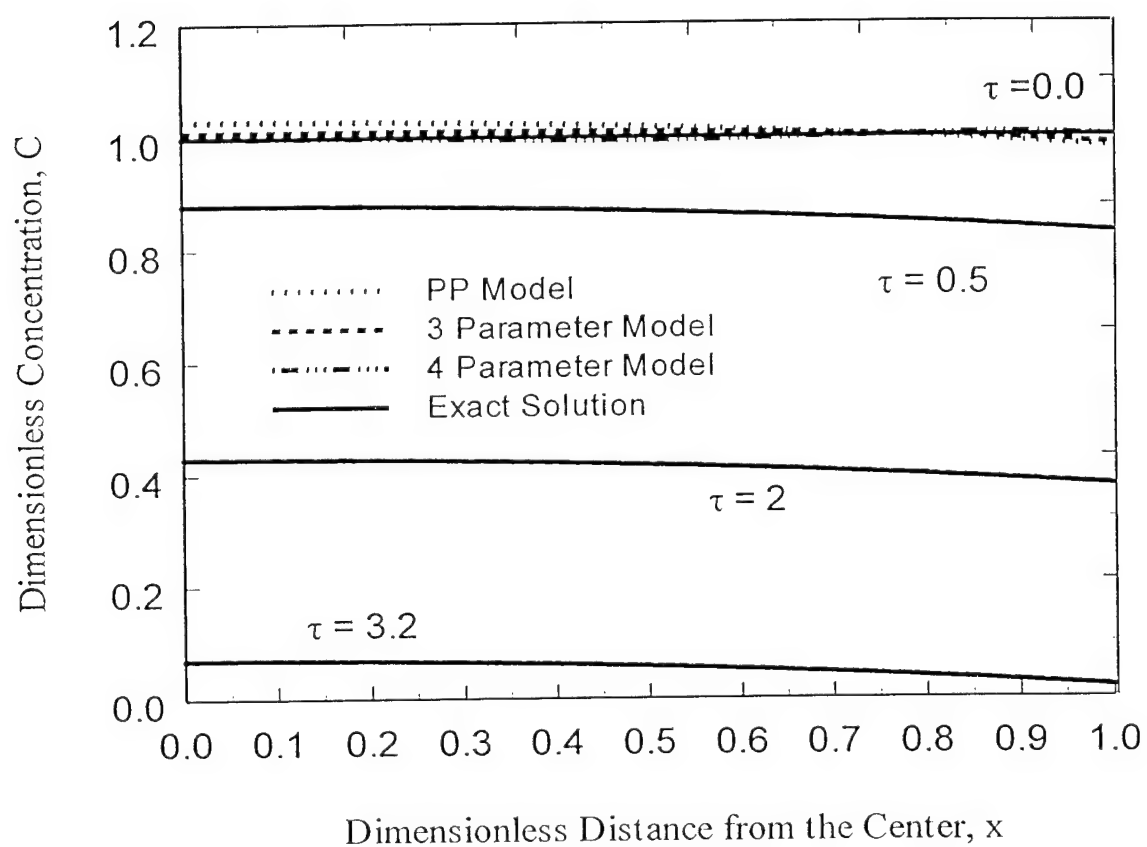


Figure 2. Subramanian *et al.*

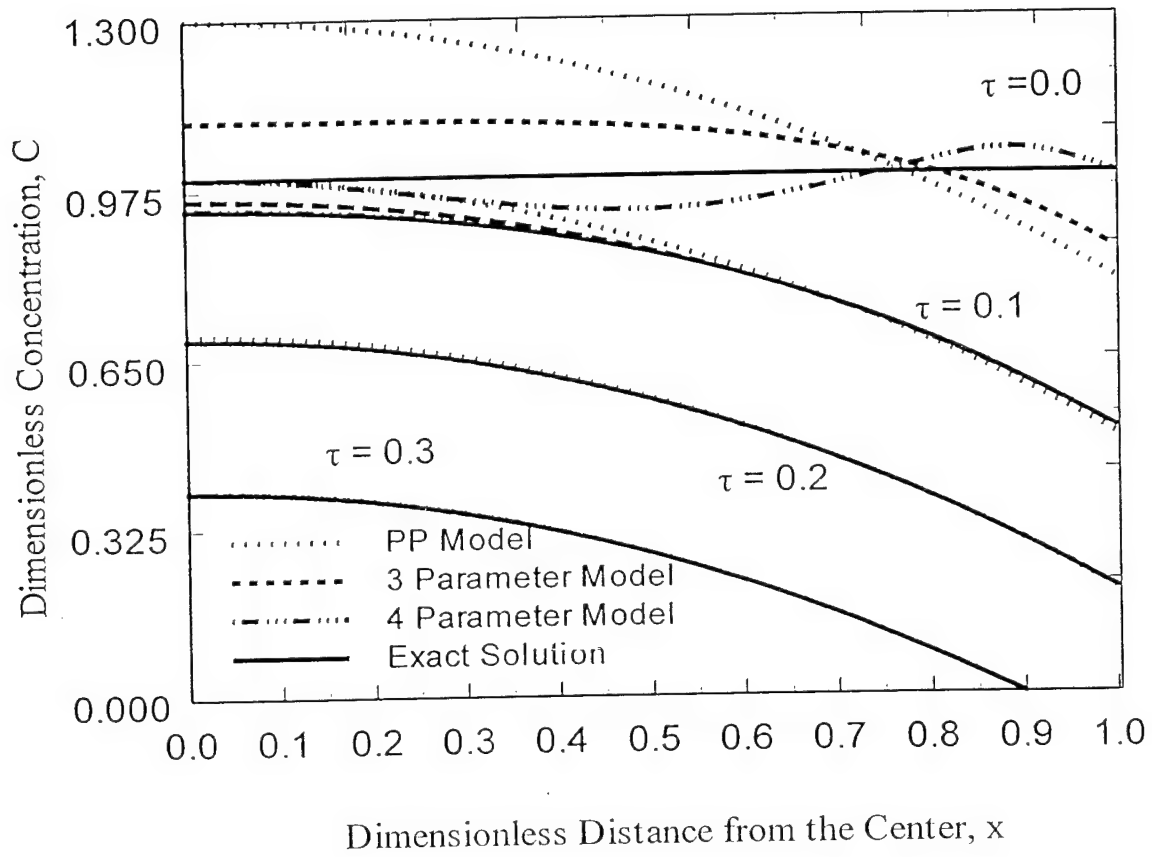


Figure 3. Subramanian *et al.*

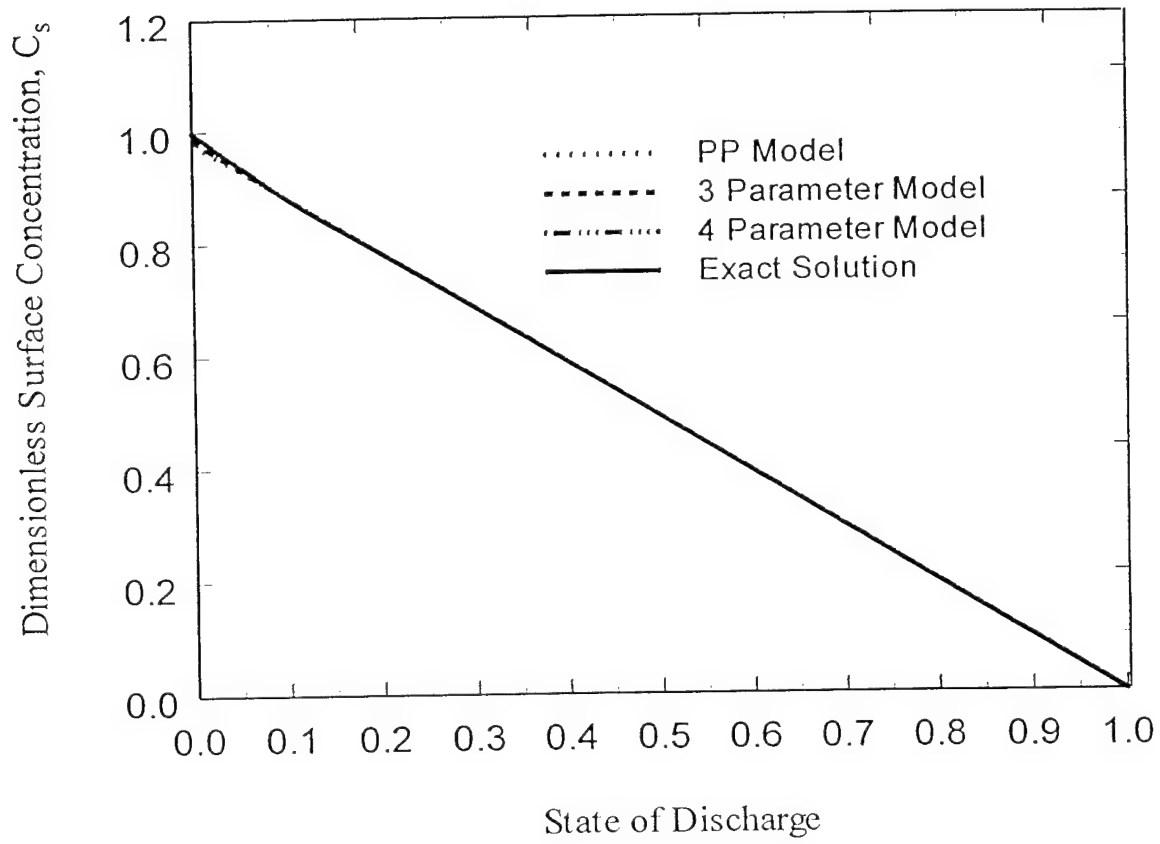




Figure 4. Subramanian *et al.*

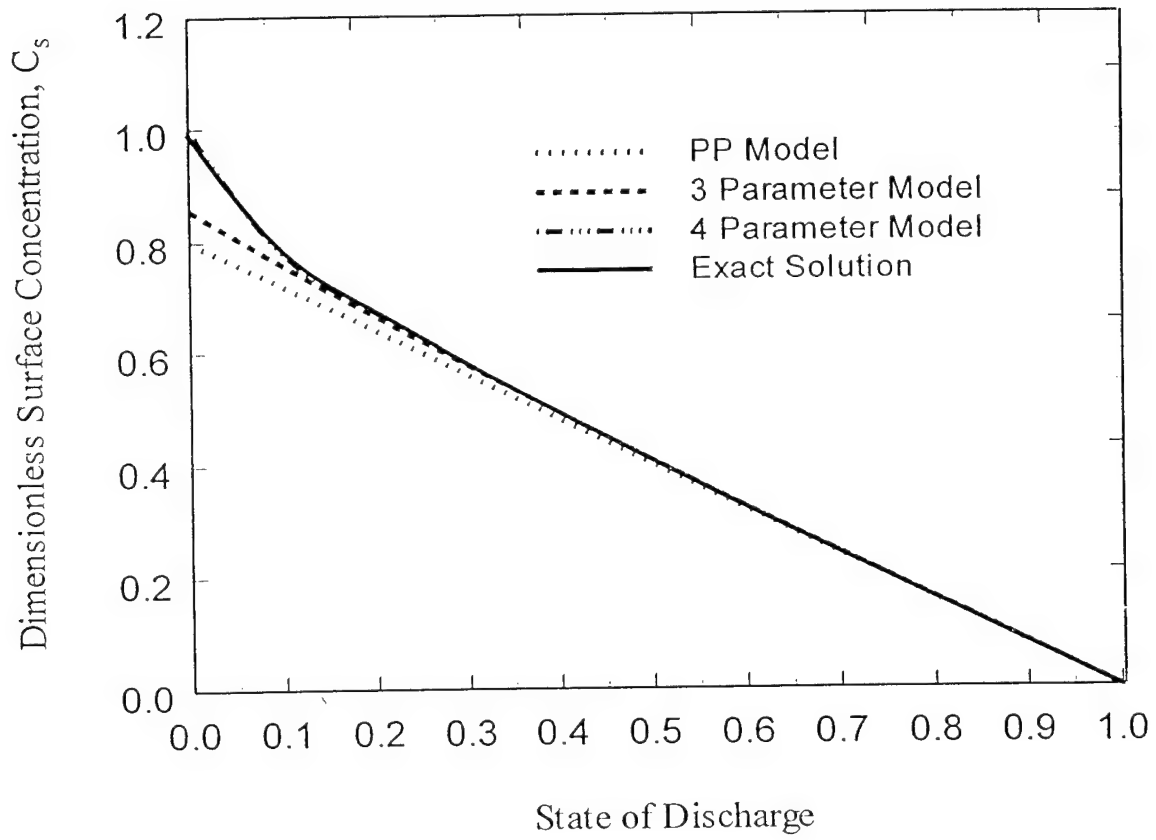


Figure 5. Subramanian *et al.*

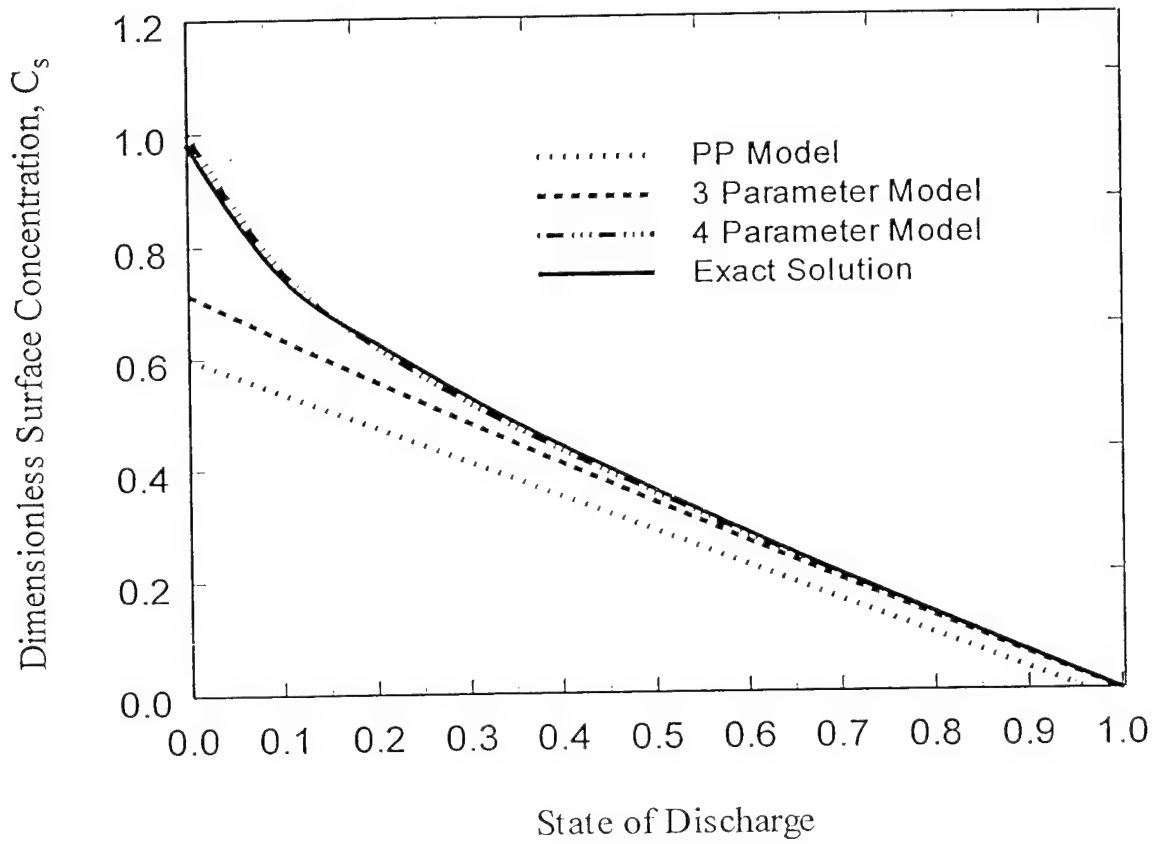


Figure 6. Subramanian *et al.*

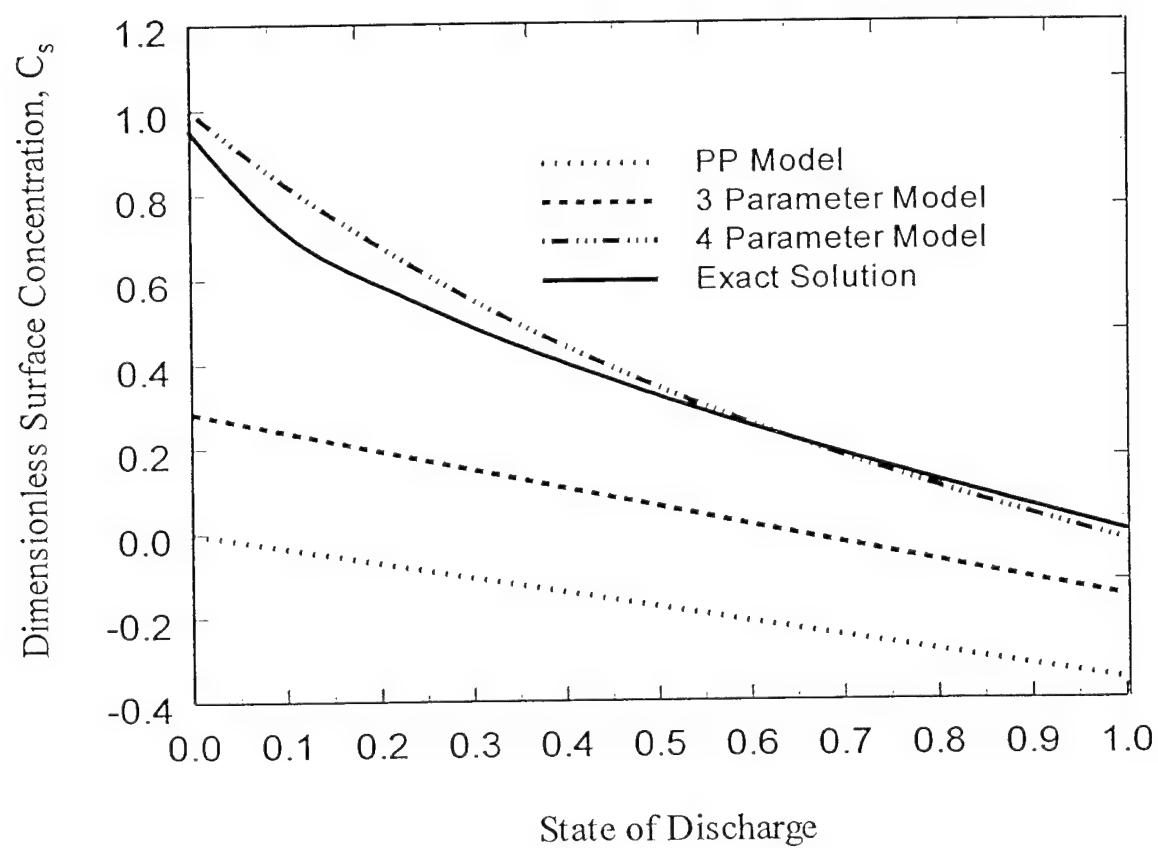


Figure 7. Subramanian *et al.*

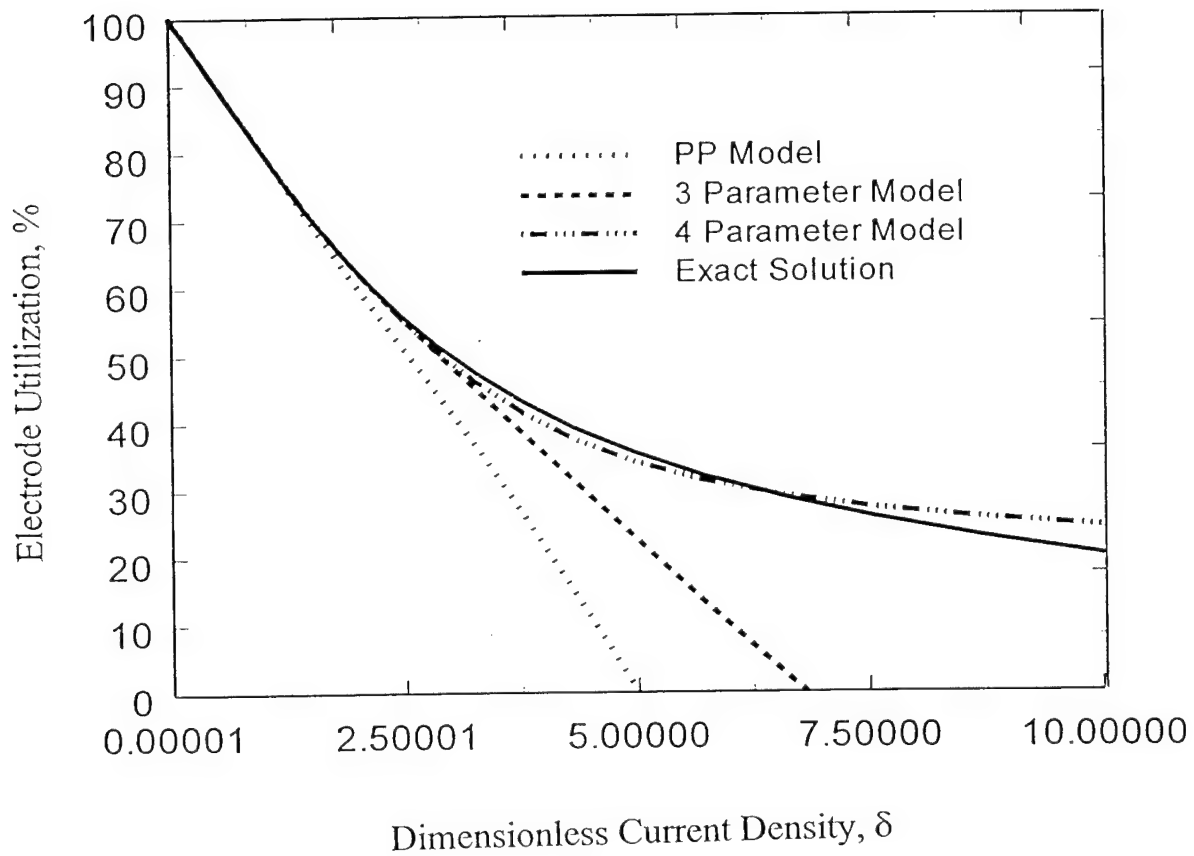
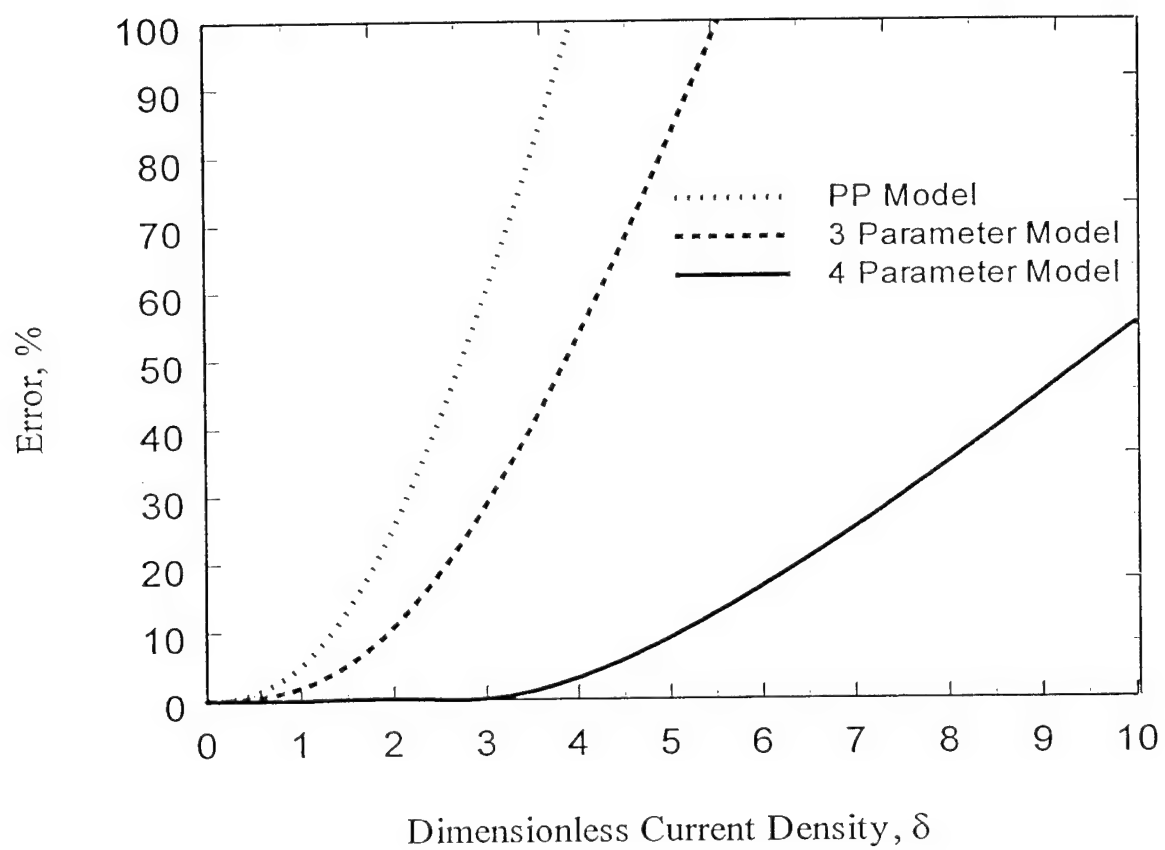


Figure 8. Subramanian *et al.*



# Hysteresis during Cycling of Nickel Hydroxide Active Material

Venkat Srinivasan<sup>\*,1</sup> and John W. Weidner<sup>\*\*</sup>

Department of Chemical Engineering  
University of South Carolina  
Columbia SC 29208

John Newman<sup>\*\*\*</sup>

Department of Chemical Engineering  
University of California  
Berkeley, CA 94720

Manuscript for Submission to  
*Journal of the Electrochemical Society*  
as a Technical paper

Submission Date: November 1, 2000

---

\* Electrochemical Society Student Member

<sup>1</sup> Present address: Department of Mechanical and Nuclear Engineering, Pennsylvania State University,  
University Park, PA-16802

\*\* Electrochemical Society Active Member

\*\*\* Electrochemical Society Fellow

## Abstract

The nickel hydroxide electrode is known to exhibit a stable hysteresis loop, with the potential on charge being higher than that on discharge at every state-of-charge. What we show here is that this loop created during a complete charge and discharge (*i.e.*, boundary curves) is not sufficient to define the state of the system. Rather, internal loops within the boundary curves (*i.e.*, scanning curves) can be generated that access potentials between the boundary curves. The potential obtained at any state-of-charge, as well as how the material charges and discharges from that point, depends on the cycling history of the material. Analysis of the boundary and scanning curves suggests that the electrode consists of a number of individual units or domains, each of which exhibits two or more metastable states. The cycling behavior of the nickel hydroxide electrode is discussed within the context of previously developed theoretical arguments regarding domain theory. Although the specific cause for the metastability in each domain is not understood, considerable insights are provided into the history-dependent behavior of the nickel hydroxide electrode. Finally, an empirical procedure is developed to predict the scanning curves based on the boundary curves.

## Introduction

Hysteresis is a characteristic of a system in which a change in the direction of the independent variable leads to the dependent variable failing to retrace the path it passed in the forward loop.<sup>1</sup> In other words, the dependent variable lags behind in an attempt to track the changes in the independent variable. Consequently, the system exhibits "history" dependence, with the path of the system dictated by its previous history. The phenomenon is manifested as a closed loop with two values of the dependent variable for each independent variable, one in the forward loop, and the other in the reverse. Most often, the size of the loop changes depending on the rate with which the independent variable is changed. A common electrochemical example of such a "time-dependent hysteresis" is cyclic voltammetry. The anodic and cathodic loops do not overlap due to kinetic, mass-transfer, and ohmic resistances, and therefore they move closer together as the rates are lowered. However, in a few systems, the loops generated are stable, reproducible, and rate-independent. Such loops are termed "permanent hysteresis,"<sup>1</sup> and they are the focus of this paper. From this point forward, the term "hysteresis" will refer only to this rate-independent phenomenon.

Hysteresis is well-studied in adsorption<sup>1</sup> and magnetism,<sup>2</sup> but there are only a few documented examples in electrochemical systems. This includes the history-dependent equilibrium potential observed during the intercalation of lithium ions into carbon<sup>3,4</sup> and  $\text{LiMnO}_2$  electrodes,<sup>5,6</sup> hydrogen in  $\text{LaNi}_5$ ,<sup>7</sup> and protons into nickel hydroxide.<sup>8-10</sup> In the latter example, the "equilibrium potential" measured during charge (*i.e.*, proton extraction) is 40 to 90 mV higher than that measured during discharge (*i.e.*, proton intercalation) at room temperature.<sup>8-10</sup> The potential offset between charge and discharge



decreases approximately 0.5 mV for every 1°C increase in temperature,<sup>8</sup> and at room temperature the offset decreases by 40 mV with the addition of cobalt to the active material.<sup>9,10</sup>

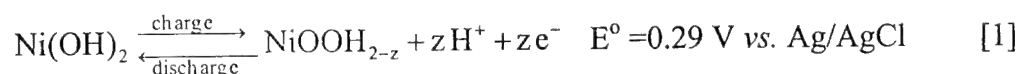
The hysteresis loop generated during a complete charge and discharge reveals that such loops are stable, reproducible, and rate-independent. However, it has been shown in adsorption and magnetism studies that these “boundary curves” reveal only limited aspects of the hysteresis phenomenon.<sup>1</sup> Curves generated on partial cycling of the independent variable (*i.e.*, “scanning curves”) are required to analyze the system completely. To date, no thorough study of the hysteresis in an electrochemical system has been performed.

The purpose of this paper is to gain insight into the hysteresis during the exchange of protons in nickel hydroxide. This is achieved by first measuring and comparing the boundary curves from films of different structure (pure Ni, cobalt doped Ni, and aged films). Subsequently, the “permanent” nature of the hysteresis effect in nickel hydroxide is confirmed by conducting experiments as a function of time. Following this, various theories that have been proposed to explain hysteresis are examined, which illustrate the importance of the scanning curves in understanding the material’s history dependence. extent of applicability of these theories to the nickel hydroxide electrode is discussed by comparing them to experimental data. Finally, an empirical approach to predict the scanning curves based on the boundary curves is illustrated. It should be noted that the history or memory that is described in this paper is not the oft described “memory effect” in nickel batteries.<sup>11</sup> While the “memory effect” is exhibited as an inability to discharge fully the electrode after it has been partially discharged repeatedly, the memory in this

paper deals with the potential being dependent on the proton intercalation history. The electrodes described here do not exhibit the “memory effect” seen in nickel batteries.

## Equilibrium Potential of the Nickel Electrode

The measurement of the equilibrium potential of the nickel electrode as a function of the state of charge ( $z$ ) is complicated by three properties of the material. The first complication arises from the complex nature of the nickel hydroxide redox reaction, which leads to ambiguity in relating the measured potential to the activity of the oxidized and reduced species. The charge and discharge process in the nickel hydroxide electrode involves the extraction and intercalation of protons, respectively, into the solid crystal lattice. Ideally, this has been represented as<sup>12</sup>



Using reaction 1, previous investigators have defined the standard equilibrium potential as the point where there are equal quantities of  $\text{Ni}^{2+}$  and  $\text{Ni}^{3+}$  by assuming that the electrode is a solid solution of  $\text{Ni(OH)}_2$  and  $\text{NiOOH}$ .<sup>13-15</sup> Therefore,  $z$  is equal to the ratio of  $\text{Ni}^{3+}$  to the total nickel concentration. The problem with this approach is that reaction 1 is only an idealized representation of the redox behavior of the electrode, as the material is also known to have  $\text{Ni}^{4+}$  in the lattice.<sup>16-18</sup> Spectroscopic evidence and chemical analyses suggest that the  $\text{Ni}^{4+}$  is a consequence of the material’s considerable nonstoichiometry (*i.e.*, presence of Ni defects), with some Ni sites occupied by potassium ions or protons in addition to the protons intercalated in reaction 1.<sup>18</sup> These variations result in the number of electrons transferred per mole of nickel not necessarily being 1.0,

as implied by reaction 1. Rather, this number depends on the change in defect structure during charge or discharge.<sup>19,20</sup>

The second complication in measuring the equilibrium potential is that the potential measured when the material is charged to 50% of its total capacity ( $z=0.5$ ) is 40 to 90 mV higher than when it is discharged to that point.<sup>8-10</sup> This hysteresis has often been dismissed when reporting equilibrium potentials. It has been assumed that the potential measured on discharge is the true equilibrium of the system, with the potential on charge representing some unexplained departure from equilibrium.<sup>8,15</sup>

The third complication involves establishing “equilibrium conditions.” For convenience, low-rate, galvanostatic experiments, where potential losses due to kinetic, mass-transfer, or ohmic effects are negligible, have been used to determine the equilibrium potential as a function of  $z$ . This approach is convenient because a continuous potential vs.  $z$  curve can be generated in a single experiment. However, such measurements are complicated in the nickel electrode by the oxygen evolution reaction according to



Since the standard potential for reaction 2 is less than that for reaction 1, oxygen evolution occurs simultaneously with the nickel hydroxide redox reaction under normal operating conditions. This coulombic inefficiency means that not all the current going into, and removed from, the system is that due to reaction 1. Therefore, experiments designed to track the progress of reaction 1 by relating current to  $z$  have to account for

this reaction. One method of achieving this is to use a mathematical model that corrects for oxygen evolution during the charge or discharge.<sup>9,10,20,21</sup>

The use of a galvanostatic experiment, which results in an oxidation current flowing during the charge loop and a reduction current during the discharge loop, led Timmerman *et al.*<sup>22</sup> to speculate that the potential offset did not arise because of a difference in history associated with charge and discharge, but rather the direction of the current. Their argument was that the Schottky barrier formed between the metal current collector and the semiconducting nickel hydroxide caused the potential offset.<sup>22</sup> This barrier would behave as a rectifier, with a current-invariant potential offset when forward biased. In other words, a constant-potential offset would be established when a charging current is passed, with no effect when a discharging current is passed. The potentiostatic experiments performed by Ta and Newman<sup>9,10</sup> should dispel this theory. They showed that the capacity of the electrode depended on whether it was stepped to the particular potential from the discharged state or from the charged state. For either potential step, only a small oxidation current flowed once steady state was reached, corresponding to reaction 2. Therefore, they established two different equilibrium conditions that differed only by their past history (*i.e.*, a hysteresis).

## Experimental

Films of nickel hydroxide were deposited electrochemically on a 0.2 cm<sup>2</sup> gold substrate sputtered on a quartz crystal using a procedure described in detail elsewhere.<sup>23,24</sup> Cobalt doped nickel hydroxide films were deposited at room temperature in a bath containing 1.8 M Ni(NO<sub>3</sub>)<sub>2</sub>, 0.175 M Co(NO<sub>3</sub>)<sub>2</sub>, and 0.075 M NaNO<sub>3</sub> in a

solvent of 50 volume percent (v/o) ethanol using a cathodic current of 1.0 mA ( $5.0 \text{ mA/cm}^2$ ). The deposition was conducted for 690 s, which was found to correspond to a film of mass approximately  $35 \text{ } \mu\text{g}$  ( $175 \text{ } \mu\text{g/cm}^2$ ) as measured using an electrochemical quartz-crystal microbalance (EQCM). Films deposited under these conditions were determined to have a nickel to cobalt ratio in the film of 88:12.<sup>25</sup> These films are referred to as "fresh Ni-Co films." Films referred to as "fresh pure-Ni films" were deposited using these same deposition conditions and with solutions of the same composition, but devoid of cobalt.

Following the deposition, the films were rinsed in de-ionized water (resistivity  $18.2 \text{ M}\Omega\text{-cm}$ ), and the cell was filled with a solution of 3 weight percent KOH. The films were conditioned by charging at a constant current of  $1 \text{ mA/cm}^2$  until oxygen evolution, cycling 25 times at a sweep rate of  $5 \text{ mV/s}$  between 0.5 and 0.0 V vs. Ag/AgCl, and discharging at a constant current of  $100 \text{ } \mu\text{A/cm}^2$  until 0.0 V vs. Ag/AgCl. Experiments to study the effect of the first charge or the effect of aging in the KOH solution were conducted prior to this conditioning step. Aged films, termed "aged Ni-Co films," were prepared by soaking a freshly deposited film in 3% KOH for 40 hours. All experiments were conducted using a three-electrode setup with a platinum counterelectrode and a Ag/AgCl reference electrode. Experiment sets that were estimated to last more than 5 hours were conducted using a Hg/HgO (3% KOH) reference electrode immersed in a luggin capillary in order to minimize drifts in potential due to the diffusion of  $\text{OH}^-$  ions into the reference electrode solution. The potentials were then corrected by subtracting 70 mV to match the Ag/AgCl reference electrode. An EG&G M263 A potentiostat/galvanostat was used to perform the experiments. The equipment

control and data acquisition were achieved using the M270 software. All constant current experiments reported in this paper were conducted at  $100 \mu\text{A}/\text{cm}^2$ . This current density is in a range where the potential of the electrode was current independent.<sup>15</sup> In other words, kinetic, mass-transfer, and ohmic losses are negligible in the curves shown in the paper.

## Results and Discussion

*Boundary Curves for the Nickel Hydroxide Electrode.*—Figure 1(a) shows the first two constant current charge/discharges of a fresh pure-Ni film. The figure illustrates the differing electron transfer that occurs between the first charge and the subsequent charge/discharges. While the capacity on the first charge (corrected for oxygen evolution) is  $\approx 0.30 \text{ C}/\text{cm}^2$ , the capacity on the second cycle is only  $\approx 0.18 \text{ C}/\text{cm}^2$ . This differing capacity is attributed to differences in the exchange of protons and potassium ions from the Ni vacancies between the two cycles.<sup>26</sup> These variations in the structure cause the first charge to show an oxidation state change from 2.0 to 3.67 (a 1.67 electron transfer), while the discharge results in the oxidation state change from 3.67 to 2.67 (a 1.0 electron transfer).<sup>17,18</sup>

Figure 1a can be rescaled by converting the abscissa from time to  $z$ , where  $z$  is the state-of-charge defined as

$$z = z^0 + \frac{Q}{|Q_{\max}|} \quad [3]$$

where  $z^0$  is the value of  $z$  at the start of the experiment (*i.e.*,  $z^0 = 0.0$  on charge and  $1.0$  on discharge),  $Q$  is the coulombs exchanged in the nickel reaction ( $Q$  as well as the currents are positive on charge, and negative on discharge), and  $|Q_{\max}|$  is the absolute value of the

total number of coulombs exchanged in the nickel reaction from the beginning to the end of the experiment. The ratio  $Q/|Q_{\max}|$  is given by

$$\frac{Q}{|Q_{\max}|} = \frac{\int_0^t I_{\text{Ni}} dt'}{\left| \int_0^{\tau} I_{\text{Ni}} dt' \right|} \quad [4]$$

$\tau$  is the cut-off time (*i.e.*, time to reach the oxygen-evolution plateau on charge and 0.0 V on discharge), and  $I_{\text{Ni}}$  is the current to the nickel reaction. The nickel current is given by

$$I_{\text{Ni}} = I - I_{\text{ox}}(V) \quad [5]$$

$I$  is the total impressed current and  $I_{\text{ox}}(V)$  is the current to the oxygen evolution reaction given by

$$I_{\text{ox}}(V) = i_{\text{o,ox}} \exp\left(\frac{\alpha_a F(V - U_{\text{ref,ox}})}{RT}\right) \quad [6]$$

$U_{\text{ref,ox}}$  is the equilibrium potential of the oxygen evolution reaction (0.22 V vs. Ag/AgCl in 3% KOH). The exchange current density for the oxygen evolution reaction,  $i_{\text{o,ox}}$ , was determined from Eq. 6 by setting  $\alpha_a$  to 0.75,<sup>27</sup>  $V$  to the potential of the second charge plateau, and  $I_{\text{ox}}$  to the applied current. This value of  $i_{\text{o,ox}}$  was then used in Eq. 6 to get  $I_{\text{ox}}$  as a function of  $V$ .

The resulting plot of potential vs.  $z$  is shown in Figure 1(b). The most striking effect of rescaling from time to  $z$  occurs when comparing the first and second charges. Even though the first charge lasts nearly 70% longer than the second (*i.e.*, the first and second charges give a 1.67 and 1.0 electron transfer, respectively<sup>17,18</sup>), the curves are very similar to one another when the potential is plotted *versus*  $z$ . In addition, cycling the

fresh pure-Ni films results in a steady decrease in the number of electrons transferred,<sup>17,18</sup> but plotting the potential vs.  $z$  results in overlapping discharge curves.

The same qualitative trends seen in Figures 1(a) and 1(b) for fresh pure-Ni films are also seen in Figure 2 for fresh and aged Ni-Co films. However, the potential needed to charge and discharge the electrode does depend on the type of film cycled. Figure 2(a) shows the second cycle for a fresh pure-Ni film compared to the second cycle for a fresh Ni-Co film. The potential of the fresh Ni-Co film is lower,<sup>9,10</sup> and the potential offset between charge and discharge is 53 and 43 mV for the fresh pure-Ni film and fresh Ni-Co film, respectively. In comparison, Ta and Newman<sup>9,10</sup> report an offset of 92 mV for the pure Ni films and 50 mV for the Co-doped film. The differences may be due to the different film thickness employed in the two studies. While the films deposited in this study are estimated to be  $\approx 0.5 \mu\text{m}$  based on the nickel hydroxide density of  $3.5 \text{ g/cm}^3$ ,<sup>28</sup> Ta and Newman report a thickness of 20 to 40 nm.

A similar shape for the potential vs.  $z$  curve seen in Figures 1(a) and 2(a) is also obtained when the fresh Ni-Co films are aged in 3% KOH for 40 hours as shown in Figure 2(b). Although the potential of the aged film is higher by  $\approx 37 \text{ mV}$ , the shape of the curves and the offset between the charge and discharge (43 mV in the fresh film and 45 mV in the aged film at  $z=0.5$ ) are similar. Spectroscopic studies indicate that aging the film leads to a material with a lower defect content.<sup>29</sup> The lower defect content results in material that cycles between an oxidation state of 2.33 to 3.33, compared to 2.67 and 3.67 oxidation range for fresh material.<sup>26</sup> In summary, the curves in Figures 1 and 2 show that although the equilibrium potentials depend on the structure of the material, the shape of the curves when plotted against  $z$  is similar.



*Constant-Potential Experiments.*—Having established the effect of the structure of the active material on the hysteresis boundary curves, we now show that the constant current and constant-potential experiments are comparable. In other words, the hysteresis curves are shown to be independent of what variable is controlled and independent of the direction of current flowing through the material. Subsequently, we show that the hysteresis is indeed “permanent” by conducting the experiments as a function of time. All the results shown in the rest of the paper are from fresh Ni-Co films that are conditioned using the procedure described in the experimental section.

Figure 3 shows the experimental equilibrium potential as a function of extent of proton extraction,  $z$ , for galvanostatic charge and discharge (denoted by the solid lines). The hysteresis between charge and discharge is also seen in the inset in Figure 3, where the offset potential is plotted as a function of  $z$ . The inset shows that the offset is constant through most of the charge/discharge with a value of 43 mV at  $z=0.5$ , with the loop closing at  $z=1$ . The constant-potential experiment was conducted by first charging the electrode from the completely discharged state to the desired potential and then holding at that potential for 1 hour. The current decayed exponentially to reach a steady-state oxidation current of  $\approx 5 \mu\text{A}/\text{cm}^2$ , corresponding to the oxygen evolution reaction, after approximately five to ten minutes. Once this experiment was completed,  $z$  was determined from Eq. 4 following a galvanostatic discharge to 0.0 V. The resulting  $z$  and potential are plotted as the open circles in Figure 3. The constant-potential experiments yield a potential vs.  $z$  similar to that estimated using the constant current experiments. The highest deviation occurs at the low proton concentrations (circle at  $z=0.75$ ), where

the contribution of the oxygen evolution reaction becomes significant, possibly inducing errors in the estimate of  $z$ .

The same experiment was repeated in the discharge loop at the three potentials used in the charge loop. In other words, the electrode was discharged from the completely charged state to the desired potential and then held at that potential for 1 hour. Once again, a steady-state oxidation current of  $\approx 5 \mu\text{A}/\text{cm}^2$  was observed after five to ten minutes. The electrode was then discharged to 0.0 V, and  $z$  was determined from Eq. 4 (denoted by the solid circles in Figure 3). Again, the constant-potential experiment shows a hysteresis similar to that in a constant current experiment. The results shown in Figure 3 confirm the conclusion by Ta and Newman that the Schottky barrier cannot be the cause for the hysteresis, as the constant-potential experiment would have resulted in an identical  $z$  irrespective of the history of the electrode. In addition, the similarity between the two experiments suggests that determination of the equilibrium state of the system can be achieved by either controlling the current, which is equivalent to controlling  $z$ , or by controlling the potential.

Further to confirm that the offset shown in Figures 1 to 3 is indeed a “permanent hysteresis,” the potentiostatic experiments were conducted on a different film where the potential was maintained for various times. Here the electrode was set at a constant-potential on both the charge and discharge loop for four time periods ( $\frac{1}{2}$ , 3, 6, and 10 hours), and  $z$  was determined at the end of the experiment. Figure 4 plots  $z$  as a function of the time held at 319 mV vs. Ag/AgCl. There is a negligible difference between  $z$  measured after  $\frac{1}{2}$  hour and that measured after 10 hours, on both the charge and discharge loop. Note that, in the constant current experiment, the whole experiment is

completed in  $\approx 1500$  seconds, and yet Figure 3 shows that even this short a time is enough to reach equilibrium. Therefore, there indeed exist at least two stable equilibrium states. Which state is achieved is dictated by the history of the material. Furthermore, these equilibrium states can be measured from a convenient galvanostatic charge/discharge experiment.

*Domain Theory*—The similarity of the hysteresis in nickel hydroxide to those observed in gas-solid adsorption and magnetism leads us to examine domain theory, which has been offered as the description for hysteresis in these systems. For example, experimental evidence suggests that magnetic hysteresis is caused by the loss of energy due to movement of the domain walls, which can be measured in the form of sound intensity (*i.e.*, the Barkhausen effect).<sup>2</sup> In this theory, a system that exhibits hysteresis is thought to be made up of a large number of small regions or domains, each of which takes up two or more metastable states for a single value of the external independent variable. The actual cause for the metastability is immaterial at this stage—what is important is that the domains exhibit such an effect. The metastability in a generic domain was explained by Everett and Whitton<sup>30</sup> in terms of a switch that consists of a bimetallic strip with one end connected to a permanent magnet. The other end of the strip is connected to another permanent magnet through a battery. The magnets are arranged such that, at a temperature  $T_u$ , the distance between them reaches a critical value, the contact shuts, and a current flows. On cooling, the circuit is not broken at  $T_u$ , but the strip has to be cooled further to  $T_l$  where the stress in the strip overcomes the attraction between the magnets. This gives rise to a hysteresis in the system independent of the heating and cooling rate. An analogous example is described here to explain domain theory in nickel hydroxide.

Consider a hypothetical domain of nickel hydroxide, which consists of a finite number of Ni sites, with two interlamellar protons associated with each site. Analogous to the switch, assume that an interlamellar proton de-intercalates from each of the Ni sites at the same potential  $V_c$ , whereby the electrode is transformed from the fully discharged to the fully charged state (*i.e.*,  $z$  goes from 0 to 1). The resulting potential vs.  $z$  is plotted in the forward loop in Figure 5(a). However, if some irreversibility were to exist in the domain such that the potential where the proton is re-intercalated is at a lower potential, say  $V_d$ , then hysteresis would occur between intercalation and extraction. This form of irreversibility is comparable to the theory of accommodation described by Everett,<sup>1</sup> where the material is thought to undergo an irreversible step that involves “prising open” of the layers of the host material (*e.g.*, NiOOH) to accommodate the guest atom (*e.g.*,  $H^+$ ).<sup>1</sup> Once intercalation occurs, the expanded solid adopts a new position of minimum energy, so that extraction occurs under a different path. This accommodation effect was proposed by Zheng *et al.*<sup>3</sup> as the cause for the hysteresis during lithium intercalation in hydrogen-containing carbons.<sup>3</sup> They argued that, once intercalation occurs, the lithium binds on the hydrogen-terminating edges of hexagonal carbon fragments, causing a change in the  $sp^2$  bond to an  $sp^3$  bond. Therefore, extraction occurs at a different driving force, hence resulting in hysteresis. The authors assumed that the bonding is an activated process, whereby the hysteresis described in their paper is time dependent. However, the time constants were argued to be long enough such that hysteresis is seen under rates that are experimentally practical.

Another form of metastability in each domain could be due to the occurrence of first-order phase transitions. This approach has been used by Everett and Nordon<sup>31</sup> to

explain hysteresis in hydrogen absorbing alloys and has been proposed as a possible cause for the hysteresis in the nickel electrode by Milner and Thomas<sup>8</sup> and Barnard *et al.*<sup>32</sup> Consider a domain in the nickel hydroxide electrode which consists of a solid solution of  $\text{Ni(OH)}_2$  and  $\text{NiOOH}$ . Assume the Gibbs free energy of the solid solution has the form depicted by the curve AEGD in Figure 5(b). If the system followed a reversible path, then phase separation would occur at points B and C on charge and discharge, respectively. The resulting potential profile would be ABKCD, and no hysteresis would be observed. However, if on charge the solid solution became supersaturated with  $\text{NiOOH}$ , the material would be metastable from points B to E. Phase separation would not occur until the potential  $V_c$  (*i.e.*, point E), and the charge curve would be AEFD. On discharge, the solid solution could be supersaturated with  $\text{Ni(OH)}_2$ , and the material would be metastable from points C to G. At  $V_d$  (*i.e.*, point G), phase separation would occur, and the discharge curve would be DGHA, leading to hysteresis.

There are two discrepancies between the experimental hysteresis curves shown in Figures 1 to 3 and the schematics in Figures 5(a) and (b). Namely, the experimental curves are not horizontal at intermediate  $z$  (*i.e.*, the curves are S-shaped), and they are asymmetric (*i.e.*, the potential drops off sharply at  $z$  close to 0.0, but it changes more gradually at  $z$  close to 1.0). One explanation for these discrepancies can be obtained by considering the electrode to consist of a large number of domains, with each domain consisting of a finite number of Ni sites. Although this explanation applies whether the hysteresis is due to intercalation effects [Figure 5(a)] or phase separation [Figure 5(b)], the former will be used for illustrative purposes. We assume that the characteristic of each domain is similar to that seen in Figure 5(a) and each has a critical potential  $V_{c,i}$

where the proton is released from domain  $i$  on charge, and a potential  $V_{d,i}$  where the proton re-intercalates into domain  $i$  on discharge.

If all the domains have the same critical potentials,  $V_c$  and  $V_d$ , then the boundary curve would be identical to Figure 5(a). Therefore, let us assume that  $V_{c,i}$  and  $V_{d,i}$  vary among the domains as shown in Figure 5(c). For simplicity,  $V_{c,i}$  and  $V_{d,i}$  are taken to be normal distributions with the difference between the two potentials,  $\Delta$ , the same for each domain. The boundary curves can then be constructed by integrating the distribution  $V_{c,i}$  and  $V_{d,i}$  to give OAB and BCO, respectively, in Figure 5(d). Therefore, even though each domain has a flat potential profile given in Figure 5(a), a distribution of critical potentials where intercalation/deintercalation occurs results in an S-shaped profile, which more closely resembles the experimental curves. The asymmetry in the experimental boundary curves can be accounted for by having a non normal distribution of domains or by assuming a distribution where  $\Delta$  varies between the different domains.

In order to generate a scanning curve, the distribution  $V_{c,i}$  in Figure 5(c) is used until the point A. Integrating this partial distribution yields the forward scan in Figure 5(d) (solid line). If the distribution  $V_{d,i}$  does not depend on the charge history, then on reversing the direction of the scan the system reverts to the distribution  $V_{d,i}$  at the point C. Integrating  $V_{d,i}$  from C results in the reverse scanning curve as shown in Figure 5(d). The resulting scanning curve has a vertical line (AC) from the forward loop to the reverse loop indicating that intermediate potentials cannot be attained at that  $z$ . An asymmetric boundary curve would also result in an immediate drop from the charge to the discharge boundary curve as soon as the current is reversed. Ta and Newman<sup>9,10</sup> speculate that the scanning curve for nickel hydroxide would follow such a path.

However, if the discharge distribution changes as the electrode is charged, then the solid  $V_{d,i}$  curve is reached only after the electrode is fully charged. When the electrode is charged to  $z=0.5$ , the  $V_{d,i}$  distribution has only reached the dotted line in Figure 5(c). Reversing the current at this point causes the domains to discharge along a different path from that of the fully charged electrode. A changing distribution suggests that the domains do not act independently, but are dependent on the nature of the surrounding domains. The result is the S-shaped dotted-line AO. For the same set of boundary curves there could be an infinite number of scanning curves, depending on the degree to which the domains interact. Therefore, the scanning curves, not just the boundary curves, are essential to characterize the hysteresis completely.

*Scanning Curves for the Nickel Hydroxide Electrode*—Figure 6 shows the boundary curves and the discharge scanning curves for the nickel hydroxide electrode. The boundary curves were generated by correcting the potential-time charge/discharge curves for oxygen evolution as detailed previously. To generate the scanning curves, the electrode was charged until a known amount of coulombs was passed; the current was reversed, and the electrode was discharged to a cut off potential of 0.0 V. The curves were then converted to potential vs.  $z$  by correcting for oxygen evolution using

$$z = \frac{|Q_{sc}| + \int_0^t I_{Ni} dt}{|Q_{max}|} \quad [7]$$

$|Q_{max}|$  is equal to the denominator in Eq. 4,  $I_{Ni}$  is given by Eq. 5, and  $|Q_{sc}|$  is the capacity of the scanning curve, evaluated using

$$|Q_{sc}| = \left| \int_0^{\tau_{sc}} I_{Ni} dt \right| \quad [8]$$

where  $\tau_{sc}$  is the time taken to reach 0.0 V in the scanning curve. Figure 6 shows that the discharge scanning curves lie in the separation between the charge and discharge boundary curves, confirming that states within the hysteresis loop are accessible.

Figure 7 shows the charge scanning curves on the same electrode, where again the existence of the intermediate states is confirmed. The curves were generated by fully charging an electrode from the fully discharged state, following which the electrode was discharged until a known amount of coulombs was passed, and the current reversed. The curves were then corrected for the oxygen evolution reaction using equations 3 and 4 with  $z^0 = z_{rev}$  and using the discharge boundary curve to evaluate the denominator in equation 4. The confidence in the estimate of  $z$  decreases as we approach  $z = 1.0$  (*i.e.*, the fully charged state) due to the large fraction of oxygen evolution in this region. The shape of the scanning curves in Figures 6 and 7, when interpreted using domain theory, suggests two aspects of the nature of the domains, namely, (i) there is a distribution of critical potentials where metastability occurs over the domains and (ii) the behavior of each domain is history dependent within the range of metastability.

Figures 6 and 7 show that small changes in  $z$  on the boundary curves result in the potential of the material changing to values between the boundary curves. Alternatively, when the potential is the independent variable, this result can be reinterpreted to mean that even small changes in potential within the boundary curves will lead to proton intercalation/extraction (*i.e.*, changes in  $z$ ), with a finite current passing through the system—a result that was observed experimentally. Hence, techniques that involve



perturbations of the potential within the boundary curves (*e.g.*, potential step<sup>33-35</sup> and electrochemical impedance spectroscopy<sup>25,36</sup>) would involve intercalation/extraction of protons. This is in contrast to Ta and Newman's speculation that such experiments would have little meaning, as the authors assumed that intermediate potentials between the boundary curves would not result in proton intercalation/deintercalation.<sup>9,10</sup> However, Figures 6 and 7 show that, at any  $z$ , the slope of potential vs.  $z$  on the scanning curve is different from that on the boundary curve. This suggests that the amount of proton intercalated on the positive potential step from the boundary curve would be different from that on a negative step. Therefore, a more detailed understanding of the role of the domains is needed in order to estimate parameters (*e.g.*, diffusion coefficient) based on these perturbation techniques.

Not only are multiple potentials attained at each  $z$  (*e.g.*, one on the charge loop, a second on the discharge loop, and another for each scan), but also a similar S-shape is observed when comparing the boundary curves to the scanning curves, as mentioned previously. The similarity between the boundary and scanning curves is especially striking when the abscissa of the scanning curves is rescaled. The rescaling in Figure 8 is accomplished by stretching each discharge scanning curve in Figure 6 until it touches the discharge boundary curve. For example, the boundary curves and one of the scanning curves from Figure 6 are reproduced as an inset in Figure 8. The figure defines two values of  $z$ , namely  $z_{rev}$ , denoting the  $z$  at which the scan is reversed and  $z_d$ , denoting the  $z$  on the discharge boundary curve that has the same potential as  $z_{rev}$ . The abscissa is then rescaled using  $z' = \left( \frac{z_d}{z_{rev}} \right) z$  to generate Figure 8. Note that for a boundary curve,  $z_d = z_{rev}$

and therefore,  $z' = z$ . Although no physical basis exists for the rescaling, it is seen from Figure 8 that the scanning curves overlap on the boundary curve, and only the end of the very short scanning curve deviates from the boundary curve.

A similar analysis was undertaken for the charge scanning curves as shown in Figure 9(a), where the scanning curves were rescaled to touch the charge boundary curve using an equivalent procedure by defining a reversal point,  $z_{rev}$ , and an equivalent point on the charge curve,  $z_c$ . Although the quantitative overlap in Figure 9(a) is not as good as in Figure 8, the qualitative shapes are similar. The major qualitative difference is that the boundary curve has a very sharp rise in potential at the beginning of charge, where the scanning curves show a more gradual increase. This gradual increase is seen even when the current is reversed at the knee at the end of discharge where  $z \rightarrow 0$ . Only when the discharge is continued until the potential reaches 0.0 V vs. Ag/AgCl is the sharp rise in potential at the beginning of charge seen. Hence, the rescaling was changed so that the scanning curves touch the longest charge scanning curve by assuming that it was representative of the charge boundary curve. Again, the reversal point,  $z_{rev}$ , and an equivalent point on this charge boundary curve,  $z_c$ , were used for the rescaling, which is shown in Figure 9(b). Although, differences are still evident between the scanning curves, the overlap is better than that in Figure 9(a), especially at low values of  $z$ . It is known that when the nickel hydroxide electrode is completely discharged the conductivity of the material is very low and the material behaves as a semiconductor.<sup>13</sup> This low conductivity could be the cause for such differences between the boundary and scanning curves.

As mentioned earlier, there can be an infinite number of scanning curves for the same set of boundary curves depending on the distribution of the domains and their interaction with the adjacent domains. However, independent of these interactions, Everett and Smith<sup>37,38</sup> argue that the boundary and scanning curves obey certain theorems. Using various distributions to describe the boundary and scanning curves, Everett and Smith<sup>37,38</sup> outline seven theorems that describe the relationship between the boundary and scanning curves. These theorems also govern the trajectories of the system inside the hysteresis loop. Any system that exhibits a true hysteresis due to the existence of domains should follow theorems 3 to 7 and either theorem 1 or 2. We first describe the theorems in electrochemical terms, and then compare them to the nickel hydroxide electrode to see their applicability. For details of the derivation of the theorems and their limits of applicability see Everett and Smith<sup>37,38</sup> and Enderby.<sup>39,40</sup>

**Theorem 1:** If the discharge scanning curves meet the discharge boundary curves before the electrode is fully discharged, then the charge scanning curves will meet the charge boundary curves before the electrode is fully charged. The scanning curve from A to C in Figure 5(d) is an extreme case of theorem 1 where the scanning curve meets the boundary curve, but with no change in  $z$ .

**Theorem 2:** If the discharge scanning curves converge on the lower intersection point of the boundary curves ( $z=0$ ), the charge scanning curve will converge on the upper intersection point ( $z=1$ ). In other words, the scanning curves meet the boundary curve at  $z=0$  or  $z=1$  only, and not at any intermediate  $z$ . The dotted scanning curve from A to O in Figure 5(d) corresponds to theorem 2, where the scanning curve meets the boundary curve only at  $z=0$ . Figures 6 and 7 reveal that the scanning curves in the nickel hydroxide

electrode closely resemble curve AO in Figure 5(d), and therefore can be said to follow theorem 2.

**Theorem 3:** The slope of the discharge scanning curve must always be more than that of the discharge boundary curve at the same  $z$ ; similarly the slope of the charge scanning curve should be more than that of the charge boundary curve at the same  $z$ . We can see from Figure 6 and 7 that this is true for the nickel hydroxide electrode.

**Theorem 4:** The first part of this theorem predicts that if the path of the system is reversed at a particular potential  $V_A$ , with a corresponding  $z = z_A$ , and the potential scanned to  $V_B$  and back to  $V_A$ , then  $z$  will return to  $z_A$ . The experimental data in Figure 10 show the results as envisioned in this theorem. Here the electrode was charged from the completely discharged state to  $V_A = 335$  mV vs. Ag/AgCl, which corresponds to  $z_A = 0.52$ . The current was reversed to generate a discharge scanning curve until the potential reached  $V_B = 285$  mV. The current was again reversed to generate a charge scanning curve, where it returned to the point  $V_A = 335$  mV and  $z_A = 0.52$  as predicted by the theorem. The second part of this theorem predicts that cycling the potential between  $V_A$  and  $V_B$  will lead to a loop of constant shape and area independent of the position of  $z$ . In order to test this part of the theorem, the electrode was completely charged and then discharged to  $V_B = 285$  mV, corresponding to a  $z_B = 0.44$ . The current was reversed to generate a charge scanning curve until the potential reached  $V_A = 335$  mV. The current was again reversed to generate a discharge scanning curve, where it returned to the point  $V_B = 285$  mV and  $z_B = 0.44$ . As predicted, the two scanning loops have the same shape and area. These two internal loops are reproducible, and one can cycle between the

points  $V_A$  and  $V_B$  with negligible change in the shape of the loops. Such reproducible internal loops also have been seen in adsorption hysteresis.<sup>1</sup>

**Theorem 5:** If, when the systems returns to  $V_A$  as envisioned in Theorem 4,  $z$  is allowed to increase by continuing the charge, the system will move along the same curve as that which would have been followed if no loop had been traversed from  $V_A$  (*i.e.*, on the boundary curve). To test this prediction, the electrode that was used to test for theorem 4 was charged to  $z = 1$  after the loop returned to  $V_A$ . The resulting potential is also shown in Figure 10, although it is not evident as it overlaps with the boundary curve. The proximity of the two curves confirms the applicability of this theorem. A similar effect is seen on continuing the discharge past the point  $V_B$  to  $z=0$ , with the curve approximately overlapping on the discharge boundary curve. Theorem 5 is also called the “wiping-out” property of a system exhibiting hysteresis, as the memory of the systems excursion at  $V_A$  is wiped out as soon as it returns to this point and the system behaves as if there was no excursion at  $V_A$ .<sup>41</sup>

**Theorem 6:** Any point  $P$  within the hysteresis loop can be reached in a number of ways, some from lower  $z$ , others from higher. Although the system can be described by its potential and state-of-charge (*i.e.*,  $V$  and  $z$ ), its state will not be completely defined since its behavior when it moves away from  $P$  depends on its route by which this point was approached. The importance of this theorem is that the path of the system within the hysteresis loop depends on its history, or in other words, the shape of the scanning curves is related to a history-dependent distribution. This theorem has been the argument behind using the domain concept and is fundamental to the description of the scanning curves.

In addition, experimental evidence of this theorem disproves the theory for hysteresis proposed by Duhem, as described by Everett and Smith.<sup>37</sup> Duhem describes the scanning curves to be one of two families of curves, the ascending series and the descending series, such that only one of each family passes through each point. The ascending curves are the possible paths of the system when the potential is increasing, and the descending curves when the potential is decreasing. This is in contrast to what is described in theorem 6, which states that each point in the loop can be reached by an infinite number of paths. Figure 11 shows experimental data that support theorem 6 and thereby disprove the theory of Duhem in the nickel hydroxide electrode. Here the electrode was charged using a constant current until  $z \approx 0.8$ , when the current was reversed to generate a discharge scanning curve until  $z \approx 0.15$ , at which point the electrode was charged again to complete the loop. The electrode was then completely charged and then discharged, after which a second loop was traversed, but over a shorter  $z$  compared to the first, as indicated in the figure. Due to theorem 4, the system tries to return to the point where the excursion from the main loop began. This property ensures that the charge scanning curve in the shorter loop crosses the one in the longer loop at the point P. Notice that, as predicted by theorem 6, the path of the system beyond point P is different and depends on the route by which the point was reached.<sup>41</sup>

**Theorem 7:** If the system is taken through a series of oscillations of  $\Delta z$  of decreasing amplitude, after the  $n^{\text{th}}$  reversal, the system moves towards the point where the  $(n-1)^{\text{th}}$  reversal occurred; if the system is carried through this point, it moves towards the  $(n-3)^{\text{rd}}$  reversal point, and so on. This theorem is an extension of theorem 4, in that it describes the “wiping out” of the memory when the system is taken on an excursion on

the internal loops. In order to test the validity of this theorem, the system was charged from the completely discharged state until  $z \approx 0.55$ , at which point the direction was reversed. This discharge scan was maintained until  $z \approx 0.25$ , when the direction was again reversed, as shown in Figure 12(a). An internal loop to this excursion was executed by reversing this scan at  $z \approx 0.4$  and again at  $z \approx 0.3$ . The system was then allowed to charge completely to  $z = 1$ . As stated by the theorem, the system returns to the point where the secondary excursion occurred, thereby wiping out the secondary history. Charging the electrode further results in the system wiping out the primary history.

In order to observe the path of the system when  $\Delta z$  was decreased in each cycle, an experiment was conducted as shown in Figure 12(b). Here the system was charged from the completely discharged state until  $z \approx 0.6$ , at which point the direction was reversed. This discharge scan was maintained until  $z \approx 0.2$ , when the direction was again reversed. This reversal was continued at successively lower intervals. As seen from Figure 12(b), a reversal results in the curve approaching the previous reversal point, as predicted by the theorem. In addition, the curves appear to approach the midpoint between the boundary curves.

The close agreement of the predictions of these theorems with the experimental data on the nickel electrode leads us to conclude that the nickel hydroxide electrode's behavior is consistent with the existence of a number of individual units or domains, each of which exhibits two or more metastable states. While domain hysteresis is commonly studied in adsorption and magnetism, the effect seems to have been studied in only one electrochemical energy storage system, namely the  $\text{Li/LiMnO}_2$  cells. In attempting to

explain the production of heat in these cells, Murray *et al.*<sup>5</sup> conclude that a part of the heat is produced by the hysteresis effect. Although, the potential of the material appears to represent that of a “solid solution,”<sup>42</sup> the authors suggest that in reality the material could be exhibiting a first-order phase transition, the signatures of which are modified by the disorder in the material. Therefore, the system can be thought to have domains of coexisting phases. The authors also suggest that the memory of the system is stored in the position of the phase boundary, and movement of the phase boundary causes hysteresis.

In a subsequent paper, Sleight *et al.*<sup>6</sup> attempt to understand this hysteresis effect by analyzing data on short cycles within the hysteresis loop and comparing their behavior to the general theorems of hysteresis as described above. Loops similar to those shown in Figure 10, where the electrode is cycled between two points, were generated. However, the authors note that the potential within the loop is parallel to that of the discharge boundary curve, contrary to what is expected in theorem 3. In addition, the graph does not seem to satisfy the “wiping-out” property that is expected in systems that exhibit domains. Nevertheless, the effect of the history on the material’s potential and heat profile is evident, and some similarities are seen with this study.

As mentioned earlier, the material can be made to cycle reproducibly within the hysteresis loop. For example, the loop generated in Figure 10, where the reversal points touch the boundary curves, can be cycled repeatedly with no change in the shape or area. In order to test if the stability is maintained when the loops are small, such that the reversals occur well before the boundary curves, the scanning curves shown in Figure 13 were obtained. In one set of experiments, a completely discharged film was charged to z



= 0.5, and then continuously discharged and charge to approximately  $z = 0.49$  and  $0.51$ , respectively. The loop was repeated 50 times after which a similar experiment was conducted after a completely charged film was discharge to  $z = 0.5$ . In this figure, the curves were not corrected for oxygen evolution as its effects was estimated to be negligible based on Eqn. 6. Assuming that the side reaction occurs at its maximum rate over the duration of the 50 cycles, the decrease in  $z$  is estimated to be less than 3%. Even a 3% change in  $z$  though would result in a decrease in voltage of less than 2 mV. Negligible self discharge was confirmed further by discharging the material at the beginning and end of the 50 cycles, where the capacity removed did not change.

The first and fiftieth cycles on charge and discharge are shown in Figure 13. Contrary to what was expected from domain theory, it was found that the experiment on charge was not stable and the potential of the system decreases until it approaches that of the discharge boundary curve. On the other hand, the cycles on the discharge loop were fairly reproducible, with little change in the potential. This is seen more clearly in Figure 14 where the potential of the midpoint of the charge and discharge is plotted as a function of the cycle number for both the loops (*i.e.*, loops generated after a partial charge and after a partial discharge). The midpoint on the charge loop is higher than that of the discharge loop in both cases. This is because extraction occurs at a greater driving force compared to intercalation because of the metastability in the domains. However, the midpoint potentials shift downwards as the electrode is cycled. As the  $z$  at the end of the 50 cycles is the same as that at the start of the experiment, the oxygen evolution reaction can be eliminated as the cause of this drift. This drift is in contrast with the result in Figure 4, where the system was found to be stable over tens of hours. In addition, it is a

deviation from theorem 4, where the potential of the system is expected to return to the same point from where the excursion occurred. While Figure 12(b) shows that the system approaches the midpoint between the boundary curves when  $\Delta z$  is taken through scans of decreasing amplitudes, Figures 13 and 14 show that when  $\Delta z$  is the same the curves approach the discharge boundary curve. This would suggest that the memory of the system's excursion is not completely wiped out, resulting in the memory building up over the cycles, thus causing the effect seen in Figures 13 and 14. The cause for this memory buildup needs to be explored further to understand better the hysteresis in the system.

*Empirical Procedure to Predict the Scanning Curves from the Boundary Curves*—In the absence of a clear understanding of the underlying phenomenon behind the hysteresis, an empirical approach is used to predict the scanning curves based on the boundary curves. This approach can be used in nickel-based battery models to predict the transients between charge and discharge during partial cycles. The first step in the methodology is to fit the experimental discharge boundary curves to an empirical equation. A nonlinear least-squares package, DataFit,<sup>TM</sup> was used to fit Eq. 9 to the discharge boundary curve

$$E = E^0 + \frac{RT}{nF} \ln \left( \frac{z'}{1-z'} \right) + \frac{RT}{2nF} \left[ 2A_0 (1-2z') + B_0 (1-3z'^2) \right] \quad [9]$$

The parameters  $A_0$  and  $B_0$  in Eq. 9 arise from the use of a two-parameter Margules expression to correct for activities.<sup>13-15</sup> In Eq. 9,  $z'$  is the normalized  $z$  used to generate Figures 8 and 9 and is equal to  $z$  for the boundary curve. An adequate fit yielded  $E^0=0.2985$  V,  $A_0=3.9745$ , and  $B_0=-4.6795$ . The second step is to identify the point  $z_{rev}$

where the scan is reversed and the point  $z_d$  on the boundary curve, which has the same potential as the start of the scanning curve (see Figure 8). For example, the scanning curve originating at 0.48 would yield  $z_{rev}=0.48$  and  $z_d=0.85$ . Eq. 9 is then used for  $0 < z' < 0.85$  to obtain  $E$ , which is plotted against  $z$ , where  $z \equiv \left( \frac{z_{rev}}{z_d} \right) z'$ , as shown in

Figure 15. Comparison with Figure 6 shows that the predictions of the scanning curves are adequate.

A similar procedure can be used to predict the charge scanning curves as shown in Figure 16. In keeping with the observation in Figure 9(a) and (b) that the shapes of the scanning curves are qualitatively similar to each other but different from that of the boundary curve, the longest charge scanning curve was taken to be representative of the charge boundary curve. A fit of this curve to Eq. 9 yielded  $E^0=0.3398$  V,  $A_0=2.2139$ , and  $B_0= - 2.053$ . The subsequent procedure is similar to that described above. While the predictions are adequate at low and intermediate  $z$ , the deviations are clear as  $z$  approaches 1. This may be the result of the greater contribution of the oxygen evolution side reaction at high  $z$ .

## Conclusions

We confirmed that the nickel hydroxide electrode exhibits a stable hysteresis loop, with the potential on charge being higher than that on discharge at every state-of-charge. We also showed that the charge and discharge potentials vary depending upon the number of electrons transferred (*i.e.*, 1.67 and 1.0), the compositions (pure Ni and Ni-Co), and the defect content, but the shape of the hysteresis loop does not. Furthermore, we showed that the hysteresis loop created during a complete charge and discharge (*i.e.*,

boundary curves) is not sufficient to define the state of the system. Rather, internal loops within the boundary curves (*i.e.*, scanning curves) can be generated that access potentials between the boundary curves. The potential obtained at any state-of-charge, as well as how the material charges and discharges from that point, depends on the cycling history of the material.

As little information is available on electrochemical hysteresis, theories proposed in magnetism and adsorption were examined. The theory of domains, where the system is thought to be made up of many small units each of which exhibits two or more metastable states, was found to be applicable in explaining the behavior of the system. The qualitative shape of the boundary and scanning curves suggests that the domains in nickel hydroxide are characterized by two features, namely (i) there is a distribution of critical potentials where metastability occurs over the domains and (ii) the behavior of each domain is history dependent within the range of metastability. Although the actual cause for the metastability in each domain is not clear, previous research suggests either energy changes during intercalation or phase separation as possible causes for the phenomenon. The close adherence of the system to the seven theorems outlined by Everett and Smith<sup>37,38</sup> indicates the applicability of domain theory in explaining hysteresis in nickel hydroxide. Although the system follows the path predicted by the theorems closely, deviations from domain theory were seen when the electrode was cycled using a constant current over a small  $\Delta z$  for over 50 cycles. The potential of the electrode was seen to shift from the charge loop to the discharge loop, in deviation from what is expected from theorem 4. This suggests that the experiment did not result in the complete wiping out of the system's memory.

Based on the similarity of the scanning curves to the boundary curves, an empirical procedure was developed to predict the scanning curves based on the boundary curves. The procedure was shown to be adequate to predict the discharge scanning curves but yielded only qualitative agreement in predicting the charge scanning curves.

### **Acknowledgements**

The authors gratefully acknowledge the financial support from the Office of Research and Development of the United States Central Intelligence Agency, the U.S. Department of Energy under Cooperative Agreement No. DE-FCO2-91ER75666, and the U.S. Department of Defense under grant No. DAAH04-96-1-0421. Discussions with Prof. James Ritter and Michael Matthews (U. South Carolina) on adsorption hysteresis and phase separations are gratefully acknowledged.

## References

1. D. H. Everett, *The Solid-Gas Interface*, E. A. Flood, Eds., Edward Arnold Ltd., London (1967).
2. R. P. Feynman, R. B. Leighton, and M. Sands, *The Feynman Lectures on Physics II*, Addison-Wesley, 1964).
3. T. Zheng, W. R. McKinnon, and J. R. Dahn, *J. Electrochem. Soc.*, **143**, 2137 (1996).
4. M. Inaba, M. Fujikawa, T. Abe, and Z. Ogumi, *J. Electrochem. Soc.*, **147**, 4008 (2000).
5. J. J. Murray, A. K. Sleight, and W. R. McKinnon, *Electrochim. Acta*, **36**, 489 (1991).
6. A. K. Sleight, J. J. Murray, and W. R. McKinnon, *Electrochim. Acta*, **36**, 1469 (1991).
7. J. J. G. Willems, *Philips J. of Res.*, **35**, Supplement No 1, 20 (1984).
8. P. C. Milner and U. B. Thomas, *The Nickel Cadmium Cell, Advances in Electrochemistry and Electrochemical Engineering*, C. W. Tobias, Eds., Interscience Publishers, New York (1967).
9. K. P. Ta, Ph.D. Thesis, *Solid-State Diffusion Coefficient Measurement and Modeling of Intercalation Materials*, University of California, Berkeley (1997).
10. K. P. Ta and J. Newman, *J. Electrochem. Soc.*, **146**, 2769 (1999).

11. D. Linden, *Handbook of Batteries- II Edition*, Mc-Graw Hill, Inc., New York (1994).
12. H. Bode, K. Dehmelt, and J. Witte, *Electrochim. Acta*, **11**, 1079 (1966).
13. P. Barnard, C. F. Randell, and F. L. Tye, *J. Appl. Electrochem.*, **10**, 127 (1980).
14. D. Fan and R. E. White, *J. Electrochem. Soc.*, **138**, 2952 (1991).
15. M. Jain, A. L. Elmore, M. A. Matthews, and J. W. Weidner, *Electrochim. Acta*, **43**, 2649 (1998).
16. A. N. Mansour, C. A. Melenders, and J. Wong, *J. Electrochem. Soc.*, **145**, 1121 (1998).
17. W. E. O'Grady, K. I. Pandya, K. E. Swider, and D. A. Corrigan, *J. Electrochem. Soc.*, **143**, 1613 (1996).
18. Z. Xu, B. C. Cornilsen, and G. Meitzner, *Selected Battery Topics*, G. Halpert, M. L. Gopikanth, K. M. Abraham, W. R. Cieslak, and W. A. Adams, Eds., PV 98-15, p. 1, The Electrochemical Society Proceedings Series, Pennington, NJ (1999).
19. V. Srinivasan, B. C. Cornilsen, and J. W. Weidner, *Selected Battery Topics*, W. R. Cieslak, Eds., PV 98-15, p. 31, The Electrochemical Society Proceedings Series, Pennington, NJ (1999).
20. V. Srinivasan, B. C. Cornilsen, and J. W. Weidner, *J. Electrochem. Soc.*, Submitted (2000).
21. R. Darling and J. Newman, *J. Electrochem. Soc.*, **145**, 990 (1998).

22. P. Timmerman, B. V. Ratnakumar, and S. Di Stefano, *Aqueous Batteries*, P. D. Bennet and S. Gross, Eds., PV 96-16, p. 130, The Electrochemical Society Proceedings Series, Pennington, NJ (1996).
23. C. C. Streinz, S. Motupally, and J. W. Weidner, *J. Electrochem. Soc.*, **143**, 4051 (1995).
24. C. C. Streinz, A. P. Hartman, S. Motupally, and J. W. Weidner, *J. Electrochem. Soc.*, **142**, 1084 (1995).
25. S. Motupally, C. C. Streinz, and J. W. Weidner, *J. Electrochem. Soc.*, **142**, 1401 (1995).
26. B. C. Cornilsen, *Selected Battery Topics*, G. Halpert, M. L. Gopikanth, K. M. Abraham, W. R. Cieslak, and W. A. Adams, Eds., PV 98-15, p. 23, The Electrochemical Society Proceedings Series, Pennington, NJ (1999).
27. M. Jain, S. Motupally, and J. W. Weidner, *Aqueous Batteries*, P. D. Bennet and S. Gross, Eds., 96-16, p. 121, The Electrochemical Society Proceedings Series, Pennington, NJ (1996).
28. A. H. Zimmerman and P. K. Effa, *The Electrochemical Society Extended Abstracts*, Eds., 85-2, p. 43, The Electrochemical Society Proceedings Series, (1985).
29. P. L. Loyselle, P. J. Karjala, and B. C. Cornilsen, *Electrochemical and Thermal Modeling of Battery, Fuel Cell and Photoenergy Conversion Systems*, J. R. Selman and H. C. Maru, Eds., PV 86-12, p. 114, The Electrochemical Society Proceedings Series, Pennington, NJ (1986).



30. D. H. Everett and W. I. Whitton, *Trans. Faraday Soc.*, **48**, 749 (1952).
31. D. H. Everett and P. Nordon, *Proc. Roy. Soc.*, **A259**, 341 (1960).
32. R. Barnard, C F. Randell, and F. L. Tye, *Power Sources 8*, J. Thompson, Eds., Academic Press, London (1981).
33. G. W. D. Briggs and P. R. Snodin, *Electrochim. Acta*, **27**, 565 (1982).
34. C. Zhang and S. Park, *J. Electrochem. Soc.*, **134**, 2966 (1987).
35. D. Fan, Ph.D. Thesis, *Mathematical Modeling of a Sealed Nickel-Cadmium Cell*, Texas A&M University, College Station (1991).
36. S. Motupally, Masters Thesis, *Measurement of Diffusion Coefficient of Protons in Nickel Hydroxide Films as a Function of State of Charge*, University of South Carolina, Columbia (1994).
37. D. H. Everett and H. W. Smith, *Trans. Faraday Soc.*, **50**, 187 (1954).
38. D. H. Everett, *Trans. Faraday Soc.*, **50**, 1077 (1954).
39. J. A. Enderby, *Trans. Faraday Soc.*, **51**, 835 (1955).
40. J. A. Enderby, *Trans. Faraday Soc.*, **52**, 106 (1956).
41. J. P. Sethna, K. Dahmen, S. Kartha, J. A. Krumhansl, B. W. Roberts, and J. D. Shore, *Phys. Rev. Lett.*, **70**, 3347 (1993).
42. W. R. McKinnon, J. R. Dahn, J. J. Murray, R. R. Hearing, R. S. McMillan, and A. H. Rivers-Bowerman, *J. Phys. C*, **19**, 5135 (1986).

## List of Figures

**Figure 1.** Equilibrium potential of a fresh pure-Ni film over the first two cycles generated using a constant current experiment. Figure 1(a) shows the significantly greater electron transfer in the first charge. Figure 1(b) was generated by converting the abscissa to  $z$  by correcting 1(a) for the oxygen evolution reaction using Equations 3 to 7.

**Figure 2.** Equilibrium potential vs.  $z$  for a fresh pure-Ni film and a fresh Ni-Co film (a) and a fresh Ni-Co film and an aged Ni-Co film (b). The film was aged in 3% KOH for 40 hours. Note the similarity in the shape of the curves. All curves correspond to the second cycle.

**Figure 3.** Equilibrium potential vs.  $z$  for a fresh Ni-Co film. The lines were generated using a constant current experiment and the symbols were generated using a constant potential experiment. The electrode was held at a potential for one hour, and  $z$  was determined at the end of the experiment. The solid circles show the data for an electrode initially at the fully charged state, and the open circles are those for electrodes initially at the fully discharged state. The inset plot shows the offset potential as a function of  $z$ .

**Figure 4.** Effect of time on the history-dependent behavior of fresh Ni-Co films. The curves were generated by maintaining the electrode at 319 mV vs. Ag/AgCl for different times from the charged and discharged states. The value of  $z$  was then evaluated by correcting for the oxygen evolution reaction using Equations 3 to 7. The curves show that two stable oxidation states can exist at the same potential depending only on the previous history of the electrode.

**Figure 5.** Schematic representation of the domain concept applied to the nickel hydroxide electrode. Figure 5(a) shows the boundary curves in a domain which exhibits metastability due to an intercalation effect and 5(b) due to phase separation. Figure 5(c) shows a distribution of the potentials defined in Figure 5(a) for the different domains, and 5(d) is the corresponding response of the system. Two possible scanning curves are shown in figures 5(c) and (d), one by the solid line and the other by the dotted line.

**Figure 6.** Discharge scanning curves for fresh Ni-Co films. The curves were generated by discharging the electrode after a partial charge. The curves were then converted to  $z$  by correcting for the oxygen evolution reaction, as detailed in the text, and forcing the end of discharge to occur at  $z=0$ .

**Figure 7.** Charge scanning curves for fresh Ni-Co films. The curves were generated by charging the electrode after a partial discharge. The curves were then converted to  $z$  by correcting for the oxygen evolution reaction, as detailed in the text, and forcing the value of  $z$  at the start of the charge to correspond to the value of  $z$  at the end of the previous discharge.

**Figure 8.** Rescaled discharge scanning curves fresh Ni-Co films. The rescaling was accomplished by stretching the scanning curves in Figure 6 until they touch the boundary curve.

**Figure 9.** Rescaled scanning curves for fresh Ni-Co films during charge. Graph (a) was normalized by forcing the potential at the start of the scan to lie on the boundary curve while (b) was generated by forcing it to lie on the longest scanning curve. The solid line indicates the boundary curves, and the dotted lines the scanning curves.

**Figure 10.** Test of the validity of Theorem 4 and 5 for fresh Ni-Co films. The scanning curves were generated by reversing the (constant) current at the potentials shown by the light dotted lines. The left loop starts from charging beginning at  $z=0$ , and the right loop starts from discharging beginning at  $z=1$ . Note that the system continues along the boundary curve after experiencing one current reversal at  $V_A$  (for the initially charging curve). For the initially discharging curve, the first current reversal occurs at  $V_B$  and the second at  $V_A$ .

**Figure 11.** Test of the validity of Theorem 6 for fresh Ni-Co films. The curves were generated by cycling the current over two different ranges of  $z$  in the charge loop. As predicted by theorem 6, the path of the system after it crosses the point 'P' is dependent on its history.

**Figure 12.** Test of the validity of Theorem 7 for fresh Ni-Co films. Figure 12(a) was generated by cycling the current over two successively smaller ranges of  $z$  in the charge loop. Note that the path of the system after a reversal approaches the point of previous reversal, thereby wiping the history of both the primary and secondary excursion. Figure 12(b) illustrates the path of the system when  $\Delta z$  was decreased in each cycle where the appear to approach the midpoint between the boundary curves.

**Figure 13.** Equilibrium curves measured as a function of cycling over a small range of  $z$ . The curves were generated by charging and discharging the electrode using a constant current over a  $\Delta z$  of 0.02 for 50 cycles in the charge and discharge loop. The inset plot shows the drift in potential towards the discharge boundary curve. The time for each

charge (or discharge) was 30 s, resulting in the completion of the 50 cycles in 3000 s. In contrast, In Figure 4 the system was shown to be relatively stable over 10 hours.

**Figure 14.** Mid point potential as a function of cycle number when the electrode is charged and discharged over a small range of  $z$  as shown in Figure 13. The plot shows drift in the potential of the curves in the charge loop towards the discharge loop.

**Figure 15.** Simulated discharge scanning curves for fresh Ni-Co films. The curves were generated using the procedure outlined in the text. Also shown are the fits of Eq. 9 to the discharge boundary curve and the longest charge scanning curve (solid lines).

**Figure 16.** Simulated charge scanning curves for fresh Ni-Co films. The curves were generated using the procedure outlined in the text. Also shown are the fits of Eq. 9 to the discharge boundary curve and the longest charge scanning curve (solid lines).

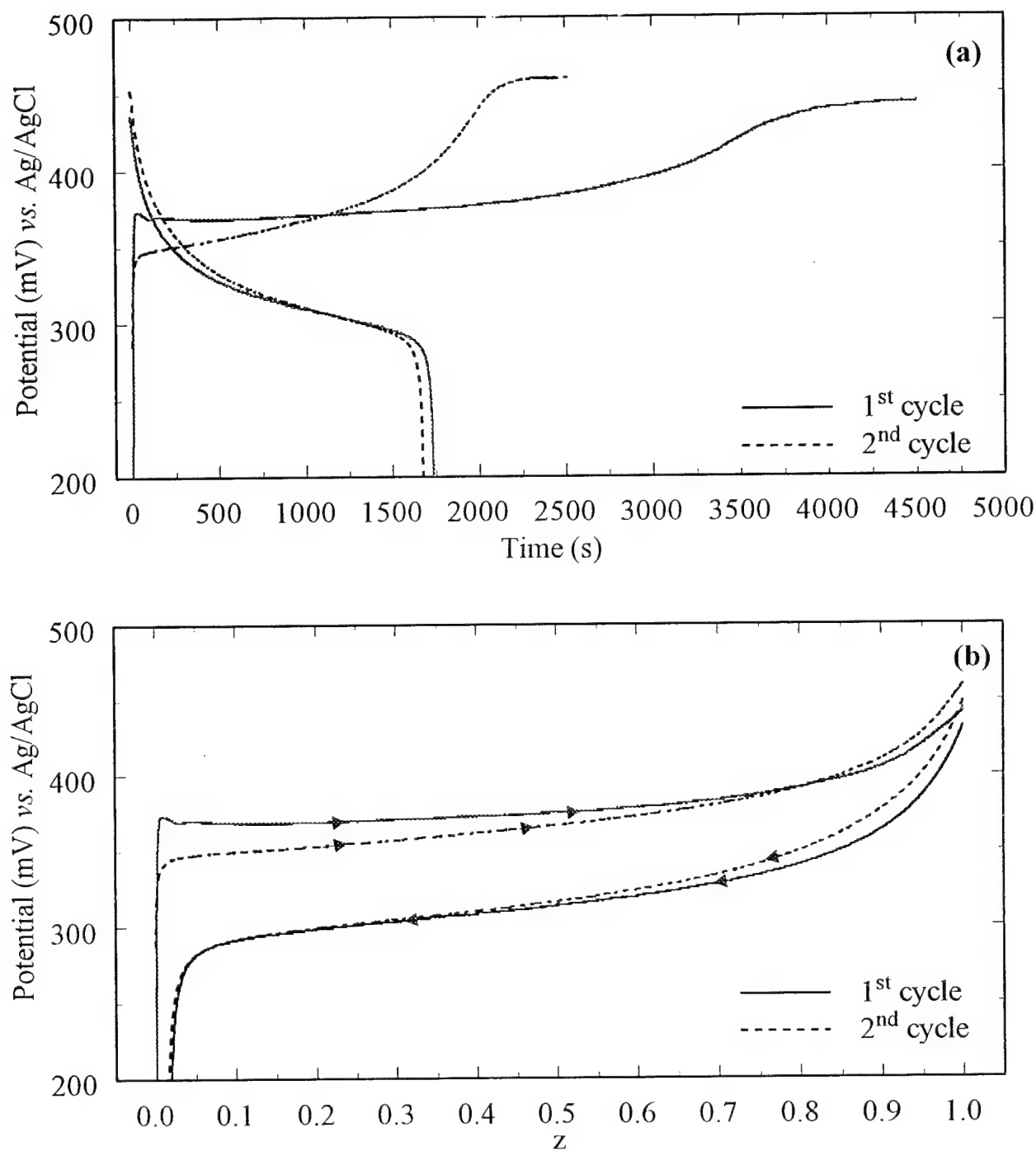


Figure 1. Equilibrium potential of a 35  $\mu\text{g}$  fresh pure-Ni film over the first two cycles generated using a constant-current experiment. Figure 1(a) shows the significantly greater electron transfer in the first charge. Figure 1(b) was generated by converting the abscissa to  $z$  by correcting 1(a) for the oxygen evolution reaction using equations 3 to 6.

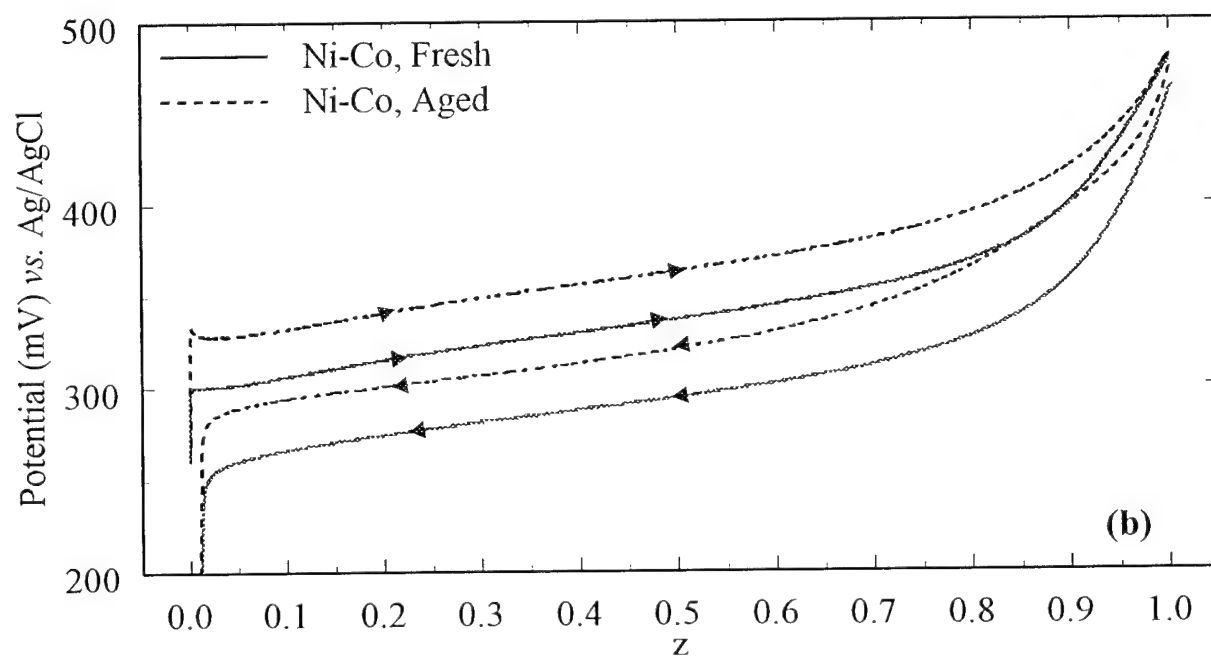
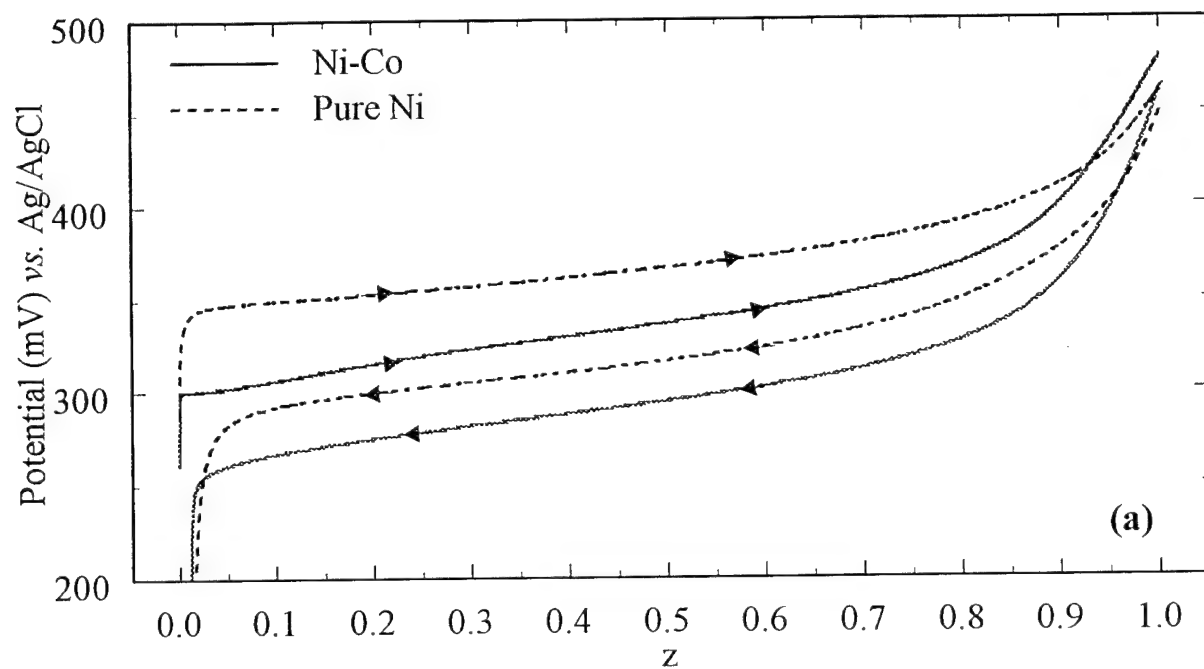


Figure 2. Equilibrium potential vs.  $z$  for a fresh pure-Ni film and a fresh Ni-Co film (a) and a fresh Ni-Co film and an aged Ni-Co film (b). The film was aged in 3% KOH for 40 hours. Note the similarity in the shape of the curves. All curves correspond to the second cycle.

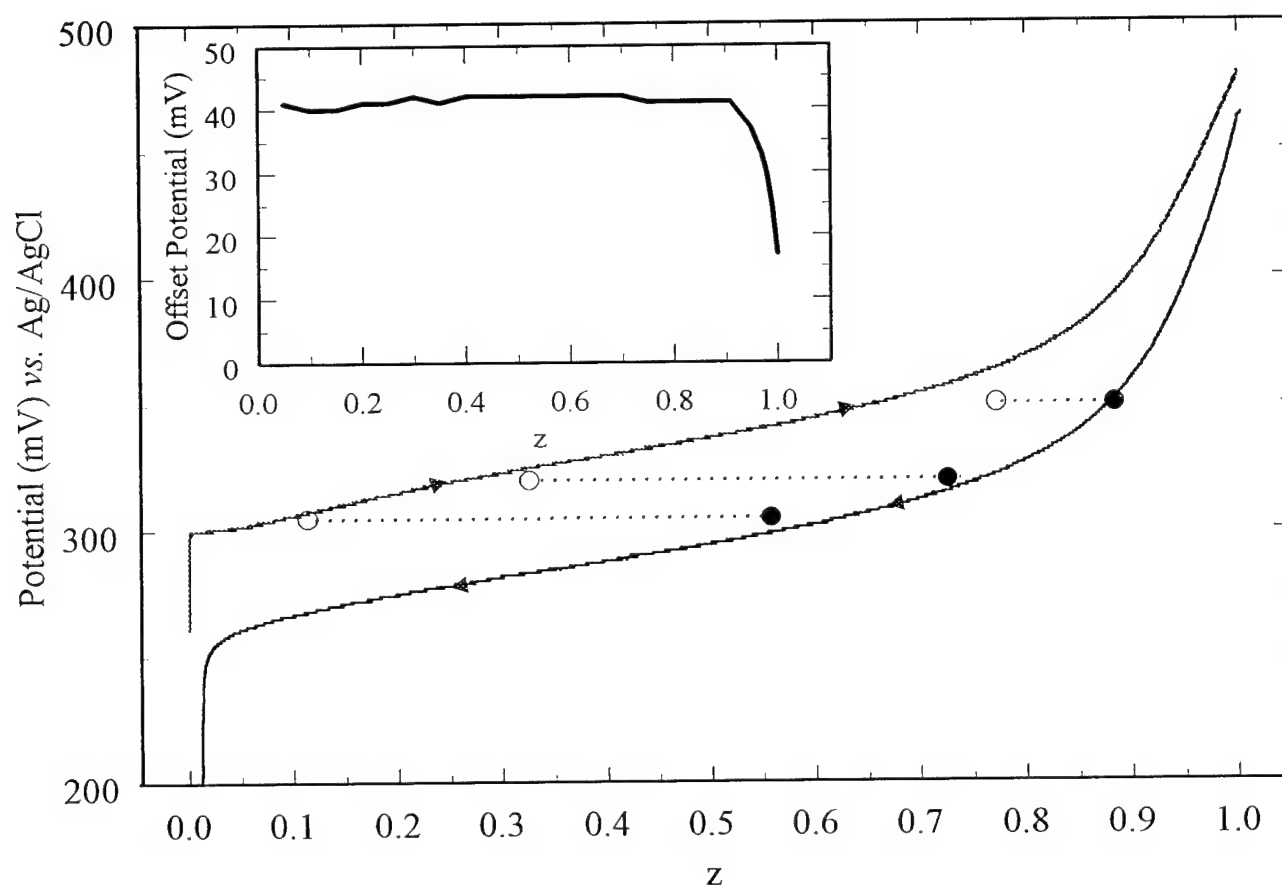


Figure 3. Equilibrium potential vs.  $z$  for a 35  $\mu\text{g}$  fresh Ni-Co film. The lines were generated using a constant-current experiment, and the symbols were generated using a constant-potential experiment. The electrode was held at a potential for one hour, and  $z$  was determined at the end of the experiment. The solid circles show the data for an electrode initially at the fully charged state, and the open circles are those for electrodes initially in the fully discharged state. The inset plot shows the offset voltage as a function of  $z$ .



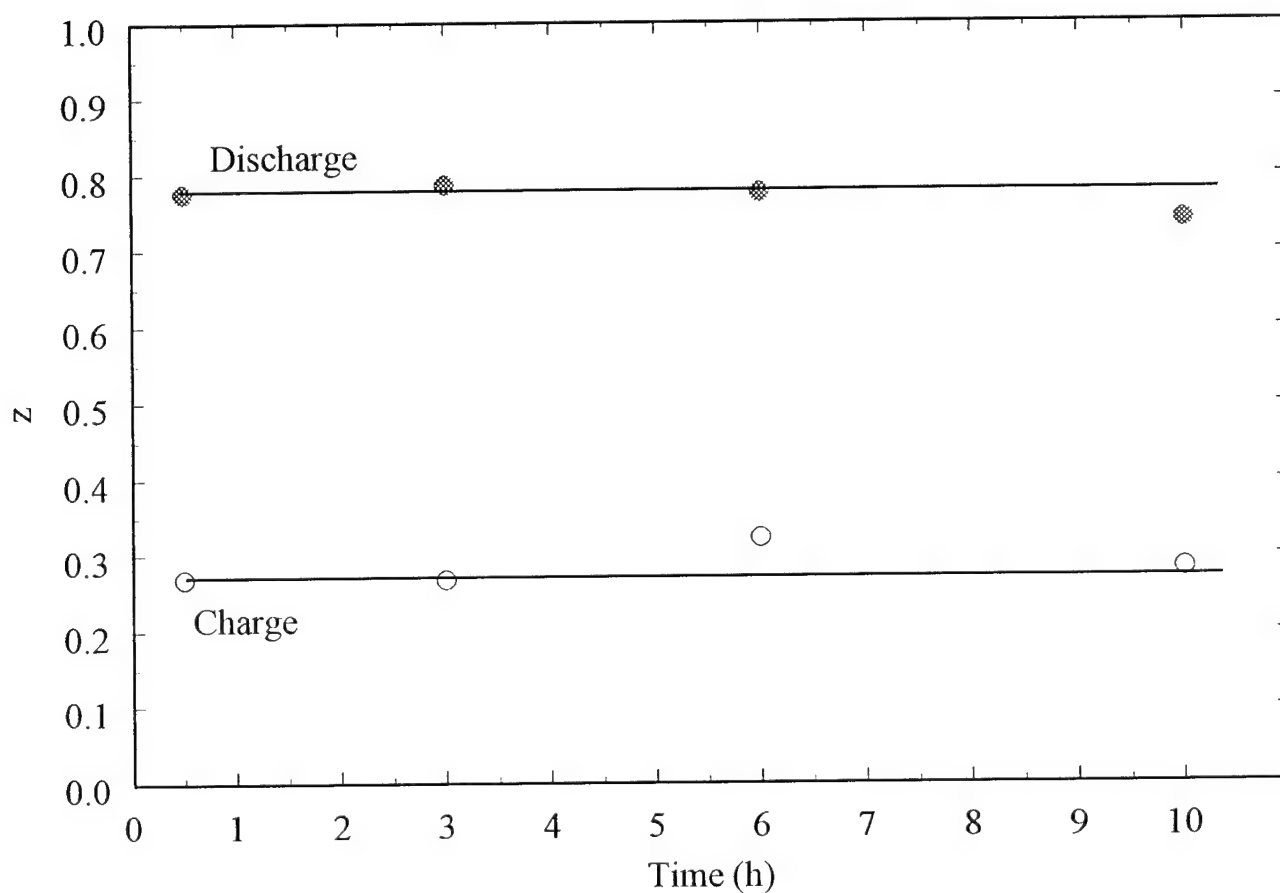


Figure 4. Effect of time on the history-dependent behavior of the nickel electrode. The curves were generated by maintaining the electrode at 319 mV vs. Ag/AgCl for different times from the charged and discharged states. The SOC was then evaluated and is plotted in the figure. The curve shows the existence of at least two states with different  $z$  for the same potential.

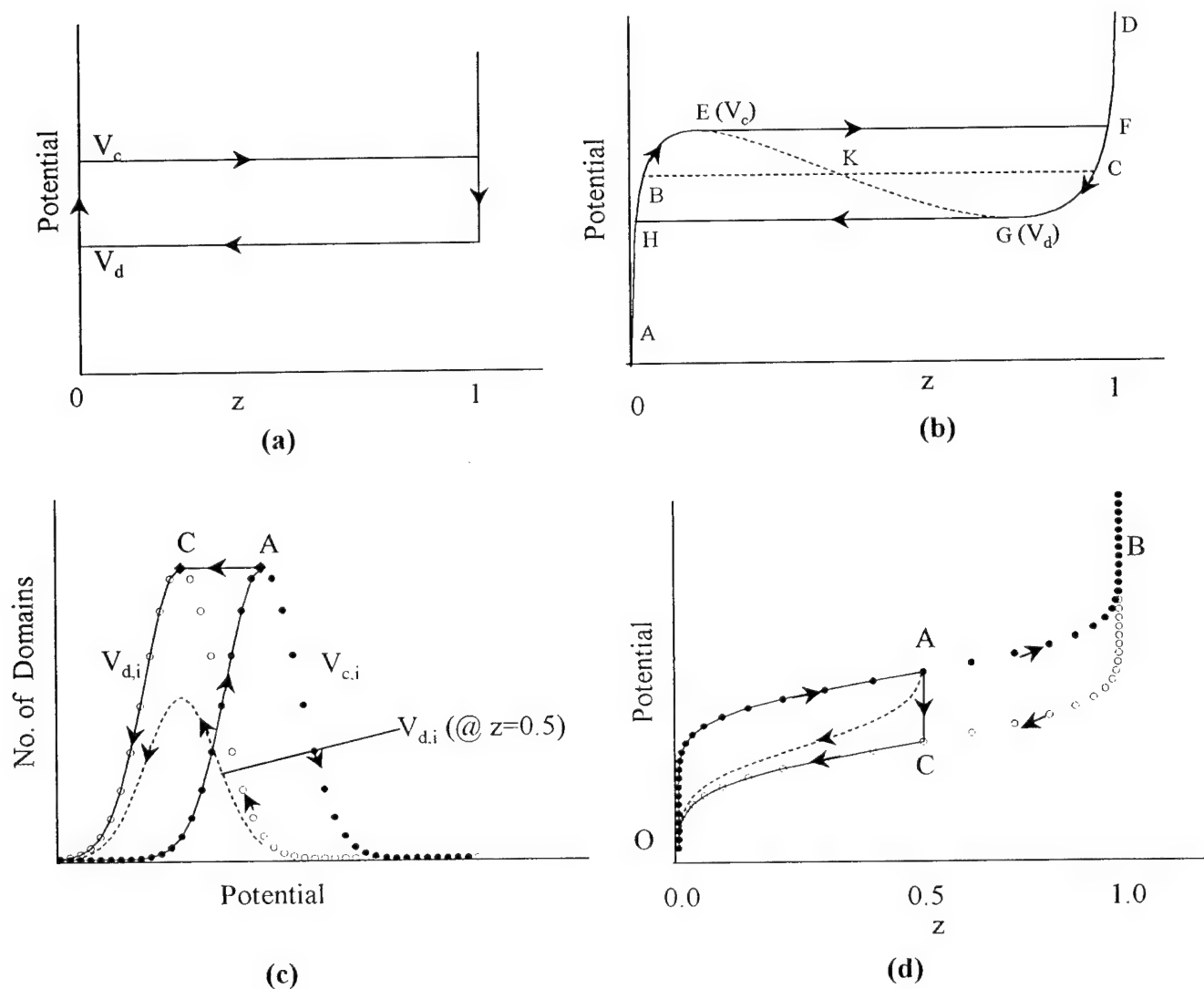


Figure 5. Schematic representation of the domain concept applied to the nickel hydroxide electrode. Figure 5(a) shows the boundary curves in a domain which exhibits metastability due to an intercalation effect and 5(b) due to phase separation. Figure 5(c) shows a distribution of the potentials defined in Figure 5(a) for the different domains, and 5(d) is the corresponding response of the system. Two possible scanning curves are shown in figures 5(c) and (d), one by the solid line and the other by the dotted line.

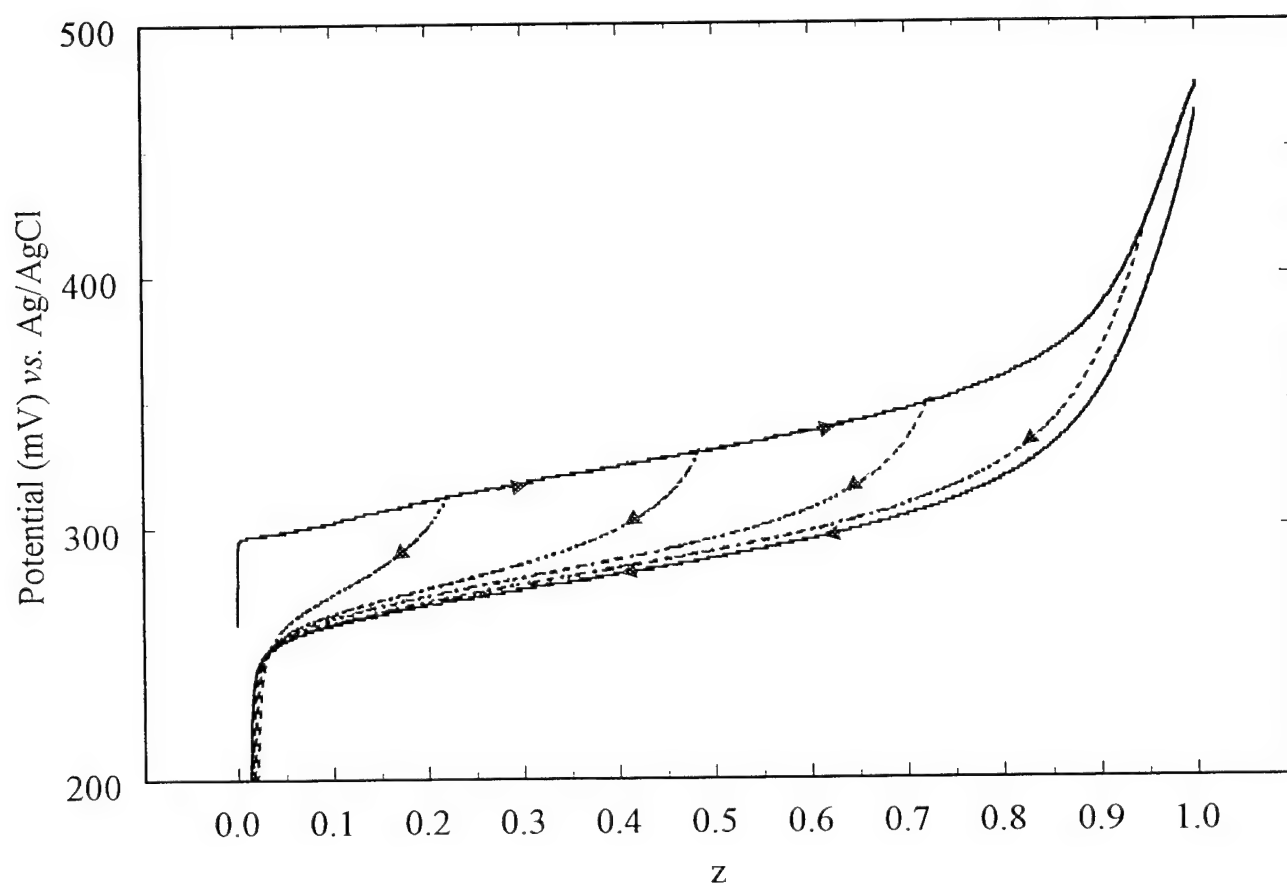


Figure 6. Discharge scanning curves for the nickel hydroxide electrode. The curves were generated by discharging the electrode after a partial charge. The curves were then converted to  $z$  by correcting for the oxygen evolution reaction, as detailed in the text, and forcing the end of discharge to occur at  $z=0$ .

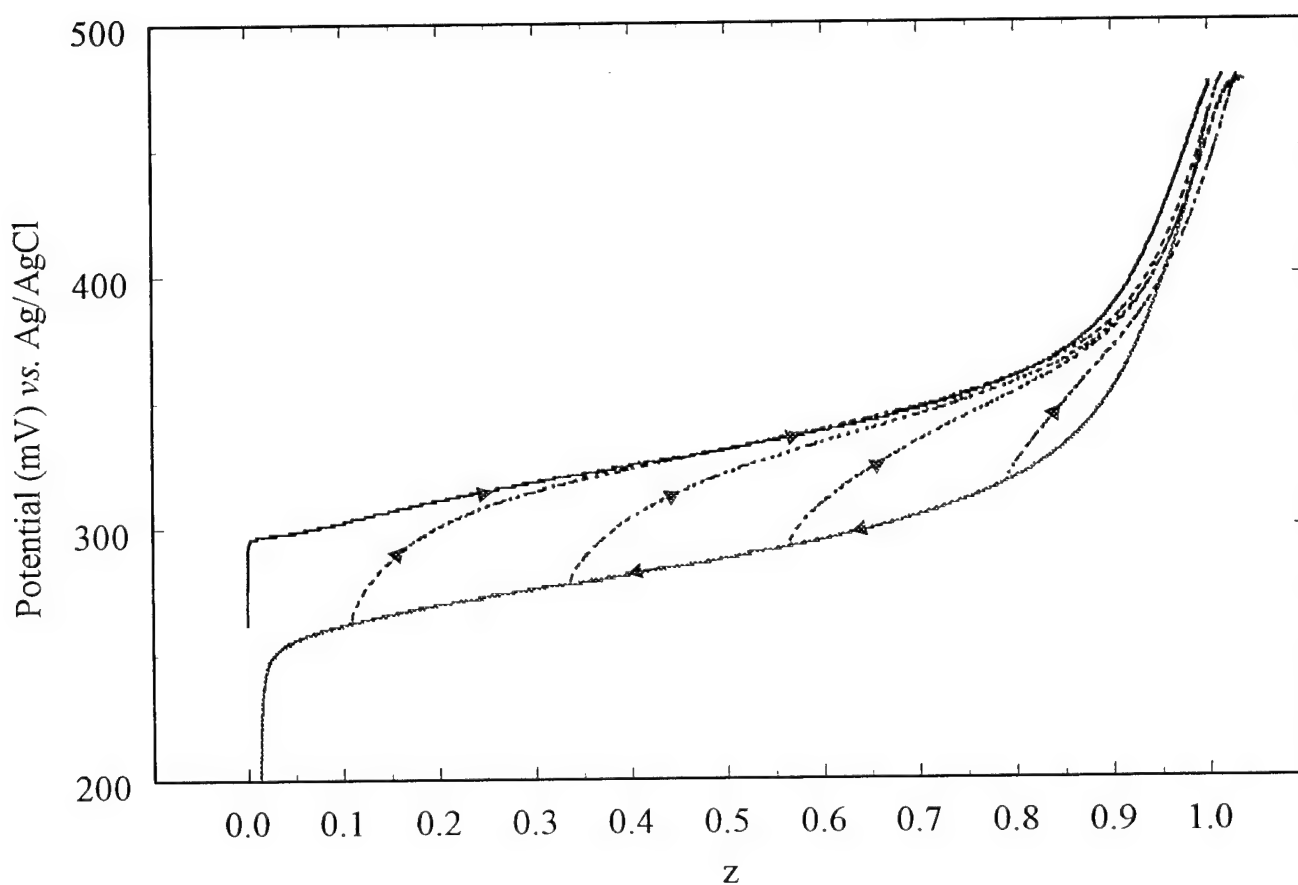


Figure 7. Charge scanning curves for the nickel hydroxide electrode. The curves were generated by charging the electrode after a partial discharge. The curves were then converted to  $z$  by correcting for the oxygen evolution reaction, detailed in the text, and forcing the  $z$  at the start of the charge to correspond to the  $z$  at the end of the previous discharge.

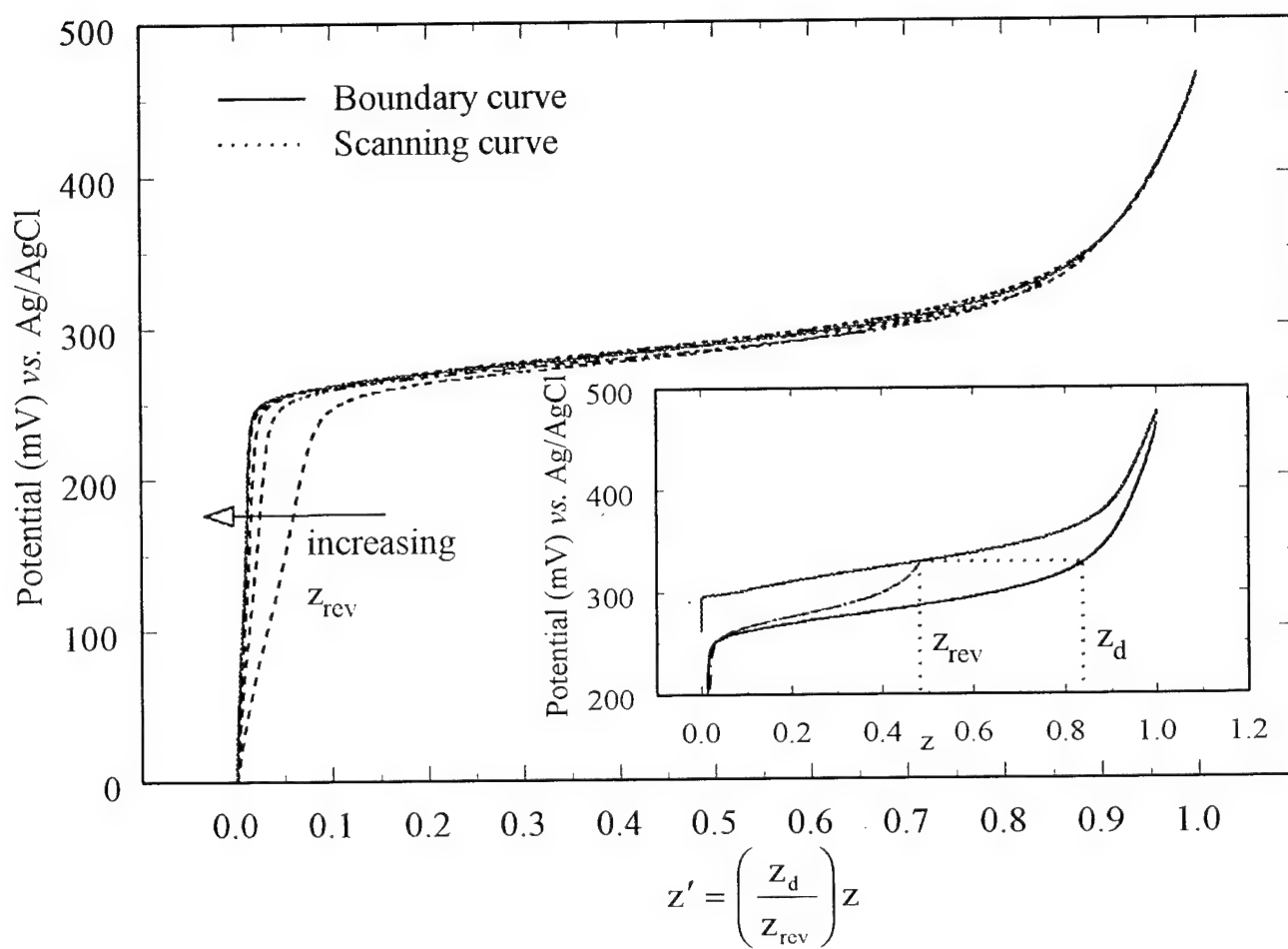


Figure 8. Rescaled discharge scanning curves for the nickel hydroxide electrode. The rescaling was accomplished by stretching the scanning curves in Figure 6 until they touch the boundary curve.

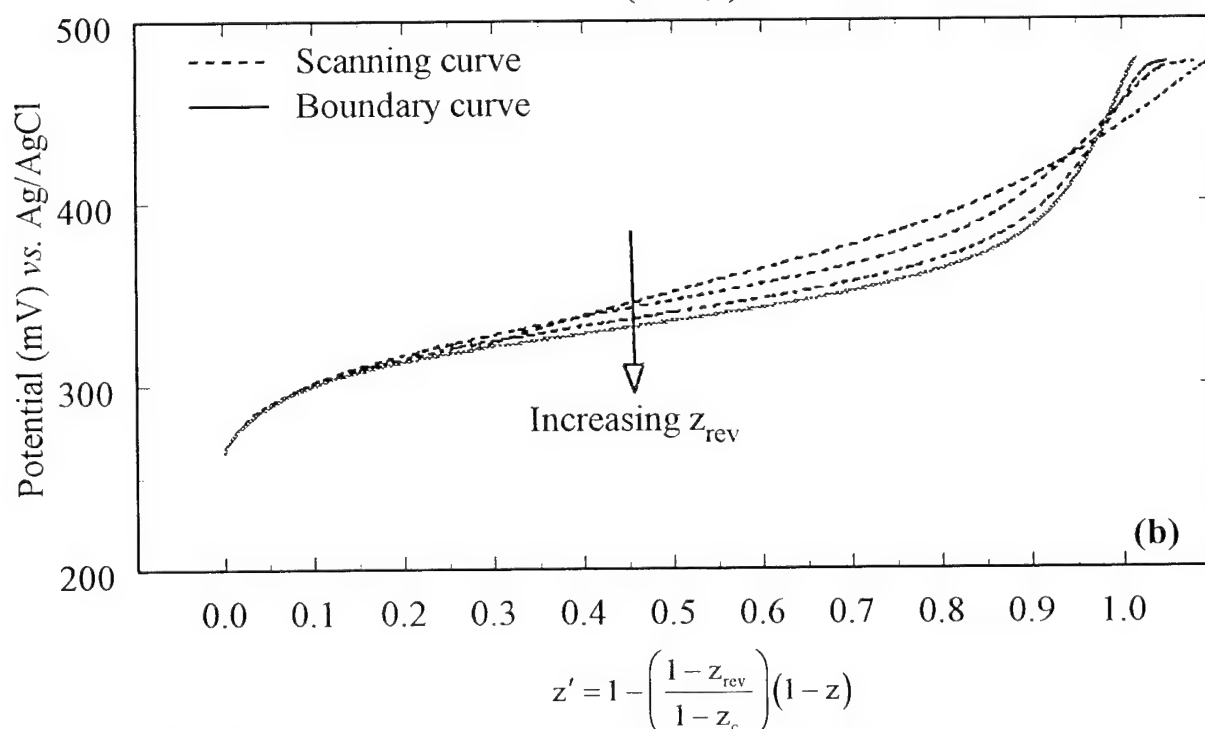
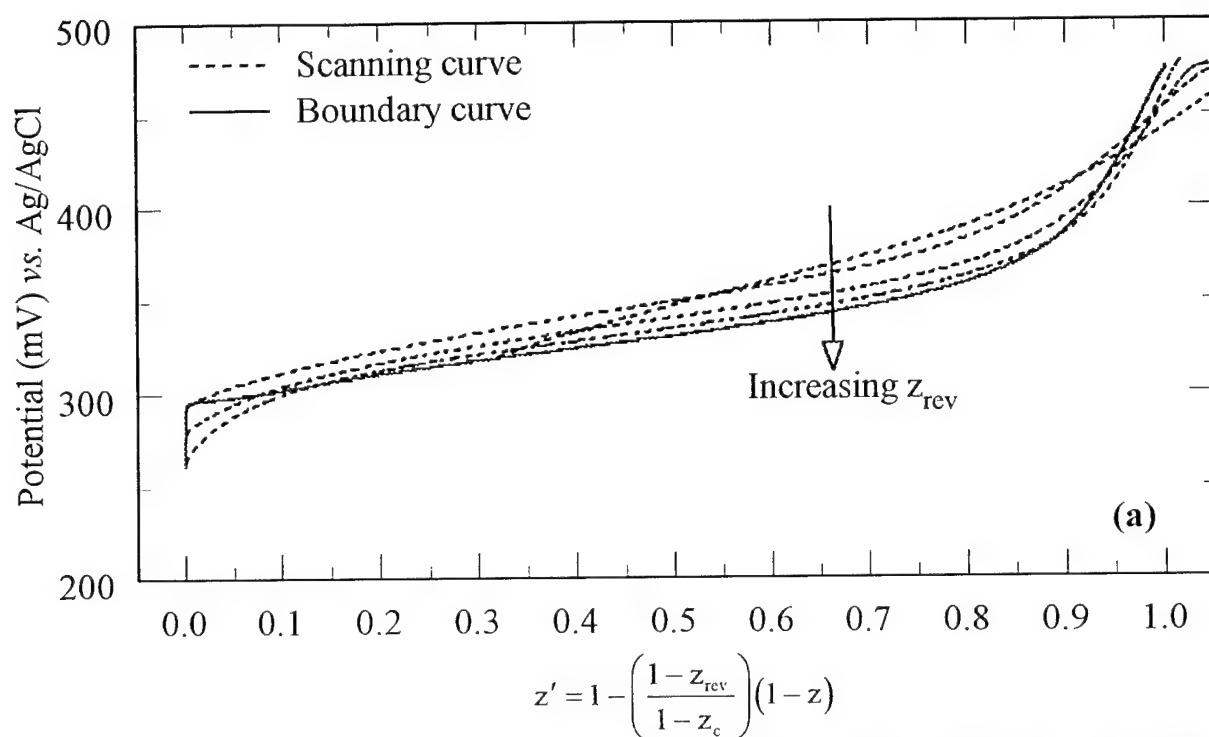


Figure 9. Rescaled scanning curves for the nickel hydroxide electrode during charge. Graph (a) was normalized by forcing the potential at the start of the scan to lie on the boundary curve while (b) was generated by forcing it to lie on the longest scanning curve. The solid line indicates the boundary curves and the

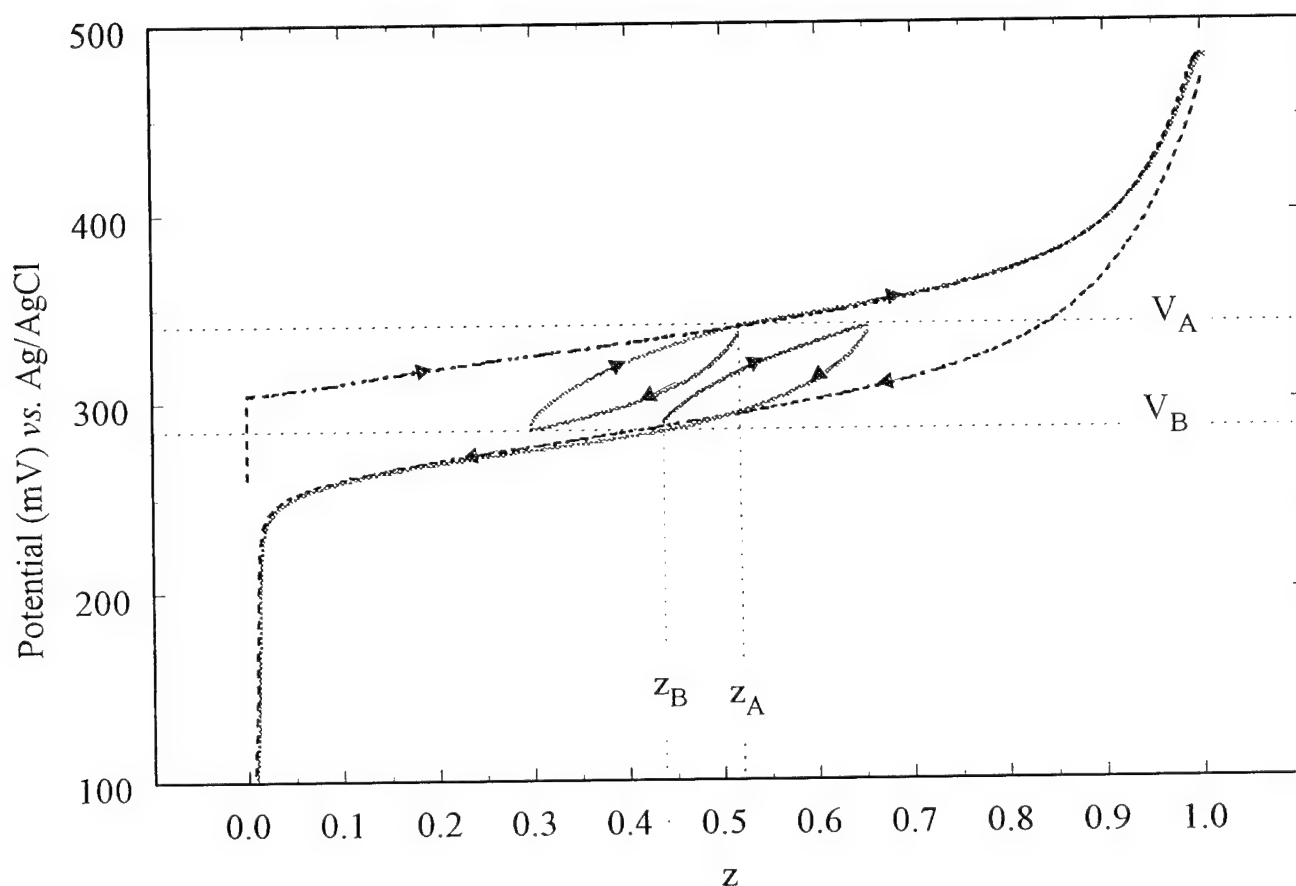


Figure 10. Test of the validity of Theorems 4 and 5 for the nickel hydroxide electrode. The scanning curves were generated by reversing the (constant) current at the potentials shown by the light dotted lines. The left loop starts from charging beginning at  $z=0$ , and the right loop starts from discharging beginning at  $z=1$ . Note that the systems continues along the boundary curve after experiencing one current reversal at  $V_A$  (for the initially charging curve). For the initially discharging curve, the first current reversal occurs at  $V_B$  and the second at  $V_A$ .

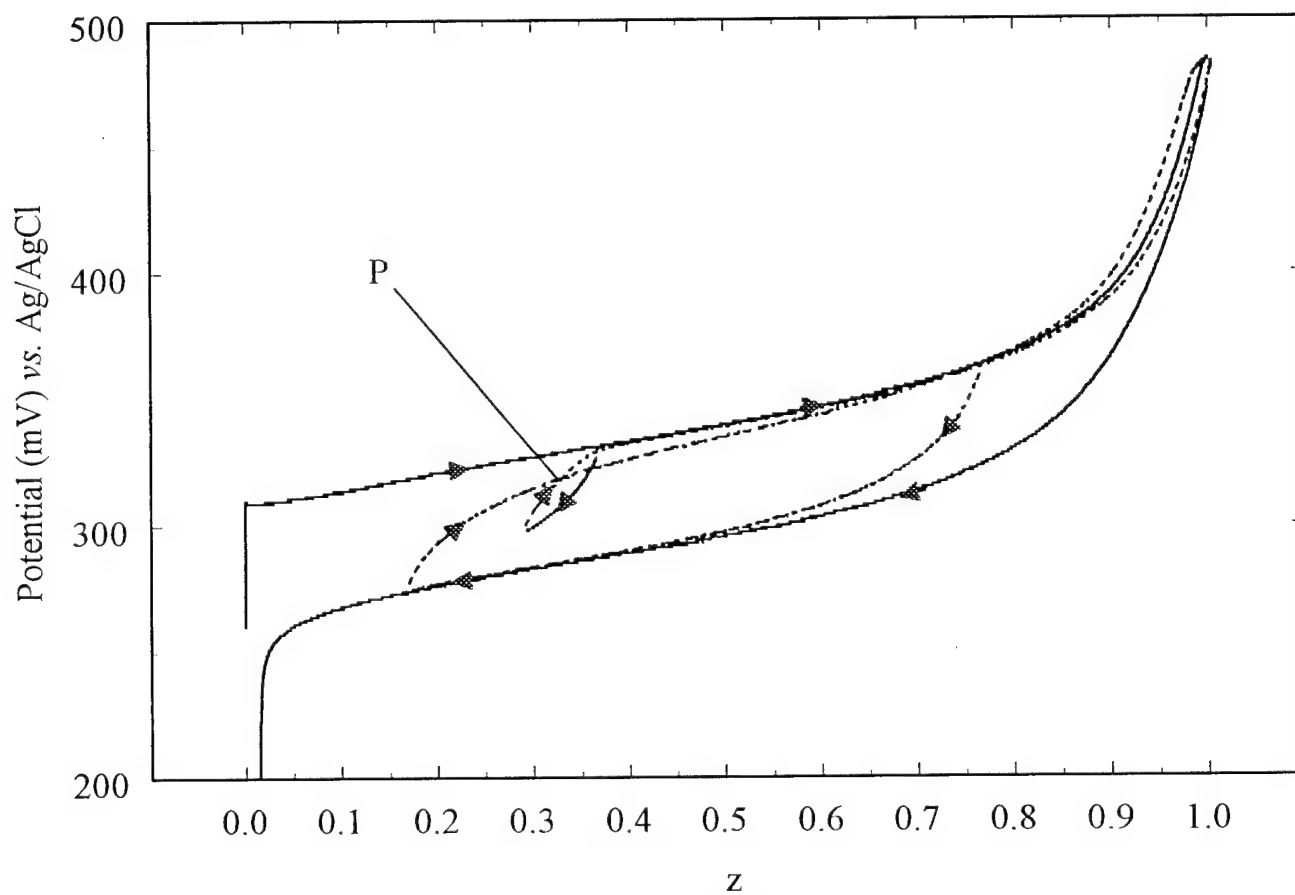


Figure 11. Test of the validity of Theorem 6 for the nickel hydroxide electrode. The curves were generated by cycling the current over two different ranges of  $z$  in the charge loop. As predicted by theorem 6, the path of the system after it crosses the point 'P' is dependent on its history.



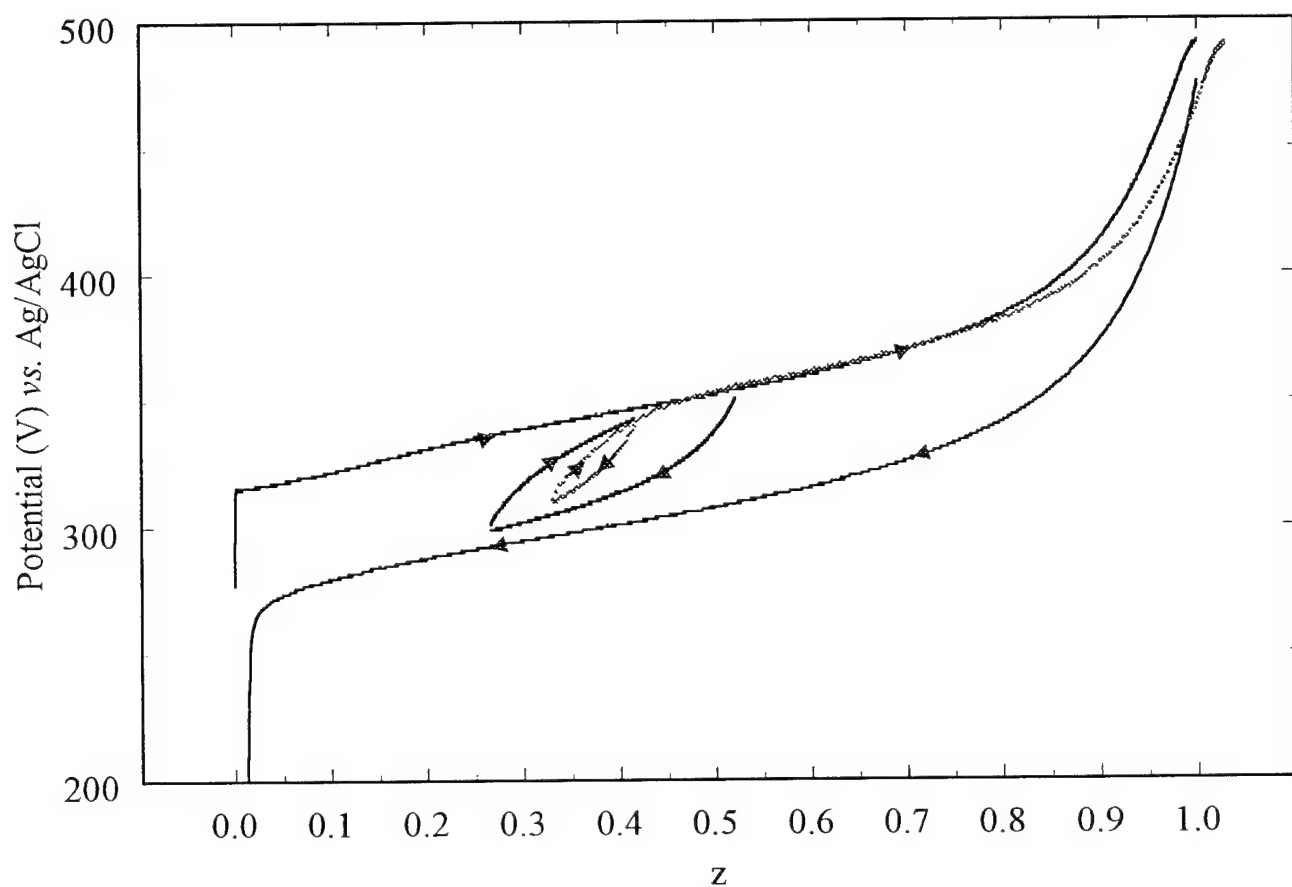


Figure 12. Test of the validity of Theorem 7 for the nickel hydroxide electrode. The curves were generated by cycling the current over two successively smaller ranges of  $z$  in the charge loop. Note that the path of the system after a reversal approaches the point of previous reversal thereby wiping the history of both the primary and secondary excursion.

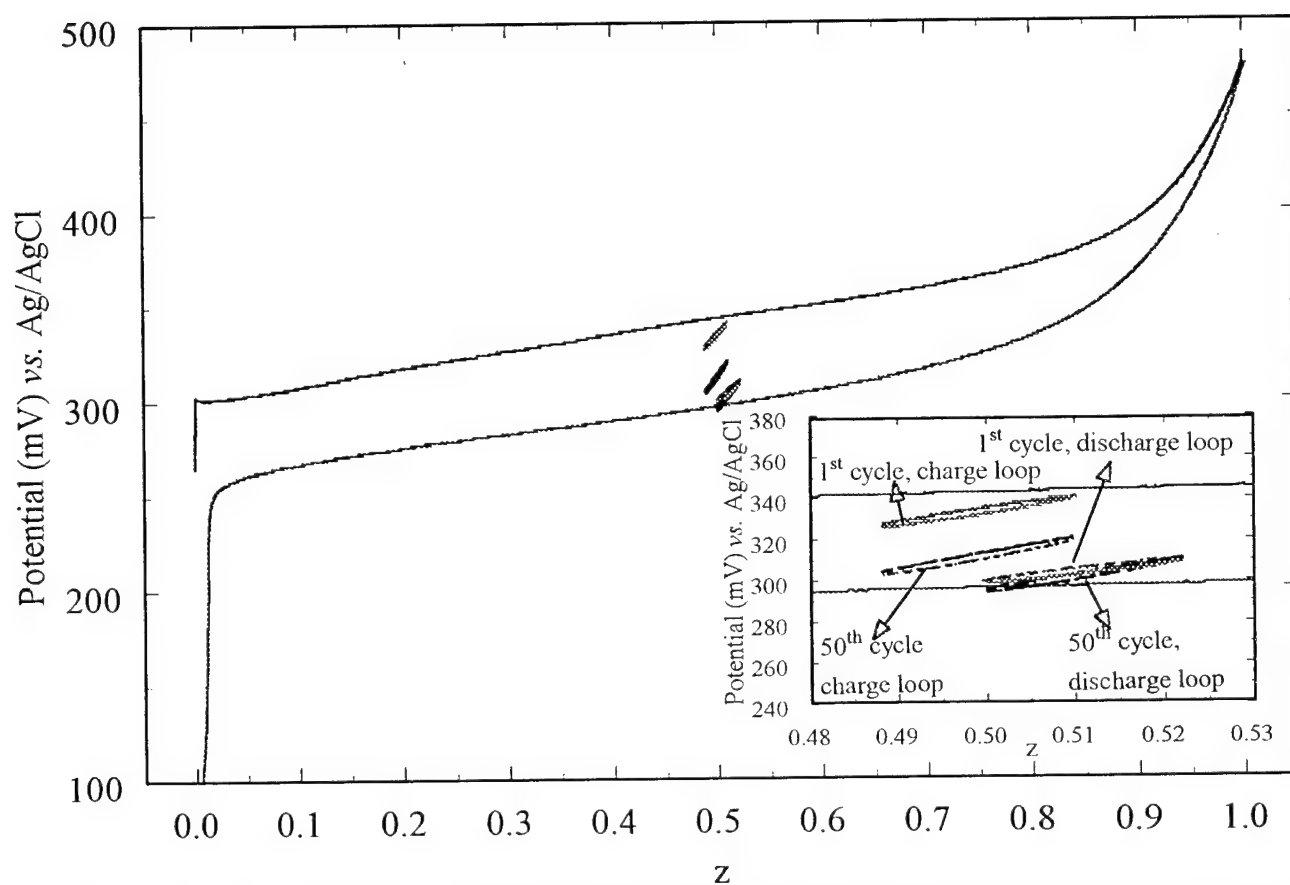


Figure 13. Equilibrium curves measured as a function of cycling over a small range of  $z$ . The curves were generated by charging and discharging the electrode using a constant current over a  $\Delta z$  of 0.02 for 50 cycles in the charge and discharge loop. The inset plot shows the drift in potential towards the discharge boundary curve. The time for each charge (or discharge) was 30 secs, resulting in the completion of the 50 cycles in 3000 secs. In contrast, in Figure 4 the system was shown to be relatively stable over 10 hours.

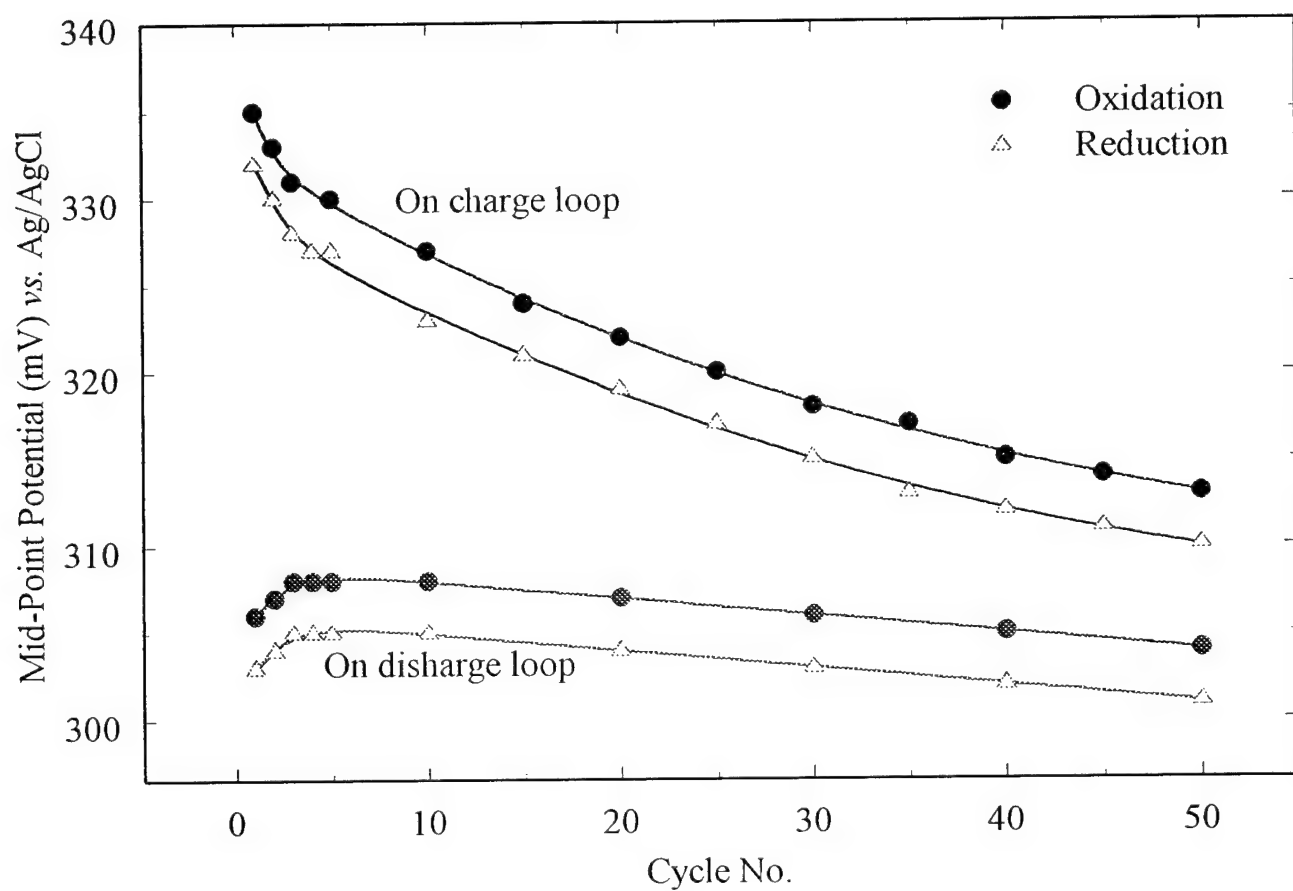


Figure 14. Mid-plateau potential as a function of cycle number when the electrode is oxidized and reduced over a small range of  $z$  as shown in Figure 12. The plot shows drift in the potential of the curves in the charge loop towards the discharge loop.

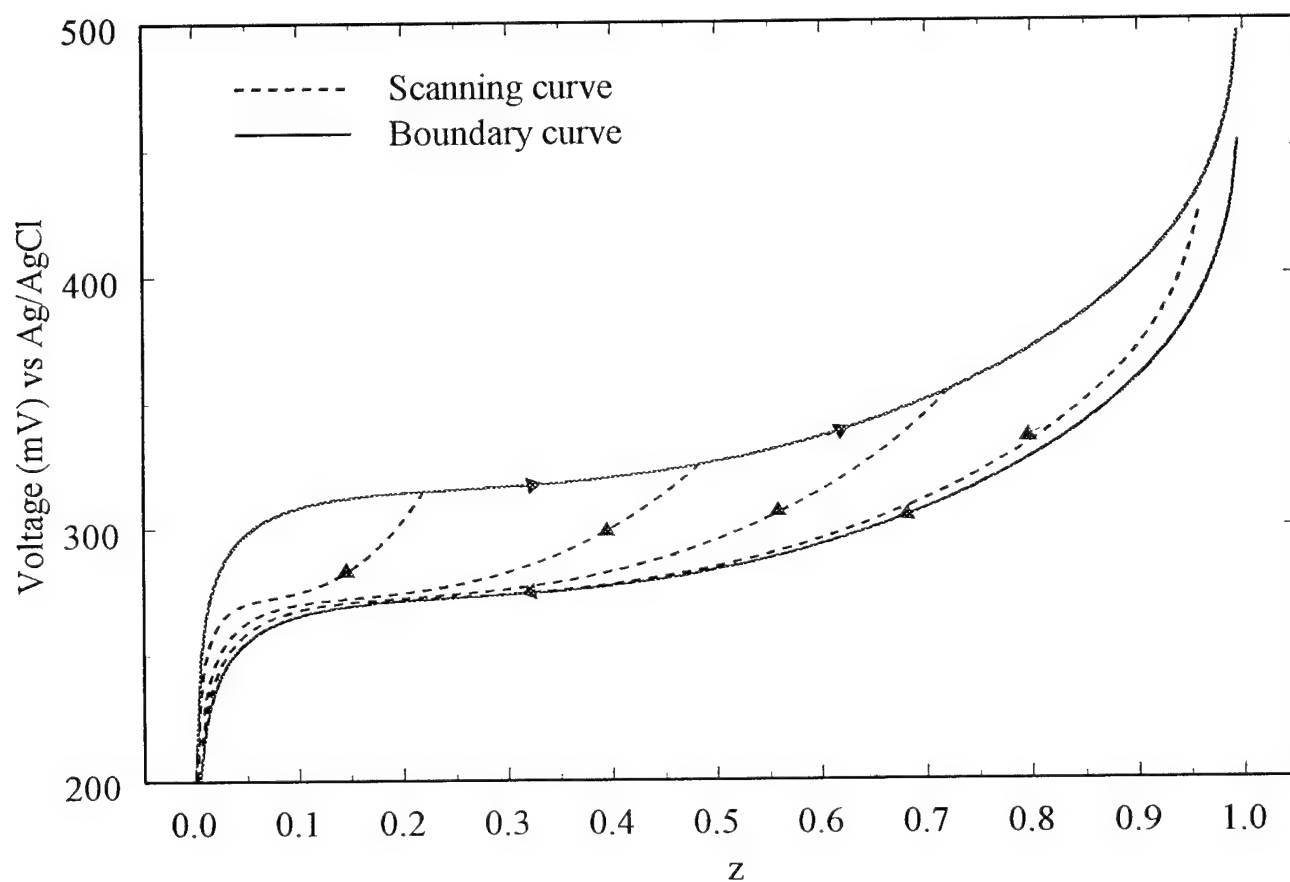


Figure 15. Simulated discharge scanning curves for the nickel hydroxide electrode. The curves were generated using the procedure outlined in the text. Also shown are the fits of Eq. 9 to the discharge boundary curve and the longest charge scanning curve (solid lines).

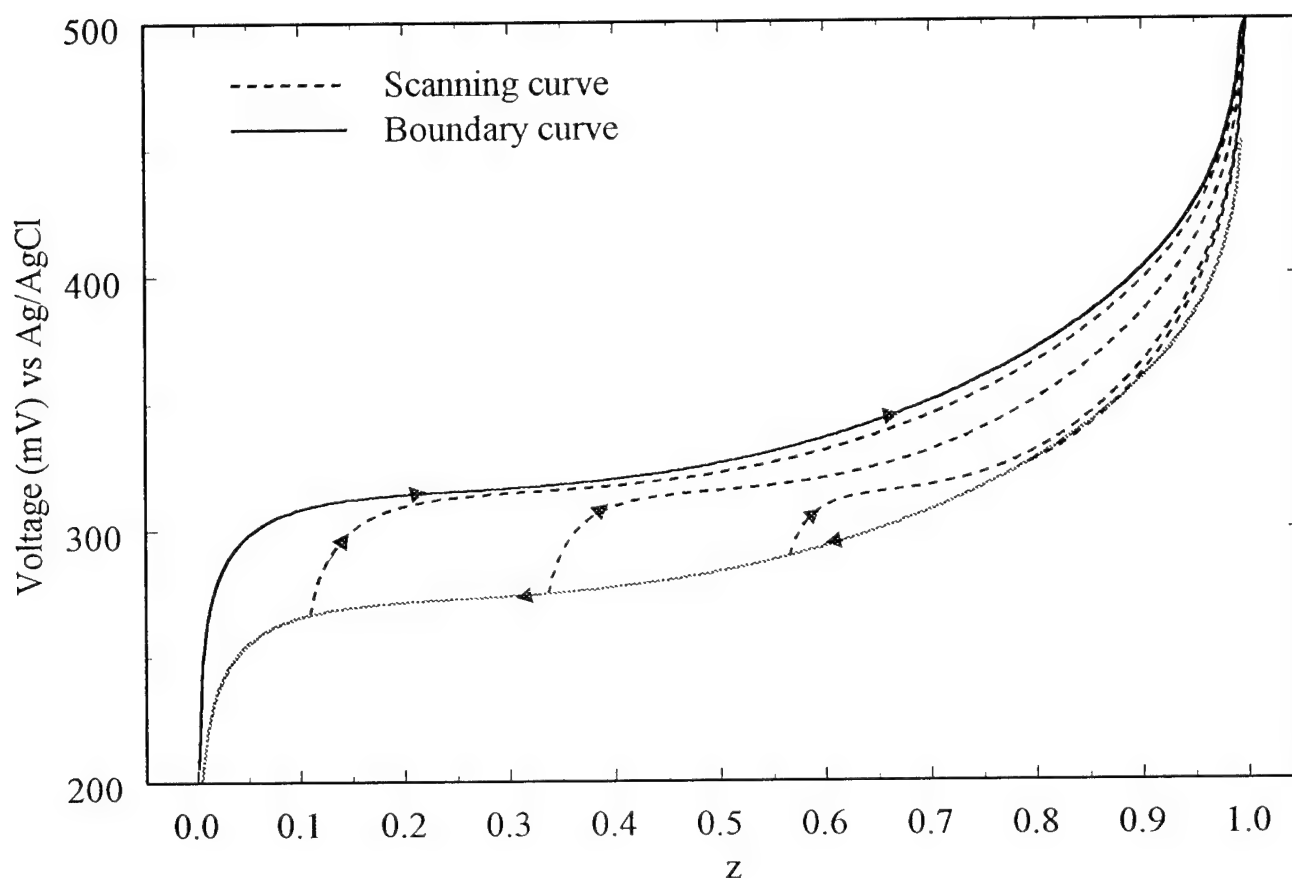


Figure 16. Simulated charge scanning curves for the nickel hydroxide electrode. The curves were generated using the procedure outlined in the text. Also shown are the fits of Eq. 9 to the discharge boundary curve and the longest charge scanning curve (solid lines).

**PRACTICAL CONSIDERATIONS IN MODELING THE  
ELECTROCHEMICAL DOUBLE LAYER BY  
DENSITY FUNCTIONAL THEORY**

Huanhua Pan, James A. Ritter\*, and Perla B. Balbuena

Department of Chemical Engineering

University of South Carolina

Columbia, SC 29208

A research note submitted to

*Langmuir*

for review and consideration for publication.

---

\* To whom correspondence should be addressed.

The electrical double layer is the inhomogeneous region of an electrolyte near a charged surface. Understanding the electrical double layer is fundamental to a variety of phenomena in electrochemical, colloidal and biological sciences. However, the theoretical description of the electric double layer has always been a major challenge in interfacial electrochemistry. The earliest theory that achieved significant success was that of Gouy and Chapman (Gileadi, et al., 1975), where the ions are simplified as point charges distributed in a dielectric continuum. This oversimplified diffuse layer model, however, does not agree well with experimental data, especially in concentrated electrolyte solutions. Stern improved this model by considering that ions have a finite size, and that there exists a plane of closest approach, i.e., the Stern plane, within which no ions exist (Usui, 1984). This is referred to as the modified Gouy-Chapman model (MGC). The MGC theory provides quantitatively accurate results for weakly coupled systems at low densities, but it also fails to represent, even qualitatively, highly coupled or dense systems.

Torrie and Valleau (1980), based on the primitive diffuse layer model of the electrical double layer, carried out Monte Carlo simulations of the ion distribution near a charged wall over a range of reduced surface charge densities  $q_s^*$ . At the higher reduced surface charge densities, e.g., at  $q_s^* = 0.7$ , they revealed two fundamental phenomena: layering of the counter-ions and charge inversion. Subsequently, many other researchers, employing different molecular modeling approaches, studied the same system under the same conditions (Nielaba and Forstmann, 1985; Ballone et al., 1986; Mier-Teran et al., 1990; Tang et al. 1990; Caillol and Levesque, 1991; Kierlik and Rosinberg, 1991). All of the results from these studies agree well with each other. However, none of them contrasted their results against those expected in an actual electrochemical system to determine whether they were physically realistic.

Therefore, the objective of this note is to report on a density functional theory (DFT) analysis of the same system and under the same conditions; but in this case, a significant effort is expended on comparing the results with those that are expected in an actual electrochemical system. The DFT approach developed by Kierlik and Rosinberg (1990) is used here to calculate ion density and potential distribution profiles, and the corresponding double layer capacitance in an aqueous-based electrolyte system. The physical conditions that give rise to reasonable predictions of these profiles and also the double layer capacitance from the DFT approach are revealed. With respect to calculating the double layer capacitance, it is also shown how these conditions, to be physically realistic, depend on accounting for the potential drop across the Stern layer in the double layer model.

## THEORY

Considering the general situation where the electrolyte solution is enclosed in a macroscopic volume  $V$  with some external charge  $q_s$  adsorbed on surface  $S$ , the grand thermodynamic potential for the total system is written as (Kierlik and Rosinberg, 1991)

$$\Omega = G[\{\rho_i\}] + \frac{1}{2} \int dr q(\mathbf{r}) \Psi(\mathbf{r}) + \int d\mathbf{r} \rho_i(\mathbf{r}) [v_i(\mathbf{r}) - \mu_i] \quad (1)$$

where  $G$  is a unique (but unknown) functional of the ionic densities  $\rho_i(\mathbf{r})$ ,  $v_i$  is the non-electrostatic part of the external potential, and  $q(r) = \int_0^r \sum e_i \rho_i(r) dr + q_s$  is the total local charge density, with  $e_i$  being the charge of the ion of species  $i$ .  $q(\mathbf{r})$  is related to the mean electrostatic potential  $\psi(\mathbf{r})$  through Poisson's equation



$$\nabla^2 \Psi(\mathbf{r}) = -\frac{4\pi}{\varepsilon} \rho(\mathbf{r}) \quad (2)$$

where  $\varepsilon$  is the dielectric constant of the medium. Combining Equations 1 and 2 leads to

$$\Omega = G[\{\rho_i\}] + \frac{1}{2} \int d\mathbf{r} q(\mathbf{r}) \Psi(\mathbf{r}) - \frac{\varepsilon}{8\pi} \int d\mathbf{r} |\nabla \Psi(\mathbf{r})|^2 + \int d\mathbf{r} \rho_i(\mathbf{r}) [v_i(\mathbf{r}) - \mu_i] \quad (3)$$

The equilibrium density profile requires  $\delta\Omega/\delta\rho_i(\mathbf{r})=0$ , so that

$$\frac{\delta G}{\delta \rho_i(r)} + e_i \Psi(r) + v_i(r) = \mu_i \quad (4)$$

Also, Poisson's equation implies (Evans and Sluckin, 1980)

$$\frac{\delta \Omega}{\delta \Psi(\mathbf{r})} = 0 \quad (5)$$

$G[\{\rho_i\}]$  is calculated using a perturbative approach by making a functional Taylor expansion of the excess part of  $G[\{\rho_i\}]$  in powers of  $\Delta\rho_i(\mathbf{r}) = \rho_i(\mathbf{r}) - \rho_i^\infty$ , where  $\rho_i^\infty$  refers to the homogeneous neutral fluid far from the surface. In this way,

$$G^{ex}[\{\rho_i\}] = G[\{\rho_i\}] - F_{id}[\{\rho_i\}]$$

$$= \int dr g^{ex}(\{\rho_i\}) + \tilde{\mu}^{ex} \int dr \Delta \rho_i(\mathbf{r}) - \frac{kT}{2} \int dr dr' c_{ij}^{sr} |r - r'| \times \Delta \rho_i(r) \Delta \rho_j(r') - \dots \quad (6)$$

where the relationships between the functional derivatives of  $G^{ex}$  and the non-Coulombic part of the direct correlation functions  $c_{ij}^{sr}$ ,  $c_{ijk}^{sr}$ , ... have been used.  $\tilde{\mu}_i^{ex}$  is the contribution to the excess chemical potential arising from the non-Coulombic terms, which is defined as

$$\tilde{\mu}_{ij}^{ex} = \mu_i^{ex} - e_i \Psi(bulk) \quad (7)$$

and  $g^{ex}$  is the helmholtz excess free-energy density of the uniform ionic mixture minus the electrostatic self-energy.  $c_{ij}^{sr}$  is written as

$$c_{ij}^{sr} = c_{ij}^{HS} + \Delta c_{ij} \quad (8)$$

where  $c_{ij}^{HS}(\mathbf{r})$  is the direct correlation function of the corresponding uniform hard-sphere fluid. The direct correlation functions of other orders in Equation 6 are treated in a similar way. By summing up the hard-sphere contributions of all orders and neglecting the higher-order terms ( $\Delta c_{ijk}^{(n)}$  with  $n > 2$ ),  $G$  is obtained as

$$G[\{\rho_i\}] = F_{HS}[\{\rho_i\}] + \int dr [g(\{\rho_i\}) - f_{HS}] + (\tilde{\mu}_i - \mu_{i,HS}) \int dr \Delta \rho(\mathbf{r}) - \frac{kT}{2} \int dr dr' \Delta c_{ij}(|r - r'|) \Delta \rho_i(r) \Delta \rho_j(r') \quad (9)$$

where  $\mu_{i,HS}$  and  $f_{HS}$  are the chemical potential and Helmholtz free-energy density of the uniform hard-sphere fluid, respectively. The final equation for the equilibrium density profile is written as:

$$-kT \ln \left[ \frac{\rho_i(r)}{\rho_i^\infty} \right] = v_i(r) + \left[ \frac{\delta F_{HS}^{ex}}{\delta \rho_i(r)} - \mu_{i,HS}^{ex} \right] + e_i [\Psi(r) - \Psi(\infty)] - kT \int dr' \Delta c_{ij}(|r - r'|) \Delta \rho_j(r') \quad (10)$$

The bulk properties of the fluid are calculated using the mean-spherical approximation (MSA) (Waisman and Lebowitz, 1972), which yields reasonably accurate analytical expressions for the direct correlation functions. The density profiles of the ions near the charged surface are obtained from the simultaneously solution of Equations 10 and 2, according to the standard Picard iteration method.

## RESULTS AND DISCUSSION

### The Diffuse Layer Model

The same system studied first by Torrie and Valleau (1980) and later by many others was investigated here, which corresponds to a 1:1 electrolyte at a bulk concentration  $c = 1$  M, with ion diameter  $d = 4.25$  Å,  $T = 298$  K, and a high reduced surface charge density  $q_s^* = q_s d^2 / e = 0.7$ . In dimensionless terms, the ion density, potential, and electron charge become  $\rho^* = \rho d^3$ ,  $\psi^* = e\psi/kT$ , and  $e^* = (e^2 / \epsilon k T d)^{1/2}$ , respectively. In this restricted primitive model of the double layer, the ions are represented as charged hard spheres next to a uniformly charged planar wall, and the solvent is assumed to be a dielectric continuum. This system is modeled with the DFT

described above. The resulting ionic and potential distributions are shown in Figures 1 and 2, respectively.

The DFT results are comparable to those published by others, in that the formation of a second layer besides an inner layer is apparent. But the magnitude of the second peak predicted by the current DFT model is slightly higher than that predicted by molecular simulations (Torrie and Valleau, 1980). This is not uncommon, however, as many different studies have predicted different heights of the second peak (Nielaba and Forstmann, 1985; Ballone et al., 1986; Mier-Teran et al., 1990; Tang et al. 1990; Caillol and Levesque, 1991; Kierlik and Rosinberg, 1991), suggesting that different approximations of the electrostatic interactions have a significant impact on the magnitude of this second peak. As a consequence of the slightly higher ionic distribution, the diffusion layer potential predicted from the current DFT model is also slightly higher than that predicted from molecular simulations.

Many authors have used the so called “contact theorem” (Henderson, et al. 1979) to check the accuracy of their models, which is given by

$$kT \sum_i \rho_i(0) = P + \frac{2\pi q_s^2}{\epsilon} \quad (11)$$

With  $q_s^* = 0.7$ , the total ionic density at the wall predicted from Equation 11, the DFT approach, and the Gouy-Chapman model are shown in Table 1, along with some results from the literature. All of the values are very close to each other, indicating consistency between the different models. However, are the values physically realistic? Taking as an example, the counter-ion density from DFT,  $\rho_i(0)/\rho_i(\text{bulk}) \cong 109$ , it is easy to determine that this value corresponds approximately to  $\rho_i^*(0) = 5.0$  when  $c(\text{bulk}) = 1 \text{ M}$ . Physically, a  $\rho_i^*(0) = 5.0$  implies that five

hard-spheres with diameter  $d$  exist within a volume of  $d^3$ , which is physically unrealistic, even for a multi-valence ion.  $\rho_i^*(0)$  should not exceed that corresponding to the ideal maximum close packing of a monolayer of hard spheres. For hexagonal close packing, it is easy to determine that  $\rho_i^*(0) = 2/\sqrt{3}$ , which is slightly greater than unity! Hence, in a 1:1 electrolyte solution that is typical of an electrochemical system, valences greater than two are extremely rare. Therefore, in a practical sense, this analysis suggests that the use of  $q_s^* = 0.7$  in the diffuse layer model is too high at least for practical electrochemical systems. The question that needs to be answered is: What is a reasonable value of  $q_s^*$ ? As shown below, even when accounting for the effect of the Stern layer, a value of  $q_s^* = 0.7$  is still too large, but only by about a factor of about two.

### The Stern Layer Model

It is well known that the diffuse layer model over predicts the surface charge density, because it ignores the potential drop that occurs across it. Clearly, this over prediction carries through in predicting the double layer capacitance from the diffuse model. For example, the diffuse layer capacitance predicted from DFT in this work is about  $300 \mu\text{F}/\text{cm}^2$ , which is an order of magnitude higher than that obtained experimentally. It is noteworthy that the differential capacitances reported by Ballone et al., (1986) for the same system are also exceedingly high. Even if the surface charge density is decreased to the point where the predicted counter-ion density at the wall is physical realistic (see below), the results are still too high. This particular problem may be alleviated, however, by accounting for the potential drop across the Stern layer, as follows.

Because of the finite size of the ion, there is a plane of closest approach, the so called “Stern plane”, within which no ions may exist (Usui, 1984). If it is assumed that no specific adsorption occurs in the Stern layer, then it effectively lies at  $x = d/2$ , as shown in Figure 3.

Since there is no charge within the Stern layer, the potential drop across it should be linear (Equation 2). The potential at  $x = 0$  is related to the surface charge by

$$\left( \frac{d\psi}{dx} \right)_{x=0} = - \frac{4\pi q_s}{\epsilon_s} \quad (12)$$

where  $\epsilon_s$  is the dielectric constant of the Stern layer, which is calculated from (James and Healy, 1972)

$$\epsilon_s = \left( \frac{\epsilon_{bulk} - 6}{1 + (1.2 \times 10^{-17}) (d\Psi / dx)^2} \right) + 6 \quad (13)$$

The value of  $\epsilon_s$  obtained here is 7.14, which is very close to that obtained by Devanathan for a similar system (Devanathan et al., 1965). Moreover, when taking into account the Stern layer, the predicted double layer capacitance decreases to about  $27 \mu\text{F}/\text{cm}^2$  at a wall potential of 1V, which is a reasonable value.

These results show that the diffuse layer potential drop is very small compared with that in the Stern layer, especially at high surface charge densities. Considering the previous case of  $q_s^* = 0.7$ , the diffuse layer potential drop is 0.17 V, while the Stern layer potential drop is 2.07 V. This corresponds to a wall potential of 2.24 V. But this is too high, especially since the dielectric constant of the medium clearly corresponds to an aqueous system, which is limited to about 1.4 V to avoid electrolysis of the water. In fact, Zheng et al. (1997) reported reasonable voltages for aqueous-based capacitor systems to be around 0.8 V for carbon electrodes and around 1.0 V for  $\text{RuO}_2 \cdot x\text{H}_2\text{O}$  electrodes. These results suggest that  $q_s^* = 0.7$  is unachievable in

an aqueous solution, without excessive reactions occurring at the electrodes. Figure 4 shows how the counter-ion density near the wall changes with the surface charge density.

The counter-ion density at the wall (more precisely at  $x = d/2$ ) increases with increasing surface charge density. As stated earlier, the upper limit for the ion density is that corresponding to a monolayer of close packed hard spheres in a hexagonal arrangement ( $\rho^* = 1.15$ ). However, because of the motion of the ion and solvent molecules, and also because of the rapid decrease in the density with respect to  $x$ , this ideal close packing arrangement is practically impossible to achieve. Nevertheless, it is reasonable to assume an upper physically realistic limit as the value above. This means that there is at most approximately one ion inside a cubic box of volume  $d^3$ . Figure 4 shows that if  $q_s^* < 0.3$ , the density profiles predicted from DFT stay within this physically realistic limit. When  $q_s^* = 0.3$ , the calculated wall potential also equals 1.0 V, which is in agreement with the upper limit of the potential reported by Zheng et al. (1997) for aqueous-based capacitors.

In conclusion, the DFT model presented here does very well in predicting reasonable values of the double layer capacitance of aqueous-based systems, based on the restricted primitive model of the double layer. But this is true only when the surface charge density ( $q_s^*$ ) is limited to physically realistic values of around 0.3 or less, and also when the effect of the Stern layer is accounted for in the analysis. The other models discussed in this work should also give reasonable values under these circumstances.

#### ACKNOWLEDGEMENT

This material is based upon work supported by the U. S. Army Research Office under Grant No. DAAH04-96-1-0421.

## NOMENCLATURE

$C$	electrolyte bulk concentration, mol/l
$C_{ij}$	direct correlation functions
$d$	ion diameter, Å
$e_i$	charge of ion $i$
$F$	Helmholtz free energy, J
$k$	Boltzmann constant, $6.61617 \times 10^{-23}$ J/K
$q(r)$	local charge density, C/m <sup>2</sup>
$q_s$	external charge density, C/m <sup>2</sup>
$r$	distance between two molecules, Å
$T$	temperature, K
$V_i$	external potential for species $i$ , J
$x$	distance between ion center and charged surface, Å

### Greek Symbols

$\Omega$	grand potential functional, J
$\varepsilon$	dielectric constant
$\mu_i$	chemical potential of species $i$ , J
$\pi$	3.1415926536
$\rho_i$	fluid density of species $i$ , Å <sup>-3</sup>
$\rho^0, \rho^\infty$	bulk density, Å <sup>-3</sup>
$\psi$	mean electrostatic potential, V

## REFERENCES



- Ballone, P.; Pastro, G.; Tosi, M. P. Restricted primitive model for electrical double layers: Modified HNC theory of density profiles and Monte Carlo study of differential capacitance. *J. Phys. Chem.* **1986**, 85, 2943.
- Caccamo, C.; Pizzimenti, G. An Improved Closure for the Born-Green-Yvon Equation for the Electric Double Layer. *J. Chem. Phys.* **1986**, 84, 3327.
- Caillol, J. M.; Levesque, D. Numerical Simulations of homogeneous and inhomogeneous ionic systems: An efficient alternative to the Ewald Method. *J. Chem. Phys.* **1991**, 94, 597.
- Davis, H. T. Statistical Mechanics of Phases, Interfaces, and Thin Films; VCH: New York, 1997.
- Evans, R.; Sluckin, T. J. A Density Functional Theory for Inhomogeneous Charged Fluids Application to the Surfaces of Molten Salts. *Mol. Phys.* **1980**, 40, 413.
- Gileadi, E.; Kirowa-Eisner, E., Penciner, J. *Interfacial Electrochemistry*. Addison-Wesley: Massachusetts, **1975**.
- Henderson, D.; Blum, L.; Lebowitz, J. L. An Exact Formula for the Contact Value of the Density Profile of a System of Charged Hard Spheres Near a Charged Wall. *J. of Electroanal. Chem. Interfacial Electrochem.* **1979**, 102, 315.
- Kierlik, E.; Rosinberg, M. L. Free-energy Density Functional for the inhomogeneous Hard-sphere Fluid: Application to Interfacial Adsorption. *Phys. Rev. A* **1990**, 42, 3382.
- Kierlik, E.; Rosinberg, M. L. Density-functional Theory for inhomogeneous fluids: Adsorption of Binary Mixtures. *Phys. Rev. A* **1991**, 44, 5025.
- Mier-y-Teran, L.; Suh, S. H.; White, H. S.; Davis, H. T. A nonlocal Free-energy Density Functional Approximation for the Electrical Double Layer. *J. Chem. Phys.* **1990**, 92, 5087.
- Nielaba, P.; Forstman, F. Packing of Ions near an Electrolyte-electrode Interface in the HNC/LMSA Approximation to the RPM Model. *Chem. Phys. Lett.* **1985**, 117, 46.

- Tang, Z.; Mier-y-Teran, L.; Davis, H. T.; Scriven, L. E.; White, H. S. Non-local Free-energy Density-functional Theory Applied to the Electrical Double Layer Part I: Symmetrical Electrolytes. *Mol. Phys.* **1990**, 71, 369.
- Torrie, G. M.; Valleau, J. P. Electrical Double Layer. I. Monte Carlo Study of a Uniformly Charged Surface. *J. Chem. Phys.* **1980**, 73, 5807.
- Usui, S. Electrical Double Layer. In *Electrical Phenomena at Interfaces*; Kitahara, A and Wantanabe, A., Ed.; Marcel Dekker: New York, 1984.
- Waisman, E.; Lebowitz, J. L. Mean Spherical Model Integral Equation for Charged Hard Sphere I. Method of Solution. *J. Chem. Phys.* **1972a**, 56, 3086.
- Waisman, E.; Lebowitz, J. L. Mean Spherical Model Integral Equation for Charged Hard Sphere II. Results. *J. Chem. Phys.* **1972b**, 56, 3093.
- Zheng, J. P.; Huang, J.; Jow, T. R. The Limitations of Energy Density for Electrochemical Capacitors. *J. Electrochem. Soc.* **1997**, 144, 2026.

Table 1. Counter-ion density at  $x = d/2$  as predicted from different models.

Method	$\rho_i(d/2)/\rho_i(\text{bulk})$	Source
DFT	109.4	This work
Modified GC Model	113.9	This work
Contact Theorem (CT)	114.0	This work
Molecular Simulation	109.2	Caillol and Levesque (1991)
BGY	115.55	Caccamo et al. (1986)
Modified HNC	$\pm 0.5\%$ of CT results	Ballone, et al. (1986)

## FIGURE CAPTIONS

- Figure 1. Ionic density profiles predicted from a DFT analysis based on a restricted primitive diffuse layer model with  $d = 4.25 \text{ \AA}$ ,  $\epsilon = 78.5$ ,  $T = 298$ , and the wall located at  $x = -d/2$ , and for a 1:1 electrolyte near a charged wall with reduced surface charge density  $q_s^* = 0.7$  and bulk concentration  $c = 1 \text{ M}$ .
- Figure 2. Potential distribution predicted from a DFT analysis based on a restricted primitive diffuse layer model with  $d = 4.25 \text{ \AA}$ ,  $\epsilon = 78.5$ ,  $T = 298$ , and the wall located at  $x = -d/2$ , and for a 1:1 electrolyte near a charged wall with reduced surface charge density  $q_s^* = 0.7$  and bulk concentration  $c = 1 \text{ M}$ .
- Figure 3. Schematic representation of the ionic distribution near a charged wall, and the corresponding electric potential of the diffuse and Stern layers.
- Figure 4. Dependence of the reduced counter-ion density at  $x = d/2$  on the surface charge density.

